UNIVERSITY OF CAPE TOWN

Thesis submitted in fulfilment of the requirements for the degree of
Master of Science in Engineering M.Sc. (Eng.) in the
Department of Electrical Engineering

Online condition monitoring of Lithium-ion and Lead acid batteries for renewable energy applications

Author
Olakunle O. Alao

Supervisor
Prof. Paul Barendse

October 1, 2018

Declaration

I know the meaning of plagiarism and declare that all the work in the document, save for that which is properly acknowledged, is my own. This thesis/dissertation has been submitted to the Turnitin module (or equivalent similarity and originality checking software) and I confirm that my supervisor has seen my report and any concerns revealed by such have been resolved with my supervisor.

Signed by candidate

Olakunle Oluwatosin Alao

October 2018

Acknowledgements

I am most grateful to Almighty God for the grace He has given me to complete this study, and to the Management of University of Cape Town for creating a safe and conducive learning environment.

I am grateful to my supervisor – Paul Barendse, for his guidance, support, meticulous reviews and endless encouragement over the course of this journey.

I am thankful to the Advanced Machines and Energy Systems (AMES) group, the Dutkiewicz Family and the University of Cape Town Postgraduate Office for funding my studies.

I am grateful to my parent – Williams and Esther for their love and moral support and to my siblings – Kayode and Kolade, who through their several inputs, have made this a dream come true.

I am indebted to Chris Wozniak, Phillip Titus and all other AMES technicians for their technical assistance and for providing electrical and electronic components for my experimental set-up.

Finally, a hearty appreciation goes to Jennifer Owie, Kenechukwu Ezenwa, Kehinde Awodele, David Otu, Ebere Judith, Olufemi Olayiwola, Sean Moore, Wikus Kruger, Anton Eberhard, Lauren Basson, Fabusuyi Aroge, Akinola Ajayi-Obe, Emmanuel Balogun, Shireen Sabodien, John Mushenya and every staff of MIRA for their contribution to this project.

Abstract

Electrochemical Impedance Spectroscopy (EIS) has been largely employed for the study of reaction kinetics and condition monitoring of batteries during different operational conditions, such as: Temperature, State of Charge (SoC) and State of Health (SoH) etc. The EIS plot translates to the impedance profile of a battery and is fitted to an Equivalent Electric Circuit (EEC) that model the physicochemical processes occurring in the batteries. To precisely monitor the condition of the batteries, Kramers-Kronig relation: linearity, stability and causality as well as the appropriate perturbation amplitude applied during EIS should be adhered to. Regardless of the accuracy of EIS, its lengthy acquisition time makes it impracticable for online measurement. Different broadband signals have been proposed in literature to shorten EIS measurement time, with different researchers favouring one technique over the other. Nonetheless, broadband signals applied to characterize a battery must be reasonably accurate, with little effect on the systems instrumentation.

The major objective of this study is to explore the differences in the internal chemistries of the lithium-ion and lead acid batteries and to reduce the time associated with their condition monitoring using EIS. In this regard, this study firstly queries the methodology for EIS experiments, by investigating the optimum perturbation amplitude for EIS measurement on both the lead acid and lithium-ion batteries. Secondly, this study utilizes electrochemical equations to predict the dynamics and operational conditions associated with batteries. It also investigates the effect of different operational conditions on the lead acid and lithium-ion batteries after EEC parameters have been extracted from EIS measurements. Furthermore, different broadband excitation techniques for rapid diagnostics are explored.

An online condition monitoring system is implemented through the utilization of a DC-DC converter that is used to interface the battery with the load. The online system is applied alongside the different broadband signals. The deviation in the broadband impedance spectroscopy result is compared against the Frequency Response Analyzer (FRA) to determine the most suitable technique for battery state estimation. Based on the comparisons, the adoption of a novel technique – Chirp Broadband Signal Excitation (CBSE) is proposed for online condition monitoring of batteries, as it has the advantage of being faster and precise at the most important frequency decade of the impedance spectrum of batteries.

Contents

Declaration i
Acknowledgements ii
Abstract iii
List of Figures viii
List of Tables xii
Nomenclature xiii
1. INTRODUCTION 1
1.1 BACKGROUND TO THE STUDY 1
1.2 RESEARCH QUESTIONS 2
1.3 OBJECTIVES OF STUDY 3
1.4 SCOPE AND LIMITATIONS OF STUDY 3
1.5 PLAN OF DEVELOPMENT 3
1.6 RESEARCH OUTPUTS 5
1.7 REFERENCES 5
2. REVIEW OF ELECTROCHEMISTRY, BATTERY TECHNOLOGIES AND MEASUREMENT TECHNIQUES 6
2.1 ELECTROCHEMICAL SYSTEMS 6
2.1.1 Thermodynamics of an Electrochemical System 7
2.1.2 Nernst Equation 8
2.1.3 Over-potential & Polarization 9
2.1.4 Butler-Volmer Equation 10
2.2 BATTERY TECHNOLOGIES 10
2.2.1 Lead-acid Battery 12
2.2.2 Lithium-ion Battery 16
2.3 MEASUREMENT TECHNIQUES 20
2.3.1 Internal (DC) Resistance 21
2.3.2 Coulomb counting 21
2.3.3 Open Circuit Voltage 21
2.3.4 Electrolyte concentration 22

2.3.5 Model-based estimation 23
2.3.6 Impedance parameters 24
2.3.7 Step response 25
2.3.8 Data-driven method 25
2.4 SUMMARY 27
2.5 REFERENCES 27
3. ELECTROCHEMICAL IMPEDANCE SPECTROSCOPY 31
3.1 EIS METHODOLOGY 32
3.2 IMPEDANCE SPECTROSCOPY DATA REPRESENTATION 34
3.3 EQUIVALENT CIRCUIT ELEMENTS 35
3.4 IMPEDANCE STUDY ON BATTERY CHEMISTRIES 39
3.4.1 Lithium-ion Battery 39
3.4.2 Lead acid Battery 42
3.5 EIS IMPLEMENTATION 45
3.5.1 Cell Conditioning and Frequency Selection 45
3.5.2 Sampling Rate and Recovery Period 46
3.5.3 Filter and Windowing 46
3.5.4 EIS curve fitting to Equivalent Circuit 47
3.6 SUMMARY 49
3.7 REFERENCES 49
4. BROADBAND EXCITATION IMPLEMENTATION 52
4.1 MULTISINE EXCITATION 53
4.1.1 Frequency Optimization 55
4.1.2 Amplitude Optimization 56
4.1.3 Phase Optimization 58
4.1.4 Multisine implementation 59
4.2 CHIRP BROADBAND EXCITATION 60
4.2.1 Short-time Fourier Transform (STFT) 61
4.2.2 Resolution Optimization 62
4.2.3 Chirp Implementation 64
4.3 PSEUDO-RANDOM BINARY SEQUENCE 64

4.3.1 Selection of PRBS length 66
4.3.2 PRBS Design and Optimization 67
4.3.3 PRBS Implementation 69
4.4 SUMMARY 70
4.5 REFERENCE 71
5. ONLINE CONDITION MONITORING SYSTEM IMPLEMENTATION 72
5.1 EXISTING ONLINE CONDITION MONITORING SYSTEMS 72
5.2 ONLINE CONDITION MONITORING TOPOLOGY 75
5.3 POWER CONVERTER DESIGN AND OPERATION 77
5.4 POWER STAGE MODELLING 80
5.4.1 State Variable Modelling 81
5.4.2 Transfer Function Derivative 83
5.5 ELECTRONIC COMPONENT SELECTION 84
5.6 IMPEDANCE SPECTROSCOPY ON POWER CONVERTER 87
5.6.1 Pulse Width Modulation (PWM) generation 87
5.6.2 Analog Signal Filter and LEM Current Transducer Design 88
5.7 POWER CONVERTER CONTROL 90
5.8 SUMMARY 101
5.9 REFERENCE 102
6. HARDWARE SET-UP 104
6.1 BATTERY CELLS 104
6.2 COMMERCIAL EIS EQUIPMENT SET-UP 107
6.2.1 Potentiostat/Galvanostat (PGSTAT) 109
6.2.2 Frequency Response Analyzer 110
6.2.3 Current Booster 110
6.2.4 Voltage Multiplier 111
6.3 ONLINE CONDITION MONITORING SET-UP 112
6.3.1 Electronic Load 112
6.3.2 Data acquisition & Signal generation 113
6.3.3 Power Electronics 114
6.4 SUMMARY 116

6.5 REFERENCE 116
7. RESULTS AND DISCUSSIONS 117
7.1 OPTIMUM PERTURBATION AMPLITUDE OF EIS MEASUREMENTS 117
7.2 CHARACTERIZATION OF BATTERIES 118
7.3 ONLINE CONDITION MONITORING OF BATTERIES 123
7.3.1 Broadband IS (offline) 123
7.4 SUMMARY 127
7.5 REFERENCES 127
8. CONCLUSION AND RECOMMENDATIONS 129
8.1 CONCLUSION 129
8.2 RECOMMENDATIONS 130
9. APPENDIX 131
9.1 APPENDIX A – LABVIEW SIGNAL DESIGN 131
9.2 APPENDIX B – MATLAB CODE AND SIMULATION 134
9.3 APPENDIX C – EIS SIGNAL DESIGN 139
9.4 APPENDIX D – BROADBAND SIGNAL DESIGN 141
9.5 APPENDIX E – REAL-TIME IMPEDANCE SPECTROSCOPY 143

List of Figures

Fig 1.1 Comparison of lead acid and lithium NCM against power and energy density [2] 1
Fig 1.2 Organization of dissertation.....4
Fig 2.1 Polarization curve [9] 9
Fig 2.2 Chemical reaction of a lead acid battery at the negative electrode [10].....13
Fig 2.3 Chemical reaction of a lead acid battery at the positive electrode [10].....13
Fig 2.4 Summary of the elements of a lithium-ion battery [13] 16
Fig 2.5 Charge/discharge reaction of a lithium-ion battery [18] 17
Fig 2.6 The interaction and flow of information between states that are estimated in a BMS [26].....20
Fig 2.7 Discharge curve of lithium-ion phosphate (LFP) battery at room temperature [28]...22
Fig 2.8 Charge/Discharge effect on electrolyte concentration of a lead acid battery [28] 23
Fig 2.9 Equivalent circuit model [31].....23
Fig 2.10 1-Dimension electrochemical/mathematic model of a Lithium ion cell 24
Fig 2.11 (a) equivalent electric circuit (b) potential response to a current step.....25
Fig 3.1 (a) Sinusoidal current response for the conventional EIS technique applied in a linear system [5] (b) Lissajous curve, indicating linearity of the system [7].....32
Fig 3.2 Harmonic oscillations due to nonlinear transfer function of sinusoidal response signal [11].....33
Fig 3.3 Nyquist plot with a single time constant [6].....34
Fig 3.4 Bode plot with a single time constant (a) impedance magnitude against log frequency (b) phase angle against log frequency [5] 35
Fig 3.5 Representation of the semi-circle depression [13] 38
Fig 3.6 (a) Schematic representation of a Li-ion battery (b) Comprehensive equivalent electric circuit; (c) Simplified equivalent electric circuit of the Nyquist plot (d) Nyquist plot of a typical Lithium-ion battery 40
Fig 3.7 EIS plot of different lithium-ion chemistry at varying state-of-charge (a) [24], (b) [27], (c) [28], (d) [25] 41
Fig 3.8 EIS plot of different lithium-ion chemistry at varying temperature (a) [26], (b) [28] 42
Fig 3.9 EIS plot of different lithium-ion chemistry (a) varying DC current [24](b) varying cycles [27].....42
Fig 3.10 (a) Schematic representation of a Lead acid battery (b) Comprehensive equivalent electric circuit; (c) Simplified equivalent electric circuit of the Nyquist plot (d) Nyquist plot of a Lead acid.....43
Fig 3.11 (a) EIS plots of a 2 V-390 Ah lead-acid battery at different SoC [19] (b) SoC and intercept frequency relationship [17] 44
Fig 3.12 EIS plots of a 45Ah lead acid battery at different (a) charge and (b) discharge rates [22].....44
Fig 3.13 Procedure for EIS measurement. 45

Fig 3.14 Time domain excitation signal (a) before filter (b) after filter 47
Fig 3.15 EEC often used for description of the electrochemical processes and their corresponding Nyquist shape 47
Fig 3.16 Simplified EEC of (a) Lithium NCM battery and (b) Lead acid battery 48
Fig 3.17 Curve fitting of EIS plots (a) Lithium NCM (b) Lead Acid 48
Fig 4.1 Flowchart for carrying out broadband excitation measurement. 53
Fig 4.2 Unoptimized multisine signals for (a) lithium NCM battery – CF = 4.39 (b) lead acid battery – CF = 4.12 54
Fig 4.3 Frequency spectrum of the multisine signal 54
Fig 4.4 Frequency optimized multisine (a) lithium NCM – C.F = 3.43 (b) lead acid – C.F = 3.29.....56
Fig 4.5 EIS (bode) plot at 50% SoC and room temperature for lithium NCM (a) and lead acid (b).....56
Fig 4.6 Excitation amplitude against user frequencies of interest for lithium NCM (a) & lead acid (b) 57
Fig 4.7 Amplitude and frequency optimized multisine (a) lithium NCM – C.F = 3.16 (b) lead acid – C.F = 3.04.....57
Fig 4.8 Phase, amplitude and frequency optimized multisine (a) lithium NCM – C.F = 2.86 (b) lead acid – C.F =2.79 59
Fig 4.9 Effect of multisine signal optimization on EIS plot for lithium NCM (a) and lead acid (b).....60
Fig 4.10 Chirp broadband signal generated from LabVIEW software – CF = 1.4.....60
Fig 4.11 Frequency spectrum of the chirp signal.....61
Fig 4.12 Procedure for the Short-time Fourier Transformation of a non-stationary signal [2]61
Fig 4.13 Time window analysis of time domain chirp signal [2] 62
Fig 4.14 Comparison of STFT resolution for lithium NCM battery: wide window (a) - better frequency resolution and narrow window (b) - better time resolution. 63
Fig 4.15 Comparison of STFT resolution for lead acid battery: wide window (a) - better frequency resolution and narrow window (b) - better time resolution. 63
Fig 4.16 Effect of chirp signal period on EIS plot for lithium NCM (a) and lead acid (b) 64
Fig 4.17 8-bit PRBS generator.....65
Fig 4.18 Time-domain PRBS signal generated from LabVIEW 65
Fig 4.19 Power spectrum of a PRBS highlighting usable frequency band. 66
Fig 4.20 An 8-bit PRBS generator (Adapted from [3]) 67
Fig 4.21 Time-domain PRBS signal for lithium NCM at frequency bands – 0.02:0.02:3.4, C.F = 1.77 (a) and 5.865:5.865:2000, C.F = 1.74 (b) 68
Fig 4.22 Time-domain PRBS signal for lead acid at frequency bands –0.1:0.1:8.5, C.F = 1.63 (a) and 17.6:17.6:6000, C.F = 1.57 (b) 69
Fig 4.23 Effect of PRBS signal sampling selection on EIS plot for lithium NCM (a) and lead acid (b) 70

Fig 5.1 Principle of applying EIS through a power converter [3]. 73
Fig 5.2 Schematic of online EIS achieved through single perturbation cycle 73
Fig 5.3 Schematic of connection between the DC–DC converter and FCVM for online condition monitoring 74
Fig 5.4 A typical DC-DC converter system 75
Fig 5.5 Schematic of online condition monitoring system 77
Fig 5.6 Buck-boost converter 78
Fig 5.7 When buck-boost converter switch is closed (ON state): 79
Fig 5.8 When buck-boost converter switch is opened (OFF state): 79
Fig 5.9 Buck-boost converter state-variable waveforms – capacitor voltage (up) and inductor current (down) 80
Fig 5.10 Stages in the buck-boost converter modelling 81
Fig 5.11 Methodology for PWM generation 87
Fig 5.12 PWM generator configuration 88
Fig 5.13 Multisim connection of 4th order Butterworth filter. 89
Fig 5.14 Frequency response of 4th order low-pass Butterworth analog filter 89
Fig 5.15 Analog filtered current response. 90
Fig 5.16 LEM LA55 current transducer connection [19] 90
Fig 5.17 Gain and Phase margins for lithium NCM battery: GVC (a) and GIL (b) 91
Fig 5.18 Gain and Phase margins for lead acid battery: GVC (a) and GIL (b) 92
Fig 5.19 Time domain Step Response GVC (a) and GIL (b) for lithium NCM battery 93
Fig 5.20 Time domain Step Response GVC (a) and GIL (b) for lead acid battery 93
Fig 5.21 Flowchart of proposed online condition monitoring control algorithm. 94
Fig 5.22 Schematic of closed loop control 95
Fig 5.23 Frequency response of open loop and closed loop control for lithium NCM battery (a) and closed loop control at different operating conditions (b) 99
Fig 5.24 Frequency response of open loop and closed loop control for lead acid battery (a) and closed loop control at different operating conditions (b) 100
Fig 5.25 Validation of closed-loop control sensitivity to disturbances: lithium NCM battery (a) and lead acid battery (b). 100
Fig 6.1 Lithium NCM Batteries (a) and lead acid battery (b) 104
Fig 6.2 Discharge characteristics of a lithium-ion battery (a) and lead acid battery (b). 106
Fig 6.3 Experimental set-up of the Autolab Potentiostat/Galvanostat and 20A current booster. 107
Fig 6.4 Calibration to obtain (a) C1 (b) C2 108
Fig 6.5 Autolab PGSTAT electrodes with their associating colour code 108
Fig 6.6 The two (2) electrode cell setup 109
Fig 6.7 Schematic representation of the Autolab Potentiostat/Galvanostat. 110
Fig 6.8 Schematic connection of the voltage multiplying feature of the Autolab PGSTAT . 111
Fig 6.9 TTI LD400 current monitor and voltage control (a) and front view (b) 112

Fig 6.10 Schematic for the FS, GS (a) and physical connections of the BNC cable with the NI USB 6366 input and output channels (b) 113
Fig 6.11 Power electronics set-up (Top View) 114
Fig 6.12 Front view of power electronics set-up showing input and output connections. 115
Fig 6.13 Overall set-up of online condition monitoring system 115
Fig 7.1 EIS plot for lithium NCM & lead acid battery at different perturbation amplitude (% of DC current) 117
Fig 7.2 THD at different perturbation amplitude for lead acid and lithium NCM battery. 118
Fig 7.3 EIS plots for lithium NCM at varying state of charge (a) and parameter variation (b) 119
Fig 7.4 EIS plots for lithium NCM at varying temperature (a) and parameter variation (b) 120
Fig 7.5 EIS plots for lithium NCM at varying DC current (a) and parameter variation (b) 120
Fig 7.6 EIS plots for lead acid at varying state of charge (a) and parameter variation (b) 121
Fig 7.7 EIS plots for lead acid at varying temperature (a) and parameter variation (b) 122
Fig 7.8 EIS plots for lead acid at varying DC current (a) and parameter variation (b) 122
Fig 7.9 EIS plots for different broadband signals – offline (a) lithium NCM (b) lead acid 124
Fig 7.10 EIS plots for different broadband signals – online (a) lithium NCM (b) lead acid 124
Fig 9.1 THD analysis LabVIEW code 131
Fig 9.2 EIS signal generation and processing LabVIEW code 131
Fig 9.3 Broadband impedance spectroscopy processing LabVIEW code 132
Fig 9.4 Multisine generation LabVIEW code 132
Fig 9.5 Chirp signal generation LabVIEW code 133
Fig 9.6 PRBS generation LabVIEW code 133
Fig 9.7 Closed-loop control of buck-boost converter on LabVIEW 134
Fig 9.8 Buck-boost converter configuration on MATLAB simulink for lithium NCM battery 139
Fig 9.9 Buck-boost converter configuration on MATLAB simulink for lead acid battery 139
Fig 9.10 Real-time EIS plot for optimized multisine signal lithium NCM (a) and lead acid (b) 143
Fig 9.11 EIS plot from optimized chirp signal for lithium NCM (a) and lead acid (b) 144
Fig 9.12 Real-time Lithium NCM EIS plot from optimized PRBS signal at frequency bands – 0.02:0.02:3.4 and 5.865:5.865:2000 144
Fig 9.13 Real-time lead acid EIS plot from optimized PRBS signal at frequency bands – 0.1:0.1:8.5, 17.6:17.6:6000 144

List of Tables

Table 2.1 Comparison of different batteries based on certain performance metrics [14] - [16] 12
Table 2.2 Summary of the different types of lead acid batteries 15
Table 2.3 Summary of the different types of lithium-ion batteries.....19
Table 2.4 Summary of techniques for SoC, SoH and Temperature estimation.....26
Table 3.1 Common circuit elements with their defining relation and impedance. 35
Table 4.1 Design instances for PRBS length selection. 68
Table 5.1 Parameters resulting from a variation in load resistance 91
Table 5.2 Gain margin, phase margin and bandwidth values for open-loop control.....92
Table 5.3 Effect of PID Controllers on online condition monitoring control system. 96
Table 5.4 Gain margin, phase margin and bandwidth values for closed-loop control 98
Table 5.5 Gain margin, phase margin and bandwidth values for gain-tuned closed-loop control 99
Table 6.1 Specifications of the Booster20A 111
Table 7.1 Parameter extracted from FRA measurement for both offline and online investigation. 125
Table 7.2 EIS plots for varying DC current (a) and parameter variation (b) 125
Table 7.3 Key impedance parameters required for state estimation of the lithium NCM and lead acid batteries.....127
Table 7.4 Broadband signals compared against different measurement metrics for both the lithium NCM and lead acid batteries 127
Table 9.1 EIS signal design for lithium NCM battery 139
Table 9.2 EIS signal design for lead acid battery 140
Table 9.3 Multisine optimization for lithium NCM battery 141
Table 9.4 Multisine optimization for lead acid battery.....141
Table 9.5 PRBS design for lithium NCM battery.....142
Table 9.6 PRBS design for lead acid battery 142
Table 9.7 Polynomial Order for PRBS signal design 143

Nomenclature

BIS – Broadband Impedance Spectroscopy

BMS – Battery Management System

CF – Crest Factor

CNLS – Complex Non-linear Least Square

CPE – Constant Phase Element

EEC - Electrical Equivalent Circuit

EIS - Electrochemical Impedance Spectroscopy

FRA – Frequency Response Analyzer

Li-Ion - Lithium Ion

LMA – Levenberg Marquardt Algorithm

NCM – Nickel Manganese Cobalt-Oxide

NI DAQ – National Instrument Digital Acquisition

OCM – Online Condition Monitoring

OCV - Open Circuit Voltage

PGSTAT – Potentiostat/Galvanostat

PID – Proportional Integral Derivative

PRBS – Pseudo-Random Binary Sequence

PWM – Pulse Width Modulation

SEI - Solid Electrolyte Interface

SNR - Signal to Noise Ratio

SoC – State of Charge

SoH – State of Health

THD - Total Harmonic Distortion

1. INTRODUCTION

1.1 BACKGROUND TO THE STUDY

There is an insatiable demand for energy in the modern society, with more applications tending towards grid independence and mobility. Previously, the energy demand has been met by fossil fuel technologies. The increasingly diminutive nature of fossil fuel as well as greenhouse gas emissions associated with their exploitation has prompted the need for renewable (clean) energy sources. Renewable energy sources such as solar and wind are experiencing rapid growth, with most new investments in the global electricity sector focused towards their development. Due to the variability of renewable energy systems, energy storage systems must be readily available to ensure reliable, efficient and optimal operation [1]. Energy storage systems development is therefore paramount if renewable energy technologies are to supplement and eventually phase-out fossil fuel technologies.

Lead acid batteries are the oldest type of rechargeable batteries and have found applications in several industries due to their reliability, affordability and recyclability. They are used as starter batteries and for powering various electronics embedded in automobiles. They also provide back-up power to the national grid when connected with inverters [2] – [3]. On the other hand, lithium NCM, a category of the lithium-ion family has attracted the most attention due to their high energy and power density, long service life, low self-discharge rate and low pollution. Lithium NCM have found wide applications in electric vehicles: pure Electric Vehicles (EVs), Plug-in Hybrid Electric Vehicles (PHEVs) and Hybrid Electric Vehicles (HEVs) [4] – [5]. See Fig. 1.1 for the comparison of the lead acid and lithium-ion batteries against power and energy density.

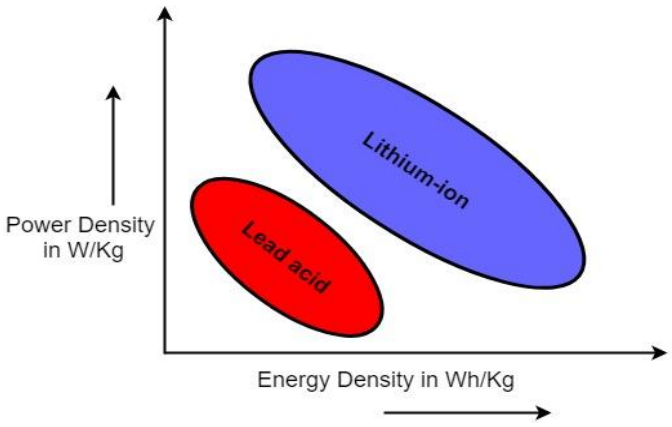

Fig 1.1 Comparison of lead acid and lithium NCM against power and energy density [2]

Considering that both batteries are applied in critical applications that require high reliability and fidelity, it is critical to accurately monitor the operational conditions of the battery: temperature, state of charge and state of health. The condition monitoring of a battery is not a straightforward process and requires thorough knowledge and understanding of the possible operational conditions that occur, and the various diagnostic methods and procedures that can be employed to estimate fault conditions. Because of the complex nature of electrochemical systems, the available methods are difficult to implement and are severely limited in terms of measurement time and accuracy. Therefore, the goal of this research is to understand the internal chemistry and operational conditions of these batteries and how they differ from each other, and design broadband signals that can quantify these operational conditions rapidly for online impedance estimation purposes.

1.2 RESEARCH QUESTIONS

The major research questions that require addressing in this thesis are as follows:

- What is currently known about the operational behaviour, electrochemistry and thermodynamics of electrochemical systems, and how does it differ for lead-acid and lithium-ion batteries?
- What are the limitations of the present and previous conventional diagnostic tools employed to estimate the state of these battery technologies?
- What state estimation techniques can be applied that will have minimal deviation from the Kramers-Kronig relations and how can this technique be optimized to further minimize the deviation from the Kramers-Kronig relations for the lead acid and lithium-ion batteries?
- What are the behaviours of the lead acid and lithium NCM battery to different operational conditions like temperature, available capacity and ageing?
- How can the time associated with the selected fault diagnostic tools employed in condition monitoring of the lead acid and lithium-ion batteries be reduced?
- How can the accuracy associated with the selected fault diagnostic tools employed in condition monitoring of the lead acid and lithium-ion batteries be increased?
- How can a condition monitoring system that closely resembles that utilized in real-life for online dynamic applications be developed?
- To what magnitude does the power converter topology that interfaces the batteries with the load affect the accuracy of the online condition monitoring system?

1.3 OBJECTIVES OF STUDY

The objectives of this study are to address the above-mentioned research questions and they are as follows:

- Develop an understanding of the electrochemistry and thermodynamics of electrochemical systems in relation to lead-acid and lithium-ion batteries.
- Conduct a detailed literature review on conventional diagnostic tools employed to estimate the state of batteries; identifying the advantages and disadvantages of each technique.
- Optimize the methodological measurement process of the selected state estimation tools to ensure it is in congruence with the Kramers-Kronig relationship.
- Propose a rapid diagnostic tool that can improve accuracy and reduce measurement time for condition monitoring (state estimation) of lithium ion and lead acid batteries.
- Propose a novel system that incorporates a power converter alongside the selected rapid diagnostic tool for online condition monitoring.

1.4 SCOPE AND LIMITATIONS OF STUDY

This study is focused on online condition monitoring of lead acid and lithium NCM chemistries using EIS diagnostic technique. Therefore, other diagnostics tools were only briefly discussed in the literature review. The testing of the online condition monitoring system was also performed only under laboratory conditions.

1.5 PLAN OF DEVELOPMENT

Chapter 2: This Chapter gives a detailed analysis of the electrochemistry and thermodynamics of electrochemical systems, with a focus on batteries. It also identifies the prevalent battery technologies in the market, with emphasis on the lead acid and lithium NCM battery. Lastly, it briefly discusses the different measurement techniques that can be utilized in a Battery Management System (BMS) with their advantages and disadvantages.

Chapter 3: This Chapter discusses the EIS technique as a tool for condition monitoring of batteries. Impedance study on both lithium NCM and lead acid batteries is also studied in detail. Lastly, implementation of EIS is discussed.

Chapter 4: This Chapter describes broadband signals application for rapid condition monitoring. The time and frequency analysis of the different broadband techniques are also shown. The implementation and optimization of these techniques are also discussed.

Chapter 5: This Chapter discusses the power converter topology to be utilized for the online condition monitoring system. Also discussed is the design of the different components of the online condition monitoring system.

Chapter 6: This Chapter presents the hardware and experimental setup. It discusses the individual connections and the overall hardware set-up for both the low-cost, commercial EIS equipment and online condition monitoring system.

Chapter 7 and 8: This Chapter presents the results, discussions and conclusion from the experiments.

The outline of this research is summarized as below:

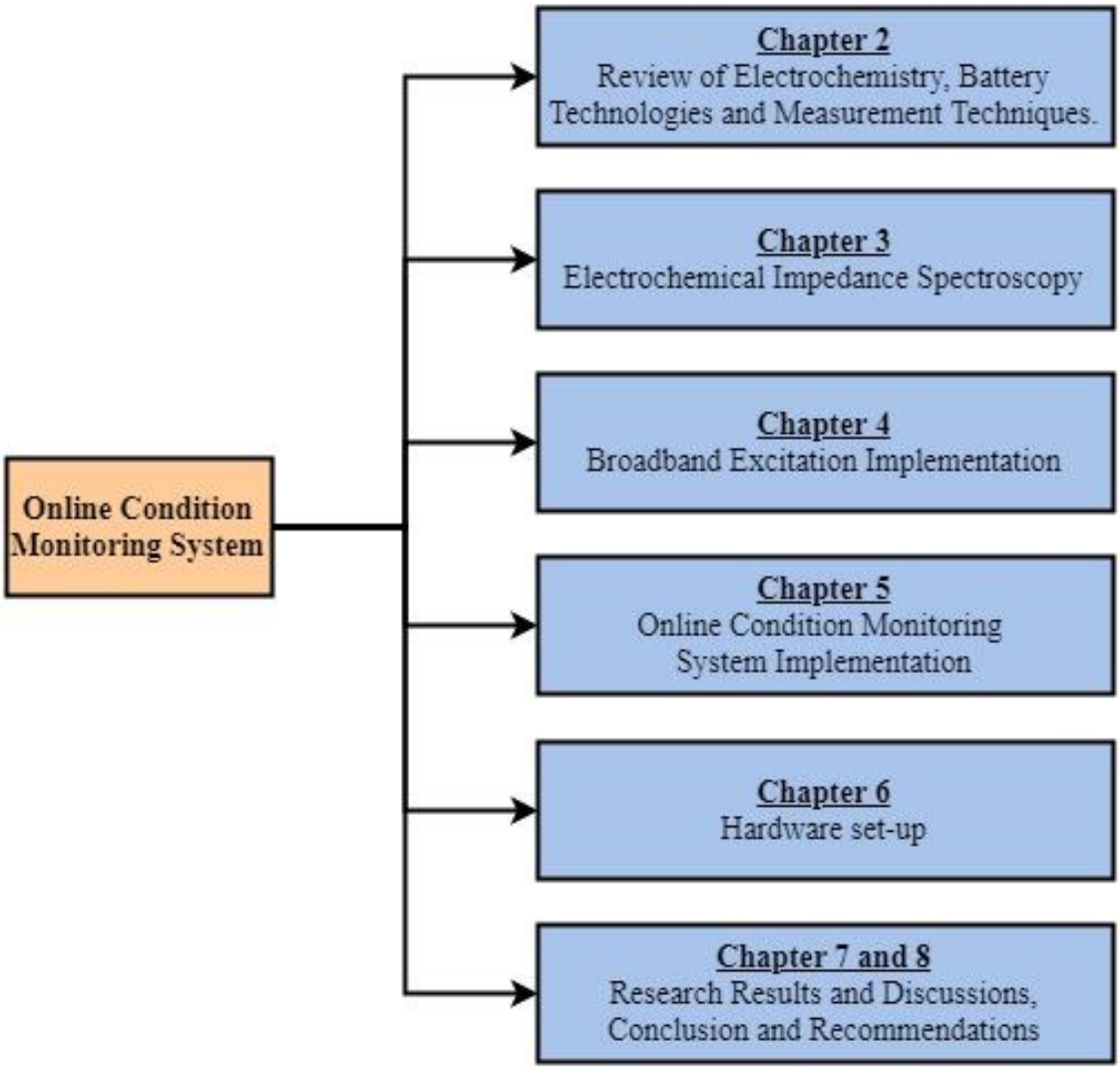

Fig 1.2 Organization of dissertation

1.6 RESEARCH OUTPUTS

Conference Publications:

(a) Olakunle Alao & Paul Barendse, "Characterization of Lithium NCM and Sealed Lead Acid Batteries using Electrochemical Impedance Spectroscopy," IEEE Power Africa, Cape Town, South Africa, June 2018.

(b) Olakunle Alao & Paul Barendse, "Online Condition Monitoring of Sealed Lead Acid & Lithium Nickel-Cobalt-Manganese Oxide Batteries using Broadband Impedance Spectroscopy," ECCE – IEEE, Portland – Oregon, USA, September 2018.

Journal Publication:

(a) Olakunle Alao & Paul Barendse, "Online Impedance Estimation of Sealed Lead Acid & Lithium Nickel-Cobalt-Manganese Oxide Batteries using a Rapid Excitation Signal," IEEE Transaction on Industrial Applications. Under Review.

1.7 REFERENCES

[1] D. Klot, "Characterization and Modeling of Electrochemical Energy Conversion Systems by Impedance Techniques," Ph.D. Thesis, Karlsruher Institut Für Technologie (KIT), 2012.

[2] Ross Kerley, "Automotive Lead-Acid Battery State-of-Health Monitoring System," master's Thesis, Virginia Polytechnic Institute and State University, 2014.

[3] B. Holger, et al. "Sauer Impedance measurements on lead–acid batteries for state-of-charge, state-of-health and cranking capability prognosis in electric and hybrid electric vehicles," Power Sources, 144 (2005) 418–425.

[4] D.I Stroe, et.al. "Diagnosis of Lithium-Ion Batteries State-of-Health based on Electrochemical Impedance Spectroscopy Technique," Energy Conversion Congress and Exposition (ECCE) pp. 4576-4582, 2014.

[5] D. Andre et al, "Characterization of high-power lithium-ion batteries by electrochemical impedance spectroscopy. II: Modelling," J. Power Sources, vol. 196, pp. 5349-5356, 2011.

2. REVIEW OF ELECTROCHEMISTRY, BATTERY TECHNOLOGIES AND MEASUREMENT TECHNIQUES

2.1 ELECTROCHEMICAL SYSTEMS

Electrochemical systems convert chemical energy into electrical energy and vice versa. The term 'system' implies that the most elemental practical realization of such an energy converter, called a 'cell,' can be considered as a system [1]. The general definition of an electrochemical system is that it consists of two electrodes – anode and cathode, separated by an electrolyte. The main difference between an electrochemical reaction taking place in a cell and its associated redox (reduction-oxidation) reaction; is that reduction and oxidation do not occur at the same site but are separated by the electrolyte as two half-reactions in the so-called 'half-cells' [2] – [3].

In the electrochemical redox reaction, one reactant is an acceptor of electrons, while the other reactant is a donor of electrons and to attain electroneutrality, ions are exchanged. For an electrochemical cell, these ions are exchanged via the ionic conducting electrolyte which blocks the exchange of electrons [1] – [3]. Instead, these electrons flow through the external conductor connected to the electrode, to power the load it was intended for. The major application of an electrochemical cell is to convert chemical energy into electrical energy. These electrochemical reactions are usually reversible and the conversion results from a chemical substance with a low internal chemical energy into a substance with higher internal chemical energy [1] – [4]. An electrochemical cell with the ability to provide electrical current is called a voltaic or galvanic cell. There are three (3) types of voltaic cell namely:

- ***Primary voltaic cells***

The primary voltaic cells' electrochemical reactions are irreversible, and they contain the fuel that is used for conversion into electricity. Example includes; primary or non-rechargeable batteries.

- ***Secondary galvanic cells***

The secondary galvanic cells' reaction is reversible; they operate in both discharge mode – the conversion of electrical energy from chemical energy, and charge mode – the conversion of electrical energy to chemical energy [1]. More so, all reactants and products that take place in the reaction are all contained within the cell. The lithium-ion and lead acid batteries studied in this thesis, fall under this category.

- ***Tertiary galvanic cells***

This type of voltaic cell is usually referred to as a fuel cell. These cells function on fuels not contained in the device itself but are supplied externally [2].

2.1.1 Thermodynamics of an Electrochemical System

Thermodynamics is the study of energy changing from one state to another. Thermodynamic concepts allow for electrochemical systems state estimation, such as potential, pressure, volume and temperature. When discussing thermodynamics in electrochemical systems, there are three terms that are considered, namely: Enthalpy, Entropy and Gibbs free energy [8].

- ***Enthalpy (H)***

The absolute enthalpy of an electrochemical system consists of both its thermal energy (Δh_s) – the difference between the enthalpy reference and given state, and chemical energy or the enthalpy of formation (h_f) – the energy of the chemical bonds [3], [7]. In thermodynamics, enthalpy is expressed as the sum of the internal energy (U), the product of pressure (P) and volume (V). This is mathematically denoted as (2 – 1):

$$H = U + PV \qquad (2-1)$$

- ***Entropy (S)***

Entropy is a measure of the quantity of heat that is converted into useful work. It is defined as the extent of "disorder" in an electrochemical system [4], [8]. Entropy is mathematically expressed as (2 – 2). In (2 – 2), ΔQ is the reverse of the heat and T is temperature.

$$S2 - S1 = \left[\int_1^2 \frac{\Delta Q}{T}\right] int\ rev \qquad (2-2)$$

- ***Gibbs Free Energy (G)***

Gibbs Free Energy is the energy associated with a chemical reaction that can be used to perform work [4]. It is the energy required for a system at a constant temperature after removing the energy transferred to the environment due to heat. Gibbs Free Energy is expressed as the difference between enthalpy (H) and the product of temperature (T) and entropy (S). This is mathematically expressed as (2 – 3):

$$G = H - TS \qquad (2-3)$$

Electrochemical energy conversion is the conversion of the free energy change associated with a chemical reaction into electrical energy [10]. This free energy change quantifies the

maximum electrical work (W_{elec}) that can be performed by a system at a constant pressure and temperature. In (2 – 4) – (2 – 7), (W_{elec}) is the maximum electrical work, *n* is the number of moles, *F* is Faraday's constant and *E* is the equilibrium voltage. *G*, *H*, *T* and S retain their definitions.

$$W_{elec} = nFE \quad (2-4)$$

$$\Delta G = -nFE \quad (2-5)$$

$$W_{elec} = -\Delta G \quad (2-6)$$

$$-W_{elec} = \Delta G = \Delta H - T\Delta S \quad (2-7)$$

2.1.2 Nernst Equation

Nernst equation is a fundamental thermodynamic expression of the state of equilibrium of an electrochemical reaction. The Nernst Equation points out the reaction direction and determines the value of the thermodynamic electrode [8], [11]. In addition, it depicts the relationship between the reduction potential of an electrochemical reaction and the standard electrode potential of the chemical specie that is undergoing redox reaction. From (2 – 3), (2 – 8) can be deduced:

$$E = \frac{-\Delta G}{nF} = -\left(\frac{\Delta H - T\Delta S}{nF}\right) \quad (2-8)$$

(2 – 8) implies that the potential of an electrochemical system decreases with increasing temperature. However, other reactions such as ionic conduction and mass transport occur faster at higher temperatures, consequently offsetting the drop-in potential of the electrochemical system [4], [5].

In (2 – 9), ΔG is the actual free energy change, ΔG^o is the free energy change at standard condition, Red is the activity of products at equilibrium, Oxd is the activity of reactants at equilibrium. The Nernst Equation relates standard conditions of an electrochemical system to its actual condition [3]. From ΔG^o – Gibbs Free Energy at standard state, the maximum possible potential (E^o) of an electrochemical cell can be determined.

$$\Delta G = \Delta G^o + RT \times ln\left[\frac{Red}{Oxd}\right] \quad (2-9)$$

(2 – 10) is the Nernst Equation. In (2 – 10), R is the universal gas constant, E is the actual cell potential and ($E^o = \frac{-\Delta G}{nF}$) is the potential at standard state. More so, the energy balance between reactants and products can be used to calculate the potential of an electrochemical system at non-standard conditions.

$$E = E^o + \frac{RT}{nF} \times ln\left[\frac{Red}{Oxd}\right] \qquad (2-10)$$

2.1.3 Over-potential & Polarization

For an electrochemical reaction, if the forward reaction rate is equal to the backward reaction rate, no net electric current is produced because the net reaction rate is zero. To obtain net current from the reaction, it is pertinent that there is a deviation from E^o – the Nernst potential. Over-potential (η) is the difference between the applied potential (E) and the Nernst potential (E^o); the higher the over potential, the higher the current [14] – [15].

$$\eta = E - E^o \qquad (2-11)$$

Polarization implies that the potential of the electrode surface deviates from equilibrium, resulting in an electrochemical reaction. The polarization curve (see Fig 2.1) determines battery performance and is represented as voltage against current density [6].

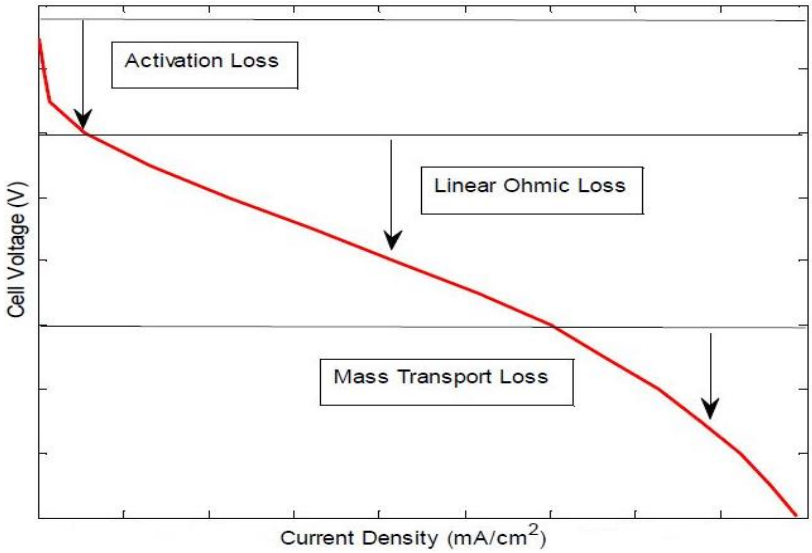

Fig 2.1 Polarization curve [9]

Polarization is composed of three (3) mechanisms, namely: activation over-potential, ohmic over-potential and mass transport over-potential. Activation over-potential and mass transport over-potential relates to the rate at which a reaction can proceed [3]. The activation over-potential is due to the kinetic effects initiated by the inherent rates of the chemical reaction. The mass transport over-potential is due to effects from the movement of reactants to the electrode. The ohmic over-potential accounts for resistive drop in the battery. The over-potential results in a deviation of the available potential of the battery from the Nernst potential that was calculated in (2.1.2) [8]. During charging, a potential greater than the Nernst potential is required and during discharging, the battery potential is lower than the Nernst potential.

Polarization has a profound impact on the efficiency of a battery and the way a battery can be discharged or charged [11]. The total losses (over-potential) in a battery which results in a shift from the ideal potential is expressed as (2 – 12):

$$V(i) = V_{Nernst} - V_{act\_anode\_and\_cathode} - V_{ohmic} - V_{conc\_anode\_and\_cathode} \quad (2-12)$$

2.1.4 Butler-Volmer Equation

The Butler-Volmer equation relates electrode potential of an electrochemical system to its reaction rate. It is essential to determine from equilibrium, the balance state of the energies of the reaction since useful net current is derived from the reaction of an electrochemical system – cell [2] – [5]. From (2 – 10), at standard state condition (equilibrium), the current density becomes the exchange current density. Thus, by deviating from equilibrium and taking into consideration different current densities, (2 – 13) and (2 – 14) are obtained:

$$j_1 = j_0(e^{\frac{\alpha nF\eta}{RT}}) \quad (2-13)$$

$$j_2 = j_0(e^{\frac{-(1-\alpha)nF\eta}{RT}}) \quad (2-14)$$

The net current j is the difference between $j1\ and\ j2, i.e. (j1 - j2)$ as shown in (2 – 15):

$$j = j_0(e^{\frac{\alpha nF\eta}{RT}} - e^{\frac{-(1-\alpha)nF\eta}{RT}}) \quad (2-15)$$

Given that a change in potential results in a change in the reaction rate, the change in reactant surface concentration and product surface concentration is taken into consideration. This is achieved by the introduction of the actual surface concentrations denoted as $(C_R^*\ and\ C_P^*)$.

$$j = j_0(\frac{C_R^*}{C_R} e^{\frac{\alpha nF\eta}{RT}} - \frac{C_P^*}{C_P} e^{\frac{-(1-\alpha)nF\eta}{RT}}) \quad (2-16)$$

(2 – 16) is the Butler-Volmer equation. It relates the current density (j), surface concentration of the reaction $(C_R^*\ and\ C_P^*)$ and over-potential (η) in an electrochemical system. The Butler-Volmer equation states that in an electrochemical reaction, an increase in activation over-potential (η) results in an exponential increase in the net current. Likewise, it implies that in an electrochemical system, there will be a voltage drop with an increase in load (current).

2.2 BATTERY TECHNOLOGIES

There are several battery chemistries available. Some of the chemistries commercially available, include:

(a) Lead Acid

(b) Nickel Metal Hydride

(c) Lithium-ion

(d) Sodium Nickel

(e) Redox flow

Battery chemistries have unique strengths and weaknesses (see Table 2.1). Some of the metrics used to compare them as in [1], [15], [19] are defined below:

i. Specific Power (W/Kg)

Specific power is the maximum permissible power per unit mass and is a metric used in determining the battery weight required to accomplish a certain performance target. It is usually a function of the chemistry and packaging of the battery.

ii. Specific Energy (Wh/Kg)

Specific energy is a ratio of a battery's nominal energy to its mass and is a metric used in determining the weight of a battery required to accomplish a certain electric range. It is a function of the chemistry and packaging of the battery.

iii. Self-discharge (%/day)

Self-discharge rate of a battery is the percentage of the initial cell capacity per day if left unused. This is an important metric in comparing battery efficiency as different battery chemistries have unique self-discharge rates.

iv. Cost ($/KWh)

This is a ratio of the cost of a battery to its energy output. This metric is used to define how cost efficient a battery is.

v. Cycle Life (Cycles)

The cycle life of a battery accounts for the number of charge-discharge cycles the battery experiences before failing to meet the design performance criteria. In the automotive industry, this stands at 80% of the battery's initial capacity.

vi. Thermal runaway (^{o}C)

Thermal runaway of a battery occurs when the internal heat rate exceeds the rate of heat expulsion. This result in a catastrophic reaction, hence, this metric is a safety indicator used to define the onset temperature of a battery.

Table 2.1 Comparison of different batteries based on certain performance metrics [14] - [16]

Battery	***Cost***	***Specific Energy***	***Specific Power***	***Cycle Life***	***Thermal Run-away***
Lead Acid					
NiMH					
NaNiCl					
NiCd					
LCO					
LMO					
NMC					
LFP					
NCA					
LTO					
Li-S					
Li-O					
Li-Polymer					

Key	*Excellent*	*Very good*	*Good*	*Fair*	*Poor*

2.2.1 Lead-acid Battery

Lead-acid batteries are constructed with two electrodes immersed in an electrolyte. The negative electrode (cathode) is made from pure lead (Pb) which is spongy or porous to expedite the formation and dissolution of lead. The positive electrode (anode) is lead dioxide (PbO_2) (i.e. an oxide where lead is in "+4" oxidation state). Both electrodes are immersed into the sulfuric acid which serves as the electrolyte [16].

(a) Lead acid battery operation

Both electrodes of the lead-acid battery (lead and lead-dioxide) are good conductors of electricity and the mechanism for conduction is through electrons jumping from one atom to the other. The electrolyte comprises of aqueous ions of $H^+ and\ SO_4{}^{2-}$ and the mechanism for conduction within the electrolyte is "ion migration" achieved through diffusion. Due to redox

reaction, there is charge transfer from ions in the solution to conducting electrons in the electrode [10].

Negative electrode surface:

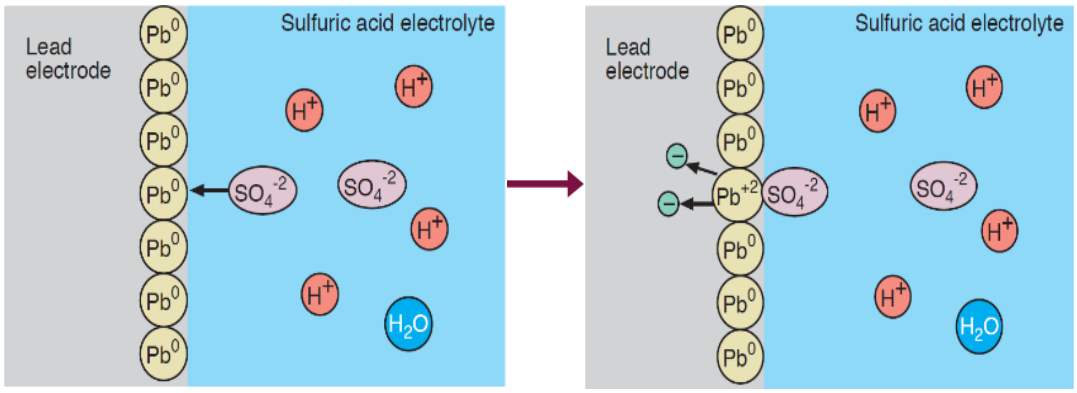

Fig 2.2 Chemical reaction of a lead acid battery at the negative electrode [10]

Fig 2.2 displays the chemical reaction (half-reaction) that occurs at the negative electrode (lead) of the lead acid battery. In Fig 2.2 (a), the uncharged lead atom on the electrode surface is approached by charged sulfate ion. This results in the ionization of the lead atom (ionic bond with sulfate ion) with two (2) electrons released into the negative electrode (lead) as Fig 2.2 (b). This reaction shown in (2 – 17), results in the release of an energy of $0.356\ eV$.

$$Pb(s) + SO_4{}^{2-}(aq) \longrightarrow PbSO_4(s) + 2e- \qquad (2-17)$$

Positive electrode surface:

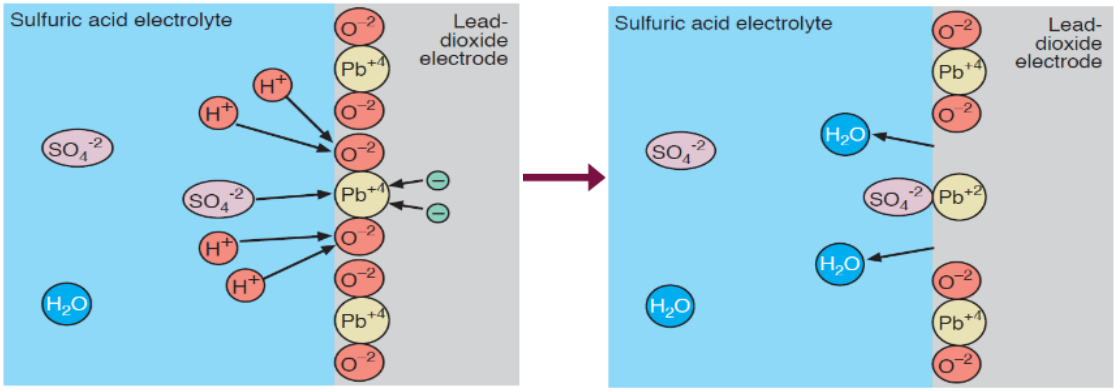

Fig 2.3 Chemical reaction of a lead acid battery at the positive electrode [10]

Fig 2.3 shows the chemical reaction (half-reaction) that occurs at the positive electrode (lead dioxide) of the lead acid battery. In Fig 2.3 (a), the lead dioxide molecule (net uncharged) at the electrode surface is approached by charged sulfate and hydrogen ions. In Fig 2.3 (b), the ionization of the lead atom is changed to form electrovalent (ionic) bond with sulphate ion, resulting in the release of two water molecules into the solution.

$$PbO_2(s) + SO_4{}^{2-}(aq) + 4H + 2e- \longrightarrow PbSO_4(s) + 2H_2O \qquad (2-18)$$

(2 – 18) results in the release of an energy of $1.685\ eV$. More so, the oxidation state of the lead atom changes from +4 to +2. Both half reactions results in coating of the electrodes (positive and negative) with lead sulphate, thus, reducing the acid electrolyte concentration. If both electrodes are placed inside an electrolyte, and there is no external electrical circuit connected across; excess electrons will be formed at the negative electrode and electron deficits will be formed at the positive electrode without a path to flow outside the cell. The system attains equilibrium at the point where the required energy to remove or deposit an electron equals the generated energy of the chemical reaction. The total battery voltage at 25^oC and at 1 molar acid electrolyte concentration is $2.041V$, expressed as the sum of the reduction potential of both electrodes.

During discharge, electrons flow from the negative to positive electrode of the cell. This results in the reduction of the charge and the electrode potential. As the battery undergoes discharging, the electrode gets coated with sulphate and becomes lead sulphate while the acid electrolyte gets weaker. During charging, electrons flow from the positive to negative electrode of the cell. This increases the charge and the electrode potential. As the battery undergoes charging, the lead sulphate coating on both electrodes get depleted while the acid electrolyte gets more concentrated [20].

(b) Types of Lead acid battery

The three (3) types of lead acid batteries are Wet cell (flooded), Gel cell, and Absorbed Glass Mat (AGM); and they are all discussed as below.

i. Wet Cell (Flooded)

The wet cell lead acid battery is of two types – serviceable and maintenance-free. Both versions are filled with electrolyte. For the serviceable version, the specific gravity can be frequently observed using a hydrometer. The advantages of this battery are its easy replaceability, low-cost and suitability for higher current applications. The disadvantages are of this battery are its proneness to spillage and its emission of corrosive gases [21] – [22].

ii. Gel Cell (Gelled Electrolyte)

The gel cell is a type of lead acid battery that constitutes a mixture of a silica gelling agent and electrolyte. This mixture results in the formation of a semi-stiff paste, originating from the

liquid interior of the cell. Gel cells have a high boiling point and a low freezing point compared to the liquid electrolytes in flooded and AGM cells. Gel cells and AGMs are usually referred to as – sealed lead acid batteries. Gel cells are safe, don't require maintenance and can be used in different orientations. The disadvantage of the gel cell is that its, "gel design," impedes the rate of ions in the electrolyte [21] – [22].

iii. Absorbed Glass Mat (Absorbed Electrolyte)

AGM is designed in such a way that the spaces between its individual cells are substituted with a glass fiber mat immersed in electrolyte. The packed mat is slightly compressed but soldered in place, enabling it to be resistant to vibration. Typically, there is an optimum amount of electrolyte in the mat that ensures its wetness; and supposing the battery is punctured, the mat disallow electrolyte outflow. Like the gel cell, the AGMs are completely sealed because the mat reduces evaporation. AGM stores charges very well and don't sulphate or degrade easily. They are mechanically strong, safe and vastly utilized in solar, audio, power sports, RV, marine and storage battery applications. Excess charging of AGMs causes gassing, venting and eventual water depletion. The AGM and Gel cell are thus unable to be charged to their full capability. Their charging voltage must also be lower than the Flooded Cell [21] – [22]. The summary of the different types of lead acid batteries is provided in Table 2.2

Table 2.2 Summary of the different types of lead acid batteries

Types of Lead acid	***Advantages***	***Disadvantages***	***Applications***
Wet cell (flooded) [21] – [22]	Low initial cost, water can be added (maintainable), suitable for high current applications and can be charged to its full capability.	Spillable, designed to operate only upright and emits corrosive gases.	High current applications.
Gel cell (gelled electrolyte) [21] – [22]	Completely maintenance free, safe and possesses a superior deep cycle life compared to AGM.	Rate of ions in the electrolyte are impeded, high initial cost and cannot be charged to its full potential.	Off-grid systems.
Absorbed Glass Mat (AGM) [21] – [22]	Completely maintenance free, mechanically strong, vibration-resistant, safe and cheaper compared to Gel cell.	Their cycle life is half that of the Wet and Gel cell. Likewise, they cannot be charged to their full potential.	Solar PV & battery etc.

2.2.2 Lithium-ion Battery

There are several materials that are used in the construction of a lithium-ion cell. The cathode of a lithium-ion is usually an oxide variant of lithium metal amalgams. Some of the commercially available lithium-ion batteries are Manganese (LMO), Nickel iron–phosphate (LFP) and Cobalt (LCO) [13], [25]. Likewise, some lithium-ion batteries contain blends of aluminum mixtures such as Nickel cobalt aluminum (NCA) and Nickel Manganese cobalt (NMC). The anode is usually a graphite. However, some other anode materials that have been utilized in consumer electronics includes silicon–carbon compounds, hard carbon, cobalt alloys, lithium titanate, tin, and silicon–carbon blends [15].

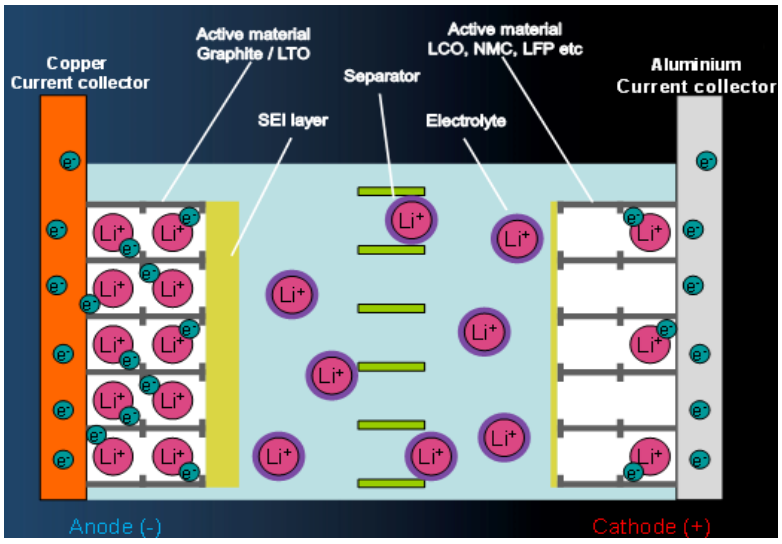

Fig 2.4 Summary of the elements of a lithium-ion battery [13]

The electrolyte of a lithium-ion chemistry is usually composed of lithium phosphate hexafluoride (lithium salt) dissolved in one of these solvents (ethyl carbonate, propene carbonate, di-methyl carbonate or ethyl-methyl carbonate) [17]. In addition, alongside the lithium salt and solvents combination; a typical lithium-ion cell has up to five additives for several purposes such as: vinylene carbonate, impedance reducers – trimethoxyboroxine, 1-3 propane sultone or wetting agents. The lithium salt stabilizes the systems, aids the transport of lithium-ion and limits side reactions that may occur. Whereas, the solvents are mixed to arrive at a compromise of a good low temperature performance, a much lower boiling point, fast transfer rate, good conductivity or passivation layers at the anode [17].

(a) Lithium-ion Operation

During the charging and discharging process in Fig 2.5, lithium-ions are intercalated and de-intercalated from the anode and cathode respectively resulting in electric current flow in

either direction. The transport process of the lithium-ions is achieved through the electrolyte of the cell.

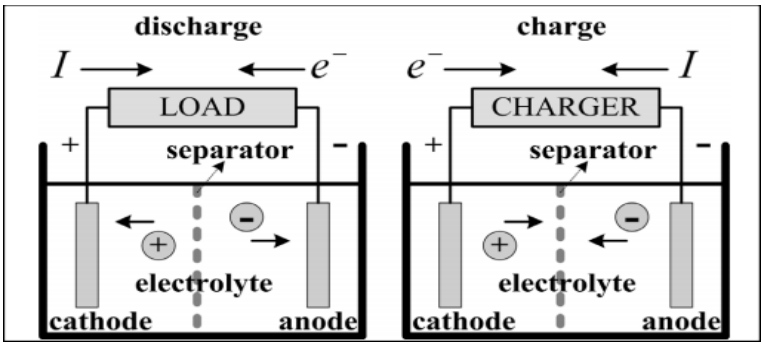

Fig 2.5 Charge/discharge reaction of a lithium-ion battery [18]

The NMC chemistry was used in this research because it is currently dominating the Electric Vehicle market – possessing a significant increase in operating voltage, energy and power capabilities [15]. The cathode side reaction of the NMC battery is shown in (2 – 19), the anode side reaction is shown in (2 – 20) and the whole process is shown in (2 – 21)

$$LiNiMnCo \rightleftharpoons Li_{1-x}\,NiMnCo + xLi^{+} + xe^{-} \quad (2-19)$$

$$6C + xLi^{+} + xe^{-} \rightleftharpoons Li_{x}6C \quad (2-20)$$

$$LiNiMnCo + 6C \rightleftharpoons Li_{1-x}\,NiMnCo + Li_{x}6C \quad (2-21)$$

(b) Types of Lithium-ion battery

Lithium-ion batteries are uniquely identified by their cathode, which are oxide variants of lithium metal amalgams. The summary of the different types of lithium ion batteries is provided in Table 2.3.

i. Lithium Cobalt Oxide

The Lithium Cobalt Oxide's (LCO) anode is made of graphite and the cathode – lithium cobalt. The Lithium Cobalt Oxide was the first lithium-ion battery to be pioneered and was first sold in 1991 by Sony. In this chemistry, the oxygen and cobalt bond to establish octahedral cobalt oxide structure layers that are separated by lithium sheets. The structure also permits cobalt ions, to alter their valence state between $Co^{+2}$and Co^{+4} during discharging and charging. Amongst all commercially available lithium-ion batteries, the LCO possesses the highest energy density, consequently enabling them find vast application in consumer electronics – phones, laptops and digital cameras. Their drawback is their limited life span and their thermal

instability. Their anodes are liable to overheating, while their cathode can decompose (i.e. producing oxygen) at high temperatures [23] – [24].

ii. Lithium Manganese Oxide

The Lithium Manganese Oxide's (LMO) anode is made of graphite, while the cathode can be made from either spinel or layered lithium manganese. The "spinel" type is more popular because the "layered" type has poor cycling stability and capacity. The structure of the spinel has good thermal stability and low internal resistance, thus, resulting in fast charging and discharging which is attractive in the EV industry. Their drawback is that they have a low capacity and short life span. They also have about 33% less capacity than the LCO, which speaks to why they are sometimes connected alongside the NMC to improve system capacity [23] – [24].

iii. Lithium Nickel Manganese Cobalt Oxide

The Lithium Nickel Manganese Cobalt Oxide (NMC or NCM) are the batteries of choice in electric power trains, e-bikes and EV etc. Nickel offers high specific energy and manganese spinel offers a low internal resistance, good stability and a high charging rate. Therefore, when these two elements are combined, it results in a battery that possesses both the characteristics of both elements. The cathode of these batteries is evenly distributed (i.e. one-third of nickel, manganese and cobalt). The ratio could also vary based on Manufacturers. Their major advantage is their high specific energy and cycle life [23] – [24].

iv. Lithium Iron Phosphate

The cathode of a Lithium Iron Phosphate is made of negatively charged phosphate anions that are bonded with positively charged iron cations. Their morphology is such that they can store lithium ions within the molecules of the iron phosphate. The cathode has a high chemical stability because of its bonding arrangement that allows tight bonding of the oxygen atoms to the structure. They have found wide applications in EV due to their long-life span, high specific power capability and safety feature (high thermal stability) in comparison with NMC and LMO. Their high specific power capability enables them to be discharged for about 25 times their C rating. Although their properties are like LCO; they have a higher self-discharge rate and energy density compared to LCO. Because of their low nominal voltage (3.2V), they only possess half the capacity of the NMC. This makes them ideal replacements for lead acid batteries in engine starting applications where high burst of power is required [23] – [24].

v. Lithium Nickel Cobalt Aluminum Oxide

The Lithium Nickel Cobalt Aluminum Oxide's advantages and disadvantages are like that of the NCM. They possess a high-power capability and long-life span. They have also found applications in EV (Tesla model). They are relatively expensive and fall just below par the NCM on the safety metric [23].

vi. Lithium Titanate

The Lithium Titanate chemistry constitutes a graphite anode and a Lithium Titanate cathode. This battery possesses a very low specific energy and nominal cell voltage (about 2.4V). Nonetheless, they have an almost infinite cycle life because they do not develop a Solid Electrolyte Interface (SEI) layer whilst undergoing cycling. They can be fast charged and discharged, because they allow a quick burst of power in a very short time. They are also very safe but expensive [23].

Table 2.3 Summary of the different types of lithium-ion batteries

Types of Lithium ion	***Advantages***	***Disadvantages***	***Applications***
Lithium Cobalt Oxide [23] – [25]	High specific energy and also has the highest energy density amongst all commercially available lithium-ion batteries.	Low thermal stability and limited: life span and specific power.	Phones, laptops and digital cameras.
Lithium Manganese Oxide [23] – [25]	High current discharging and fast charging, and high thermal stability.	Low capacity and limited cycle life.	Electric vehicles.
Lithium Nickel Manganese Cobalt Oxide [23], [25]	High specific energy and energy density, long cycle life, low internal resistance, good stability, and high charging rate.	Low thermal stability.	Electric power trains, e-bikes and EV.
Lithium Iron Phosphate [23] – [25]	Long life span, very high specific power capability and high thermal stability.	High self-discharge rate, low nominal voltage and susceptible to "memory effect".	Electric vehicles and engine starting in gasoline vehicles.
Lithium Nickel Cobalt Aluminum Oxide [23]	High power capability and long-life span.	Relatively expensive and has safety issues.	Electric vehicles.
Lithium Titanate [23], [25]	Fast charging and discharging, and an almost infinite life cycle.	Expensive, low specific energy and cell nominal cell voltage.	Electric transportation.

2.3 MEASUREMENT TECHNIQUES

The Battery Management System (BMS) as shown in Fig 2.6, ensures that crucial operational conditions of a battery: State of Charge (SoC), State of Health (SoH), available power, state of health and temperature are continuously monitored to increase life expectancy.

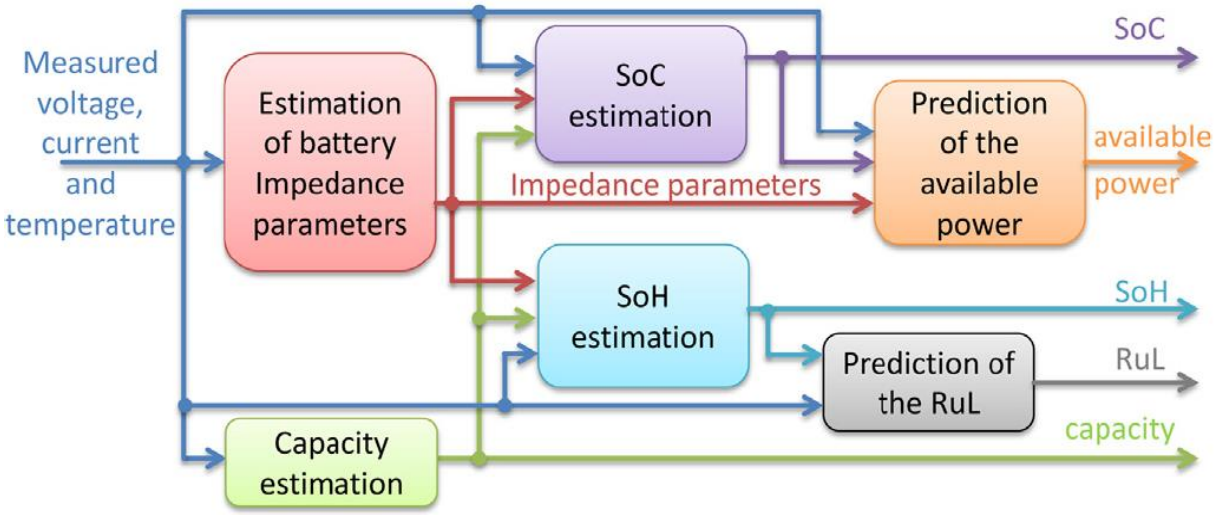

Fig 2.6 The interaction and flow of information between states that are estimated in a BMS [26].

In this study, the methods applied in estimating SoC, SoH and Temperature of the battery will be discussed. Besides, most of the techniques applied to monitor SoC, SoH and Temperature are applicable in calculating other parameters to be monitored as will be briefly discussed. The SoC of a battery is one of the most important parameter of a BMS. The SoC of a battery is defined as the ratio of available charge of a battery to that full-charge. This is expressed mathematically as (2 – 22):

$$SoC = \frac{Q_{available}}{Q_{fully\ charged}} \times 100\% \qquad (2-22)$$

Accurate SoC estimation of the battery averts unexpected system interruption and over-discharging or over-charging of the battery which could result in irreparable damage to the batteries internal structure [29]. The SoC of a battery in an electric vehicle is analogous to a fuel gauge in a gasoline vehicle. On the other hand, the lack of control of temperature can lead to thermal runaway of a battery, which occurs when the internal heat rate generated exceeds the rate of heat expelled [26]. Lastly, the measurement of the remaining useful life, age or SoH of the battery is of paramount significance for averting unexpected failure from gradual capacity fading. The SoH of a battery is the ratio of the charge available when the battery is fully charged to the initial charge when the battery was at the beginning of life as (2 – 23):

$$SoH = \frac{Q_{available\,(fully\,charged)}}{Q_{original\,(BOL)}} \times 100\% \quad (2-23)$$

2.3.1 Internal (DC) Resistance

Aging of a battery is determined by loss of capacity and increase in internal resistance (R_i). Measurement of internal resistance is used for evaluating degradation during life cycle test of the battery. To measure the DC or internal resistance of a battery, a current pulse (I) is applied, and the associating voltage drop (V) is quantified [30]. The resistance relationship follows ohm's law as shown in (2 – 24):

$$R_i = \frac{\Delta V}{\Delta I} \quad (2-24)$$

The voltage drops from OCV depending on the applied load (current). The change in current is due to the applied load alone because there is no current flowing through the battery at OCV. The DC resistance technique is quite limited, as it does not take into consideration the time-dependent losses occurring in the battery [30].

2.3.2 Coulomb counting

Coulomb counting (CC) is a measurement technique used to quantify battery SoC. Since, a battery's capacity is measured as the product of current (amps) and the discharge duration (hours); thus, CC expressed as (amp-hour) is used to determine SoC by quantifying the difference between the previous capacity history and the discharged or charged capacity [29]. The SoC of a battery is shown in (2 – 25). From the knowledge of the initial SoC or capacity history and the discharged or charged rate, the battery's current SoC can be determined as (2 – 26) and (2 – 27).

$$SoC = \frac{Q_{available}}{Q_{fully\,charged}}\, x\, 100\% \quad (2-25)$$

$$SOC = SOC_o + \frac{1}{Q_{fully\,charged}}\, x \int_{t_o}^{t_o+\tau} |I|.dt \quad - Charge \quad (2-26)$$

$$SOC = SOC_o - \frac{1}{Q_{fully\,charged}}\, x \int_{t_o}^{t_o+\tau} |I|.dt \quad - Discharge \quad (2-27)$$

2.3.3 Open Circuit Voltage

The open circuit voltage (OCV) technique has been applied for determining battery SoC [28]. This method is not applicable to all batteries, because not every battery's OCV has a linear relationship with their SoC. For instance, the lithium iron phosphate (LFP) battery has a flat discharge characteristic between 10% – 90% available capacity (see Fig 2.7) [27].

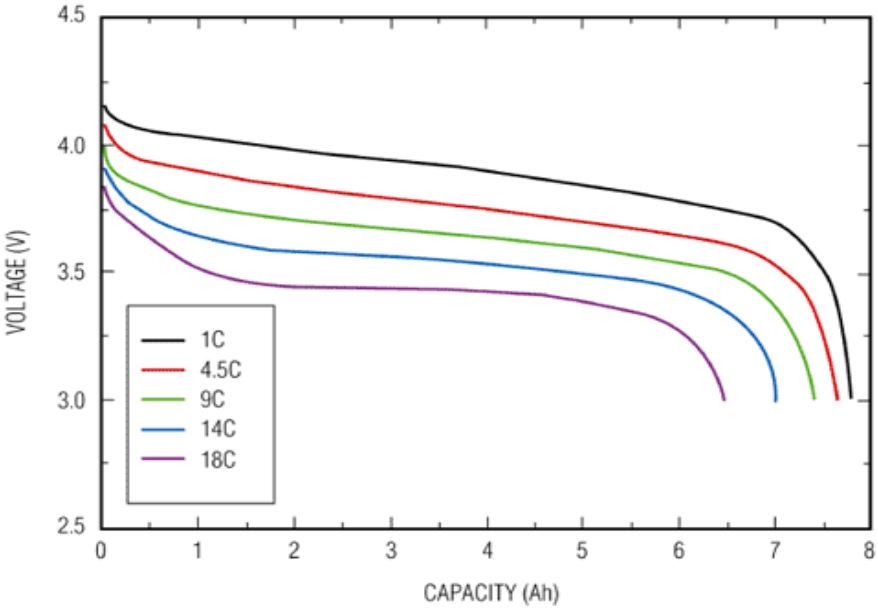

Fig 2.7 Discharge curve of lithium-ion phosphate (LFP) battery at room temperature [28]

For a lead acid battery, like the Absorbed Glass Mat (AGM) used in this thesis, the OCV can be partly used to roughly estimate SoC as (2 – 28); where V_{oc} represents the open circuit voltage, θ the SoC, A_θ the slope of the OCV change with SoC, and OCV_{min} the OCV at zero SoC. This expression could be further re-written in terms of SoC as (2 – 29)

$$\mathrm{V}_{oc} = \theta * A_\theta + \mathrm{OCV}_{min} \qquad (2-28)$$

$$\theta = \frac{V_{oc} - EMF_{min}}{A_\theta} \qquad (2-29)$$

2.3.4 Electrolyte concentration

From [10], it was observed that electrolyte (sulphuric acid) concentration of a lead acid battery relates to its OCV, because the electrolyte solution ions or solvent molecules participate in the electrode reactions. This relationship is supported by the Nernst equation. From Faraday's constant, $F = e \times N_A$. e is charge per electron and N_A is Avogadro's constant. Also, from the Boltzmann constant ($R = N_A \times k$). Since $\frac{k}{e} \alpha \frac{R}{F}$, therefore, the Nernst equation can also be expressed as (2 – 30):

$$E = E^o + \frac{kT}{ne} * ln\,(Q_r) \qquad (2-30)$$

The term Q_r relates to the concentration of reactants and products. For a lead acid battery, the "ln (Q_r)" term is expressed as {ln (electrolyte concentration)/ 1 molar} and decreases with available capacity [10]. For a gelled electrolyte or sealed lead acid and lithium-ion battery, this is not the case and hence, this technique is not applicable to all batteries.

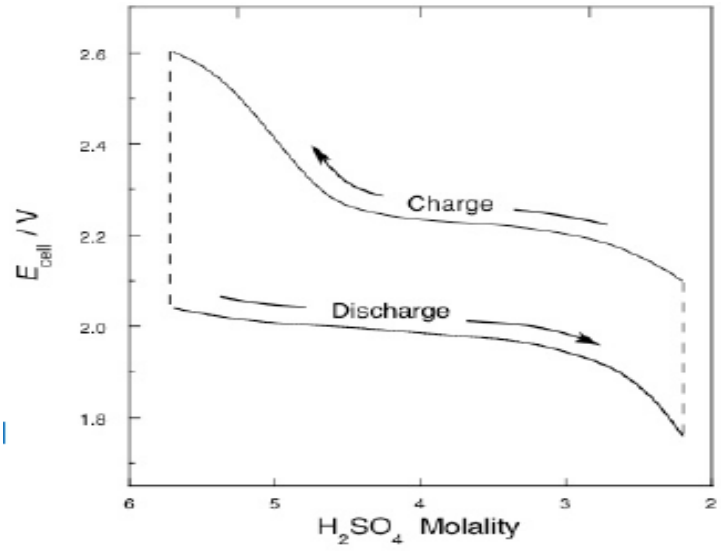

Fig 2.8 Charge/Discharge effect on electrolyte concentration of a lead acid battery [28]

From Fig 2.8, it is observed that there is a relationship between the lead acid battery OCV and electrolyte molality – a measure of a solute's concentration in a solution with respect to the solvent.

2.3.5 Model-based estimation

The concept of the model-based estimation for SoC, is using a selected battery model to relate the signals measured from the battery (current, voltage and temperature) to the SoC of the battery. When carrying out online measurement on the battery with the signals as model input, the SoC can thus be ascertained [28]. The types of battery models that will be briefly discussed in this thesis are: electrical, electrochemical and mathematical models.

The electrical model as shown in Fig 2.9 has been extensively used for SoC estimation in batteries. The electrical model relates the battery SoC with its open circuit voltage (OCV). The electrical model estimates battery OCV by the measurement of current, voltage and temperature [31].

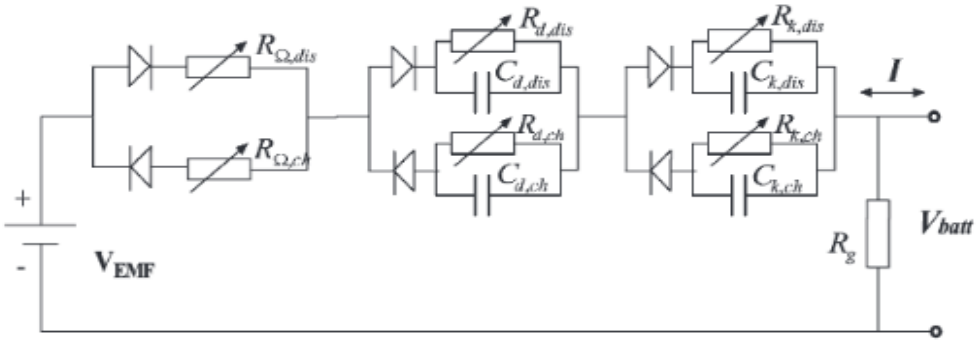

Fig 2.9 Equivalent circuit model [31]

The electrochemical model is also applied for the estimation of battery SoC. While electrical models store their parameters in look-up tables for different SoC's with associating temperature; electrochemical models inherently include the interdependencies of the battery temperature and SoC [26]. The electrochemical model segments the battery into its different regions and applies mathematical equations to represent the relation in the different regions. The electrochemical model is also termed as a "mathematical model," given that partial differential equations are applied to relate the OCV with the battery electrochemical activities – kinetics and diffusion etc. The electrochemical model of a cell is a 1-D spatial model with the dynamics of the cell considered only along a single axis as shown in Fig 2.10 [32]

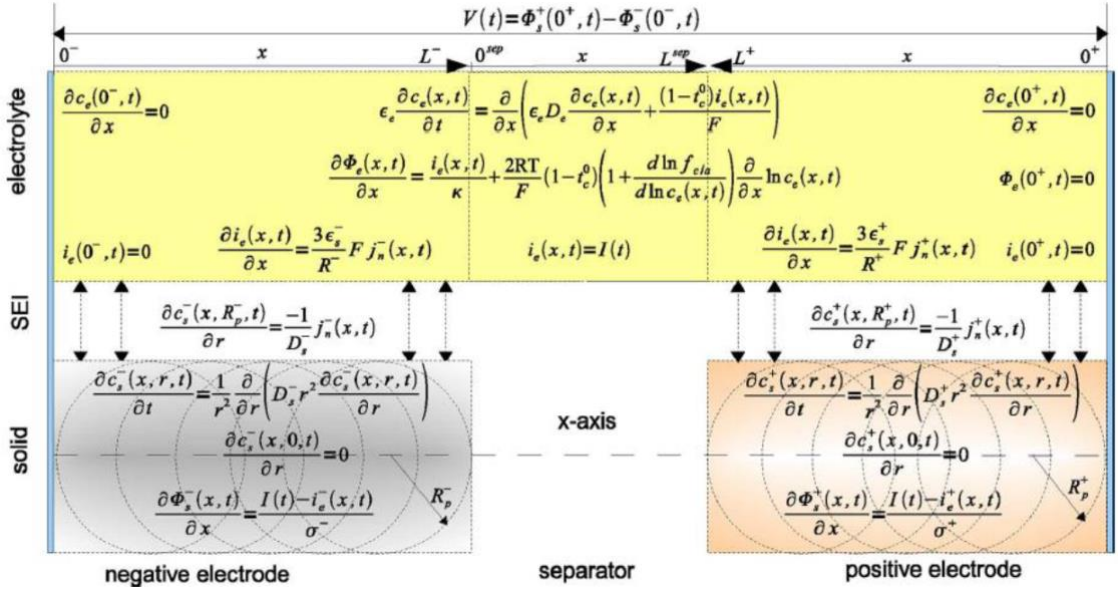

Fig 2.10 1-Dimension electrochemical/mathematic model of a Lithium ion cell

2.3.6 Impedance parameters

Critical conditions like SoC, SoH and temperature of a battery are estimated through the estimation of the actual impedance value [30]. To achieve this, Electrochemical Impedance Spectroscopy (EIS) is utilized. The EIS is an electro-analytic technique applied to batteries for the investigation of not only electrochemical kinetics but also characterization under different conditions. The impedance spectroscopy technique parameterizes battery impedances, because battery impedances vary for different conditions: SoC, SoH and temperature. Impedance spectroscopy makes it possible to measure very slow battery dynamics. Its extracted parameters derived from the electrical model are closely associated with the physicochemical processes [37]. This technique is used in this thesis and will be discussed in further details in Chapter 3.

2.3.7 Step response

The step response (potential/current step) or transient technique, like the impedance spectroscopy utilizes an electrical model for parameter extraction. The step response technique decouples the characteristic time constants of a battery – ohmic resistance and kinetics. The time constants are the R/C parallel components on the battery equivalent circuit. The step-response's accuracy is determined by current, potential and sample rate [37]. Fig 2.11 shows the potential response to a current step. It can be observed that the time constants are related to an EEC.

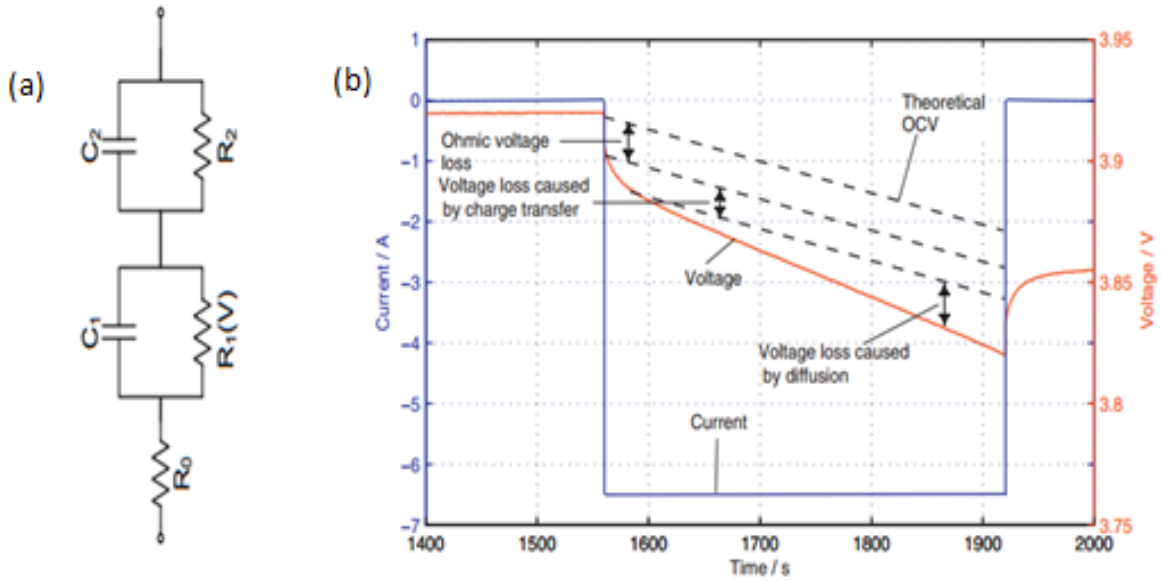

Fig 2.11 (a) equivalent electric circuit (b) potential response to a current step.

2.3.8 Data-driven method

In data-driven methods, historical battery data are learnt over time and intelligent solutions are proposed based on the data. This technique assumes that the data regime and condition stay constant until the battery fails [41]. One of the main benefits of this approach is that it can be utilized as a "black-box model," due to its ability to learn the battery behavior from the previous data and hence does not require electrochemical modeling of the battery [26], [30], [27]. The types of data-driven methods discussed in this thesis are: Fuzzy Logic, Artificial Neural Networks (ANN), Support Vector Machines (SVM) and Kalman Filter. Fuzzy Logic technique uses the Fuzzy Logic theory to model complex and nonlinear systems. An Artificial Neural Network (ANN) is made up of three layers: input, hidden and output layer. It is also composed of neurons connected for processing information from the input. The Kalman Filter is an

adaptive technique for SoH estimation. It takes several measurements over time and utilizes it for the estimation of the output variable.

The advantages and disadvantages of these techniques that have been utilized in literature to determine operational states of a battery are briefly summarized in Table 2.4

Table 2.4 Summary of techniques for SoC, SoH and Temperature estimation

Technique	***Advantages***	***Drawbacks***	***Parameters monitored***
Internal DC Resistance [30]	Easy to estimate	It does not take into consideration the time-dependent losses occurring in the battery.	SoH
Coulomb Counting *[26], [29], [30], [41]*	It is simple and does not relate to other parameters like temperature, DOD or C-rate which has a strong effect on other techniques	It requires a high storing capacity, is time consuming. Likewise, and requires precision due to cumulative errors.	SoC
Open-circuit Voltage *[27] – [28]*	Easy to estimate. Only requires a look-up table.	The relationship with OCV and SoC, changes with ageing which is not accounted for by this technique.	SoC
Electrolyte Concentration *[10]*	Estimates SoC easily with the hydrometer.	Its application is limited to flooded lead acid battery	SoC
Electrochemical & Mathematical models [26], [30], [31] – [32], [41]	Electrical models are easy to implement. The SoC can be estimated during charging or discharging. Mathematical and Electrochemical models model the battery accurately.	In these models, the parameters can be parameterized precisely for only new batteries. These models are complex, thus, reducing the amount of model parameters that can be used for online condition monitoring.	SoC SoH Temperature

Impedance Parameters *[26], [30], [37], [41]*	Very robust, accurately estimates electrochemical kinetics and can measure very slow battery dynamics – mass transfer/diffusion.	In some cases, the responsiveness of the impedance parameters of the battery to SoC is much lower compared to temperature.	SoC SoH Temperature
Step Response [37]	Easy to estimate and is relatively robust.	Unlike EIS, it is unable to estimate very slow dynamics.	SoC
Fuzzy Logic [26], [30], [33] – [34], [41]	Estimates battery condition without the need to understand the complete system process.	It is not very accurate, because it allows for some level of uncertainty in its calculations.	SoC SoH
Artificial Neural Network [26], [30], [35] – [36], [38] – [39], [41], [42]	They function automatically by training, thus, eliminating the need for coefficient and model parameters detection	Computationally intensive. Likewise, requires lot of training data that depends on the historic set of data.	SoC SoH
Kalman Filtering *[26], [30], [31] – [40], [41]*	It can run accurately and efficiently online.	Large storing of data is required because of the hand matrix operations that is applied to achieve results.	SoC SoH

2.4 SUMMARY

This Chapter introduced the concept of electrochemical systems. It provided insights on key electrochemical equations: Enthalpy, Entropy, Gibbs Free Energy, Nernst and Butler-Volmer Equation. More so, the major commercially available battery chemistries (with focus on lithium-ion and lead acid) were enumerated and compared against each other across industry-standard metrics. Finally, a few existing measurement techniques applied in a BMS were explored alongside their advantages and disadvantages.

2.5 REFERENCES

[1] D. Linden. Basic Concepts. In Handbook of Batteries, chapter 1. McGraw-Hill, 3. ed. edition, 2002.

[2] A. J. Bard and L. R. Faulkner. Electrochemical Methods: Fundamentals and Applications. Wiley, New York, 2. edition, 2001.

[3] J. S. Newman and K. E. Thomas-Alyea. Electrochemical Systems. Wiley, Hoboken, NJ [u.a.], 3. edition, 2004.

[4] Keith B. Oldham, Jan C. Myland, Alan M. Bond, Electrochemical Science and Technology, John Wiley and Sons.

[5] Ryan P. O'Hayre, Suk-Won Cha, Whitney Colella and Fritz B. Prinz, Fuel cell fundamentals, John Wiley and Sons, 2006.

[6] Bard J. Allen, Faulkner R. Larry, "Electrochemical methods- Fundamentals and Applications," second edition, John Wiley and Sons, 2006.

[7] Michel Soustelle, "Ionic and Electrochemical Equilibria," John Wiley and Sons, 2016

[8] Spiegel C, "PEM Fuel Cell Modeling and Simulation using MATLAB," Elsevier Inc. 2008.

[9] Chris de beer, "Condition Monitoring of Polymer Electrolyte Membrane Fuel Cells", PhD. Thesis, University of Cape Town, 2014.

[10] The University of Colorado's Electrical, Computer & Energy, "Lecture: Lead-acid batteries," ECEN 4517/5517.

[11] NPTEL Courses, "Introduction and overview of fuel cell, Activation Over-potential," Available online: [http://nptel.ac.in/courses/103102015/7].

[12] PV Education, Battery Information, Available online: [http://www.pveducation.org/pvcdro m/batteries/remaining].

[13] I. Hadjipaschalis et al., "Overview of current & future energy storage technologies for electric power applications," Renewable & Sust. Energy Reviews 13 (2009) 1513–1522

[14] M. Oswal, "A comparative study of Lithium-ion batteries," AME 578 project, University of Southern California.

[15] E. Chemali et al., "Electrochemical and Electrostatic Energy Storage and Management Systems for Electric Drive Vehicles: State-of-the-Art Review and Future Trends," IEEE Journal of emerging and selected topics in power electronics, Vol. 4, No. 3, Sept 2016

[16] Gabor Barany, "Lead-Acid Battery State Detection for Automotive Electrical Energy Management," PhD Thesis, Budapest University of Technology March 18, 2015.

[17] Peter Hilbig et al, "Ethyl Methyl Sulfone-Based Electrolytes for Lithium-ion Battery Applications," Energies 2017, 10, 1312; doi:10.3390/en10091312.

[18] Weilin Luo, Chao Lv, Lixin Wang, Chao Liu, "Study on Impedance Model of Li-ion Battery," 978-1-4244-8756-1/11/$26.00, 2011 IEEE.

[19] MIT Electric Vehicle Team, "A Guide to Understanding Battery Specifications," December 2008.

[20] C.-H. Dustmann, "Advances in ZEBRA batteries," Elsevier Journal of Power Sources vol. 127, nos. 1–2, pp. 85–92, 2004.

[21] Battery stuff, "Knowledge Base: Tutorials: Battery Articles: Battery Basics: A Layman's Guide to Batteries," Available online: [https://www.batterystuff.com/kb/articles/battery-articles/battery basics.html]

[22] The Worlds of David Darling - Encyclopedia of Alternative Energy, Available online: [http://www.daviddarling.info/encyclopedia/L/AE_lead-acid_battery.html]

[23] Battery University, "Types of Lithium ion." Available online: [https://batteryuniversity.com/learn/article/types_of_lithium_ion] (last updated in 2018)

[24] Andrew Chu, Paul Braatz, "Comparison of commercial supercapacitors and high-power lithium-ion batteries for power-assist applications in hybrid electric vehicles: I. Initial characterization." Elsevier Journal of Power Sources, vol. 112, pp. 236-246, 2002.

[25] Australian Academy of Science – Lithium ion batteries, Available online: [https://www.science.org.au/curious/technology-future/lithium-ion-batteries] (last updated in 2016)

[26] Wladislaw Waag et al. "Critical review of the methods for monitoring of lithium-ion batteries," Elsevier Journal of Power Sources, vol. 258, pp. 321-339, 2014.

[27] Noshin Omar, Peter Van den Bossche, Thierry Coosemans & Joeri Van Mierlo, "Peukert Revisited - Critical Appraisal and Need for Modification for Lithium-Ion Batteries," Energies 2013, 6, 5625-5641; doi: 10.3390/en6115625.

[28] Martin Coleman et al, "State-of-Charge Determination from EMF Voltage Estimation: Using Impedance, Terminal Voltage, and Current for Lead-Acid and Lithium-Ion Batteries," IEEE Transactions on Industrial Electronics, Vol. 54, No. 5, October 2007.

[29] Reinhardt Wagner, "Battery Fuel Gauges: Accurately Measuring Charge Level," Available online: [https://www.maximintegrated.com/en/app-notes/index.mvp/id/3958]

[30] M. Berecibar et al. "Critical review of state of health estimation methods of Li-ion batteries for real applications," Elsevier Renewable and Sustainable Energy 56 (2016) 572–587.

[31] Plett GL, "Extended Kalman filtering for battery management systems of LiPB-based HEV battery packs, Elsevier Journal of Power Sources 2004; 134 (2): 252–61.

[32] Il-Song Kim, “A Technique for Estimating the State of Health of Lithium Batteries Through a Dual-Sliding-Mode Observer,” IEEE Trans. Power Electron., vol. 25, no. 4, pp. 1013–1022, Apr. 2010.

[33] A.J. Salkind, C. Fennie, P. Singh, T. Atwater, D.E. Reisner, J. Power Sources 80 (1999) 293-300.

[34] A. Zenati, P. Desprez, H. Razik, in: Proceedings of 36th Annual Conference on IEEE Industrial Electronics Society (IECON), 2010, pp. 1773-1778.

[35] C. Cai, D. Du, Z. Liu, J. Ge, in: Proceedings of 9th International Conference on Neural Information Processing (ICONIP ’02), 2002, pp. 824-828.

[36] F. Zhou, L. Wang, H. Lin, Z. Lv, in: Proceedings of IEEE ECCE Asia Downunder (ECCE Asia), 2013, pp. 513e517.

[37] Evgenij Barsoukov, J. Ross Macdonald, “Impedance Spectroscopy Theory, Experiment, and Applications,” Published by John Wiley & Sons, Inc., Hoboken, New Jersey, 2005.

[38] Yanqing, Shen, Energy Convers. Manage. 51 (2010) 1093-1098.

[39] S. Malkhandi, S.K. Sinha, K. Muthukumar, in: Proceedings of 27th Annual Conference of the IEEE Industrial Electronics Society (IECON), 2001, pp. 131-136.

[40] Remmlinger J et al. “On-board state-of-health monitoring of lithium-ion batteries using linear parameter-varying models. Journal of Power Sources 2013; 239: 689–95.

[41] Seyed Mohammad et al. Journal of Power Sources 256 (2014) 110-124.

[42] C.H. Piao, W.L. Fu, W. Jin, Z.Y. Huang, C. Cho, IEEE Telecommunications Energy Conference, 2009.

3. ELECTROCHEMICAL IMPEDANCE SPECTROSCOPY

Electrochemical Impedance Spectroscopy (EIS) is a formidable electro-analytic technique that has been largely employed for the investigation of electrochemical kinetics in batteries, by fitting an impedance plot to an Equivalent Electric Circuit (EEC) model [1] – [2]. EIS is the technique of choice for characterizing electrochemical systems because its computationally non-intensive, robust and can measure very slow dynamics compared to other techniques discussed in Chapter 2.3. EIS is measured by applying a sinusoidal excitation (current or potential) through the cell and observing the associated response (potential or current). EIS measurement can be carried out in two modes: potentiostatic or galvanostatic. The potentiostatic mode of EIS is when a potential signal is applied, and current signal is observed; the galvanostatic mode is when a current signal is applied, and potential signal is observed. For energy conversion systems, the potentiostatic mode is more popular, however, for this research, the galvanostatic mode is applied. This is because the battery is a low-impedance device and an application of a $10mV$ (potentiostatic mode voltage) sine wave produces amperes of current-flow resulting in the evolution of the system during the measurement [3]. The sinusoidal excitation signal applied to a battery as a function of time (t), is expressed in (3 – 1). In a linear system, the response voltage (V) to the sinusoidal excitation current (I), is shifted in phase ϕ with a different amplitude, expressed in (3 – 2).

$$\Delta I = I_{max}\,(sin\,2\pi ft) \qquad (3-1)$$

$$\Delta V = V_{max}\,(sin\,2\pi ft + \phi) \qquad (3-2)$$

In (3 – 1) and (3 – 2), I_{max} and V_{max} are the maximum current and potential amplitude respectively, f is the angular frequency and ϕ is the phase shift. The excitation and response signals are analysed as a sum of sinusoidal function, repeated several times over the frequencies of interest. The complex impedance (Z) is calculated using the ohmic relationship shown in (3 – 3), and is separated into its real and imaginary part as shown in (3 – 4) – (3 – 6):

$$Z = \frac{\Delta V}{\Delta I} \qquad (3-3)$$

$$Z' = |Z| \times cos(\phi) \qquad (3-4)$$

$$Z'' = |Z| \times sin(\phi) \qquad (3-5)$$

$$|Z| = \sqrt{Z'^2 + Z''^2} \qquad (3-6)$$

3.1 EIS METHODOLOGY

For Electrochemical Impedance Spectroscopy measurements to be acceptable, conditions such as the Kramers–Kronig relation should be adhered to [4]. These conditions are: linearity, stability, and causality of the system. Alongside Kramers–Kronig relation, the amplitude of the perturbation – excitation signal must also be selected properly.

i. Kramers-Kronig relation

The excitation signal (perturbation) and response of general electrochemical systems (battery) are described by a set of linear differential laws. These laws require that the impedance be independent of the amplitude of the perturbation [4]. Consequently, EIS is measured by the application of small signal excitations. This is so that the cell's response to a sinusoidal excitation signal is a sinusoid at the same frequency with a corresponding phase shift [5] as shown in Fig 3.1 The system must also be stable by returning to its initial state after the perturbation is removed. For accurate EIS measurements, the battery must attain steady state before another excitation signal of a different frequency is applied. Lastly, the response of the system should only be due to the perturbation applied and must not contain substantial components from façade sources [6].

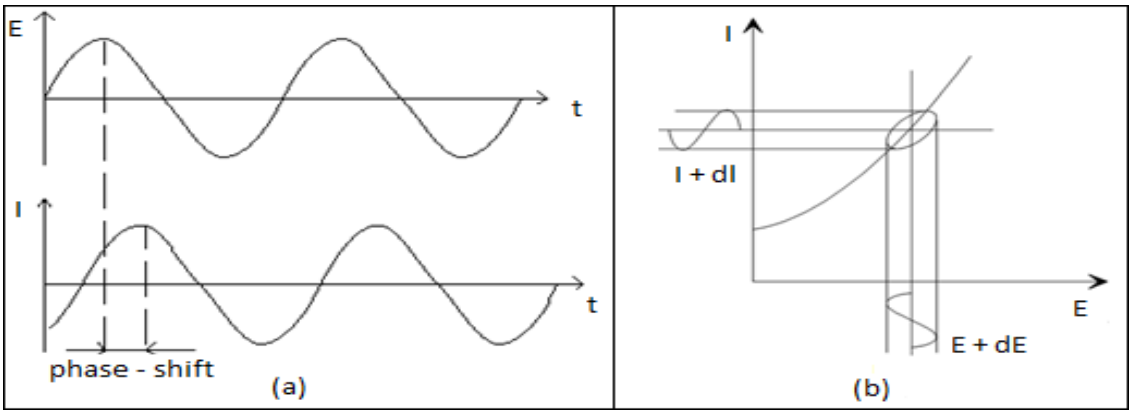

Fig 3.1 (a) Sinusoidal current response for the conventional EIS technique applied in a linear system [5] (b) Lissajous curve, indicating linearity of the system [7].

ii. Amplitude of perturbation

The larger the amplitude of the injected signal, the higher the Signal-to-Noise Ratio (SNR) of the measured data and the greater the signal power. For the battery to adhere to Kramers–Kronig relations, the amplitude of the injected signals must be small enough that the response

is still in the acceptable linear regions [8]. Hence, the excitation signal must be set up in such a way as to maximize signal power at the user frequencies of interest, while minimizing system disturbance. There have been several arguments regarding the optimal perturbation amplitude for EIS measurements on electrochemical systems. [9] suggested an amplitude perturbation of 5% of the DC point of an electrochemical system (fuel cell). Likewise, [3] – an EIS instrument vendor proposed an amplitude perturbation of 10% of the DC current of the battery. These values have been extensively used in literature. Nonetheless, [10] analytically verified that the optimal amplitude perturbation varies from one system to the other.

When a single frequency sinusoidal perturbation is applied to a linear system (the pseudo-linear point of a battery's $V - I$ curve), the corresponding response is also a single frequency out of phase sinusoidal signal but of a different amplitude. For a non-linear system, the response is a multi-frequency signal composed of a superposition of several sine waves of different frequencies – the fundamental components and other undesirable harmonics (see Fig 3.2). These undesirable harmonics corresponds to integer multiples of the fundamental frequency. The non-linearity of the battery relates to the harmonic generated in the response signal. Therefore, analysis of the Total Harmonic Distortion (THD) of the frequency spectrum of the response signal will furnish us with information on the optimal perturbation amplitude for EIS measurements [11].

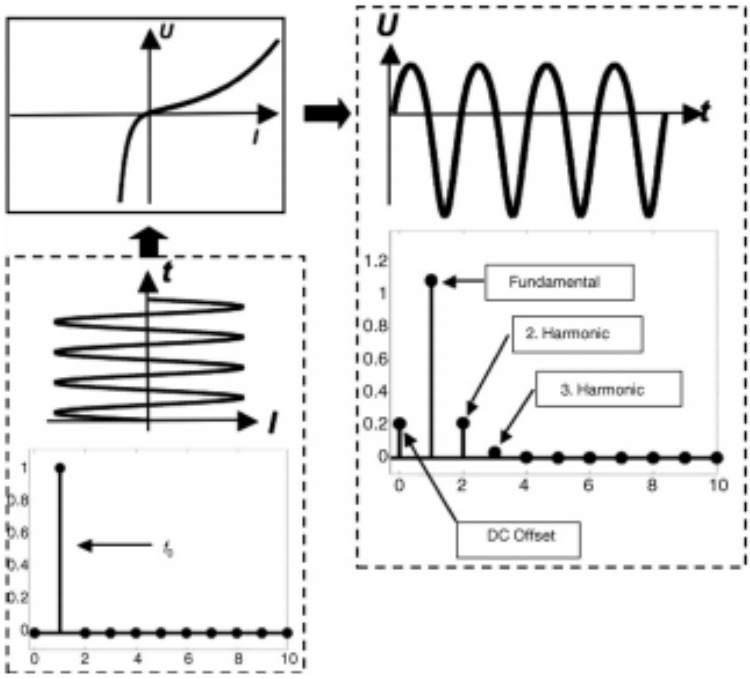

Fig 3.2 Harmonic oscillations due to nonlinear transfer function of sinusoidal response signal [11].

THD measures the energy contained in the fundamental of a signal with respect to the energy contained in the harmonics. THD has been extensively applied for the quantification of the level of harmonics in electric signals [4]. The THD of a signal is defined in (3 – 7):

$$THD = \frac{\sqrt{H_2^2+H_3^2+H_4^2+H_5^2+\cdots+H_N^2}}{\mathrm{F}} \qquad (3-7)$$

In (3 – 7), H_i is amplitude of the i^{th} harmonic, F is amplitude of the fundamental frequency and THD is the Total Harmonic Distortion, usually expressed in percentage as (%THD).

3.2 IMPEDANCE SPECTROSCOPY DATA REPRESENTATION

From (3 – 6), it can be observed that the complex impedance is composed of a real and imaginary part. If the complex impedance is plotted at different frequencies with the real part on the horizontal axis and the imaginary part on the vertical axis, a Nyquist plot as Fig 3.2 is obtained.

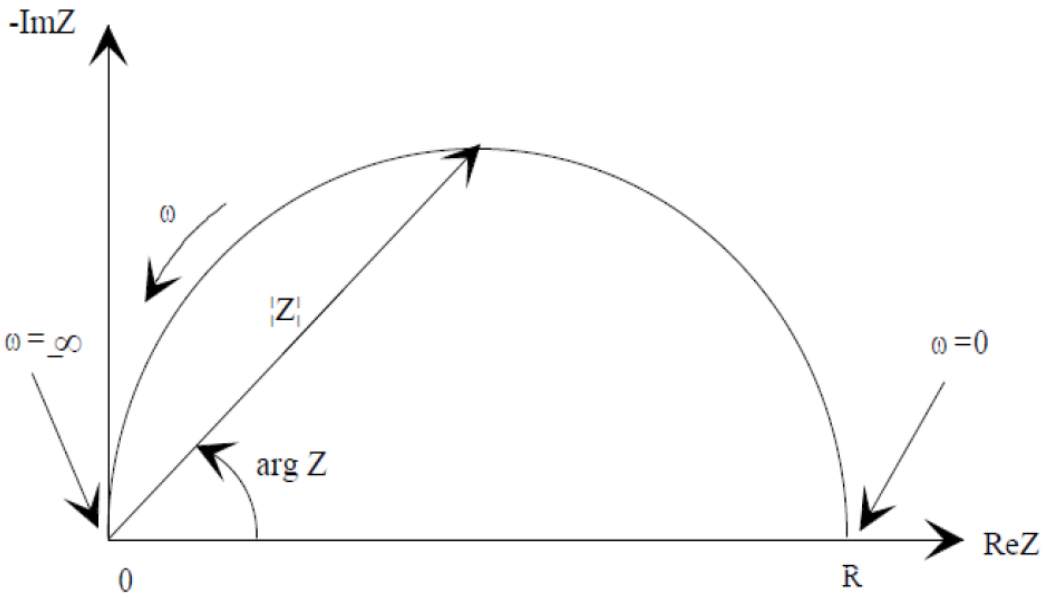

Fig 3.3 Nyquist plot with a single time constant [6]

From Fig 3.3, it can be observed that the vertical axis plot is negative and the frequency decreases from left to right. More so, the impedance on the Nyquist Plot can be represented as a vector – diagonal arrow of length |Z|. The angle between the vector and the horizontal axis, called the "phase angle," is $\phi = arg\ Z$ [6]. The inability to ascertain where each frequency point lies on the impedance plot is a drawback of the Nyquist plot. Typically, the Nyquist plot of a battery is fitted to an equivalent circuit as will be discussed in Chapter 3.5.4. The EIS plots of batteries contain several semicircles, but most times, only a portion of the semicircles can

be visualized. Be that as it may, the frequency can be plotted against the impedance magnitude ($|Z| = Z_o$) and the phase response. This type of plot is known as the Bode Plot (see Fig 3.4). Unlike the Nyquist plot, the Bode plot provides frequency specific impedance information.

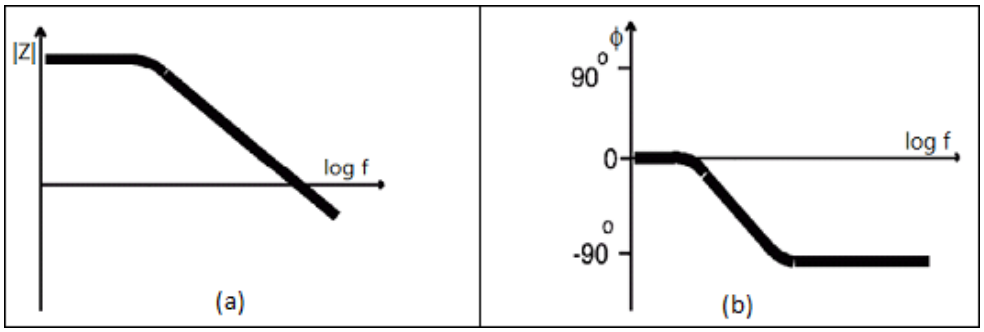

Fig 3.4 Bode plot with a single time constant (a) impedance magnitude against log frequency (b) phase angle against log frequency [5]

3.3 EQUIVALENT CIRCUIT ELEMENTS

Measured EIS data represented on a Nyquist plot are usually analysed by curve fitting to an EEC model. The components of the circuit elements in the model are: resistors, capacitors, and inductors (see Table 3.1) [7]. The elements selected in the model represents an associating physicochemical process in the battery [5] – [6].

Table 3.1 Common circuit elements with their defining relation and impedance.

Passive Elements	***Symbol***	***Defining Relation***	***Impedance***
Resistor		$V = I \times R$	$Z_R = R$
Capacitor		$I = C \times \frac{dV}{dt}$	$Z_C = \frac{1}{j\omega C} = \frac{j}{\omega C}$
Inductor		$V = L \times \frac{dI}{dt}$	$Z_L = J\omega L$

The impedance of a resistor has only a real component because it is independent of frequency, thus, current through a resistor is in phase with voltage. The impedance of an inductor increases with frequency. The inductor has an imaginary impedance component with current lagging voltage by 90 degrees. On the contrary, the impedance of a capacitor decreases with frequency. The capacitor has an imaginary impedance component, with current leading the voltage by 90 degrees. From this understanding, it can be observed from the Nyquist plot that the real resistance – impedance without frequency components, increases from left to right. The imaginary (negative) impedance corresponds to the capacitive components of the battery

and the imaginary (positive) impedance corresponds to the inductive components of the battery. However, since the battery is capacitive in nature, the Nyquist plot's vertical axis is graphed to laser-focus on the information in the negative imaginary component.

i. Electrolyte Resistance

The resistance of the electrolyte solution has a profound impact on the total battery impedance. The electrolyte resistance is dependent on the ionic concentration, ion type, temperature and geometric area – which current flows through. In a bounded area, the resistance (R_Ω) is defined as the ratio of the product of the solution resistivity (ρ) and length (l) to its area (A) [6]. This is expressed as:

$$R_\Omega = \rho \times \frac{l}{A} \qquad (3-8)$$

Arrhenius equation shown in (3 – 9), indicates that the chemical reaction rate is dependent on the temperature. The ohmic resistance is subsequently modelled as an inverse of the rate constant, as shown in (3 – 10)

$$k = A \times e^{(\frac{-E_a}{RT})} \qquad (3-9)$$

$$R_\Omega = \frac{1}{k} = \frac{1}{A} e^{(\frac{-E_a}{RT})} \qquad (3-10)$$

From (3 – 9) and (3 – 10), k is the rate constant, E_a is the activation energy for the reaction, R is the universal gas constant and T is temperature (in Kelvin). The main challenge in estimating the solution resistance is the flow path of current and the electrolyte geometry that carries the current; because a battery cell's current distribution through its electrolyte area is not uniform [7]. However, the electrolyte resistance is easily calculated from curve fitting the experimental EIS (Nyquist) plot to an EEC; rather than calculating the electrolyte resistance from its ionic conductance. On the EIS plot, the electrolyte, electrode and separator's physical resistance all culminates to the ohmic resistance (R_Ω).

ii. Double Layer Capacitance

There is an electrical double layer on the interface between the electrode and its surrounding electrolyte. The formation of the double layer is due to ions being adsorb onto the surface of the electrode. Moreover, the charged ions are separated from the charged electrode by an insulating space, which is usually in the order of angstrom [5]. Charges are separated by an insulator, resulting in the formation of a capacitor. Thus, electrode immersed in an electrolyte will behave as a capacitor. A battery has two double layer capacitances, because it

has two electrodes: anode and cathode. These capacitances are dependent on the electrode potential, temperature, adsorption of impurities, oxide layers, ionic concentrations, type of ions and electrode roughness [6].

iii. Polarization Resistance

Polarization of an electrode occurs when the potential of the electrode deviates from OCV. This results in the flow of current via electrochemical reactions occurring at the electrode surface. The level of current is determined by the reaction kinetics and sufficient diffusion of reactants both away and towards the electrode [7]. As already discussed in Chapter 2.1.3, the different types of polarization resistances are: activation polarization over-potential – which corresponds to the charge transfer (rate of reaction) resistance and the concentration polarization over-potential – which corresponds to the diffusion (of reactants) [12].

iv. Charge Transfer Resistance

The charge transfer resistance is formed by a single kinetically controlled electrochemical reaction. When the electrode of a battery is in contact with an electrolyte, the electrode molecules will electrolytically dissolve into the electrolyte as (3 – 11).

$$Red \rightleftharpoons Ox + ne- \qquad (3-11)$$

The forward reaction electrons get into the electrode and the electrode ions become diffused into the electrolyte, resulting in a charge transfer. The charge transfer reaction possesses a certain speed that is dependent on the: kind of reaction, concentration of the reaction products, temperature and potential, (see Chapter 2.1.4).

v. Diffusion (Warburg)

The Warburg impedance is created by the diffusion process and is dependent on the excitation signal frequency. At high frequencies, the Warburg impedance is small because the diffusing reactants do not diffuse far from the reaction location. At low frequencies, the Warburg impedance increases, because the reactants diffuse far from the reaction location. On the Nyquist plot, the infinite Warburg impedance is represented as a 45-degree line [18], whereas, on the Bode plot, it is represented as a 45-degree phase shift [5]. The infinite Warburg impedance is expressed as (3 – 12) and the Warburg coefficient (σ) as (3 – 13).

$$Z_W = \frac{\sigma}{\sqrt{\omega}}(1-j) \qquad (3-12)$$

$$\sigma = \frac{RT}{n^2F^2A\sqrt{2}}\left(\frac{1}{C^o\sqrt{D_o}} + \frac{1}{C^R\sqrt{D_R}}\right) \qquad (3-13)$$

In (3 – 12) and (3 - 13), ω is the radial frequency, D_o is the diffusion coefficient of the oxidant, D_R is the diffusion coefficient of the reductant, n is the number of electrons transferred, A is the surface area of the electrode and C is the bulk concentration of the diffusing species in $moles.cm^{-3}$. (3 – 12) and (3 – 13) are only valid when the diffusion layer has an infinite thickness, which is usually not the case. Hence, for a bounded diffusion layer, the lower frequency impedance would not follow (3 – 12) and (3 – 13); instead is expressed as a "finite" Warburg as shown in (3 – 14).

$$Z_o = \sigma\omega^{-\frac{1}{2}}(1\text{-}j)\tanh\left(\left(\delta\frac{j\omega}{D}\right)^{\frac{1}{2}}\right) \qquad (3-14)$$

In (3 – 14), δ is the Nernst diffusion layer thickness and D is the mean value for the diffusion coefficients of the diffusing species [4]. All other symbols retain their definitions.

vi. Constant Phase Element

The Constant Phase Element (CPE) is introduced to replace the capacitors in EIS experiments because capacitors do not behave in an ideal manner. In state estimation of batteries, the double layer capacitance usually behaves like a CPE instead of a capacitor [5], [7]. The CPE is defined as (3 – 15):

$$Z = A(i\omega)^{-\beta} \qquad (3-15)$$

In (3 – 15), the constant – A, is the inverse of the capacitance value. For a pure capacitor, the exponent (β) is equals unity. However, when β is less than one, it is expressed as a CPE. The exponent (β) is also referred to as a depression constant because it affects the shape of depression of the Nyquist plot semi-circle (that is CPE-resistor parallel combination), shown in Fig 3.5 [7].

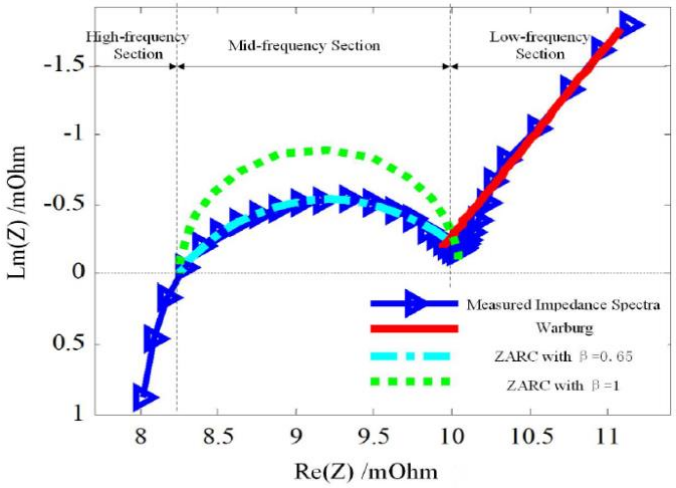

Fig 3.5 Representation of the semi-circle depression [13]

vii. Virtual Inductor

Batteries impedance at high frequencies is modelled as an inductor. On the Nyquist (EIS) plot, this is displayed at the positive imaginary impedance.

3.4 IMPEDANCE STUDY ON BATTERY CHEMISTRIES

Impedance Spectroscopy can be applied for analysis of kinetic reactions, relating to the process of insertion or extraction of lithium-ions in intercalation materials such as: Solid Electrolyte Interface (SEI) and charge transfer resistance. Impedance Spectroscopy is also very useful in establishing the relationship between impedance parameters: ohmic, kinetic and diffusion and operational conditions: SoC, SoH, temperature and DC current [23], [25], [26], [29]. EIS provides a robust understanding of degradation effects in batteries; resulting in an improvement of rate capability, discharge/charge cycles and optimization of electrode [20].

3.4.1 Lithium-ion Battery

In a lithium-ion battery, inductive behaviour is observed at high frequencies, (see Fig 3.6). This behaviour is due to the inductive reactance of the metals in the measurement setup, such as: the type of cable wiring and the connecting lines [27], [29]. Batteries do have an inductive component, but this is not taken into consideration in this experiment, because in all instances, the measurement setup was the same. It is therefore assumed that the inductance remained the same over the course of the tests. The ohmic series resistance is the high frequency intersection of the plot on the real impedance axis. The ohmic series resistance is due to the resistance of the connections, electrodes, separator and electrolyte [23]. More so, the ohmic series resistance is useful in quantifying the conductivity of lithium-ions and electrons.

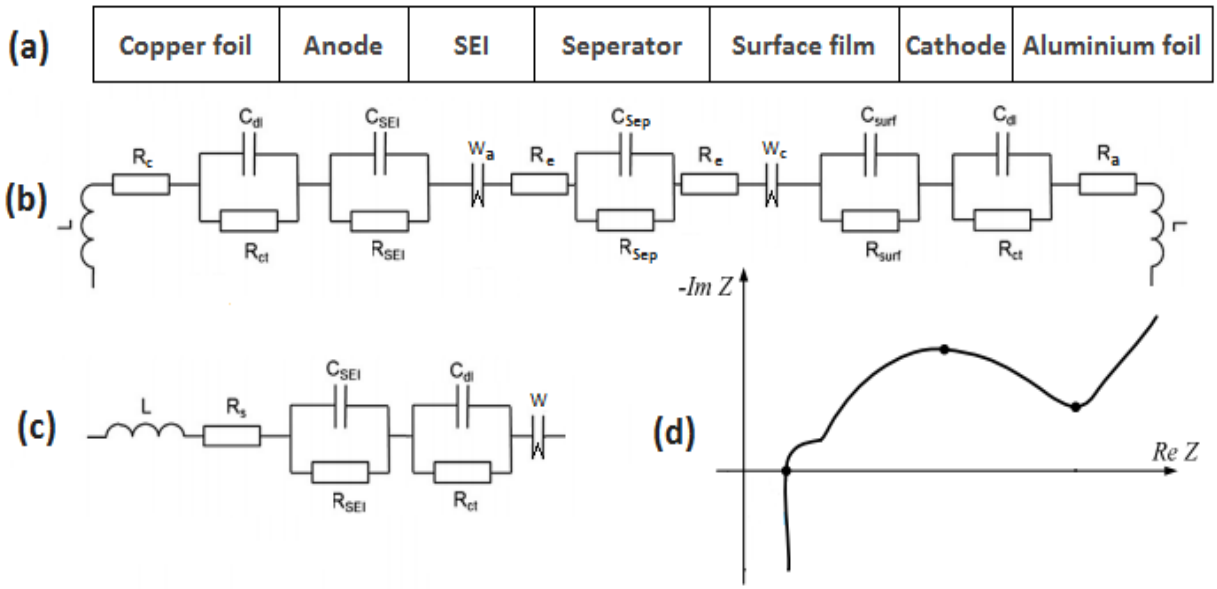

Fig 3.6 (a) Schematic representation of a Li-ion battery (b) Comprehensive equivalent electric circuit; (c) Simplified equivalent electric circuit of the Nyquist plot (d) Nyquist plot of a typical Lithium-ion battery

The smaller semi-circle represents the SEI formation at the anode surface and the surface film formation at the positive electrode. The larger semi-circle describes the charge transfer resistance and electrode-electrolyte double layer capacitance due to the lithium-ion intercalation process [20], [23], [29]. The separator is impregnated with electrolyte and possesses a micro-porous structure that allows the passage of lithium-ion, whilst ensuring that both electrodes never come in contact. The separator is represented as a resistor-capacitor parallel combination, but is neglected in the simplified EEC, because of its negligible impact compared to other parameters. At the low-frequency range, lithium-ion diffusion to the electrodes dominates. This is represented on the Nyquist plot as a 45-degree line [20], [23], [29], although in some cases, the Warburg component might not be accurately 45-degrees [27]. It is pertinent to note that the impedance of both electrodes as in Fig 3.6 (b) can be combined, resulting in a simplified equivalent electric circuit consisting of an ohmic resistance, a double layer capacitance-charge transfer resistance and diffusion impedance as in Fig 3.6 (c). EIS has been extensively applied to different lithium-ion chemistries to ascertain: SoC, SoH, temperature and effect of DC current.

i. State of Charge

From Fig 3.7, it can be observed that the impedance relationship for varying state of charge for different lithium-ion chemistries is unique. In some cases, the impedance due to SEI and film formation increases with reducing state of charge, while in other cases, the state of charge

is more dependent on the diffusion process. The only consistency is that the ohmic series resistance of a lithium-ion battery is not a function of state of charge.

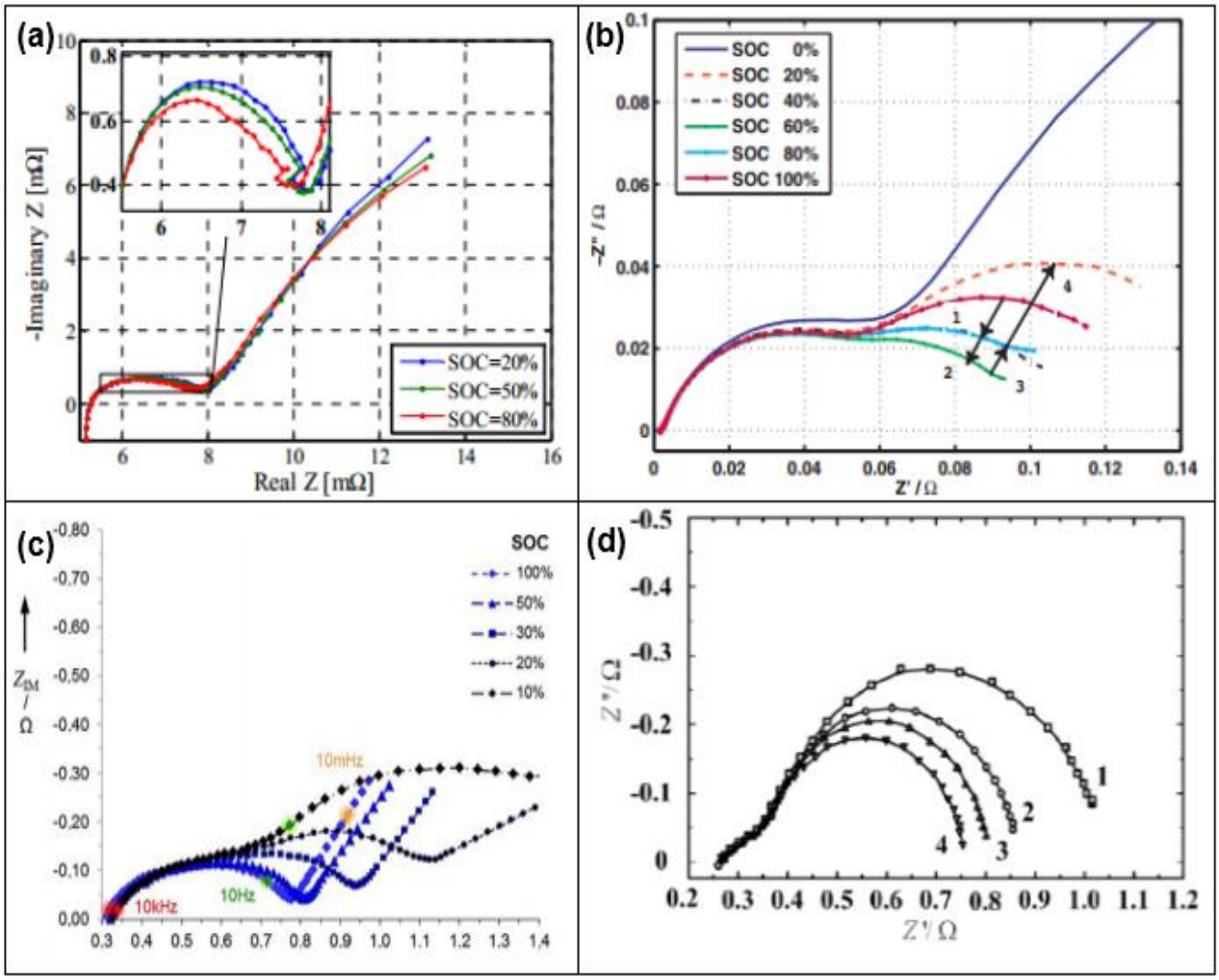

Fig 3.7 EIS plot of different lithium-ion chemistry at varying state-of-charge (a) [24], (b) [27], (c) [28], (d) [25]

ii. Temperature

From the EIS plots in Fig 3.8, it can be observed that the impedance shifts rightwards with a reduction in temperature. Apart from the increasing ohmic series resistance, an enlarging of the semi-circles can also be observed as temperature reduces.

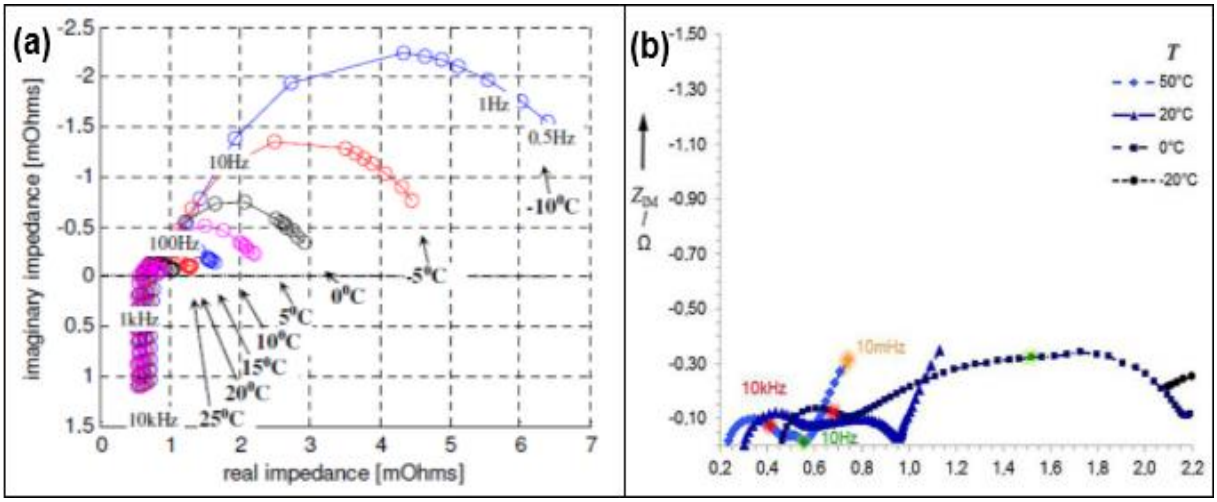

Fig 3.8 EIS plot of different lithium-ion chemistry at varying temperature (a) [26], (b) [28]

iii. Effect of DC current & Ageing

From Fig 3.9 (a), a shrinking of the semi-circle can be observed, with an increase in DC current. This was also experienced in [26]. On the other hand, with ageing of the battery, the impedance spectrum shifts rightwards. This is due to increase in the ohmic series resistance and formation of SEI film, resulting from the depletion of lithium ions from the electrolyte [28].

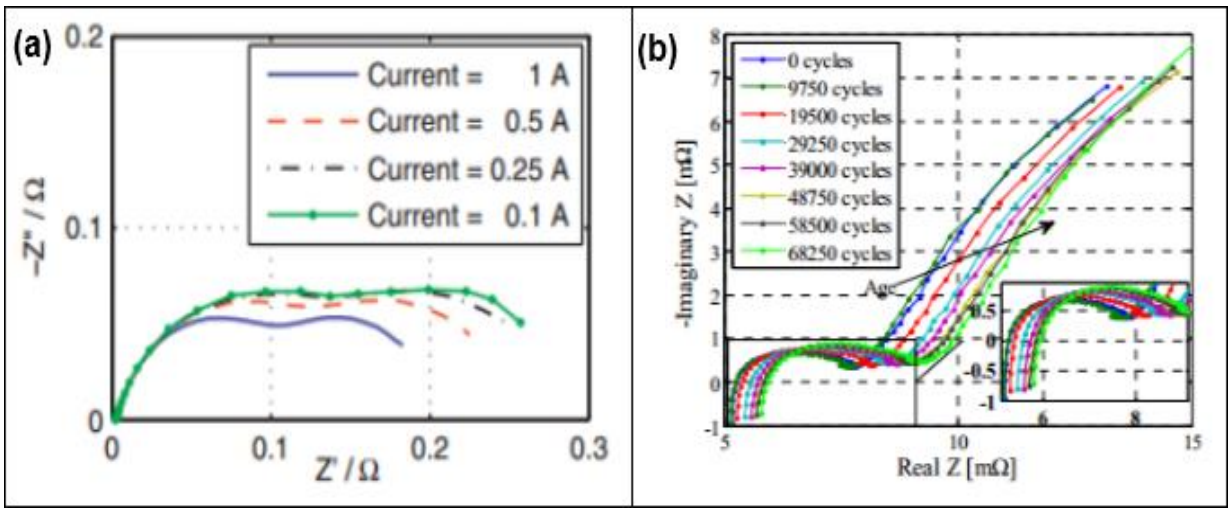

Fig 3.9 EIS plot of different lithium-ion chemistry (a) varying DC current [24](b) varying cycles [27]

3.4.2 Lead acid Battery

EIS has been largely applied for characterizing lead acid battery's SoC, SoH, temperature and effect of DC current. The lead acid battery used in this research is divided into four (4) parts, namely: two porous electrodes, a gelled electrolyte reservoir and a porous separator [30], (see Fig 3.10). At the low frequencies of a lead acid battery, the inductive reactance dominates [16]. The impedance of both electrodes contributes to the lead inductance, double layer

capacitance, charge and mass transfer processes. The electrolyte solution and separator also contribute to the total battery impedance [16]. The geometric capacitance is very small and is therefore negligible. Like the lithium-ion batteries, both electrodes of the lead acid battery behave in a similar manner. The impedance of both electrodes can thus be combined, resulting in a simplified equivalent electric circuit consisting of an ohmic resistance, a double layer capacitance-charge transfer resistance and diffusion impedance [17].

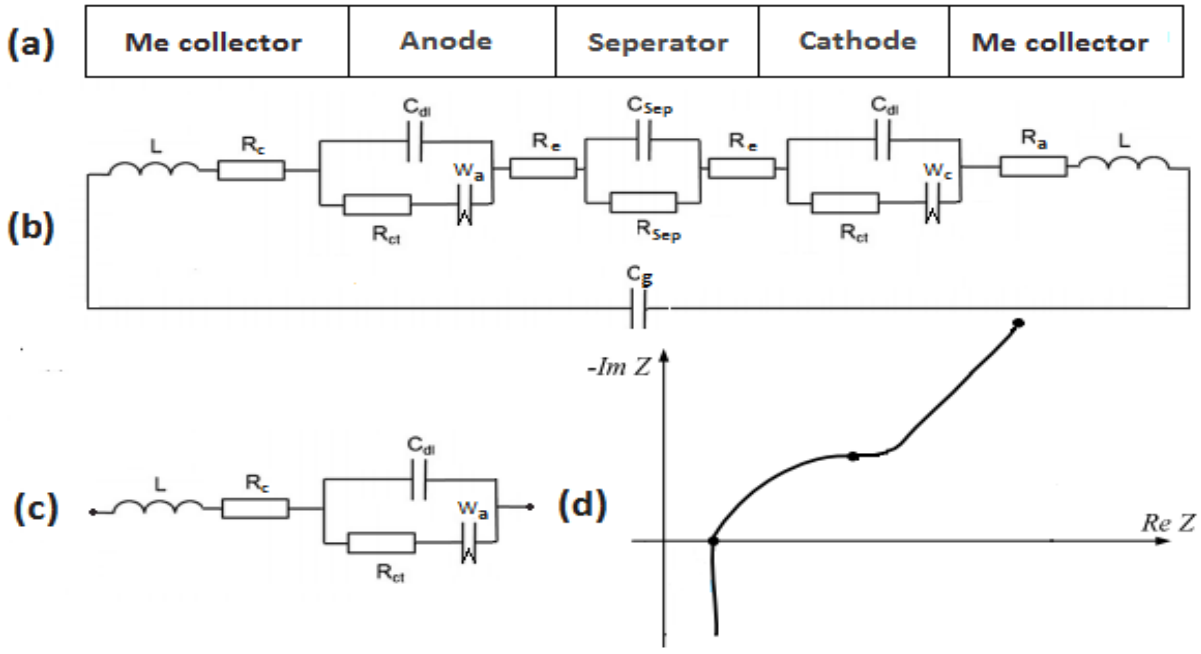

Fig 3.10 (a) Schematic representation of a Lead acid battery (b) Comprehensive equivalent electric circuit; (c) Simplified equivalent electric circuit of the Nyquist plot (d) Nyquist plot of a Lead acid

The high frequency inductive reactance is due to the electrode geometry and connections within the cell [19]. The ohmic resistance is due to the electrolyte conductivity, separators and surface coverage of both electrodes by crystallized lead sulphate [16] – [19]. The double layer capacitance models the active surface area [18] – [20]. The charge transfer process occurs at the double layer electrode (pore wall) – electrolyte (active material) interface. The charge transfer – double layer capacitance combination, models the transient behaviour and is related to the electrodes porosity. The mass transfer process models the diffusion of Pb2+ ions along the pore's axis [16]. EIS has also been extensively applied in estimating SoC, SoH, temperature and effect of DC current in lead acid batteries.

i. State of Charge

From Fig 3.11, it can be observed that for a decrease in the state of charge, the impedance spectrum moves rightwards, indicating an increase in real impedance. More so, in [17], there

is a relationship between the state of charge and the intercept frequency – the frequency where the phase shift is equals zero.

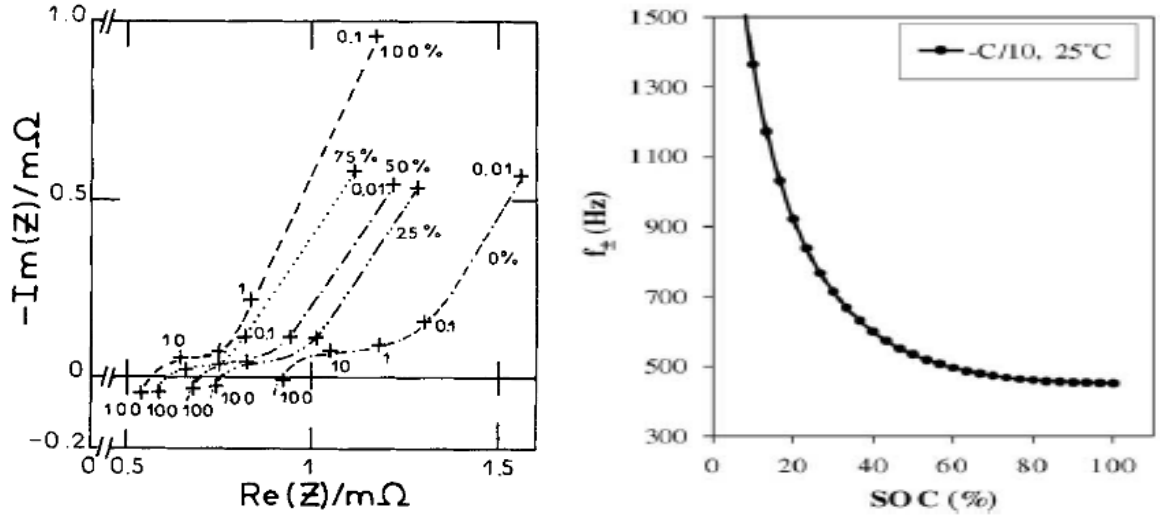

Fig 3.11 (a) EIS plots of a 2 V-390 Ah lead-acid battery at different SoC [19] (b) SoC and intercept frequency relationship [17]

ii. Effect of DC current

The DC current of the battery during charge or discharge at a given SoC when EIS experiments are conducted; illustrates that the EIS plots can look very dissimilar for the same SoC as shown in Fig 3.12. Therefore, care must be taken in estimating lead acid battery SoC from the shape of its EIS plot because any given pair of impedances (imaginary and real) may correspond to several SoC's (at different C-rates).

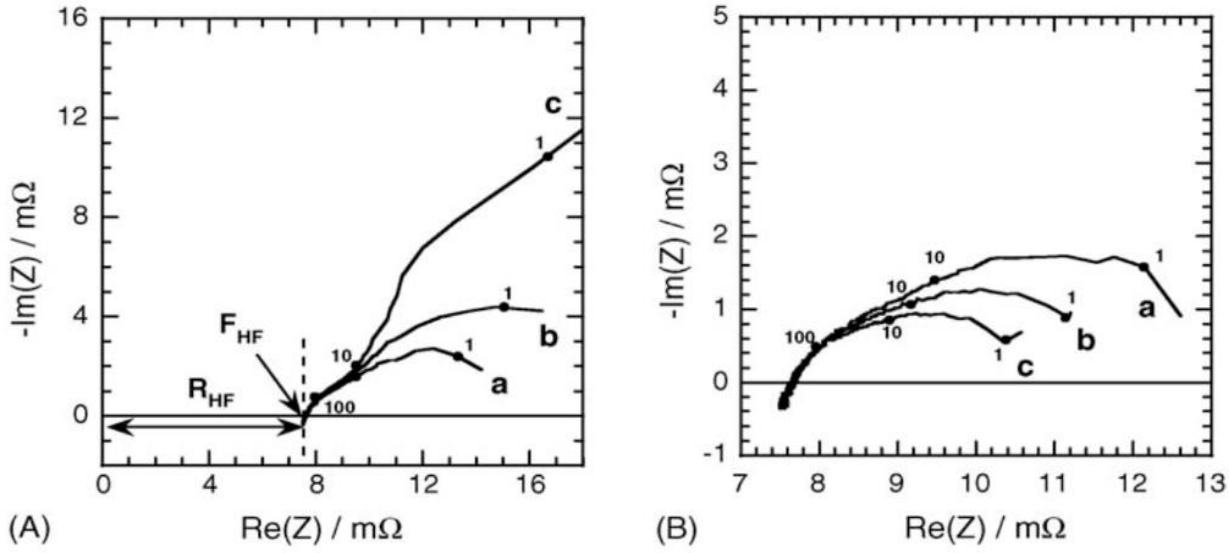

Fig 3.12 EIS plots of a 45Ah lead acid battery at different (a) charge and (b) discharge rates [22]

iii. Ageing and Temperature

Corrosion at the grid of the positive plate (and negative plate in some rare instances) and water loss at the separator dominate the ageing or capacity fading process of a lead acid battery [18] – [19]. On the Nyquist plot, ageing is observed as a sharp increase in the ohmic resistance. On the other hand, for temperature condition monitoring, [21] varied SoC and temperature and analysed the data for the different parameters of the EEC. The notable observation is that the ohmic resistance increased as temperature decreased.

3.5 EIS IMPLEMENTATION

Fig 3.13 shows the procedure for EIS measurement. The "$battery$" represents either the lead acid or lithium NCM. The $i(t)$ and $v(t)$ are the time domain excitation and response signals respectively. The $low-pass\ filter$ with a window is used to eliminate the high frequency noise component in the response signal. Fast Fourier Transform (FFT) is used to compute the frequency response of the excitation (current) and response (voltage) signal. The complex impedance is calculated based on the ohms law relationship.

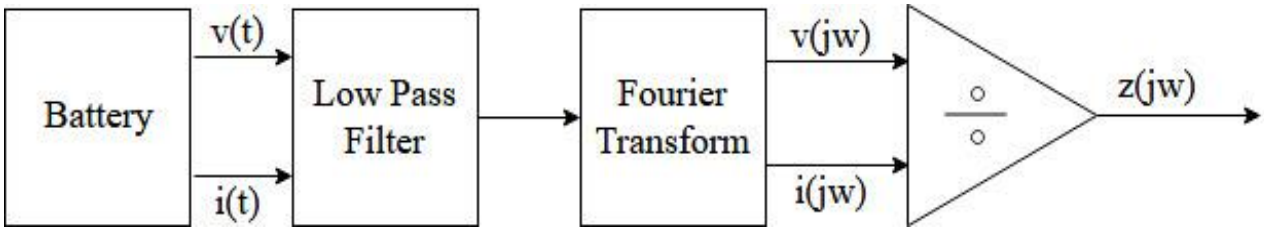

Fig 3.13 Procedure for EIS measurement.

3.5.1 Cell Conditioning and Frequency Selection

The lead acid battery utilized in this test was charged through a constant voltage profile and discharged through a constant current load. The lithium NCM battery was charged through a constant current-constant voltage charging mechanism and discharged through a constant current load. Before EIS measurements are carried out on a cell, it is expected that the cell has undergone cycling. In this study, the batteries that were used to carry out EIS tests, had previously undergone cycling with over 30 charge-discharge cycles. For the frequency selection – the injected frequencies of interest (f_{n}) were chosen on a logarithmic scale to provide a quality Nyquist plot as shown in (3 – 16):

$$f_{\mathrm{n}} = (f_o \times 2^n) \qquad \mathrm{n} = 0, 1, 2, 3, \ldots, N-1 \qquad (3-16)$$

In (3 – 16), The first and last frequencies were selected carefully by investigating the shape of the Nyquist plot of both batteries. This ensured that the critical kinetic features of the battery were covered. The critical frequency range of the lead acid battery was $6kHz - 100mHz$, whereas that of the lithium NCM battery was $2kHz - 20mHz$. EIS measurement is therefore completed in 3.4 minutes for the lead acid battery and 6.8 minutes for the lithium NCM battery.

3.5.2 Sampling Rate and Recovery Period

According to the Nyquist sampling theorem, the sampling frequency must be two times greater than the highest measured frequency. In all experiments carried out in this study, the sampling frequency was over 10 times greater the user frequency of interest. For the recovery period – the longer the period of the excitation signal, the more time it takes for the battery to attain chemical stability. It took the lead acid battery a longer time to attain chemical stability compared to the lithium NCM battery when the excitation signal was removed. The waiting time before frequency excitation for different periods of both batteries is shown in the Appendix.

3.5.3 Filter and Windowing

Prior to the application of Fast Fourier Transform (FFT), a filter and window are applied to the time-domain signals (see Fig 3.14). The filter selected is a 4th order digital low-pass Butterworth. This filter eliminates high-frequencies introduced by noise into the system greater than the cut-off frequencies [14]. When FFT is applied to a signal, the FFT computation assumes that each data blocks' signal is periodic. However, if this is not the case, like a non-periodic signal, the resulting frequency response suffers from leakage. This leakage causes the energy of the signal to smear over a wide range of FFT frequencies, instead of a narrow range of frequencies. Thus, a window is applied to reduce and correct leakages by coercing the signal to be periodic. It is important to note that though FFT windows reduce leakages, it cannot eliminate it. Besides, FFT windows alter the shape of the leakage, thus, care must be taken in selecting the appropriate window, depending on the application. For this study, a Hanning window is utilized because it produces a very good frequency resolution compared to other windows available in National Instruments – LabVIEW.

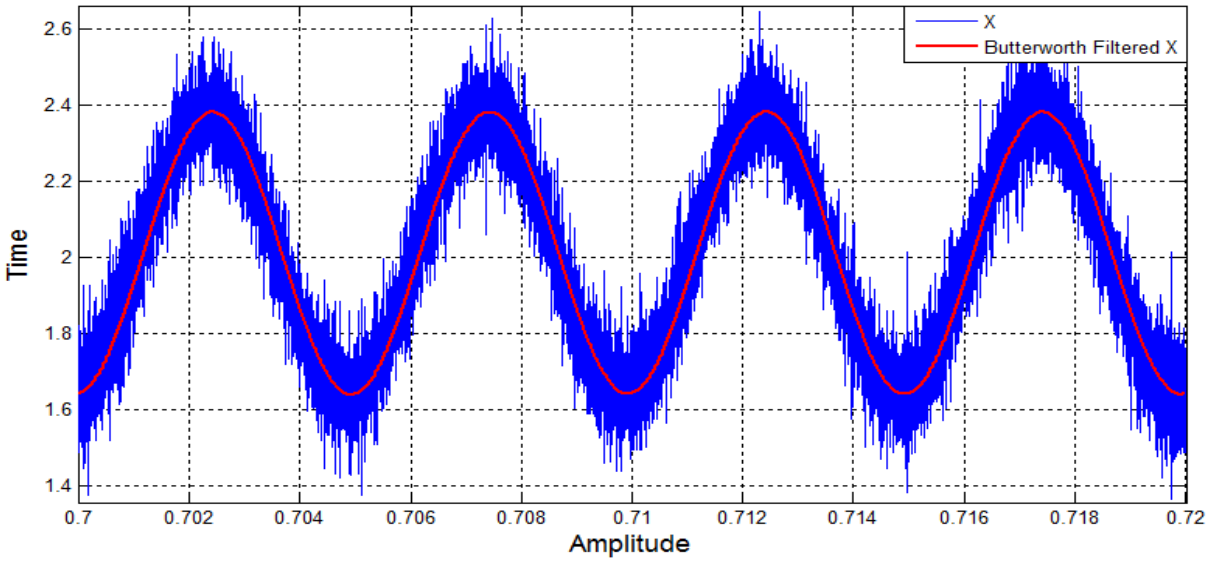

Fig 3.14 Time domain excitation signal (a) before filter (b) after filter

3.5.4 EIS curve fitting to Equivalent Circuit

EIS plots are fitted to an EEC, for state estimation purposes. Fig 3.15 describes the relationship between the Nyquist plot and EEC. In Fig 3.15, L is the virtual inductor, R is the ohmic series resistance, $Z_{arc} = (R_{2/3}//C_{DL})$ is the charge transfer resistance – double layer capacitance and W is the Warburg impedance. CPE is used instead of C_{DL} to account for the depression of the semi-circle as earlier discussed in Chapter 3.3

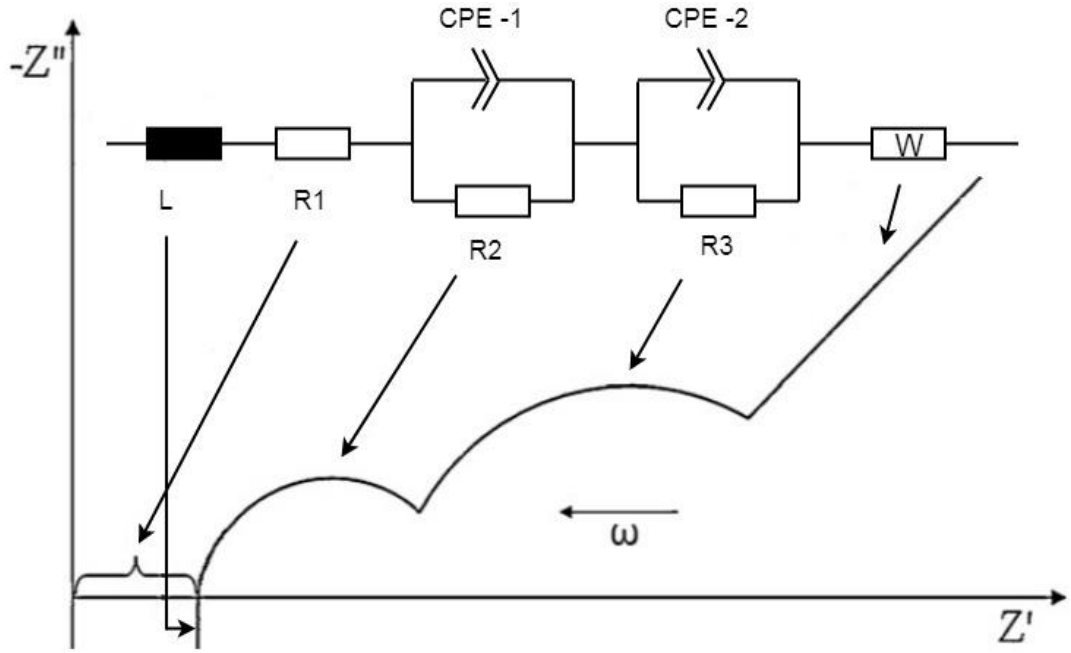

Fig 3.15 EEC often used for description of the electrochemical processes and their corresponding Nyquist shape

The Complex Nonlinear Least Squares (CNLS) technique is used to fit the Nyquist plot to an EEC that correlates to the physicochemical processes occurring in the battery. From electrochemical modelling of the lead acid and lithium NCM in Chapter 3.4, the simplified EEC model for both batteries is presented in Fig 3.16:

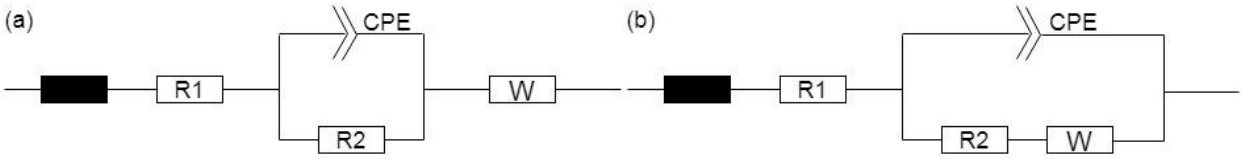

Fig 3.16 Simplified EEC of (a) Lithium NCM battery and (b) Lead acid battery

When applying CNLS, it is important to select an appropriate initial value, to ensure that the algorithm locates the global minimum and not the local minimum. The CNLS technique is utilized to set the parameters in such a way that the sum of squared deviations is minimized [28]. The algorithm is shown in (3 – 17):

$$Min\ f(x) = min\ (L, R, CPE, W) \sum_{n=f_{min}}^{f_{max}} [Z_{EC}\ (L, R, CPE, W, f_n) - Z_{measure,n}\ ]^2 \quad (3-17)$$

In (3 – 17), *L* is inductance, *R* is resistance, *CPE* is Constant Phase Element, *W* is Warburg and *Z* is impedance. The parameters in (3 – 17) are varied in the global minimum path via the Levenberg–Marquardt Algorithm (LMA). In LMA, the step size iteration is designed to increase by a factor that is repeatedly calculated in each step, resulting in a robust algorithm that converges regardless of the accuracy of the initial parameters. LMA combines the advantages of both the steepest descent method and Gauss–Newton [28]. The Nyquist plot data fitted to the EEC model of both batteries at room temperature and 50% state of charge is shown in Fig 3.17:

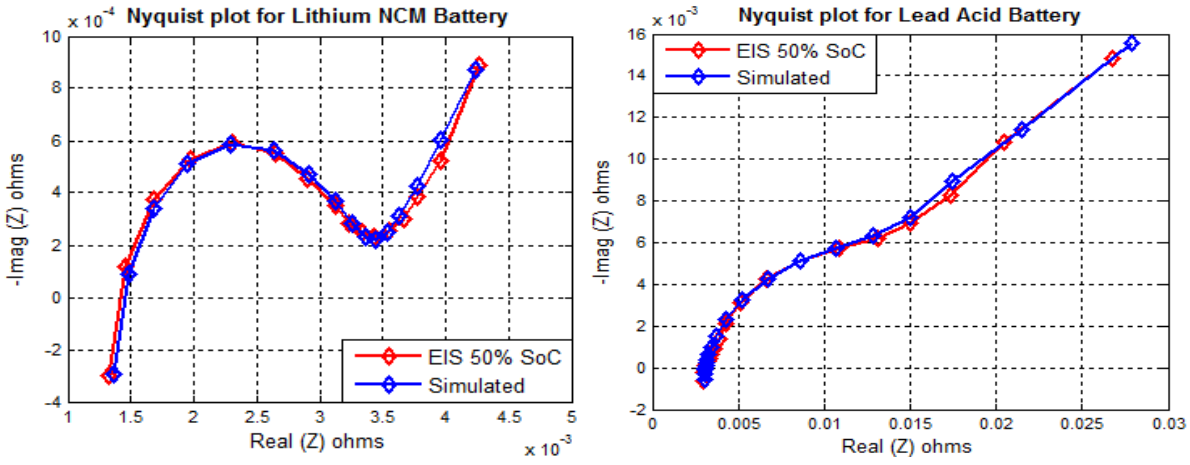

Fig 3.17 Curve fitting of EIS plots (a) Lithium NCM (b) Lead Acid

3.6 SUMMARY

This Chapter discusses the Electrochemical Impedance Spectroscopy (EIS) technique. Firstly, EIS methodology: Kramers–Kronig relation and the optimum perturbation amplitude for batteries is discussed. Subsequently, EIS data representation on a Nyquist plot or Bode plot and equivalent circuit elements (resistor, capacitor and inductor) is studied in detail. Impedance study on the lead acid and lithium NCM batteries are also carried out; and the simplification of their equivalent circuit and their response to different operational conditions is explored. Lastly, EIS implementation on software is discussed, with focus on: frequency selection, sampling rate, filter and windowing and EIS plot curve fitting to an EEC.

3.7 REFERENCES

[1] Natalia A. Canasa, Kei Hirosea, Brigitta Pascuccia, Norbert Wagner, K. Andreas Friedrich, Renate Hiesgen, "Investigations of lithium–sulfur batteries using electrochemical impedance spectroscopy," Elsevier Journal, Electrochimica Acta 97 (2013) 42– 5.

[2] Zhaofeng Deng, Zhian Zhang, Yanqing Lai, Jin Liu,a Jie Li and Yexiang Liua, "Electrochemical Impedance Spectroscopy Study of a Lithium/Sulfur Battery: Modeling and Analysis of Capacity Fading," Journal of The Electrochemical Society, 160 (4) A553-A558 (2013)

[3] Gamry Instruments, "EIS: Potentiostatic or Galvanostatic Mode?" Available online: [https://www.gamry.com/application-notes/EIS/eis-potentiostatic-galvanostatic-mode/]

[4] Evgenij Barsoukov, J. Ross Macdonald, "Impedance Spectroscopy Theory, Experiment, and Applications," Published by John Wiley & Sons, Inc., Hoboken, New Jersey, 2005.

[5] Gamry Instruments, "Basics of Electrochemical Impedance Spectroscopy," Available online: [https://www.gamry.com/application-notes/EIS/basics-of-electrochemical-impedance-spectroscopy/]

[6] Cornelia Breitkopf, "Impedance Spectroscopy, Old Technique – New Applications," Lecture Series at Fritz-Haber-Institute Berlin, Modern Methods in Heterogeneous Catalysis, Fakultät Maschinenwesen | Institut für Energietechnik | Professur für Technische Thermodynamik, Technische Universität Dresden, 7.12.2012.

[7] Princeton Applied Research, "Basics of Electrochemical Impedance Spectroscopy," Application Note AC- 1, Available online: [http://www.ameteksi.com/-/media/ameteksi/download_links/documentations/library/princetonappliedresearch/app_note_ac-1.pdf]

[8] Chris de beer, “Condition Monitoring of Polymer Electrolyte Membrane Fuel Cells”, PhD. Thesis, University of Cape Town, 2014.

[9] P. Gode, F. Jaouen, G. Lindbergh, A. Lundblad, G. Sundholm, Electrchimica Acta 2003, 48, 4175.

[10] J. J. Giner-Sanz, E.M.Ortega, V. Perez-Herranz, “Optimization of the Perturbation Amplitude for Impedance Measurements in a Commercial PEM Fuel Cell Using Total Harmonic Distortion,” 5th EUROPEAN PEFC & H2 FORUM (EFCF2015), June 30 – July 3, 2015 held in Lucerne, Switzerland. Organized by the European Fuel Cells Forum

[11] M. Kiel, O. Bohlen, D. U. Sauer, Electrochimica Acta 2008, 53, 7367.

[12] Weilin Luo, Chao Lv, Lixin Wang, Chao Liu, “Study on Impedance Model of Li-ion Battery,” School of Electrical Engineering and Automation Harbin Institute of Technology.

[13] Jun Xu and Binggang Cao, “Battery Management System for Electric Drive Vehicles – Modeling, State Estimation and Balancing,” Available online: [http://dx.doi.org/10.5772/61609]

[14] Steven W. Smith,” The Scientist and Engineer’s Guide to Digital Signal Processing,” DSP Guide, 2nd Ed., 1999.

[15] National Instrument, “Understanding FFTs and Windowing,” NI white paper

[16] M.L. Gopikanth, S. Sathyanarayana, “Impedance Parameters and the State-Of-Charge (II) Lead-Acid Battery,” Journal of Applied Electrochemistry 9 (1979) 369-379.

[17] Holger Blanke, Oliver Bohlen, Stephan Buller, Rik W. De Doncker, Birger Fricke, Abderrezak Hammouche, Dirk Linzen, Marc Thele, Dirk Uwe Sauer Impedance measurements on lead–acid batteries for state-of-charge, state-of-health and cranking capability prognosis in electric and hybrid electric vehicles, Journal of Power Sources 144 (2005) 418–425

[18] Dr. Hong Shih, Dr. Tai-Chin Lo, “Electrochemical Impedance Spectroscopy for Battery Research and Development, Technical,” Report 31, Solartron 1996

[19] Huet, “A review of impedance measurements for determination of the state-of-charge or state-of-health of secondary batteries,” Journal of Power Sources 70 (1998) 59-69

[20] Quan-Chao Zhuang, Xiang-Yun Qiu, Shou-Dong Xu,Ying-Huai Qiang and Shi-Gang Sun, “Diagnosis of Electrochemical Impedance Spectroscopy in Lithium-Ion Batteries,” Lithium Ion Batteries – New Developments, www.intechopen.com

[21] Alvin J. Salkind et al. “Impedance modeling of intermediate size lead–acid batteries,” Journal of Power Sources 116 (2003) 174–184.

[22] S. Rodrigues, N. Munichandraiah, and A. K. Shukla, “A review of state-of-charge indication of batteries by means of a.c. impedance measurements,” J. Power Sources, vol. 87, no. 1–2, pp. 12–20, Apr. 2000.

[23] Barsoukov, E.; Macdonald, J. R. Impedance Spectroscopy Theory, Experiment, and Applications. John Wiley & Sons, Inc. Hoboken, New Jersey, 2005.

[24] Stroe, D. I., Swierczynski, M. J., Stan, A-I., Knap, V., Teodorescu, R., & Andreasen, S. J. (2014). Diagnosis of Lithium-Ion Batteries State-of-Health based on Electrochemical Impedance Spectroscopy Technique. In Proceedings of the 2014 Energy Conversion Congress and Exposition (ECCE) (pp. 4576-4582).

[25] L. Ran et al, "Prediction of state of charge of lithium-ion rechargeable battery with electrochemical impedance spectroscopy theory," in 2010 5th IEEE Conference on Industrial Electronics and Applications, 2010, pp. 684-688.

[26] L. W. Juang et al, "The impact of DC current current on the modeling of lithium iron phosphate and lead-acid batteries observed using electrochemical impedance spectroscopy," in 2014 IEEE Energy Conversion Congress and Exposition (ECCE), 2014, pp. 2575-2581.

[27] D. Andre et al, "Characterization of high-power lithium-ion batteries by electrochemical impedance spectroscopy. II: Modelling," J. Power Sources, vol. 196, pp. 5349-5356, 2011.

[28] Uwe Westerhoff, Kerstin Kurbach, Frank Lienesch and Michael Kurrat, “Analysis of Lithium-Ion Battery Models Based on Electrochemical Impedance Spectroscopy,” Energy Technol. 2016, 4, 1620 – 1630]

[29] L.H.J. Raijmakers, D.L. Danilov, J.P.M. van Lammeren, M.J.G. Lammers, P.H.L. Notten Sensorless battery temperature measurements based on electrochemical impedance spectroscopy, Journal of Power Sources 247 (2014) 539-544

[30] Eckhard Karden, Peter Mauracher &Friedhelm Schijpe, “Electrochemical modelling of lead/ acid batteries under operating conditions of electric vehicles,” Journal of PowerSources64 (1997) 175-180.

4. BROADBAND EXCITATION IMPLEMENTATION

Electrochemical Impedance Spectroscopy (EIS) measurements are time consuming [1]. An alternative to reduce the time, is the application of a broadband signal. However, an increase in the measurement speed results in a compromise in the impedance spectrum accuracy. An area in which broadband techniques have been significantly applied, is the biomedical industry [1] – [5]. For these applications, a high Signal to Noise Ratio (SNR) is required to make meaningful tissue measurements. These measurements usually involve high magnitude excitation signals with a large crest factor. In any application, the observation of linearity and time invariance is critical. Various broadband techniques that have been utilized in impedance spectroscopy measurements include: multisine signal, chirp excitation and pseudo-random binary sequence (PRBS) excitation. Each of these techniques has its own frequency and time properties, thus, the Crest factor is a metric used to compare these techniques. The Crest Factor (CF) of an excitation $u[n]$ is the ratio of its peak value l_{max} to its root mean square value l_{rms} [1].

$$CF\ (u)\ = \frac{l_{max}}{l_{rms}} = \frac{\underset{n\in[0,N-1]}{max}\ |u[n]}{\sqrt{\frac{1}{N}\sum_{n=0}^{N-1}|u[n]|}} \qquad (4-1)$$

CF estimates how much amplitude the signal will consume to inject a certain power level into the system. CF implies the signals compactness. The lower the CF, the more energy is transferred to the system, resulting in a better signal-to-noise ratio. The CF ranges from 1 – the ideal to infinity – the worst possible case. The reduction of CF will permit a larger energy to be injected into the system. It will also ensure that the system is operating in the linear region – since excitation signals with high CF are likely to disturb the system outside the EIS measurement band; hence increasing the likelihood that the system will deviate from its (quasi) linear region.

Fig 4.1 describes the procedure for broadband impedance spectroscopy measurement in this study. It can be observed that, the most important consideration in processing a broadband signal, is determining whether it is a periodic or non-periodic signal. Fast Fourier Transform (FFT) is the technique applied in processing periodic signals, whereas the Short Time Fourier Transform (STFT): a time-window frequency analysis tool, is the technique applied in processing non-periodic signals.

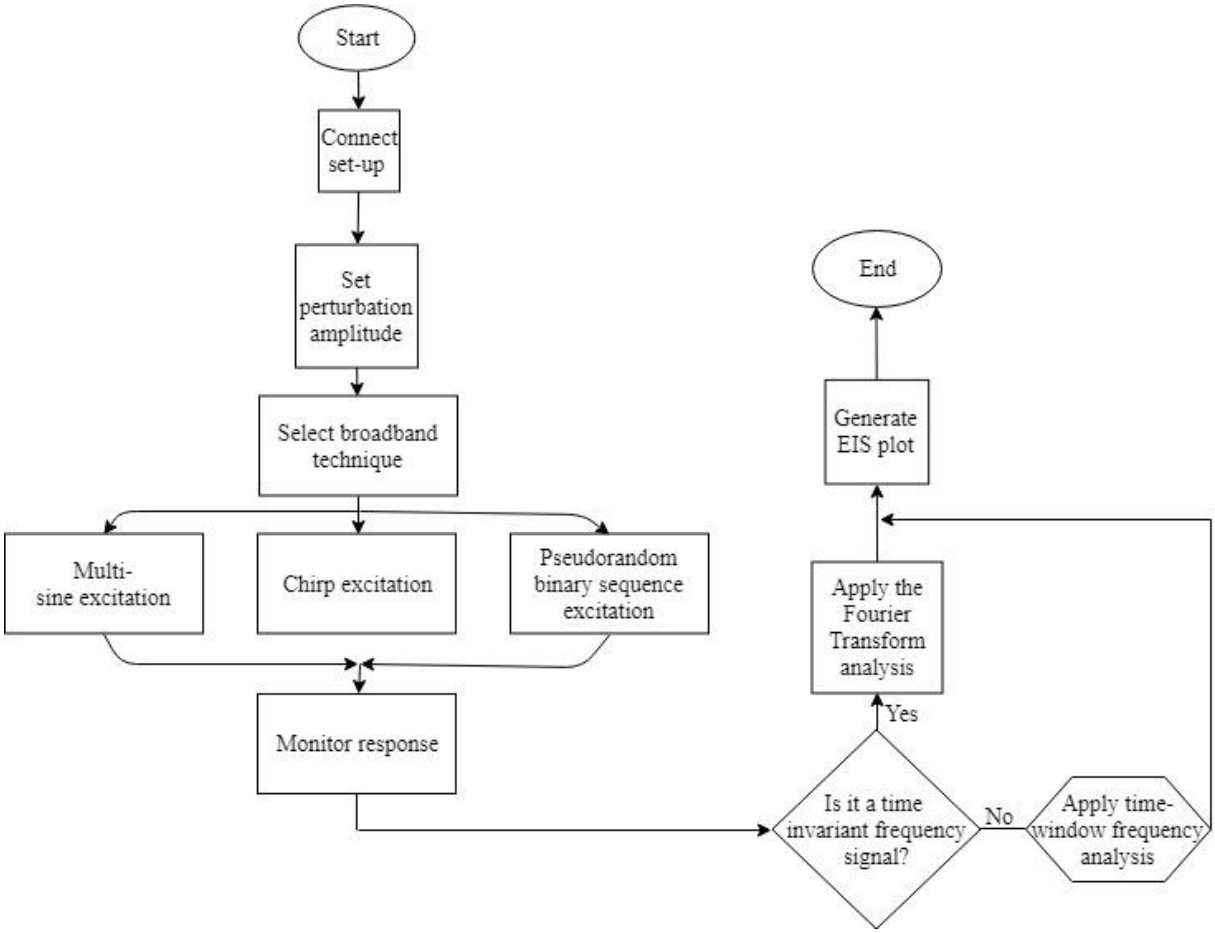

Fig 4.1 Flowchart for carrying out broadband excitation measurement.

4.1 MULTISINE EXCITATION

The multisine signal is composed of the integral of N frequencies – with each one having its own amplitude and phase. In a real-valued multisine, the expression in the time-domain is a Fourier series of order *N*

$$u(t) = \sum_{n=0}^{N-1} a_n \cos(2\pi f_n t + \varphi_n) \qquad (4-2)$$

In (4 – 2), *N* is the number of selected excitation frequencies in the signal, a_n is the amplitude matrix, f_n is the excited frequencies and φ_n is the phase matrix. Fig 4.2 shows the unoptimized multisine signal for both the lithium NCM and lead acid batteries. More so, the frequency spectrum of a multisine signal is flat and its excitation energy is distributed evenly across the user-defined set of frequencies as shown in Fig 4.3.

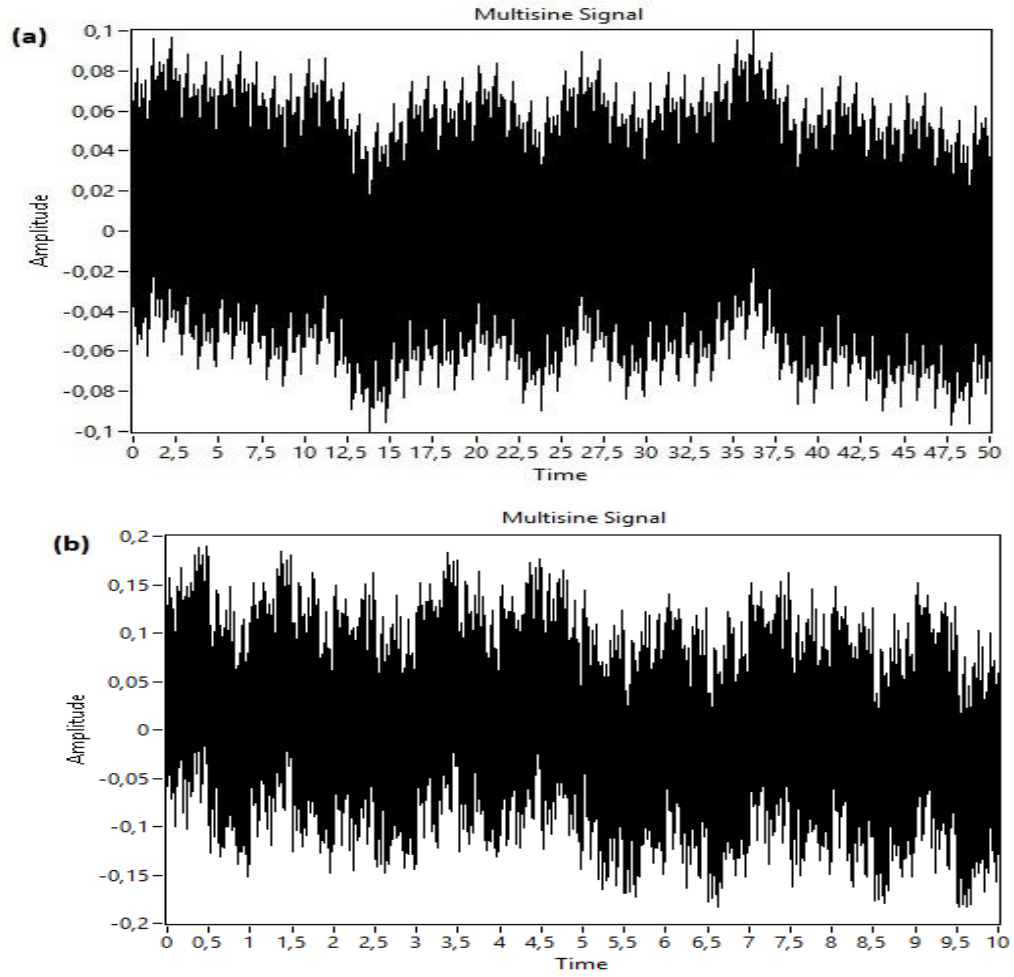

Fig 4.2 Unoptimized multisine signals for (a) lithium NCM battery – CF = 4.39 (b) lead acid battery – CF = 4.12

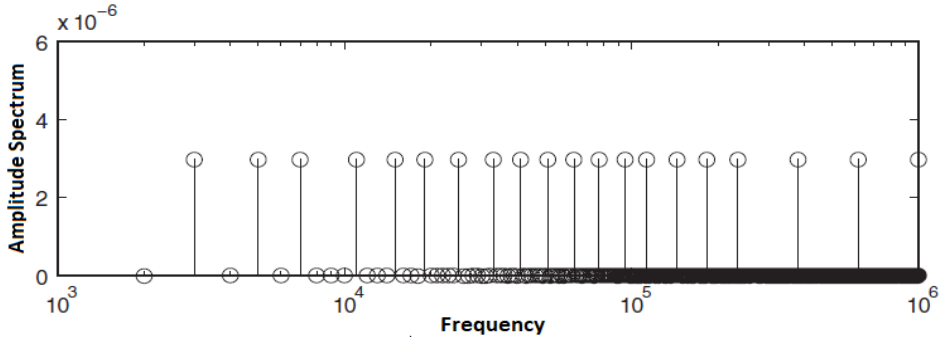

Fig 4.3 Frequency spectrum of the multisine signal

In an unoptimized signal, the amplitudes of all excitation frequencies are constant, and the excitation frequencies and phases are randomly selected over the user-bandwidth of interest. It is evident from Fig 4.2, that the unoptimized (traditional) multisine signal possesses a large crest factor (CF) or peak to peak magnitude. Also evident is the fact that the CF for the multisine excitation of a lithium NCM is greater than that of the lead acid. This can be attributed to the associated time constants of both batteries. Because of the higher time constant of a

lithium NCM battery compared to the lead acid battery, a greater number of excitation frequencies are typically required for appropriate system characterization. This increasing number of excitation frequencies associated with the battery's time constant, ultimately increases the CF as will be discussed in Chapter 4.1.2.

The CF of a multisine can be reduced by amplitude, frequency and phase optimization. The rms of the multisine is independent of the phases (φ) but is dependent on the amplitude (a_n) and number of signals considered. However, the maximal peak can be considerably compressed based on the choice of the phase vectors of the selected frequency, which results in the minimization of the Crest Factor [1] – [6]. In this study, the frequency, magnitude and phase of the multisine signal is optimized as will be discussed in the proceeding section.

4.1.1 Frequency Optimization

The frequency is distributed to maximize the resolution of the measured impedance and minimize signal time. An evenly spaced frequency distribution with a small number of excited frequencies will yield the same information as that with logarithmic spacing but with less accuracy [1]. The disadvantage of an evenly spaced frequency distribution however, is the need for high number of excitation frequencies in the EIS frequency range. More so, evenly spaced frequency distribution results in the appearance of harmonics at the fundamental frequencies. To avoid the presence of harmonic frequencies that results from even nonlinearities, a log-odd frequency distribution is applied as [1] and shown in (4 – 3). Fig 4.4 shows the CF reduction following frequency optimization; f_{n} represents the injected frequency and f_o represents the initial frequency.

$$f_{\mathrm{n}} = (f_o \times 2^n) + 1 \qquad n = 0, 1, 2, 3, \ldots, N-1 \qquad (4-3)$$

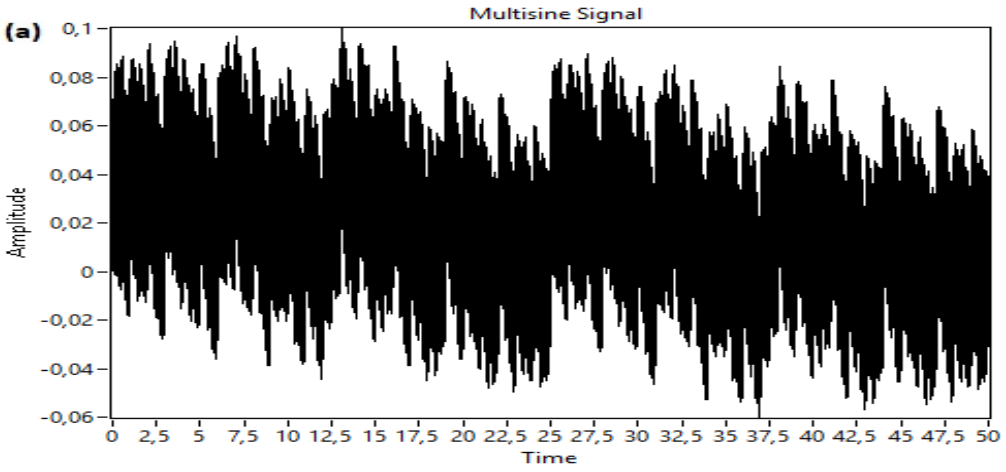

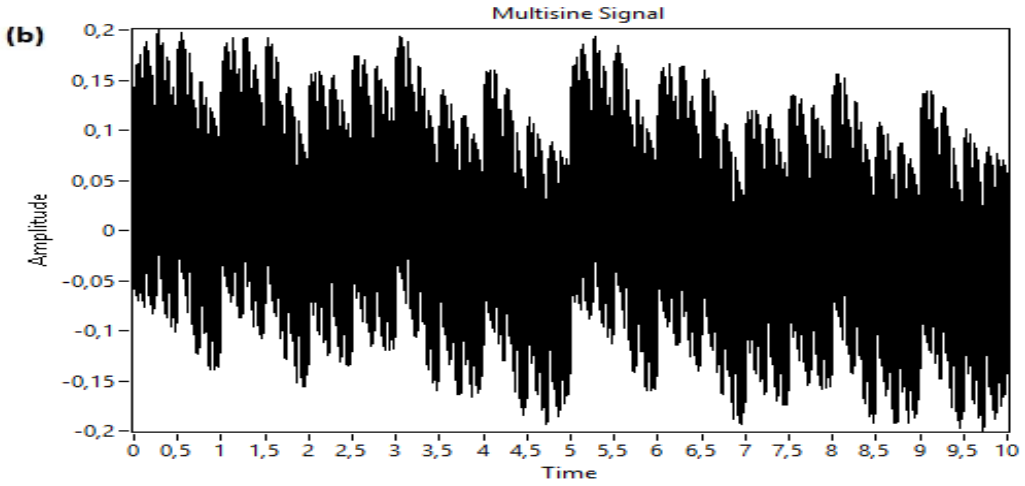

Fig 4.4 Frequency optimized multisine (a) lithium NCM – C.F = 3.43 (b) lead acid – C.F = 3.29

4.1.2 Amplitude Optimization

The addition of sine waves ultimately increases the excitation signal amplitude. For the assumption of linearity, it is pertinent for the overall signal amplitude to be kept low. The magnitude is optimized to determine the appropriate amplitudes of the harmonic spectrum to maximize signal energy at the frequencies of interest.

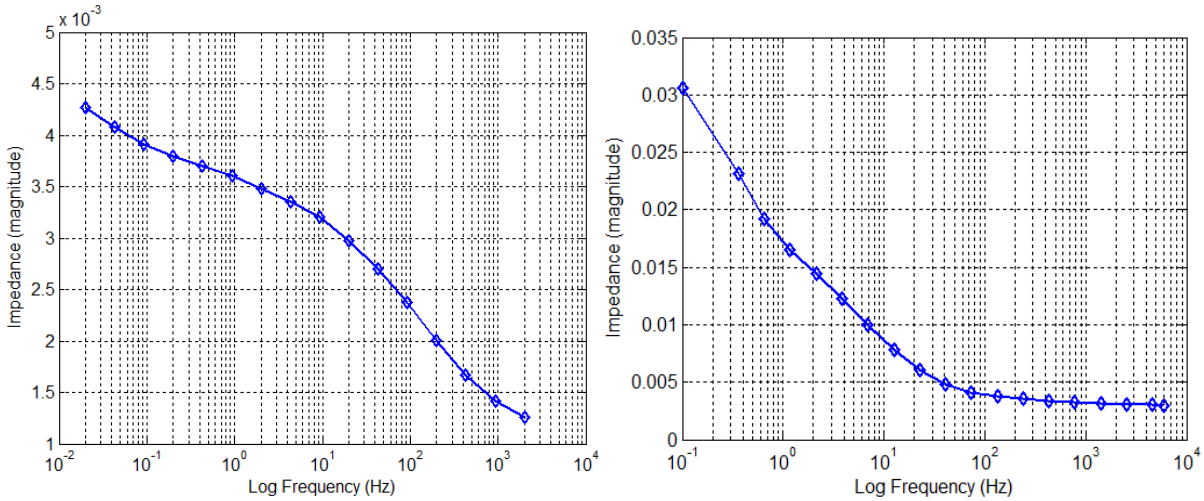

Fig 4.5 EIS (bode) plot at 50% SoC and room temperature for lithium NCM (a) and lead acid (b)

From the Bode plot of both batteries in Fig 4.5, it can be observed that the impedance decreases with increasing frequency. This insight is utilized in optimizing the BIS signals. Consequently, the excitation amplitude is varied against frequency – as an inverse of the Bode plot. This was also applied in [7] (see Fig 4.6).

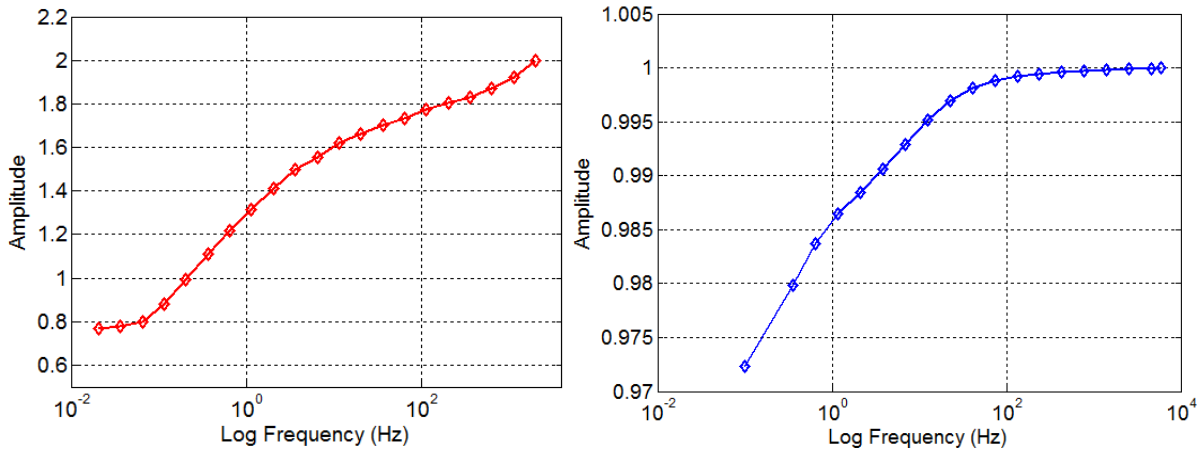

Fig 4.6 Excitation amplitude against user frequencies of interest for lithium NCM (a) & lead acid (b)

Magnitude optimization makes it possible to control the signal power to obtain optimal results, which is not possible with the flat magnitude spectrum [5]. It also proportionately scales the excitation amplitude against frequencies in the broadband signal; thus, overcoming the noise effects during response measurements of lower systems [1]. Fig 4.7 shows the CF reduction following magnitude optimization.

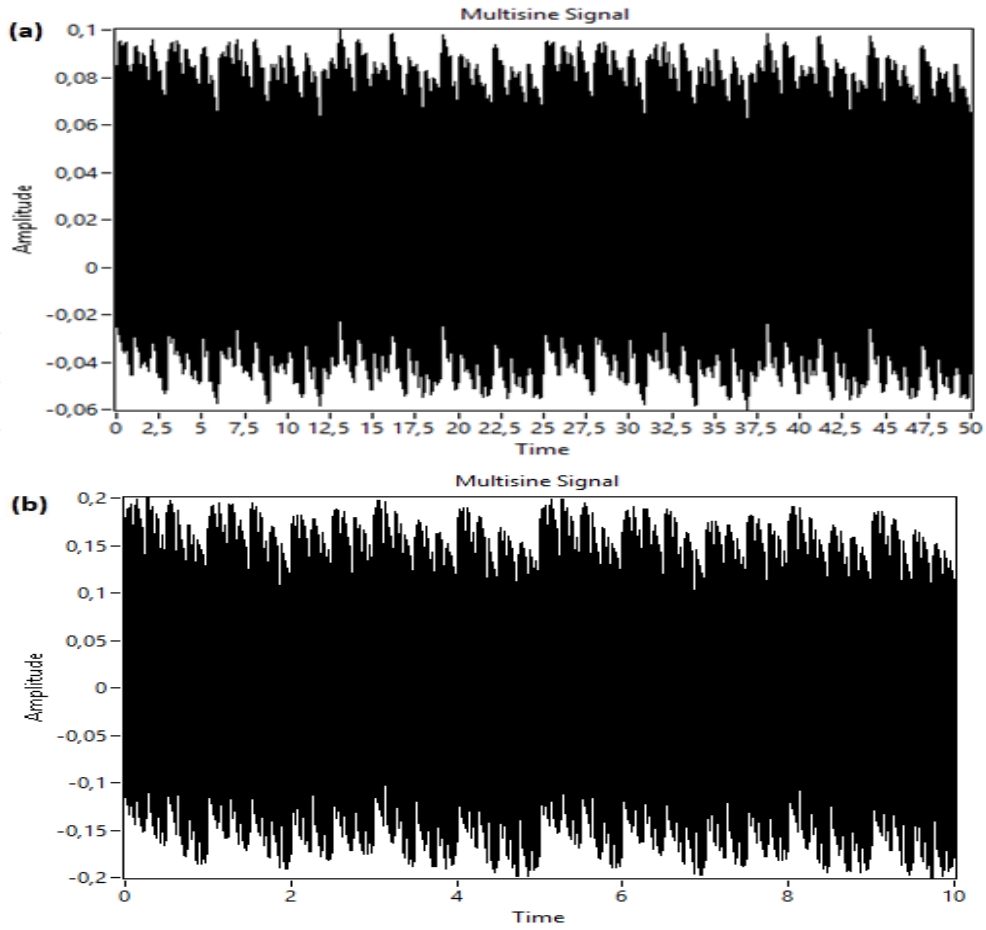

Fig 4.7 Amplitude and frequency optimized multisine (a) lithium NCM – C.F = 3.16 (b) lead acid – C.F = 3.04

4.1.3 Phase Optimization

The phase optimization minimizes the overall signal amplitude period in the time domain, to maintain the same power level of the excitation frequencies. Simply varying the phase difference from 0 to 360 degrees $(0 - 2\pi)$ between the consecutively adjacent frequency results in a low CF. However, a more appropriate relationship was propounded by Schroeder in [1] – where it was assumed the number of excited frequencies at the user selected power spectrum is large and concentrated in a bandwidth: small, in comparison to the center frequency. The Schroeder equation is shown in (4 – 4). Newman later proposed (4 – 5):

$$\phi_m = \phi_n - 2\pi \sum_{n=0}^{m-1}(m-n) \times \frac{|a_m|^2}{\sum_{k=0}^{M-1}|a_k|^2} \quad m = 1,\ldots,M-1, \phi_n \in [-\pi,\pi] \quad (4-4)$$

$$\phi_n = \frac{\pi n^2}{N}, \quad n = 0{:}\,N-1 \quad (4-5)$$

In the Newman phases [1], it is only the number – N of the excitation frequencies in the multisine that is required for optimization. On the contrary, for the Schroeder phases, the amplitude is considered, resulting in better results for the non-constant multisine amplitudes case. The phases associated with Schroeder's method gives only a reasonable result for a flat and wideband user-defined spectrum, but under different conditions, has an undesirable result [1]. The Newman's phase was therefore applied in this study. Fig 4.8 shows the CF reduction following phase optimization.

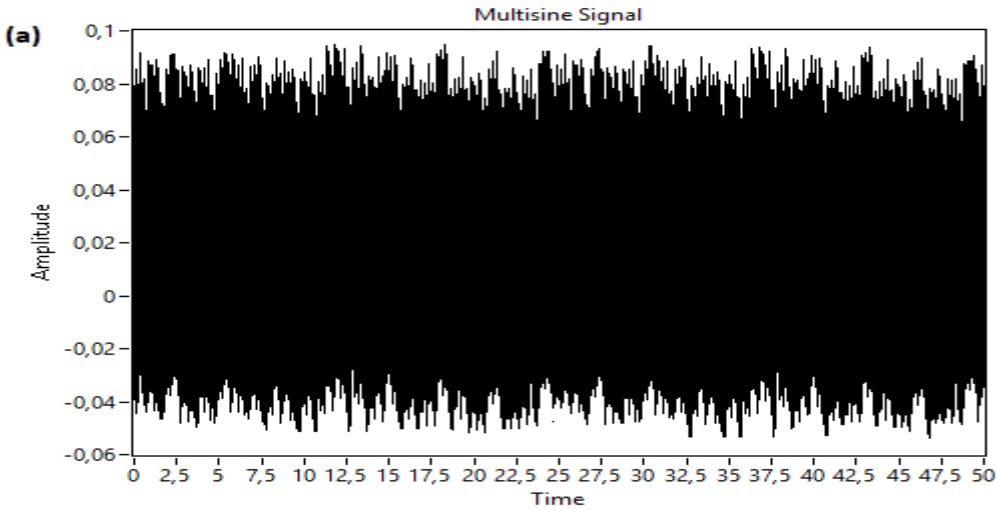

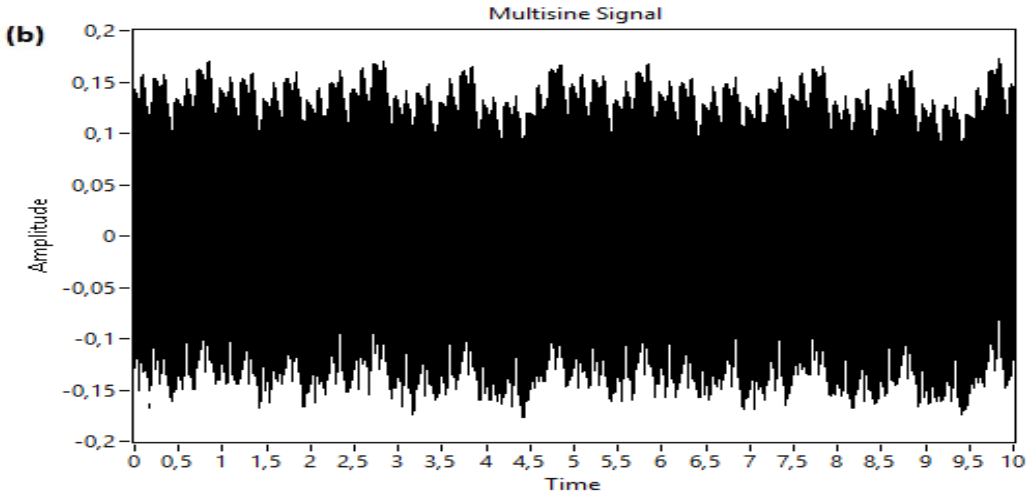

Fig 4.8 Phase, amplitude and frequency optimized multisine (a) lithium NCM – C.F = 2.86 (b) lead acid – C.F =2.79

4.1.4 Multisine implementation

In this study, the multisine perturbation is generated in software using the Multitone Generator Virtual Instrument block of the NI LabVIEW software [4]. The three main parameters used to design the multisine signal in the LabVIEW software are: tone amplitudes, tone frequencies and tone phases. All three parameters constitute an array, where all elements in the array represents a single amplitude, frequency and phase. The size of each array of the parameters must also be in tandem with one another.

Following optimization of the multisine, it took the multisine signal 10 seconds to complete EIS measurement for the lead acid battery and 50 seconds for the lithium NCM battery, mainly attributed to the lowest frequency component associated with each battery. Fig 4.9 shows the effect of multisine signal optimization on the Nyquist plot for both batteries. It can be observed that multisine signal optimization significantly improves the quality of the impedance (Nyquist) plot shape. Also evident from the internal chemistry point of view, is the fact that, the lead acid battery is more sensitive to the effect of multisine signal optimization. This could be because the lead acid battery has a lower chemical stability/rapid pulse capability compared to the lithium NCM battery [9].

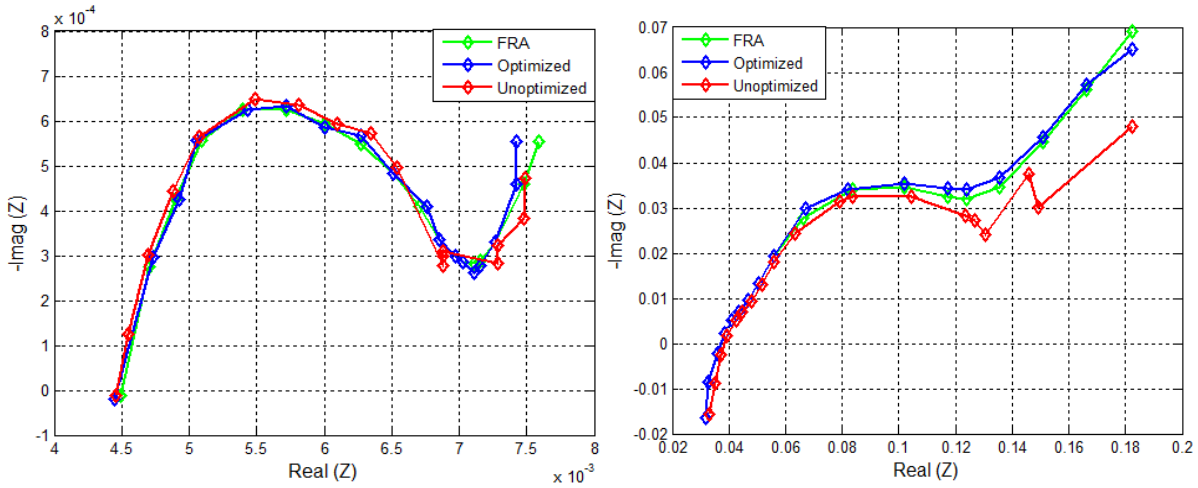

Fig 4.9 Effect of multisine signal optimization on EIS plot for lithium NCM (a) and lead acid (b)

4.2 CHIRP BROADBAND EXCITATION

The chirp signal is a sine sweep excitation, which can be simply generated from either a direct digital synthesizer or a field programmable gate array. Based on the type of frequency variation, a chirp signal's frequency can increase continuously (up-chirp) or decrease continuously (down-chirp) with time [8]. The chirp time domain function is expressed in (4 – 6) and the chirp rate in (4 – 7):

$$c(t) = A\,sin\,(2\pi f(t)\,t) \qquad (4-6)$$

$$f(t) = f_{min} + \left(\frac{f_{max} - f_{min}}{2T}\right) t \qquad (4-7)$$

In (4 – 6) and (4 – 7), A is the amplitude, t is the simulation time, f_{min} is the initial frequency and T is the target time. The advantage of the chirp signal is that it can be generated in a very short time and has a large bandwidth. Fig 4.10 is the time domain chirp-signal excitation generated from the LabVIEW software.

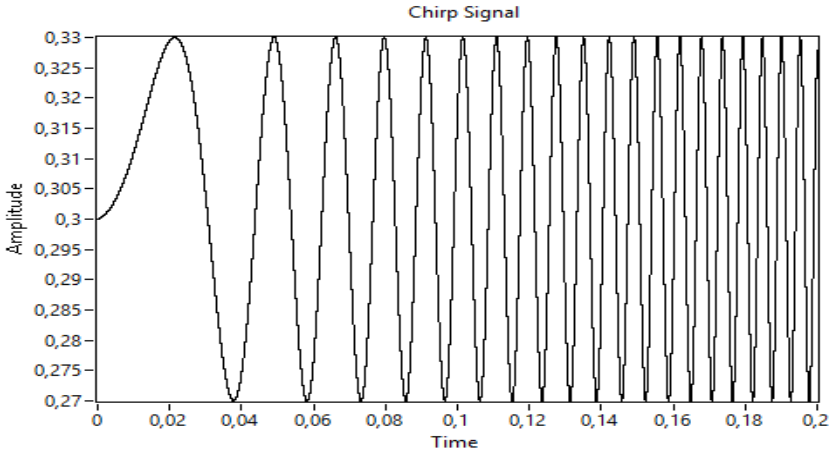

Fig 4.10 Chirp broadband signal generated from LabVIEW software – CF = 1.4

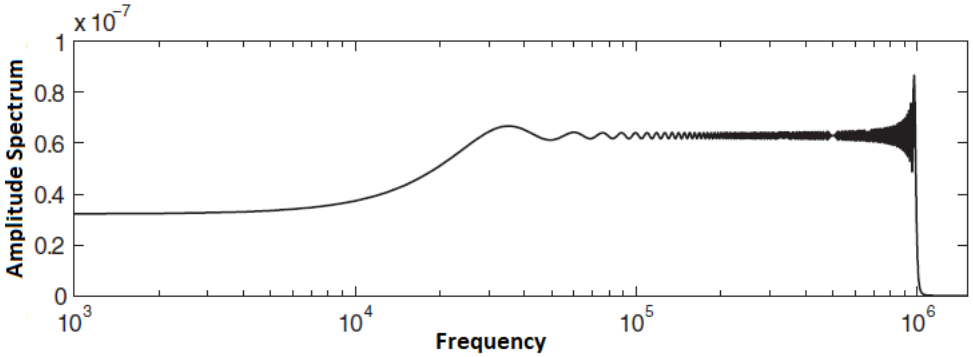

Fig 4.11 Frequency spectrum of the chirp signal

Typically, the user doesn't have control over the frequency points or period within the chirp signal. From Fig 4.11 it can be observed that the signal energy is concentrated only at the high frequency. Therefore, the drawback of the chirp signal is that the low frequency impedance data is scattered due to poor signal-to-noise ratio at these frequencies. More so, the chirp signal function is different from the multisine function because it is a time-varying frequency (non-stationary signal). The Short-time Fourier transform (STFT) or Short-term Fourier transform – a time-frequency transformation based on Fourier Transforms [2], is required to maximize the information in the chirp signal.

4.2.1 Short-time Fourier Transform (STFT)

The STFT uses the Discrete Fourier Transform (DFT) to analyse the properties of a time-varying frequency signal. In a time-varying frequency signal, time analysis obfuscates frequency and frequency analysis obfuscates time. In practice, the STFT is computed by dividing a longer time signal into several time windows of equal length that usually overlap each other to decrease the artefacts at the boundary. The Fourier Transform is then applied separately on each window as described in Fig 4.12.

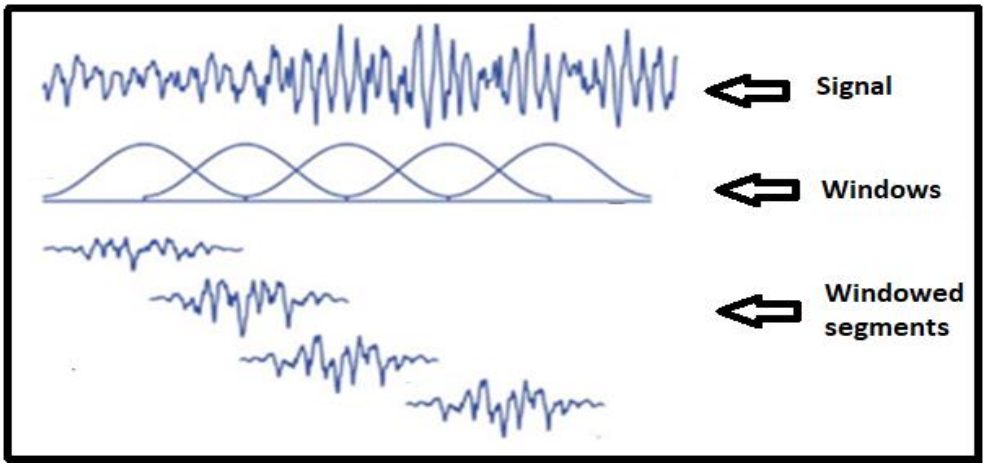

Fig 4.12 Procedure for the Short-time Fourier Transformation of a non-stationary signal [2]

The STFT of a signal is expressed as (4 – 8):

$$X\,[m,k]\; = \sum_{n=0}^{L-1} x[m+n]e^{-j\frac{2\pi}{L}nk} \qquad (4-8)$$

From (4 – 8), m is the starting point for the localized Discrete-time Fourier Transform (DFT), k is the index of the DFT at that point and $[m+n]$ is the signal samples. From (4 – 8), it can be observed that the values of the STFT coefficient for m and k are given by the sum from 0 to $L-1$. From Fig 4.13, it can also be observed that the window L is moved through the time-domain signal, while the DFT is taken before the m point is moved again [2].

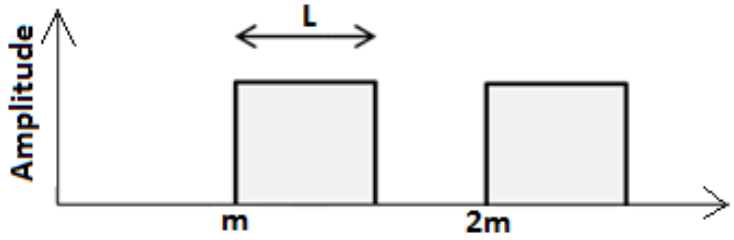

Fig 4.13 Time window analysis of time domain chirp signal [2]

Since the STFT analysis is a complex function, a 3-Dimensional graph is required to display it. A spectrogram is used to represent STFT results. The spectrogram is a technique used for displaying non-stationary signals on a single plot. The magnitude of the Fourier Transform is colour coded, with dark lines for small values and whitish lines for large values. A logarithm is then applied to the magnitude to compress its range of values. This is mathematically expressed in (4 – 9):

$$10log_{10}(|\,X\,[m;\;k]\,|) \qquad (4-9)$$

In (4 – 9), m and k retain their definitions in (4 – 8). Lastly, spectral slices are applied one after the other to obtain an image-like display of the time-varying frequency signal.

4.2.2 Resolution Optimization

The major drawback of STFT is the time-frequency trade-off. In STFT, the sampling frequency, also known as the system clock is expressed as $F_s = \left(\frac{1}{T_s}\right)$ Hz, the highest positive frequency is $\left(\frac{F_s}{2}\right)$ Hz, frequency resolution is $\left(\frac{F_s}{L}\right)$ Hz, width of time slice is $(L \times T_s)$ seconds and time resolution is $(\Delta t\; =\; L)$ seconds. From these expressions, it can be observed that the width of the window (L) of the signal determines whether the spectrogram will have a good time or frequency resolution. A long window results in a narrow band spectrogram, more DFT

points, less precision in time, thus, a better frequency resolution. A short window results in a wide band spectrogram, many time slices, thus, a better time resolution [2].

Fig 4.14 and Fig 4.15 depicts the time and frequency resolution compromise for a lithium NCM and lead acid battery respectively. It was empirically observed that a better frequency resolution suited EIS applications because EIS requires a high frequency resolution for both perturbation and response signal for accurate impedance computation. Moreover, the chirp signal generated from the function generator software tool, constitutes a uniformly increasing time-varying frequency signal over the spectrum. In this regard, for both batteries, the window length for the time-optimized spectrogram is 128 (narrow), whereas, the window length for the frequency-optimized spectrogram is 512 (wide). The selected window was a wide Hanning window, resulting in a good frequency resolution. Lastly, the spectrogram was analyzed to be in tandem with the EIS measurement bandwidth of both batteries.

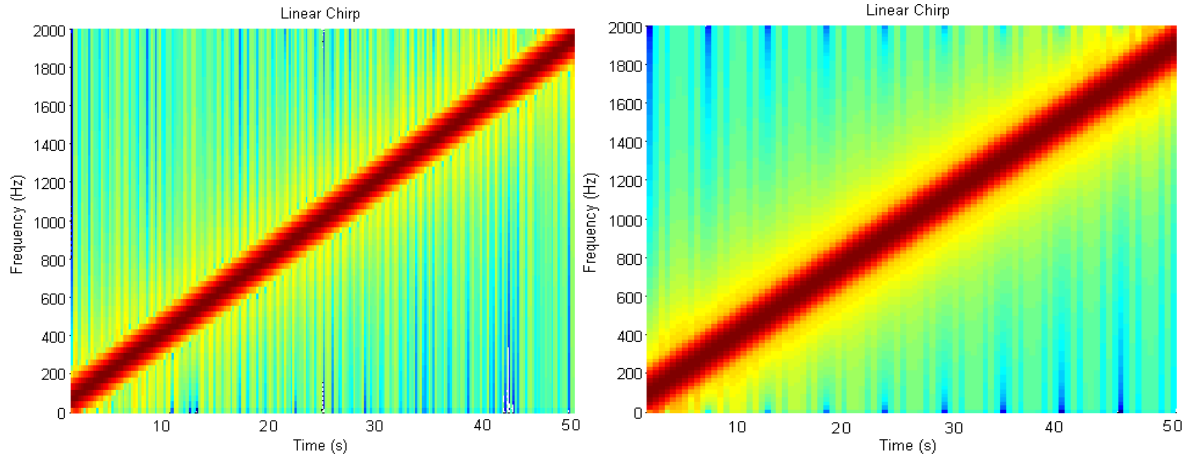

Fig 4.14 Comparison of STFT resolution for lithium NCM battery: wide window (a) - better frequency resolution and narrow window (b) - better time resolution.

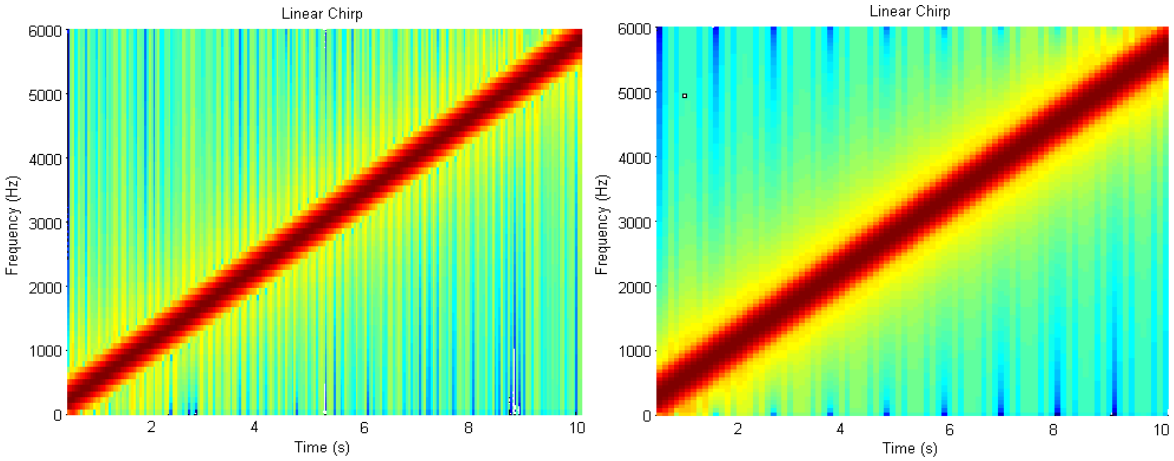

Fig 4.15 Comparison of STFT resolution for lead acid battery: wide window (a) - better frequency resolution and narrow window (b) - better time resolution.

4.2.3 Chirp Implementation

Unlike multisine, chirp signals are easily generated and possess the same perturbation amplitude which results in a low CF (usually about 1.45) [8]. The chirp perturbation is generated in software using the Chirp Pattern Virtual Instrument block of the NI LabVIEW software [4]. The three main parameters used to design the chirp signal in the LabVIEW software are: amplitude of the chirp pattern, the start and stop frequency.

The chirp signal is a large bandwidth and short duration signal. It can be generated in an infinitesimal time – as low as one-tenth the time of the lowest frequency. Fig 4.16 shows the chirp signal generated in one, one-half and one-third the lowest frequency of the impedance spectrum of the lithium NCM and lead acid batteries. It can be observed that, although, the chirp signal can be generated in an infinitesimal time, its duration must be long enough to maximize the signal energy and thus SNR. From the results in Fig 4.16, after the one-half period chirp signal, the quality of the Nyquist plot becomes poor.

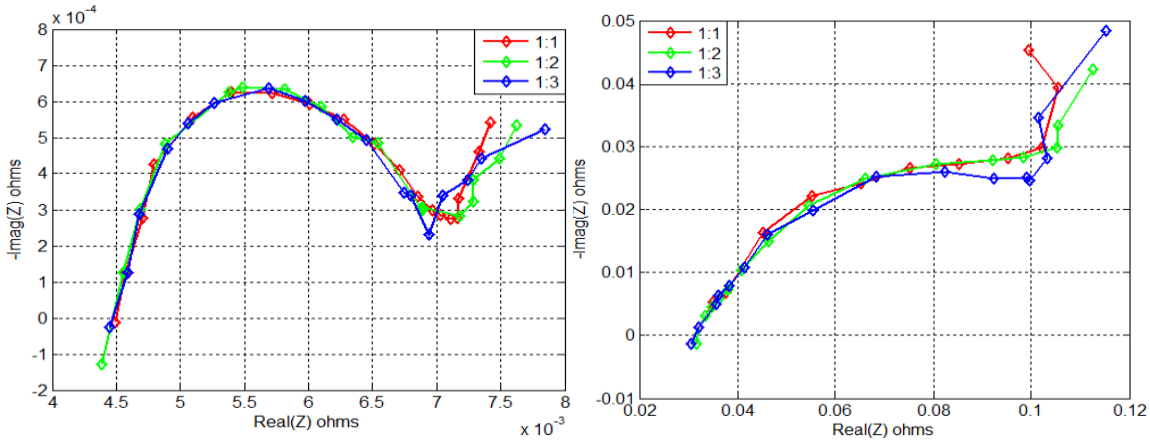

Fig 4.16 Effect of chirp signal period on EIS plot for lithium NCM (a) and lead acid (b)

Consequently, in this study, the chirp signal was designed to be generated in one-half the period of the impedance spectrum of both batteries. This corresponds to 25 seconds for the lithium NCM battery and 5 seconds for the lead acid battery. The real-time impedance plot obtained from this large bandwidth and short-time excitation is presented in Appendix E. Just like the impedance results of the multisine excitation, it is evident that the lead acid battery performs poorly to low SNR chirp excitation signals, compared to the lithium NCM battery.

4.3 PSEUDO-RANDOM BINARY SEQUENCE

The Pseudo-Random Binary Sequence (PRBS) signal, sometimes known as a deterministic random bit generator (DRBG) is a binary periodic signal that possesses white-noise-like properties; which makes it suitable as an excitation signal for system identification [6], [10].

PRBS are generated digitally, are able to characterize linear systems within a range of frequencies and can be generated through linear feedback shift registers (LFSR) or a combination of XOR Logical Operator and Unit Delay as shown in Fig 4.17 [3], [10]. The time-domain PRBS is shown in Fig 4.18.

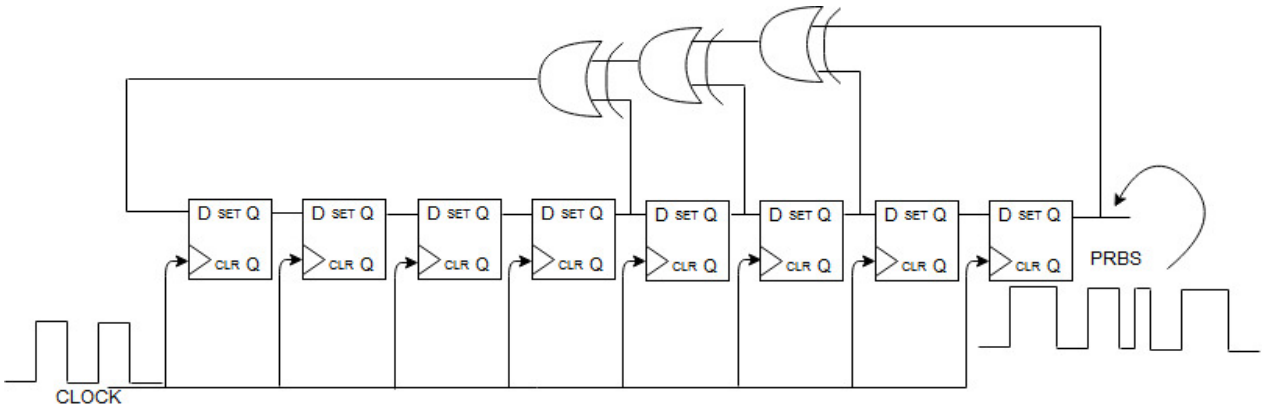

Fig 4.17 8-bit PRBS generator

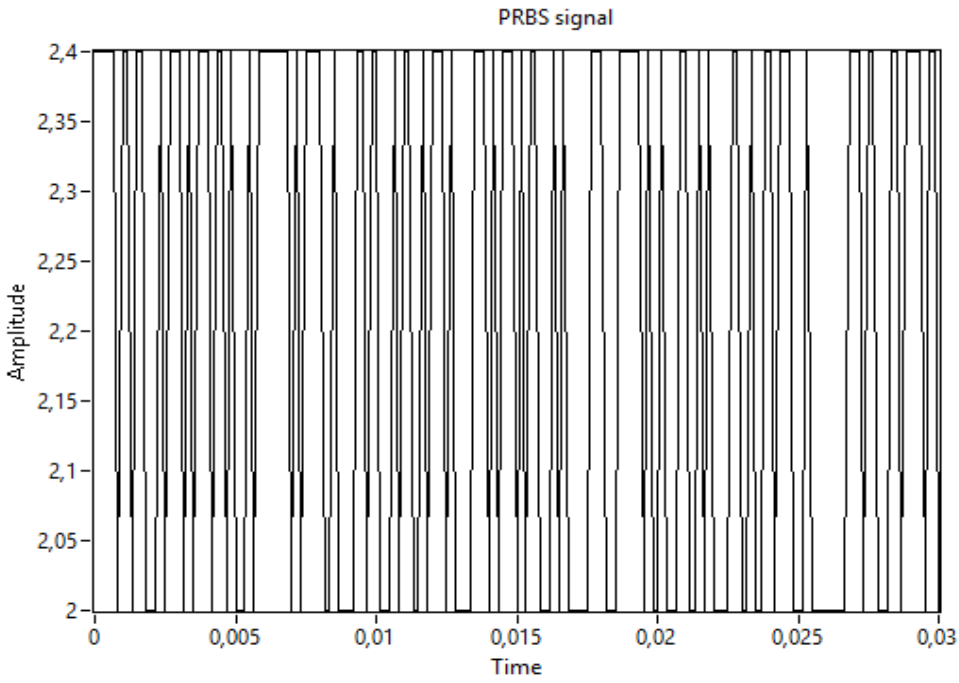

Fig 4.18 Time-domain PRBS signal generated from LabVIEW

The pseudorandom binary sequences' crest factor varies as a function of the spectral bands decrease towards 1, whereas the band increases toward infinity [3].

$$CF\left(\Omega \xrightarrow{u(t)} \infty\right) \longrightarrow 1 \qquad (4-10)$$

In (4 – 10), $u(t)$ is any binary periodic signal. This implies that the PRBS's power is not all concentrated at the impedance frequency band of interest; hence, for a flat spectrum, only a minor portion of the energy is utilized. The Fourier transform of the associating frequency response of the time-domain PRBS in Fig 4.18, can be utilized to determine the usable range

of frequencies. The usable range of frequencies is defined by the half-power bandwidth – $3dB$ as shown in Fig 4.19.

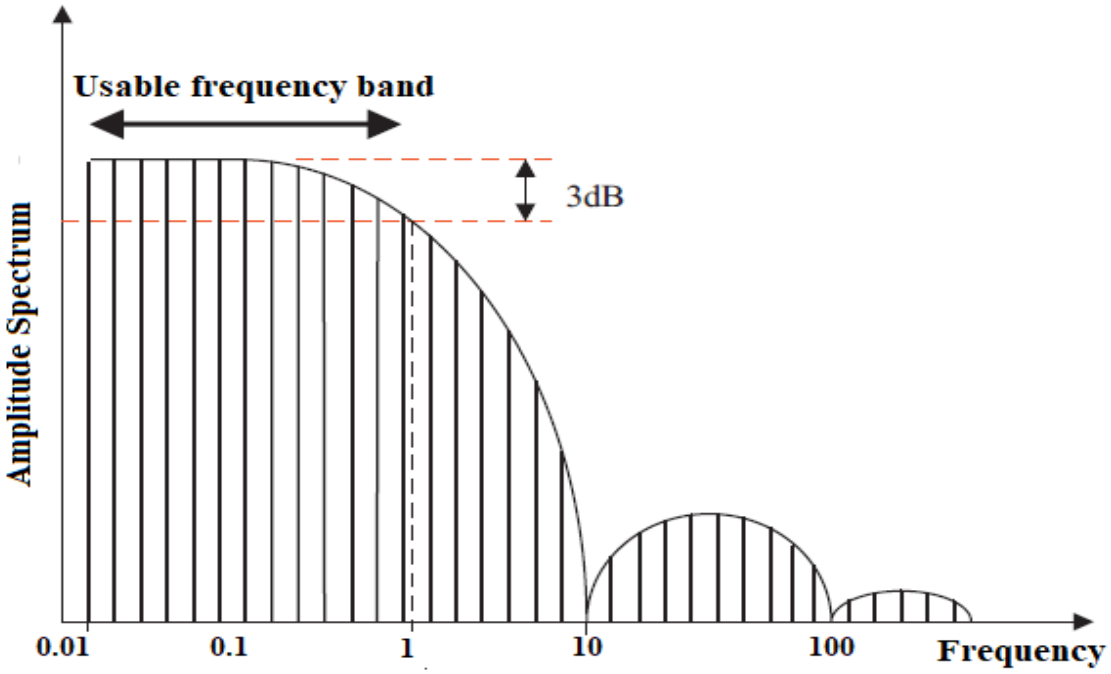

Fig 4.19 Power spectrum of a PRBS highlighting usable frequency band.

The parameters that determine the usable frequency range of a PRBS are the number of states N and the clock pulse frequency f_c. The minimum and maximum frequency are expressed as (4 – 11). A PRBS signal's information is embedded in some certain points of the frequency band, termed "frequency step." The frequency step corresponds to the magnitude of the minimum frequency and is expressed as (4 – 12) and (4 – 13).

$$f_{min} = \frac{f_c}{N} \text{ and } f_{max} = \frac{f_c}{3} \quad (4-11)$$

$$f_{step} = f_{min} \quad (4-12)$$

$$f_{min} : f_{step} : f_{max} \quad (4-13)$$

4.3.1 Selection of PRBS length

An increase in bit-length results in an increase in the number of states, usable bandwidth and test time [10]. Therefore, for the design of a PRBS signal, the following parameters must be considered:

i. *Frequency of interest.*

ii. *Usable bandwidth*

iii. *Test time*

For a PRBS with $n - bit$ (polynomial – order of shift register), the number of possible states N is mathematically expressed as (4 – 14). The order n, alongside the delay time interval T_c defines the length of the maximum period T_{max} of the PRBS as (4 – 15). The power spectrum of a periodic PRBS signal with a delay time interval T_c is expressed as (4 – 16).

$$N = 2^n - 1 \tag{4 – 14}$$

$$T_{max} = (2^n - 1) \times T_c = N \times T_c \tag{4 – 15}$$

$$\Phi^p\left(m\frac{2\pi}{NT_c}\right) = \frac{1}{N}\,\Phi^d\,(m)\left|\frac{\sin\frac{m\pi}{N}}{\frac{m\pi}{N}}\right|^2 \tag{4 – 16}$$

Fig 4.20 shows the compromise in the design of the PRBS signal. As the bit length increases, the bandwidth and test time exponentially increases. It is thus recommended for the chosen bit length to fall at the flattest region of the plot [3].

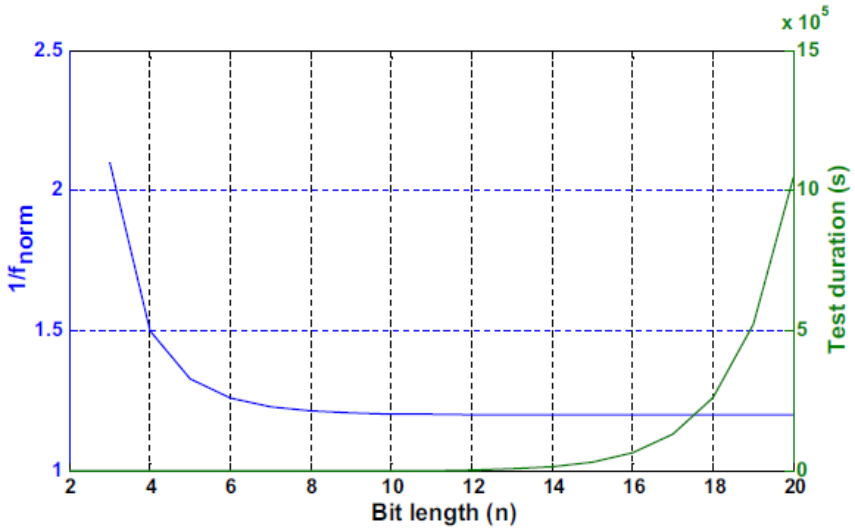

Fig 4.20 An 8-bit PRBS generator (Adapted from [3])

4.3.2 PRBS Design and Optimization

From impedance study on both batteries (see Chapter 3.4), it can be observed that the critical frequency range that covers the key kinetic features of the lead acid and lithium NCM batteries are $(6kHz - 100mHz)$ and $(2kHz - 20mHz)$ respectively. Since both frequency ranges span four decades, the PRBS (excitation signal) for both batteries were designed with two excitations of different clock frequencies, such that the kinetic features are covered. The PRBS was designed to ensure a balance between robustness and speed (see Table 4.1). For both batteries, the design that consituted the lowest time was selected for broadband impedance spectroscopy measurements. Fig 4.21 and 4.22 shows the time-domain PRBS excitation for the lithium NCM and lead acid batteries respectively at Design C (i.e. the selected design instance).

Table 4.1 Design instances for PRBS length selection.

Design Instances	***PRBS Parameters***	***Lithium NCM***	***Lead Acid***
Design A	Frequency Range (Hz)	0.02:0.02:0.42, 1.465:1.465:2000	0.1:0.1:1.03, 1.1:1.1:6000
	Clock Frequency (Hz)	1.26, 6000	3.1, 18000
	PRBS Bits - n	6, 12	5, 14
	Testing Time (sec)	50, 0.68	10, 0.91
	Total Testing Time (sec)	50.68	10.91
Design B	Frequency Range (Hz)	0.02:0.02:0.1, 0.36:0.36:2000	0.1:0.1:2.1, 4.4:4.4:6000
	Clock Frequency (Hz)	0.3, 6000	6.3, 18000
	PRBS Bits - n	4, 14	6, 12
	Testing Time (sec)	50, 2.7	10, 0.23
	Total Testing Time (sec)	52.7	10.23
Design C	Frequency Range (Hz)	0.02:0.02:3.4, 5.865:5.865:2000	0.1:0.1:8.5, 17.6:17.6:6000
	Clock Frequency (Hz)	10.22, 6000	25.5, 18000
	PRBS Bits - n	9, 10	8, 10
	Testing Time (sec)	50, 0.17	10, 0.056
	Total Testing Time (sec)	***50.17***	***10.056***

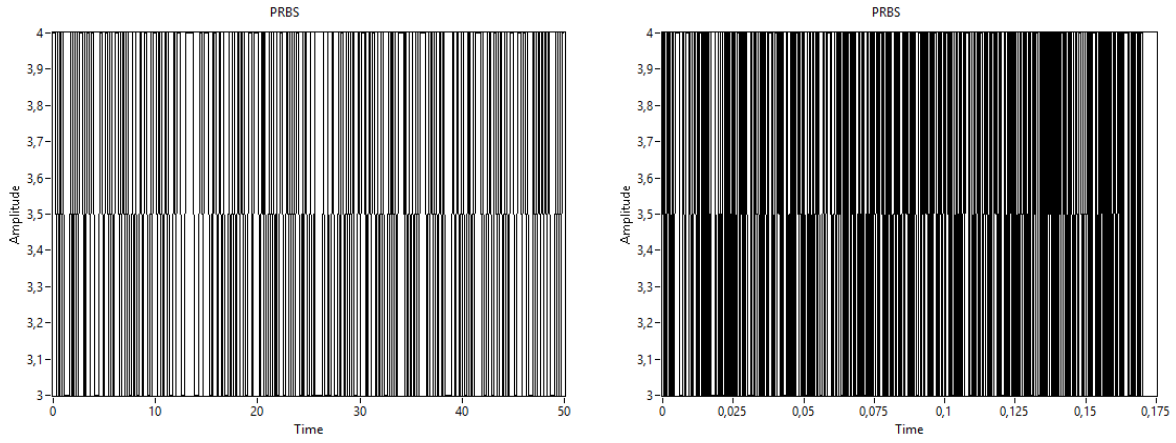

Fig 4.21 Time-domain PRBS signal for lithium NCM at frequency bands – 0.02:0.02:3.4, C.F = 1.77 (a) and 5.865:5.865:2000, C.F = 1.74 (b)

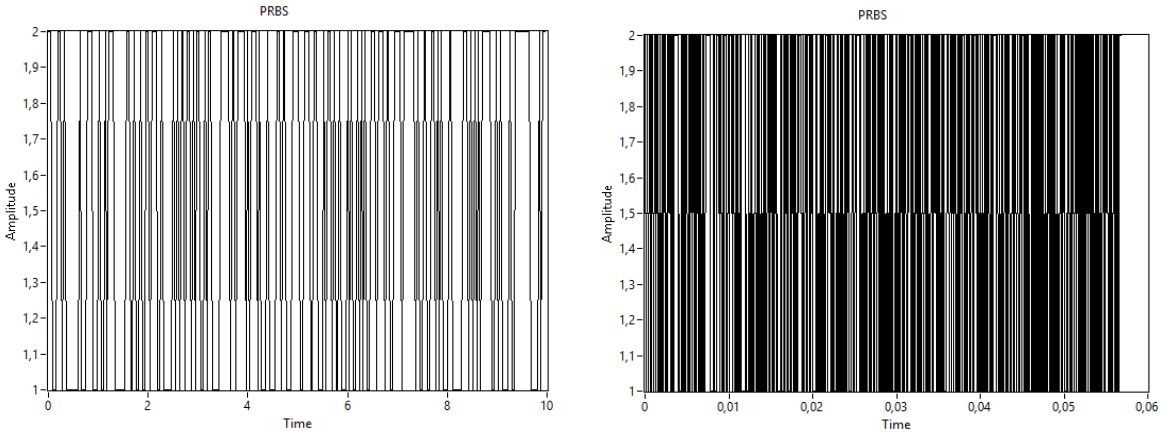

Fig 4.22 Time-domain PRBS signal for lead acid at frequency bands –0.1:0.1:8.5, C.F = 1.63 (a) and 17.6:17.6:6000, C.F = 1.57 (b)

4.3.3 PRBS Implementation

The PRBS signal is periodic because it repeats every N states. The PRBS signal was generated via the Maximum Length Sequence Virtual Instrument tool of the NI LabVIEW software by controlling the current (excitation signal) and observing the associated voltage (response signal). The (3) main parameters used to design the PRBS signal in the LabVIEW software are: samples, polynomial order and seed [4]. The *samples* specify the sample number contained in the PRBS sequence. From the PRBS design instances, for a case where n is 10, the possible states or sample number N is 1023. The *polynomial order* specifies the modulo-2 primitive polynomial order utilized to generate the PRBS sequence. The PRBS sequence is not random because it is determined by an initial value, called *seed*. The seed determines how the internal seed state will be generated. The PRBS starts from an arbitrary initial state via a *seed* state. It also always results in the same sequence if initialized with that state.

For the generation of the PRBS in the LabVIEW software – the *samples* for the lithium NCM battery were 511 and 1023, while *clock (sampling) frequency* was 10.22Hz and 6kHz respectively. On the other hand, for the lead acid battery, the *samples* were 255 and 1023, while *clock (sampling) frequency* was 25.5Hz and 18kHz respectively. In the multisine and chirp signal's generation/acquisition, the NI-DAQ ADC's (signal acquisition) and DAC's (signal generator) *samples* and *sampling frequency* were always equal. In Fig 4.23, albeit the period to complete EIS measurement remains unchanged for both optimized and unoptimized signal; it is apparent that there is an improvement in the quality (when benchmarked against the FRA) of the Nyquist plot when the PRBS is optimized (i.e. ensuring that the ADC's *samples* and

sampling frequency are multiplied by an integer-factor compared to the DAC's *samples* and *sampling frequency*).

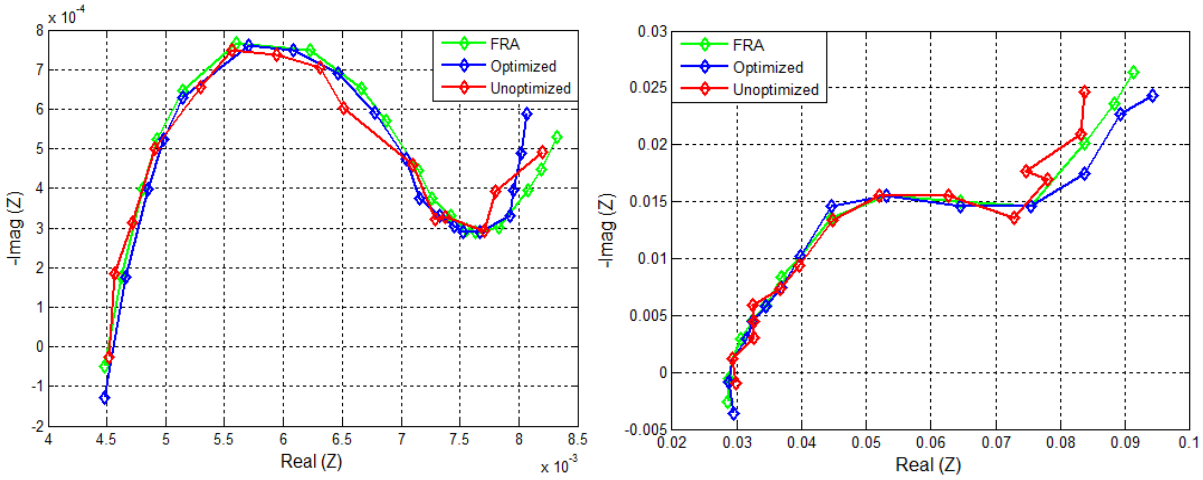

Fig 4.23 Effect of PRBS signal sampling selection on EIS plot for lithium NCM (a) and lead acid (b)

In this study, the ADC's *samples* and *clock frequency* were multiplied to the capability of the National Instruments – Digital Acquisition's (NI-DAQ's) maximum sampling capability – 2MS/s. For the lithium NCM battery, the multiplying factor at low frequency was 180,000 (i.e. *samples* = 91,980,000 and *sampling frequency* = 1,839,600). At high frequency the multiplying factor was 300 (i.e. *samples* = 306,900 and *sampling frequency* = 1,800,000). On the other hand, for the lead acid battery, the multiplying factor at low frequencies was 72,000 (i.e. *samples* = 18,360,000 and *sampling frequency* = 1,836,000). At high frequency the multiplying factor was 100 (i.e. *samples* = 102,300 and *sampling frequency* = 1,800,000).

In this study, it took the PRBS 50.17 ≈ 50 seconds to complete EIS measurement for the lithium NCM battery and 10.056 ≈ 10 seconds for the lead acid battery. From the real-time EIS results (see Appendix E), it is apparent that at the optimal (selected) *samples* and *clock frequency*, the lead acid battery performs poorly compared to the lithium NCM parameters, just like the case of multisine and chirp signals. This can also be correlated to the distinction in their chemical stability [9].

4.4 SUMMARY

This Chapter studies the time and frequency properties of broadband impedance spectroscopy signals for rapid condition monitoring of lithium NCM and lead acid batteries. The broadband impedance spectroscopy signals are also optimized for both batteries as per their time-constant. Their implementation on the LabVIEW software is also discussed. Lastly,

the results are displayed and discussed for both optimized and unoptimized signals of both batteries. An interesting deduction from this Chapter is the differences in the sensitivity of both battery chemistries to broadband (rapid) signals. While the lithium NCM batteries have a high chemical stability and can absorb high pulses of rapid signals; the lead acid battery has a low chemical stability and evolves into the diffusion mode faster in response to rapid signals [9].

4.5 REFERENCE

[1] B Sanchez, G Vandersteen, R Bragos and J Schoukens, "Basics of broadband impedance spectroscopy measurements using periodic excitations," Institute of Physics and Engineering in Medicine, Meas. Sci. Technol. 23 (2012) 105501 (14pp)

[2] Steven W. Smith," The Scientist and Engineer's Guide to Digital Signal Processing," DSP Guide, 2nd Ed., 1999.

[3] A.J. Fairweather et al., "Battery parameter identification with Pseudo Random Binary Sequence excitation (PRBS), Journal of Power Sources 196 (2011) 9398– 9406

[4] National Instrument, "LabVIEW online software support for broadband signals."

[5] Benjamin Sanchez et al. "Influence of the Multisine Excitation Amplitude Design for Biomedical Applications using Impedance Spectroscopy" 33rd Annual International Conference of the IEEE EMBS Boston, USA, August 30 - September 3, 2011

[6] Andrej Debenjak, "Fast measurement of PEM fuel cell impedance based on PRBS perturbation signals and continuous wavelet transform," Journal of Power Sources 254 (2014) 112–118.

[7] Olufemi Olayiwola, Paul Barendse, "Characterization of Silicon Based Photovoltaic Cells Using Broadband Impedance Spectroscopy," ECCE – IEEE, September 2016.

[8] Brian Bullecks, Resmi Suresh & Raghunathan Rengasway, "Rapid Impedance measurement using chirp signals for electrochemical system analysis," Journal of Computers & Chemical Engineering 106(2017) 421-436.

[9] Elena M. Krieger, John Cannarella, Craig B. Arnold, "A comparison of lead-acid and lithium-based battery behaviour and capacity fade in off-grid renewable charging applications," Energy 60 (2013) 492-500.

[10] Zeyang Geng and Charalampos Savvidis, "On-board impedance diagnostics method of Li-ion traction batteries using PRBS," MSc. Thesis, Chalmers University of Technology, Goteborg, Sweden 2015.

5. ONLINE CONDITION MONITORING SYSTEM IMPLEMENTATION

Online condition monitoring of a battery implies that fault diagnosis can be undertaken whilst the battery is operating in real-time – without disconnecting the battery from the system. Besides, in real-life applications, a converter is used to interface the source with the load. The main advantage of utilizing the converter to carry out Electrochemical Impedance Spectroscopy (EIS) measurement on the battery; is the elimination of any disturbances in the system that would have occurred by interrupting the system in operation or applying an external AC signal from a signal generator. In literature, online condition monitoring through EIS was implemented via linear amplifier injection or through the power converter that interfaces the load and the battery. This Chapter briefly discusses existing online condition monitoring systems. More so, it discusses the design and implementation of the online condition monitoring system applied for this research.

5.1 EXISTING ONLINE CONDITION MONITORING SYSTEMS

EIS measurements can be carried out when the system is in operation. In [1], EIS was performed on lithium ion, nickel–metal-hydride and lead acid batteries through the control of a DC–DC boost/buck converter and duty-cycle perturbation. The proposed technique in [1] can be performed periodically or continuously without the interruption in operation of the system. It involves the application of a duty-cycle sinusoidal perturbation, resulting in sinusoidal variations of the battery current and voltage around the steady-state DC point. In [2], a custom designed switch mode amplifier that produces perturbation current for EIS measurement was incorporated into a battery charger system for online condition monitoring. [2] also analysed the influence of the DC-link voltage and the switching frequency on the Total Harmonic Distortion (THD). In [3], a boost/buck topology was applied to perform EIS alongside control of the DC bus over a pre-selected range. When EIS measurements are undertaken, the DC bus control is suspended. Once the value of the DC bus deviates from the pre-selected range, voltage control is instantly reinstated. In this study, the DC operating point where EIS measurement is taken, is attained by firstly disabling the automatic DC bus control. Fig 5.1 describes the phases in which online condition monitoring was implemented in [3].

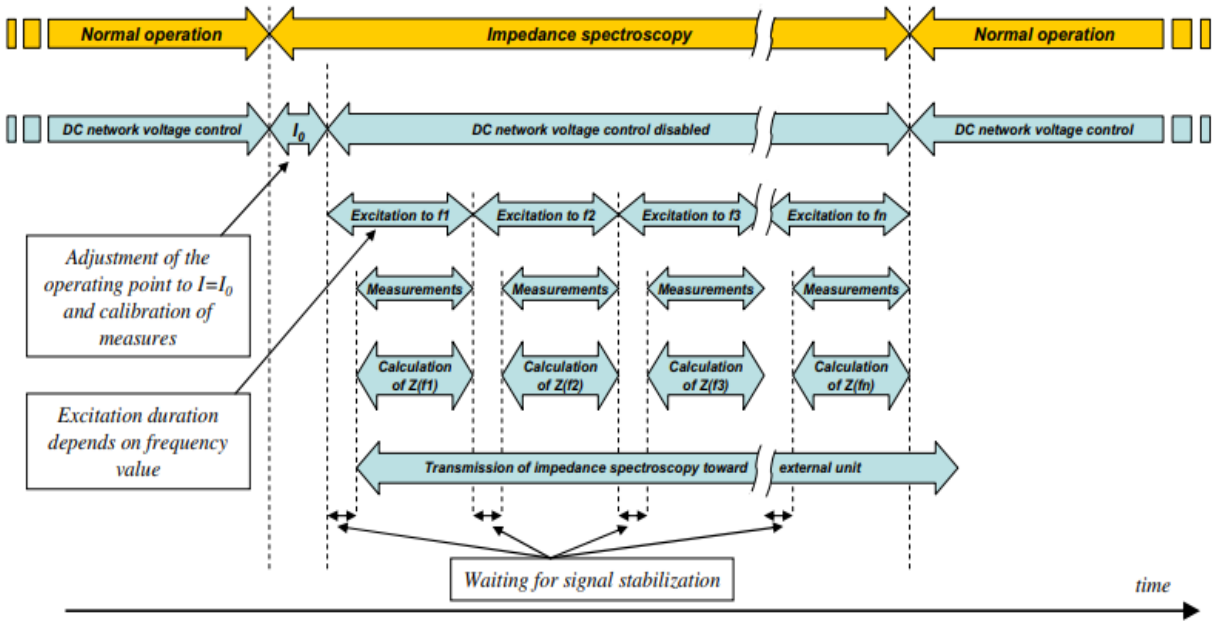

Fig 5.1 Principle of applying EIS through a power converter [3].

In [4], a switched-inductor ladder topology was designed and implemented on a PCB to perform EIS for state-of-health investigation on two series connected Panasonic 18650 cells. The converter had a high efficiency alongside an embedded control system that provided both real-time diagnostic and active balancing capability through EIS. In addition, the control mechanism for EIS measurement was the Proportional-Integral (PI). The PI controller was used to enforce sinusoidal reference signals from a direct digital synthesizer, to ensure that the power converter can inject perturbation signals on the cell and extract impedance information.

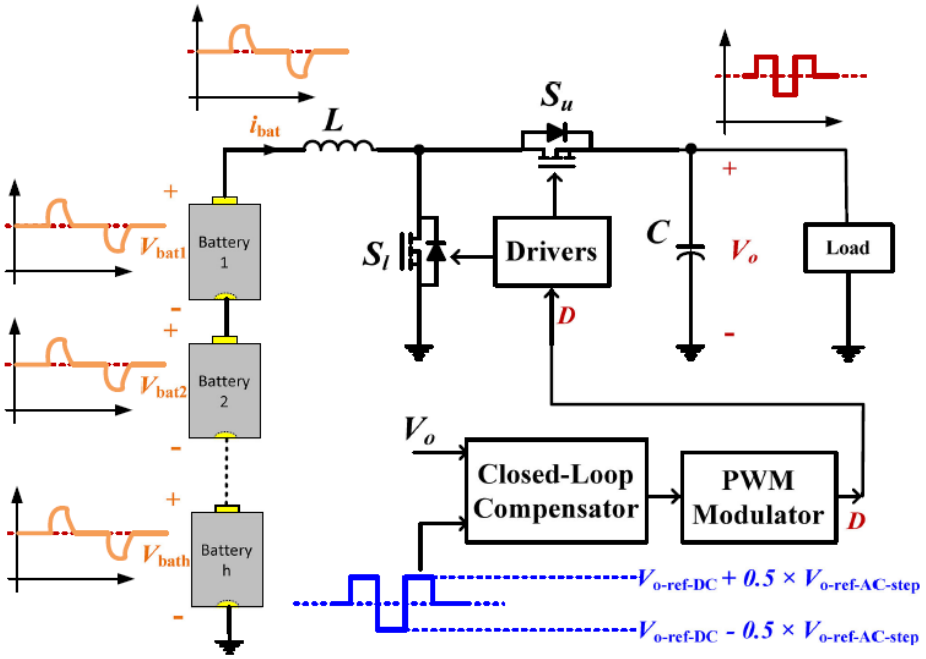

Fig 5.2 Schematic of online EIS achieved through single perturbation cycle

In [5], real-time impedance spectroscopy measurement was achieved through single perturbation cycle with closed loop control of the power converter (see Fig 5.2). This technique obtains the EIS for a range of frequencies by utilizing only the information embedded in a single perturbation cycle. The power converter closed-loop control, controls the system to generate an output voltage step function at a given frequency, while the response is monitored. An EIS plot is obtained from the impedance results of the fundamental frequency harmonics – frequencies above or equal to the perturbation frequency.

[6] and [7] utilized a converter for online condition monitoring of a Proton Exchange Membrane Fuel Cell (PEMFC). In [6], a DC-DC converter, a fuel cell voltage-monitor and an embedded diagnostic algorithm was utilized for online condition monitoring of a PEMFC system. The perturbation signal was a Pseudo-Random Binary Sequence (PRBS) signal, which enabled rapid and advanced condition monitoring. In [7], two (2) parallel boost DC/DC converters are utilized for online impedance measurement of the PEMFC stack. The converter was utilized to generate current waveform perturbations (EIS signal) and control the DC bus voltage. The voltage monitor provided a platform for an embedded condition monitoring system. The control strategy was a PI. The condition monitoring set-up is shown in Fig 5.3 [7].

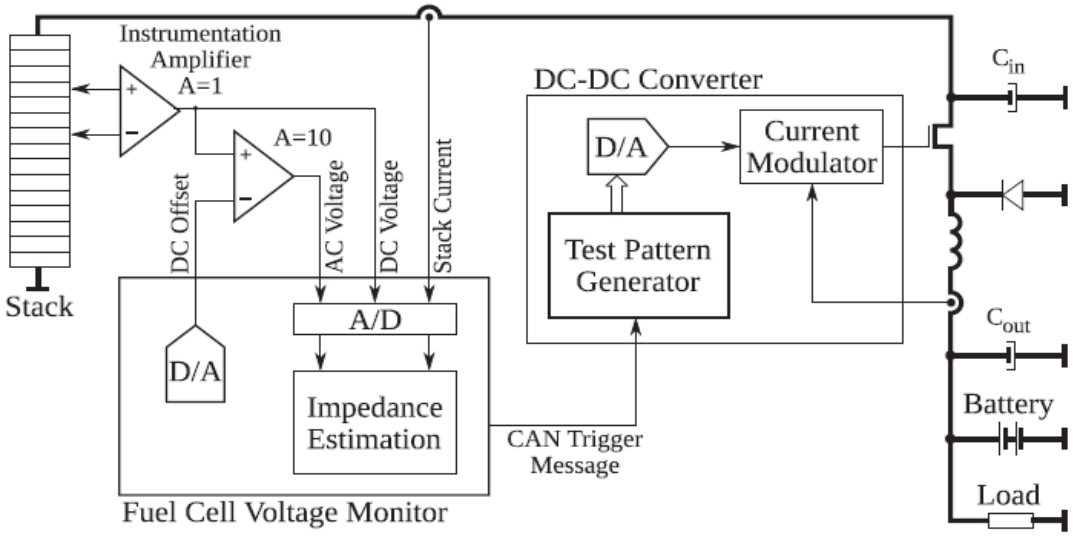

Fig 5.3 Schematic of connection between the DC–DC converter and FCVM for online condition monitoring

In [8], an intelligent charger with impedance spectroscopy measurement capability was proposed. This was achieved by controlling the charger to generate a frequency swept perturbation at the terminals of the battery. This was employed for investigation of the

degradation of a lead acid battery. The perturbation and response signals were measured through a digital lock-in amplifier embedded in the signal processor to compute its impedance.

Despite the online capabilities of [1] – [8], the single sine EIS and broadband signals that were utilized are limited by the lowest frequency of the perturbation signal. Therefore, this study aims to further reduce measurement time of impedance spectroscopy measurements for online condition monitoring purposes on batteries, as will be shown in Chapter 7 – results and discussions.

5.2 ONLINE CONDITION MONITORING TOPOLOGY

DC-DC converters – a member of the family of power converters have been extensively utilized in DC motor drive applications and switch-mode AC power supplies. Typically, the input to the converters are unregulated DC voltages, resulting from recitification of the continously line-voltage changing magnitude [9] or from batteries/fuel cells. The output of the converter is a controlled DC output at a voltage level desired by the user.

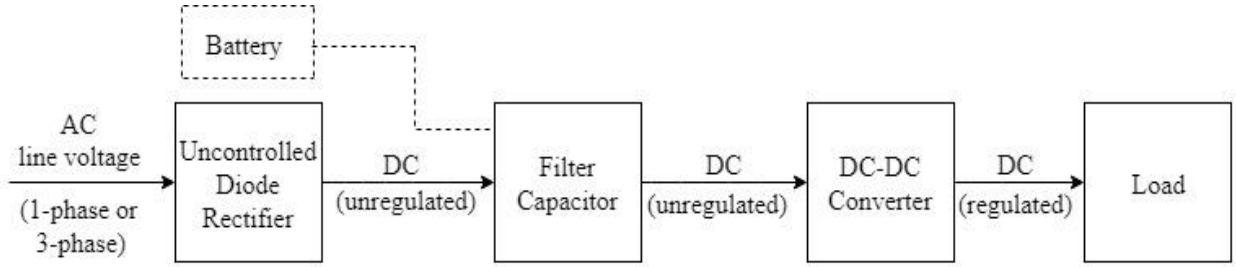

Fig 5.4 A typical DC-DC converter system

Some of the DC-DC converters commonly used includes: buck, boost and buck-boost. Moreover, the selection of a power converter for online condition monitoring is dependent on the application. Buck converters are suitable for batteries, compared to the boost converters, because they are simple to design and are efficient for several voltage ranges of the battery [9], [12]. However, in some cases, when the battery drops below a certain voltage; the converter stops functioning, resulting in a waste of the unused capacity. Thus, a buck-boost converter is used in this study. The buck-boost converter has the ability to step-down or step-up the input voltage depending on the duty cycle set by the user.

As earlier asserted, this study aims to characterize (monitor) a battery whilst operating online. As also earlier discussed, an online condition monitoring system implies that the power converter that typically interfaces the battery and load is used for condition monitoring

purposes. Therefore in this study, a robust online condition monitoring system as shown in Fig 5.5 is proposed to undertake EIS measurement on both the lithium NCM and lead acid batteries. To achieve this, a power converter capable of interfacing the battery and electronic load is firstly designed (see POWER CONVERTER in Fig 5.5). The power converter invariably requires a control mechanism to carry out condition monitoring, while maintaining its primary function of varying the output voltage as per the associated duty cycle. Since a converter is inherently dynamic – because of the non-linear time-varying nature of the PWM and switching processes, a model that is time invariant and quasi-linear is needed to be derived. In this regard, a good model representation of the converter is determined in this study by state space averaging and small-signal analysis.

The state space averaging technique is firstly utilized to eliminate the time variance in the power stage; however, this induces certain nonlinearities to the power stage average model. Therefore, linearization of the operating point of the power stage is realized using a small-signal model. This ultimately results in a linear time-invariant small-signal model, which is converted into the frequency-domain, to provide the power stage dynamic's transfer function. Following modelling of the converter, the open-loop control system is realized. The open-loop system depicts the transfer function of the inductor current and duty cycle; and the capacitor voltage and the duty cycle. Nonetheless, the open-loop system has no information of the system output, which is critical in battery application due to its varying voltage.

A robust closed loop control system is consequently applied to control the DC bus voltage (as typically required in a converter) and perform EIS measurement through duty cycle perturbation. Moreover, the parameters (gain) of the control is tuned in such a way that it satisfies the control criterion for both the lithium NCM and lead acid batteries. This control switches sequentially, commencing from the DC bus voltage control and then the EIS measurement (current control) (see CONTROL SYSTEM in Fig 5.5).

Following the derivation of the time-domain AC current and voltage, the signal is passed through a low pass-filter, so that the switching frequency components of the PWM is eliminated from the signal. The signal is then converted to the frequency domain using Fourier Transform. The frequency domain impedance information is subsequently determined (see SIGNAL PROCESSING in Fig 5.5) using the Ohm's law relationship as earlier discussed in Chapter 3. The equivalent electric circuit parameters are extracted from the impedance information using

the Complex Non-linear Least Squares (CNLS) as already discussed in Chapter 3.5.3. The equivalent electric circuit parameters are then used to characterize the batteries whilst online.

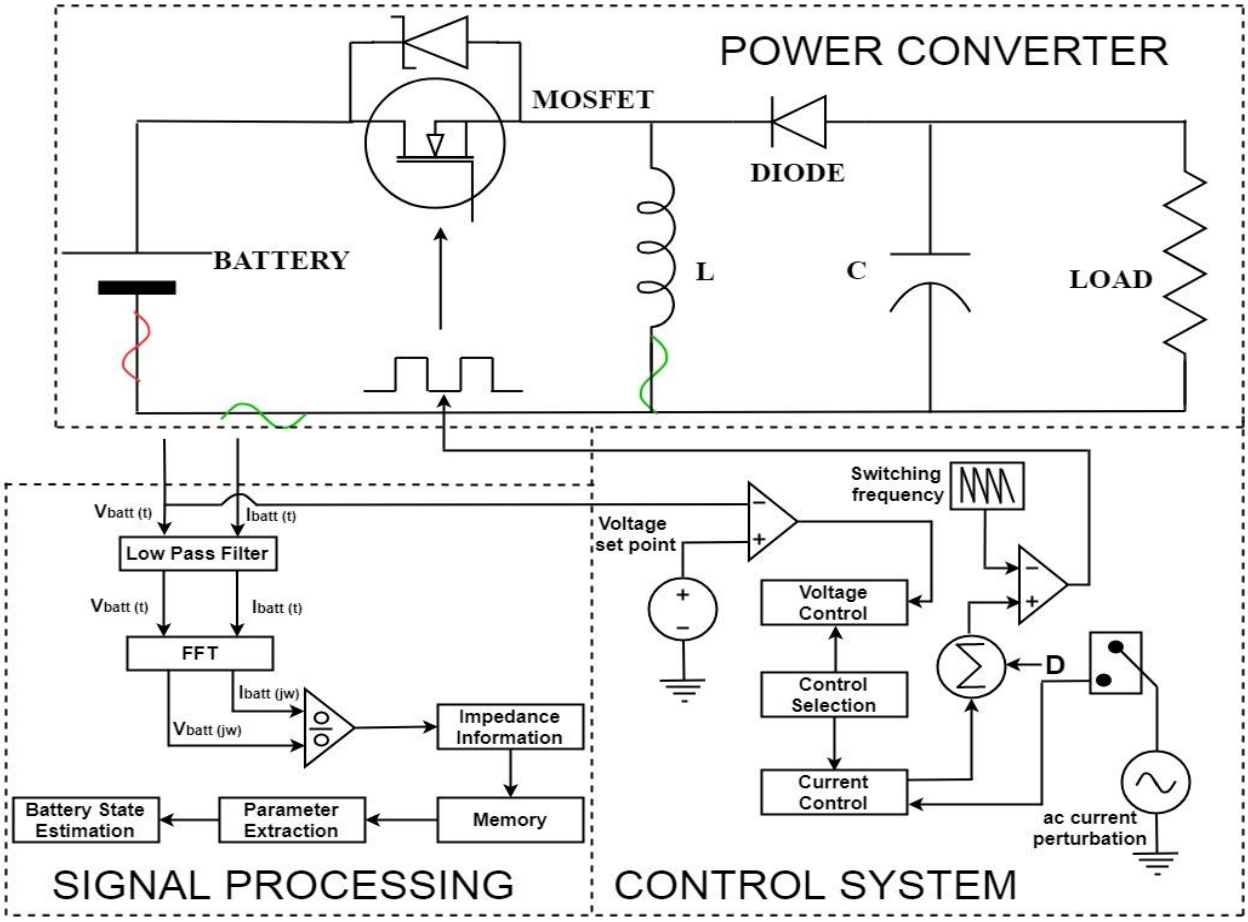

Fig 5.5 Schematic of online condition monitoring system

The proceeding sections describe in detail, the components and methodology of the proposed online condition monitoring system applied to both the lithium NCM and lead acid batteries.

5.3 POWER CONVERTER DESIGN AND OPERATION

In this study, the buck-boost converter is used to perform impedance spectroscopy measurement alongside the regulation of the output voltage. The chosen converter topology was also applied in [3], [7] to perform EIS measurements. The buck-boost converter utilizes switches (MOSFET) to transform the battery input from one level to the other. The output voltage average value is controlled by ON and OFF switch durations (t_{on} and t_{off}) over a constant frequency or constant period $T = (t_{on} + t_{off})$. This switching method is called Pulse-Width Modulation. The buck-boost converter results from a cascaded connection of a buck and boost converter and is utilized in applications where the step-down and step-up

converter capabilities are required. Moreover, it requires only a single switch, with an inverted output to perform this operation. The conversion ratio of the output to the input voltage in steady state is the product of the conversion ratio of both cascaded converters. If both switches in the two different converters have the same duty cyle, then (5 – 1) applies:

$$\frac{v_o(t)}{V_{batt}(t)} = D\,\frac{1}{1-D} \qquad (5-1)$$

In (5 – 1) , the Duty Cycle D is the ratio of the ON time to the period. Depending on D, the output voltage can either be lower or higher than the input voltage. The schematic of the buck-boost converter used for online condition monitoring in this study is shown in Fig 5.6.

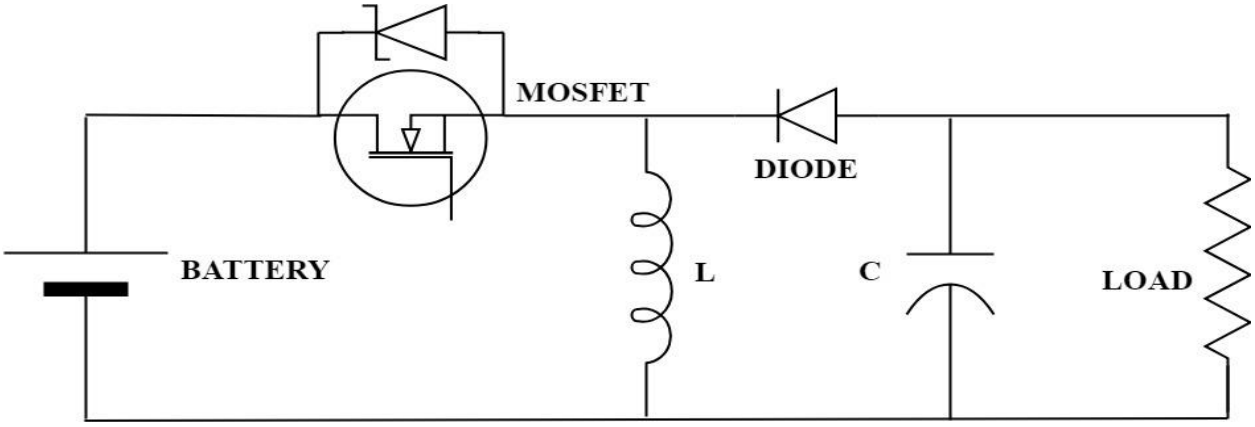

Fig 5.6 Buck-boost converter

In Fig 5.6, a large capacitor is used for filtering the ouput signal resulting in a constant output voltage – $v_o(t) \approx V_o$. Fig 5.6 is analyzed at both the ON and OFF state using Kirchhoff's Voltage and Current Law (KVL and KCL). The power converter is assumed to be in steady state, the switches are assumed to be ideal and the inductive and capacitive elements losses are ignored. The state variables of the circuit (inductor voltage, v_L and capacitor current, i_c) are expressed mathematically as (5 – 2) and (5 – 3).

$$v_L(t) = L\,\frac{dI_L(t)}{dt} \qquad (5-2)$$

$$i_c(t) = C\,\frac{dV_c(t)}{dt} \qquad (5-3)$$

When the switch is closed (ON state), as in Fig 5.7, the source provides energy to the inductor and the diode is reverse biased.

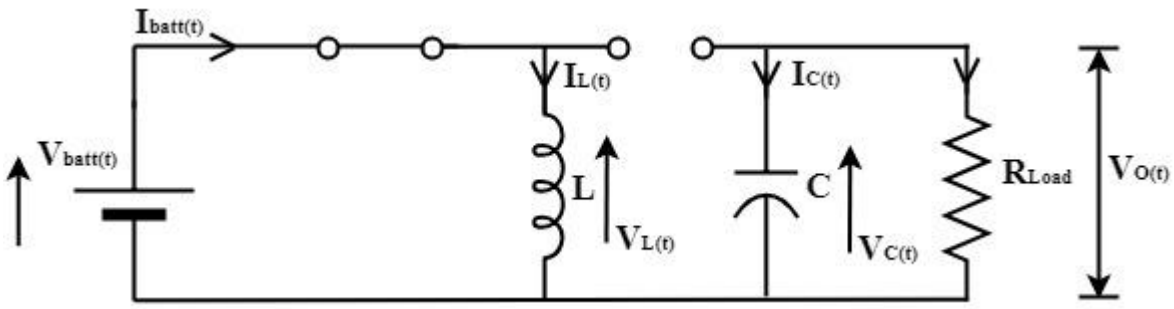

Fig 5.7 When buck-boost converter switch is closed (ON state):

$$V_{batt}(t) = v_L(t) \quad (5-4)$$

$$0 = i_c(t) + \frac{v_c(t)}{R_{load}} \quad (5-5)$$

$$v_o = V_{batt}(t) = L\frac{di_L(t)}{dt} \quad (5-6)$$

$$\frac{di_L(t)}{dt} = \frac{V_{batt}(t)}{L} \quad (5-7)$$

$$\frac{\Delta i_L(t)}{\Delta t} = \frac{\Delta i_L(t)}{\mathrm{DT}} = \frac{V_{batt}(t)}{L} \quad (5-8)$$

$$(\Delta i_{L-closed}(t)) = \frac{V_{batt}(t)DT}{L} \quad (5-9)$$

When the switched is opened (OFF state), as Fig 5.8, the diode is forward biased and the energy stored in the inductor is supplied to the output, since there is no supply from the source.

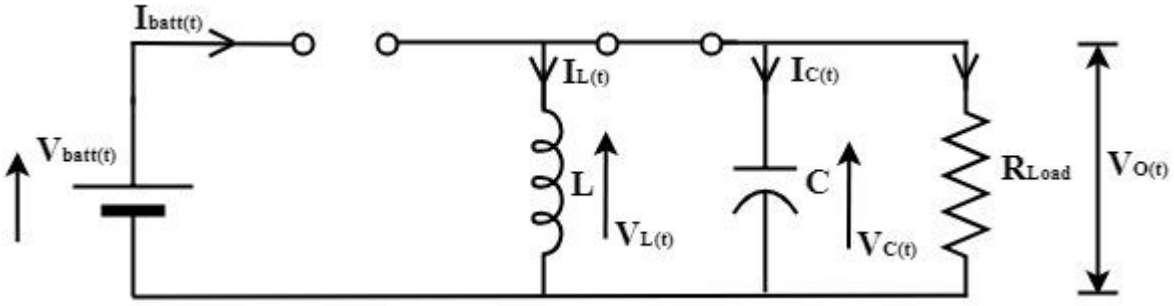

Fig 5.8 When buck-boost converter switch is opened (OFF state):

$$v_c(t) = -v_L(t) \quad (5-10)$$

$$i_L(t) = i_c(t) + \frac{V_c(t)}{R_{load}} \quad (5-11)$$

$$v_L(t) = v_o(t) = L\frac{di_L(t)}{dt} \quad (5-12)$$

$$\frac{di_L(t)}{dt} = \frac{v_o(t)}{L} \quad (5-13)$$

$$\frac{\Delta i_L(t)}{\Delta t} = \frac{\Delta i_L(t)}{(1-\mathrm{D})\mathrm{T}} = \frac{v_o(t)}{L} \quad (5-14)$$

$$(\Delta i_{L-opened}(t)) = \frac{v_o(t)(1-D)T}{L} \quad (5-15)$$

For steady state operation:

$$(\Delta i_{L-closed}) + (\Delta i_{L-opened}) = 0 \quad (5-16)$$

$$\frac{V_{batt}(t)DT}{L} + \frac{v_o(t)(1-D)T}{L} = 0 \quad (5-17)$$

$$v_o(t) = -V_{batt}(t)\left(\frac{D}{1-D}\right) \quad (5-18)$$

When *D* is greater than 50%, the output will be higher than the input; when *D* is less than 50% the output will be lower than the input. The state variables waveform – inductor current and capacitor voltage for the inverted buck-boost converter are shown in Fig 5.9.

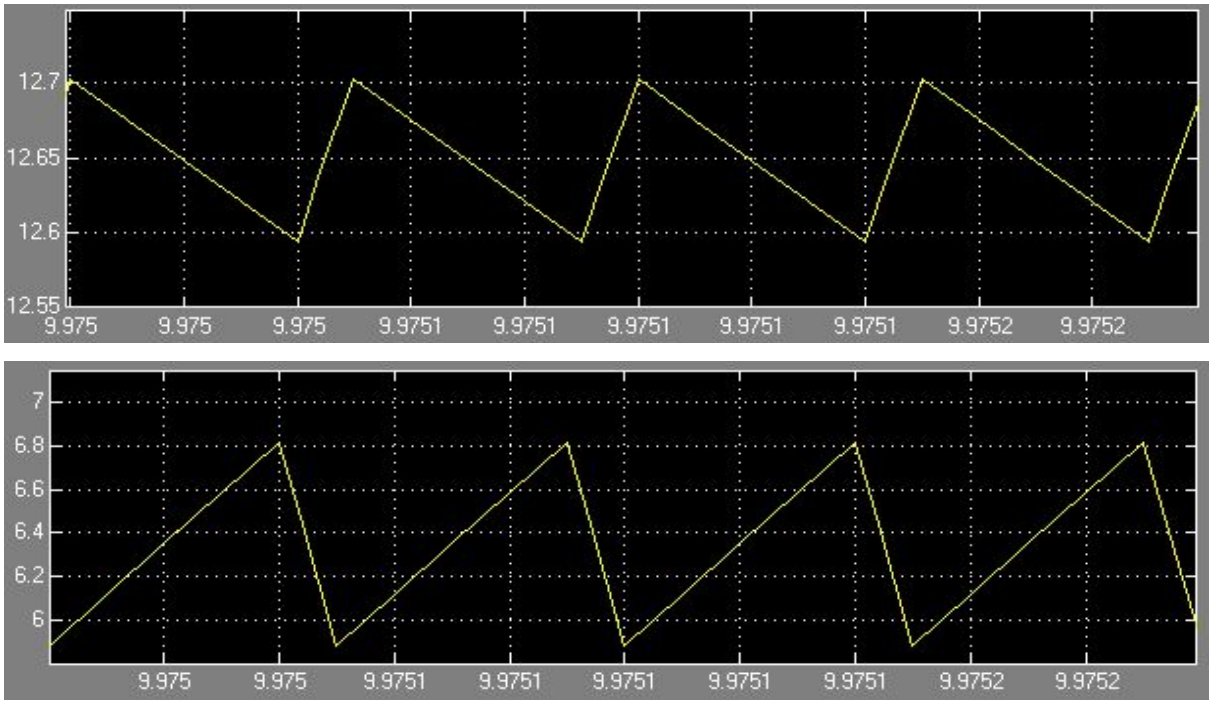

Fig 5.9 Buck-boost converter state-variable waveforms – capacitor voltage (up) and inductor current (down)

5.4 POWER STAGE MODELLING

For high performance control of the buck-boost converter, a good model representation of the converter is required. Moreover, the converter's behaviour is dynamic due to the non-linear time-varying nature of the PWM and switching process. In this study, a model that is time invariant and quasi-linear is derived. Fig 5.10 shows the process undertaken for modelling the buck-boost converter in this study.

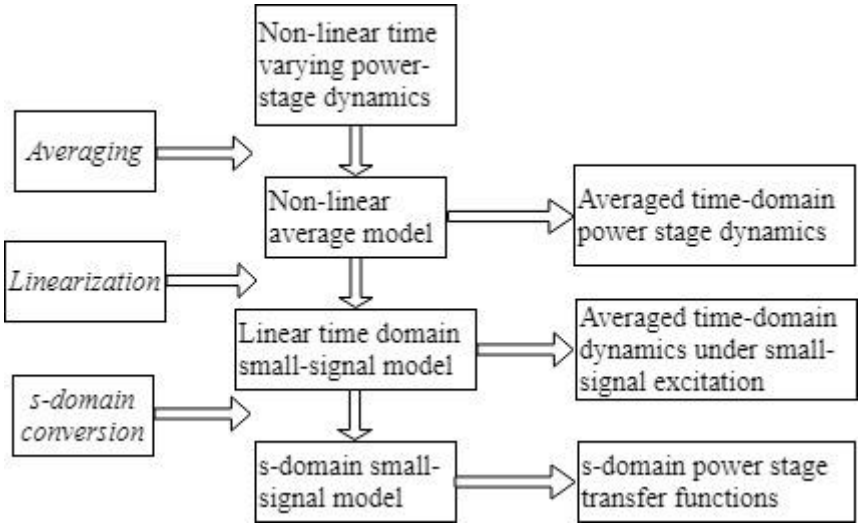

Fig 5.10 Stages in the buck-boost converter modelling

Firstly, the state space averaging technique utilizes the state space representation of the converter to determine the averaged equation of the small-signals of the converter's PWM. The state space representation removes time variance by providing an averaged model with respect to the ON and OFF duration of the switching cycle. The averaged model is now time-invariant, but still non-linear. Consequently, a small-signal model is obtained by linearization of the operating point, resulting in a linear time-invariant small-signal model. Lastly, the small-signal time-domain model is converted into its s-domain or frequency-domain, providing the power stage dynamics transfer function [10] – [11].

5.4.1 State Variable Modelling

The state variable method is a robust tool that is utilized in analyzing and understanding complex systems. In this method, a collection of variables that describe the system's internal behavior is specified. These variables are termed "state variables" and they can predict the system's future behavior with information from the current state and input of the system. In other words, if these variables are known, all other parameters of the system can be determined [11]. In the converter design, the state variable equation is important in designing the linear controller [14]. The state variable model is fundamentally expressed in (5 – 19) and (5 – 20). A, B, C and D are the system's matrix, x represents the state variable, $\dot{x}$ represents the derivative of the state variable, u represents the input and y the output.

$$\dot{x}(t) = Ax(t) + Bu(t) \qquad (5-19)$$

$$y(t) = Cx(t) + Du(t) \qquad (5-20)$$

The state variable expression can be derived from the inductor voltage and capacitor current of the ON and OFF state equations of the converter as [14]. Firstly, the state variables are

mapped as – $i_c(t) = x_1, \dot{x}_1, y_1$; that is, input, derivative of the input and output respectively. The state variables are then mapped as – $v_L(t) = x_2, \dot{x}_2, y_2$; that is, input, derivative of the input and output respectively. When the switch is closed (ON state), the state variable equations are expressed as:

$$\dot{x}_1(t) = \frac{1}{L} V_{batt}(t) \tag{5 – 21}$$

$$\dot{x}_2(t) = -\frac{x_2(\mathrm{t})}{R_{load}C} \tag{5 – 22}$$

$$\begin{bmatrix}\dot{x}_1(t)\\ \dot{x}_2(t)\end{bmatrix} = \begin{bmatrix}0 & 0\\ 0 & -\frac{1}{R_{load}C}\end{bmatrix}\begin{bmatrix}x_1(t)\\ x_2(t)\end{bmatrix} + \begin{bmatrix}\frac{1}{L}\\ 0\end{bmatrix} V_{batt}(t) \tag{5 – 23}$$

On the other hand, when the switch is closed (OFF state), the state variable equations are expressed as:

$$\dot{x}_1(t) = -\frac{x_2(\mathrm{t})}{L} \tag{5 – 24}$$

$$\dot{x}_2(t) = \frac{x_1(t)}{C} - \frac{x_2(t)}{R_{load}C} \tag{5 – 25}$$

$$\begin{bmatrix}\dot{x}_1(t)\\ \dot{x}_2(t)\end{bmatrix} = \begin{bmatrix}0 & \frac{1}{L}\\ -\frac{1}{C} & -\frac{1}{R_{load}C}\end{bmatrix}\begin{bmatrix}x_1(t)\\ x_2(t)\end{bmatrix} + \begin{bmatrix}0\\ 0\end{bmatrix} V_{batt}(t) \tag{5 – 26}$$

The buck-boost converter state space average (A and B) matrix for both the ON and OFF states can be expressed with respect to the switching cycle d as:

$$A_{average} = A_{on}d + A_{off}(1-d) \tag{5 – 27}$$

$$A_{average} = \begin{bmatrix}0 & 0\\ 0 & -\frac{1}{R_{load}C}\end{bmatrix} d + \begin{bmatrix}0 & \frac{1}{L}\\ -\frac{1}{C} & -\frac{1}{R_{load}C}\end{bmatrix}(1-d) = \begin{bmatrix}0 & \frac{1-d}{L}\\ -\frac{1-d}{C} & -\frac{1}{R_{load}C}\end{bmatrix} \tag{5 – 28}$$

$$B_{average} = B_{on}d + B_{off}(1-d) \tag{5 – 29}$$

$$B_{average} = \begin{bmatrix}\frac{1}{L}\\ 0\end{bmatrix} d + \begin{bmatrix}0\\ 0\end{bmatrix}(1-d) = \begin{bmatrix}\frac{d}{L}\\ 0\end{bmatrix} \tag{5 – 30}$$

The average matrices in (5 – 27) – (5 – 30) are substituted into the complete buck-boost converter model as (5 – 31):

$$\begin{bmatrix}\dot{x}_1(t)\\ \dot{x}_2(t)\end{bmatrix} = \begin{bmatrix}0 & \frac{(1-d)}{L}\\ -\frac{(1-d)}{C} & -\frac{1}{R_{load}C}\end{bmatrix}\begin{bmatrix}x_1(t)\\ x_2(t)\end{bmatrix} + \begin{bmatrix}\frac{d}{L}\\ 0\end{bmatrix} V_{batt}(t) = \begin{bmatrix}\frac{di_L(t)}{dt}\\ \frac{dV_c(t)}{dt}\end{bmatrix} = \begin{bmatrix}0 & \frac{(1-d)}{L}\\ -\frac{(1-d)}{C} & -\frac{1}{R_{load}C}\end{bmatrix}\begin{bmatrix}i_L(t)\\ v_c(t)\end{bmatrix}$$

$$+ \begin{bmatrix}\frac{d}{L}\\ 0\end{bmatrix} V_{batt}(t) \qquad (5-31)$$

Finally, the output state matrix is shown in (5 – 32)

$$\begin{bmatrix}y_1(t)\\ y_2(t)\end{bmatrix} = \begin{bmatrix}1 & 0\\ 0 & 1\end{bmatrix}\begin{bmatrix}x_1(t)\\ x_2(t)\end{bmatrix} + \begin{bmatrix}0\\ 0\end{bmatrix} V_{batt}(t) = \begin{bmatrix}y_1(t)\\ y_2(t)\end{bmatrix} = \begin{bmatrix}1 & 0\\ 0 & 1\end{bmatrix}\begin{bmatrix}i_L(t)\\ v_c(t)\end{bmatrix} + \begin{bmatrix}0\\ 0\end{bmatrix} V_{batt}(t) \quad (5-32)$$

The model achieved from the state space representation in (5 – 32) albeit time-invariant, is still non-linear.

5.4.2 Transfer Function Derivative

In the state space representation, the switching ripples in the capacitor voltage and inductor current were eliminated by averaging over one switching period [9] – [10], [15]. The averaging enabled the elimination of the power stage dynamic's time variance, however, this brought certain nonlinearities to the power stage average model. Hence, a transfer function of the converter is derived using small signal approximation as [9] – [11]. This analysis has also been implemented for converter modelling in [2], [15]. When applying small signal analysis, it is assumed that the input of the signal is small in magnitude (operating about a small linear point) – quasi-linear. This claim is valid, just as in other dynamic engineering systems where only the crucial behaviours are modelled; whilst other insignificant phenomena are neglected. In small signal analysis, it is assumed that input voltage $u(t)$ and duty cycle $d(t)$ equals some quiescent values $U(t)$ and $D(t)$ with some superimposed small AC variations $\tilde{u}(t)$ and $\tilde{d}(t)$.

$$u(t) = U(t) + \tilde{u}(t) \qquad (5-33)$$

$$x(t) = X(t) + \tilde{x}(t) \qquad (5-34)$$

$$d(t) = D(t) + \tilde{d}(t) \qquad (5-35)$$

In (5 – 33) – (5 – 35), the capitalized variables are the DC components and the variables with a superscript are the AC components. By inserting the DC and AC signals, (5 – 36) is obtained.

$$X(t) + \dot{x}(t) = ((A_{on}(D(t) + \tilde{d}(t)) + A_{off}(1 - D(t) - \tilde{d}(t)))(X(t) + \tilde{x}(t)) +$$
$$(B_{on}(D(t) + \tilde{d}(t)) + B_{off}(1 - D(t) - \tilde{d}(t))(U(t) + \tilde{u}(t)) \qquad (5-36)$$

Linearization of (5 – 36) is accomplished by assuming that the system is in steady state and that the second order terms are very small in magnitude. More so, only the DC component of the input vector $U(t)$ is considered, as it is assumed that the AC perturbation component is negligible. The equation is now simplified as (5 – 37):

$$\dot{x}(t) = A\tilde{x}(t) + [(A_{on} - A_{off})X(t) + (B_{on} - B_{off})]U(t)]\,\tilde{d}(t) \qquad (5-37)$$

(5 – 37) is converted to the s-domain using Laplace Transform:

$$\tilde{x}(s) = [sI - A]^{-1}[(A_{on} - A_{off})X + (B_{on} - B_{off})]U]\,\tilde{d}(s);\ \text{where } sI = \begin{bmatrix} s & 0 \\ 0 & s \end{bmatrix}$$

$$\begin{bmatrix} i_L(t) \\ v_c(t) \end{bmatrix} = \frac{1}{s^2 + \frac{s}{R_{load}C} + \frac{(1-D)^2}{LC}} \times \begin{bmatrix} s + \frac{1}{R_{load}C} & \frac{(1-D)}{L} \\ -\frac{(1-D)}{C} & s \end{bmatrix} \left(\begin{bmatrix} -\frac{1}{L}V_c \\ \frac{1}{C}I_L \end{bmatrix} + \begin{bmatrix} \frac{1}{L}V_{batt} \\ 0 \end{bmatrix} \right) d(s) \qquad (5-38)$$

$$\begin{bmatrix} i_L(t) \\ v_c(t) \end{bmatrix} = \frac{1}{s^2 + \frac{s}{R_{load}C} + \frac{(1-D)^2}{LC}} \times \begin{bmatrix} s + \frac{1}{R_{load}C} & \frac{(1-D)}{L} \\ -\frac{(1-D)}{C} & s \end{bmatrix} \begin{bmatrix} \frac{1}{L}(V_{batt} - V_c) \\ \frac{1}{C}I_L \end{bmatrix} d(s) \qquad (5-39)$$

The small signal transfer function for the inductor current I_L and capacitor voltage V_c are expressed as (5 – 40) and (5 – 41):

$$G_{Vc} = \frac{\widetilde{v_c}(s)}{\tilde{d}(s)} = \frac{-\left[\frac{(V_{batt} - V_c)(1-D)}{LC}\right] + \frac{sI_L}{C}}{s^2 + \frac{s}{R_{load}C} + \frac{(1-D)^2}{LC}} \qquad (5-40)$$

$$G_{IL} = \frac{\widetilde{i_L}(s)}{\tilde{d}(s)} = \frac{\frac{s(V_{batt} - V_c)}{L} + \frac{(V_{batt} - V_c)}{R_{load}CL} + \frac{(1-D)I_L}{LC}}{s^2 + \frac{s}{R_{load}C} + \frac{(1-D)^2}{LC}} \qquad (5-41)$$

In (5 – 40) and (5 – 41), the relationship between output voltage – perturbation current and duty cycle is observed. G_{Vc} shows the transfer function of the output voltage and the duty cycle. G_{IL} shows the transfer function of the perturbation current for impedance spectroscopy measurement and the duty cycle.

5.5 ELECTRONIC COMPONENT SELECTION

i. Inductor selection

Inductor selection determines the ripple current in the power converter. The larger the inductor size, the lower the current ripple [7]. A $144\ \mu H$ inductor was selected in this study based on the analysis in (5 – 42) – (5 – 48). More so, it is important that the chosen inductance

significantly exceeds the calculated (required) minimum value to maximize efficiency of the power converter and to avoid unexpected issues (resulting in a transition from continous conduction mode to a discontinous conduction mode) that may arise due to the wide battery volage input range [9].

If there is no power loss in the converter during operation, then the power at the source equals the power at the load ($P_o = P_s$).

$$\frac{v_o^2(t)}{R_{load}} = V_{batt(t)} i_s(t) \quad (5-42)$$

$$i_s(t) = i_L(t)D \quad (5-43)$$

$$\frac{v_o^2(t)}{R_{load}} = V_{batt}(t) i_L(t)D \quad (5-44)$$

$$I_L = \frac{v_o^2(t)}{V_{batt\,(t)} R_{load} D} = \frac{P_o(t)}{V_{batt\,(t)} D} = \frac{V_{batt\,(t)} D}{R_{load}(1-D)^2} \quad (5-45)$$

Maximum and minimum inductor current are as follows:

$$I_{max} = I_L + \frac{\Delta I_L}{2} = \frac{V_{batt\,(t)} D}{R_{load}(1-D)^2} + \frac{V_{batt\,(t)} DT}{2L} \quad (5-46)$$

$$I_{min} = I_L - \frac{\Delta I_L}{2} = \frac{V_{batt\,(t)} D}{R_{load}(1-D)^2} - \frac{V_{batt\,(t)} DT}{2L} \quad (5-47)$$

The minimum inductance for continous operation is:

$$L_{min} = \frac{R_{load}(1-D)^2}{2f} \quad (5-48)$$

Since $R = 10\,\Omega$ and switching frequency $f = 20\,kHz$.

$$L_{min} = \frac{10(1-0.05)^2}{2\times(20000)} = 22.5\ \mu H$$

For continuous operation, it is important to select an inductor value that is 25% larger than L_{min}. Hence, the inductance must exceed:

$$(22.5\ \mu H) + (\frac{25}{100} \text{ x } 22.5\ \mu H) = 28.2\ \mu H$$

ii. Capacitor Selection

A large capacitor is connected across the output voltage to reduce the output voltage ripple. A $470\ \mu F$ capacitor was selected in this study. The justification for this selection is expressed in (5 – 49) to (5 – 41). Since the minimum capacitance is:

$$|\Delta Q| = (\frac{v_o(t)}{R})DT = C\Delta V_o \quad (5-49)$$

$$\Delta v_o = \frac{v_o(t)DT}{R_{load}} = \frac{v_o(t)D}{R_{load}Cf} \quad (5-50)$$

$$r = \frac{\Delta v_o(t)}{v_o(t)} = \frac{D}{R_{load}Cf} \quad (5-51)$$

and $\left(\frac{\Delta v_o(t)}{v_o(t)}\right)$ = 0.005, then:

$$C_{min} = \frac{D}{\left(\frac{\Delta v_o(t)}{v_o(t)}\right)R_{load}f} = \frac{1}{0.05\times10\times20000} = 100\ \mu F$$

iii. Semiconductor Selection

A power semiconductor device is used as an electronic switch. There are three types of power semiconductor devices based on their controllability, namely: diodes, thyristors and controllable switches e.g. Bipolar Junction Transistor (BJT), Metal-Oxide-Semiconductor Field Effect Transistors (MOSFET), Gate-Turn-Off Thyristors (GTO) and Insulated Gate Bipolar Transistors (IGBT). For buck-boost converter design, the semiconductor must be able to withstand maximum current when ON and maximum voltage stress when OFF. The controllable switch selected for this study was a MOSFET. The MOSFET was selected because of its short switching time (high frequency) for low voltage operations; making it suitable for battery applications. The MOSFET was also used to represent a diode. This configuration is realized by ignoring the gate terminal and connecting the drain and source. For selection of the switching frequency, the following is considered: a high switching frequency reduces the inductor and capacitor size required, whilst a low switching frequency increases the heat sink requirements and the power loss in the switch. In this study, a 20kHz switching frequency was selected to avoid inteference from audio noise.

iv. Zener Diode and Gate Resistor Selection

A Zener diode is connected across the MOSFET gate and source terminal for protection purposes. The Zener diode decreases the MOSFETs high input impedance. Therefore, a gate resistor is connected to increase this value. A gate resistor is connected in series with the MOSFET gate to decrease ringing or oscillation which results from the parasitic inductance and capacitance of the MOSFET. The gate resistor also helps to limit the current spike when the MOSFET is turned ON. The selection of a gate resistor for a MOSFET is important because it reduces the gate drive current, thus, increasing the switching losses. Therefore, to attain a

balance between efficiency and ringing dampening, gate resistors in the order of 10R to 22R is preferred. In this study, a 10R resistor was selected as the gate resistor.

5.6 IMPEDANCE SPECTROSCOPY ON POWER CONVERTER

The switching frequency is the repetitive (sawtooth) waveform frequency and is kept constant. It is usually selected in the range of few kilohertz to hundred kilohertz. The duty cycle of the power converter is the control signal that determines the (ON or OFF) state of the switch. The duty cycle *D* is generated by comparing the sawtooth waveform against a set point voltage. The setpoint voltage is the summation of the impedance spectroscopy signal and the DC duty cycle. The switch turns ON when the set point signal, which varies slowly in time with respect to the switching frequency, is greater in amplitude than the switching signal. Vice-versa occurs when the switch is turned off [9], [12]. A comparator as Fig 5.11 is used to achieve this PWM signal. The switch duty ratio can be expressed as the ratio of $v_{setpoint}$ and the saw tooth waveform peak as (5 – 52):

$$D = \frac{t_{on}}{T} = \frac{v_{setpoint}}{V_{peak-st}} \qquad (5-52)$$

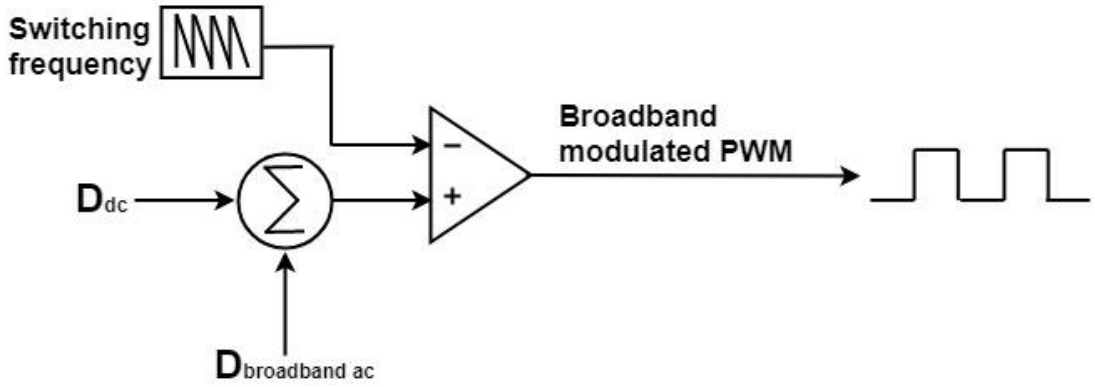

Fig 5.11 Methodology for PWM generation

5.6.1 Pulse Width Modulation (PWM) generation

PWM signals can be generated digitally; from either a function generator (like LabVIEW software) or via analogue electronics. In this study, the PWM signal was generated through analog electronics because the EIS sine signal is used to produce a duty cycle that switches the MOSFET. EIS sine signal of a certain frequency is compared to a sawtooth waveform with frequency that equals the switching frequency of the PWM. The PWM generator design was adapted from [18], where the XR-8038A precision waveform generator was selected to generate the sawtooth. The XR-8038A generates a sawtooth waveform, with a peak to peak

voltage waveform, one-third the DC voltage supply. LM311 was used to compare the sawtooth waveform to a voltage reference – EIS sine signal. Fig 5.12 shows the configuration of the PWM waveform generator.

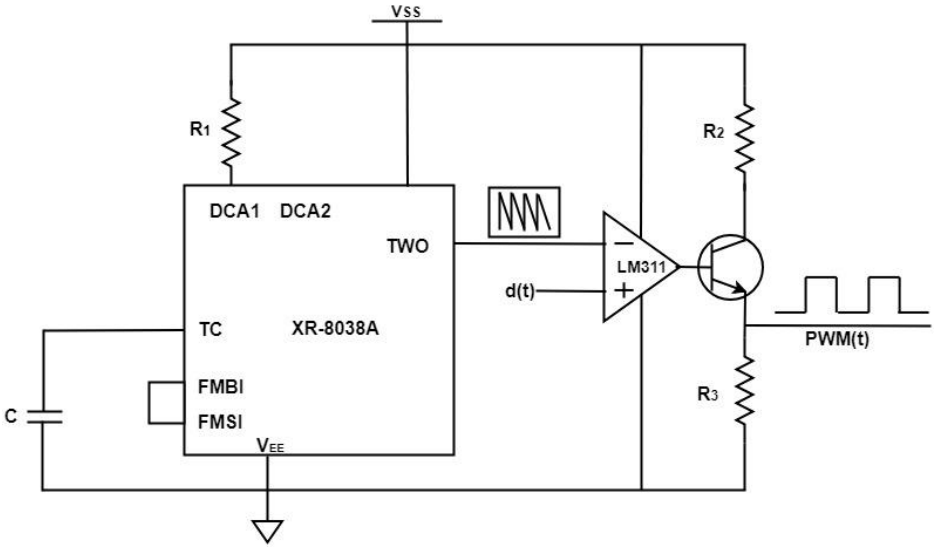

Fig 5.12 PWM generator configuration

Just as [18], the PWM waveform timing is set by the values of ($R_1$and C) – timing constant as:

$$f_{SW} = 20kHz = \frac{0.15}{R_1 C}\ ;\ R_1 C = 7.5 \times 10^{-6}$$

750 $Ohms$ is selected for R_1 and $10nF$ is selected for C. The sawtooth waveform has a peak value of 6.5 V (at 100% duty cycle) and a trough value of 3.5 V (at 0% duty cycle).

5.6.2 Analog Signal Filter and LEM Current Transducer Design

(a) Analog Signal Filter

The analog low-pass filter eliminates the 20kHz high switching frequency components of the PWM, inherent in both the perturbation (current) and response (voltage) signals; while satisfying the EIS bandwidth of both the lead acid and lithium NCM battery. A 4th order Butterworth low-pass analog filter was designed to increase the measurement accuracy of the impedance spectroscopy measurement. To ascertain the appropriate capacitor and resistor value to be utilized in the Butterworth filter, a cut-off frequency is firstly selected. The cut-off frequency is selected to be far greater than the EIS frequency range of both batteries. From [16], the quality factor Q of a Butterworth filter is 0.7071. For a unity gain Butterworth filter, $f_c = \frac{1}{2\pi RC\sqrt{mn}} = 8kHz;\ m = 1\ and\ n = 2.$

$$R_1 = mR_2 \text{ and } C_2 = nC_1$$

$$R_2 C_1 = \frac{1}{8000 \times 2\pi\sqrt{2}}$$

Since R is selected as $1.1k\Omega$, $C = \frac{1}{1100 \times 8000 \times 2\pi\sqrt{2}} = 10.3nF \approx 10nF$

The National Instrument Multisim software was used to simulate the Butterworth filter with a resistor value of $1.1k\Omega$, capacitor value of $10nF$ and cut-off frequency of $10.23kHz$. The electric circuit connection is shown in Fig 5.13.

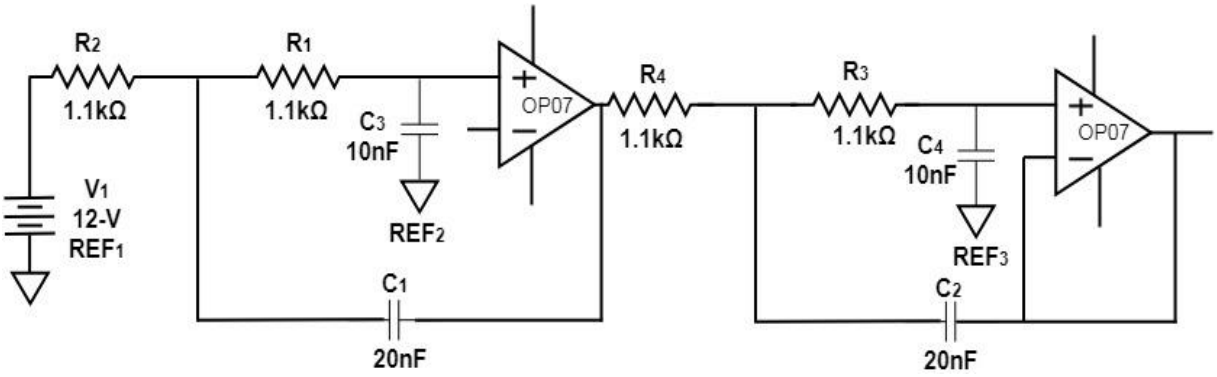

Fig 5.13 Multisim connection of 4th order Butterworth filter.

The frequency response analysis was carried out on the filter over a frequency range that covers both batteries and the switching converter. The magnitude response in decibels and phase response in degrees are shown in Fig 5.14.

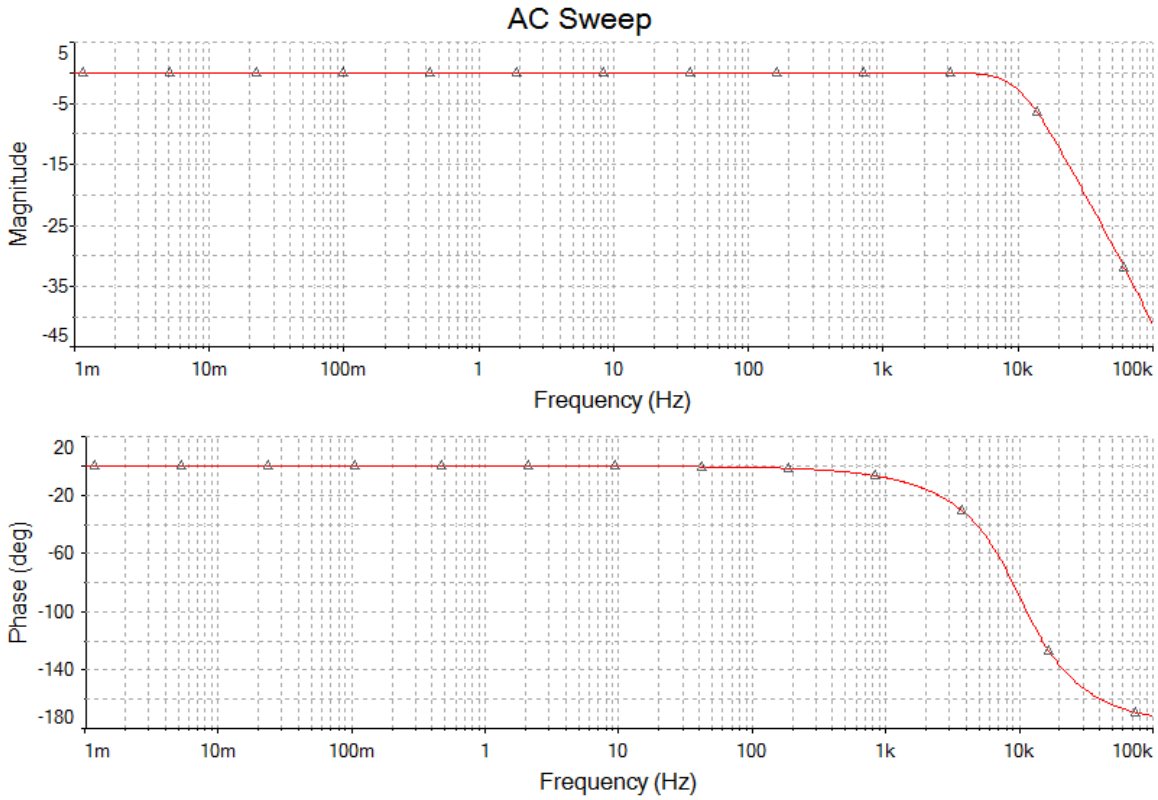

Fig 5.14 Frequency response of 4th order low-pass Butterworth analog filter

Fig 5.15 shows the battery current before and after the 4th order low-pass Butterworth analog filter was applied. It can be observed that the filter was effective in filtering the high frequency components of the signal.

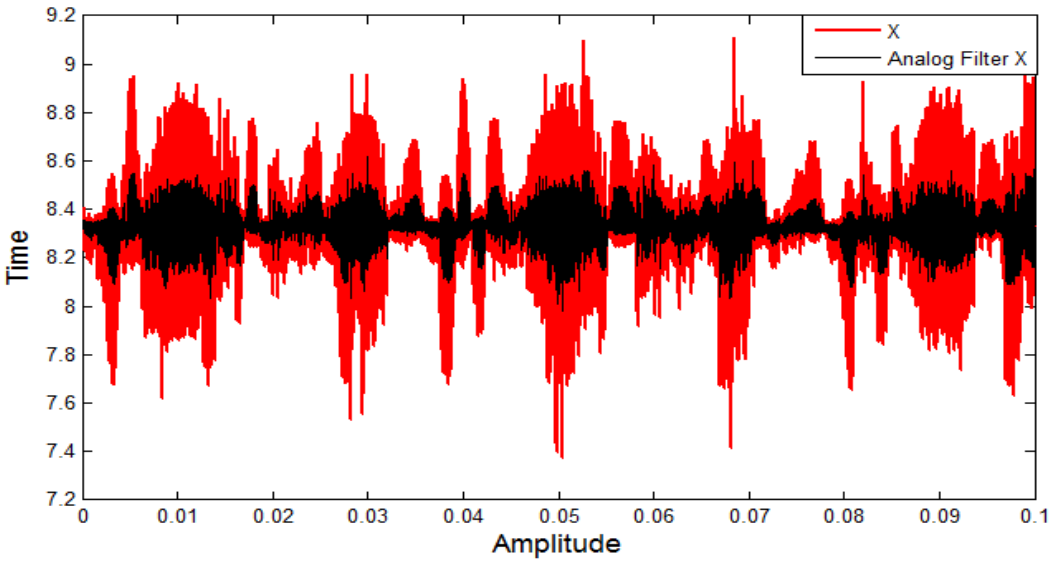

Fig 5.15 Analog filtered current response.

(b) LEM Current Transducer

The LEM LA55 current transducer in Fig 5.16, uses the Hall effect to measure the value of the low-pass filtered inductor current ($I_L = I_S$). The LEM LA55 is supplied with a +/-15V DC and is designed with a conversion ratio of 1:1000. A 1 $k\Omega$ resistor (R_M) is connected across its output, to give a 1:1 voltage to current relationship, hence, producing a voltage that equals the current.

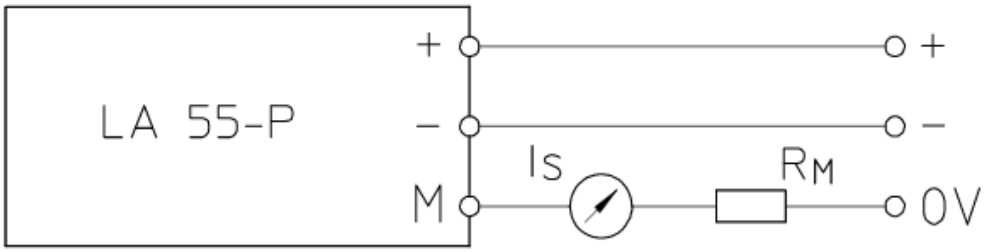

Fig 5.16 LEM LA55 current transducer connection [19]

5.7 POWER CONVERTER CONTROL

Types of control systems include: open-loop and closed-loop. The open-loop system has no information on the output signal of the converter because it does not have a feedback loop at the output. In this study, open-loop analysis was utilized to determine the relationship between the duty-cycle of the converter and the battery voltage and current. The closed-loop

control with a feedback mechanism was finally applied to ensure that the battery operation is tandem with the Kramers-Kronig relation.

(a) Frequency and Time domain analysis of Open-loop converter

The values in Table 5.1 were obtained from the DC-DC converter[1] simulation instances, due to a variation in load resistance in the MATLAB – Simulink sofware environment. The values were also used for the converter's frequency and time-domain response simulation.

Table 5.1 Parameters resulting from a variation in load resistance

	Lithium NCM			***Lead acid***		
Capacitance (μF)	470	470	470	470	470	470
Inductance (μH)	144	144	144	144	144	144
Inductor Current (A)	4.89	2.78	1.94	2.33	1.36	0.93
Capacitor Voltage (V)	7.32	7.91	8.11	7.03	7.11	7.228
Battery Voltage (V)	4	4	4	12	12	12
Load Resistance (Ω)	**5**	**10**	**15**	**5**	**10**	**15**
DC Duty Cycle	0.7	0.7	0.7	0.4	0.4	0.4

The frequency and time-domain response of the open loop converter applied to both the lithium NCM and lead acid battery was investigated. Fig 5.17 and Fig 5.18 shows the bode plot (frequency response) results of the transfer functions of the capacitor voltage V_C and inductor current I_L for the lithium NCM and lead acid batteries respectively.

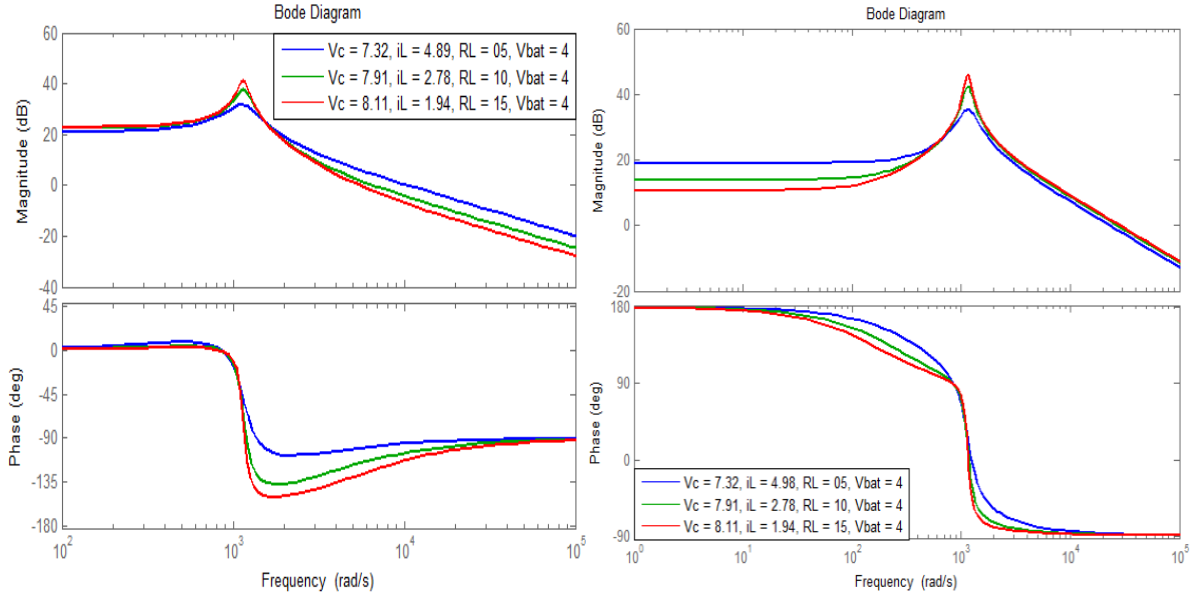

Fig 5.17 Gain and Phase margins for lithium NCM battery: G_{VC} (a) and G_{IL} (b)

[1] The batteries associated voltage drop was not considered as the voltage source was modelled as "ideal."

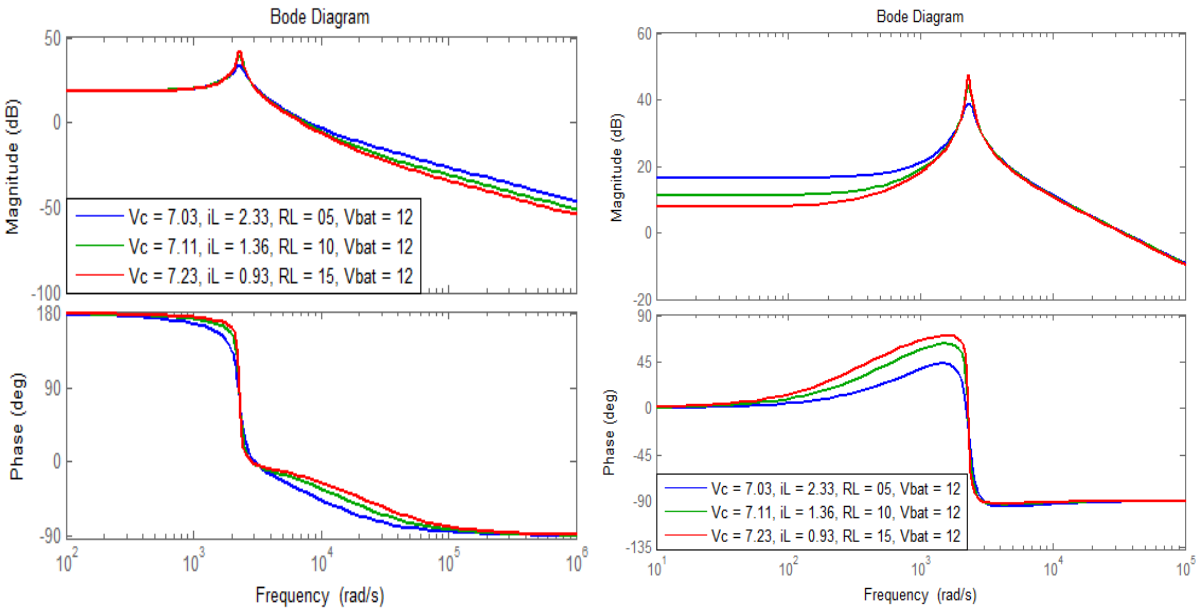

Fig 5.18 Gain and Phase margins for lead acid battery: G_{VC} (a) and G_{IL} (b)

Table 5.2 Gain margin, phase margin and bandwidth values for open-loop control

	Load	***GM (G_{VC})***	***PM (G_{VC})***	***GM (G_{IL})***	***PM (G_{IL})***
Lithium NCM	5	Inf	84.7	Inf	92.4
Lithium NCM	10	Inf	68.1	Inf	91
Lithium NCM	15	Inf	52.9	Inf	90.6
Lead acid	5	18.0	141	16.4	91
Lead acid	10	18.2	156	11.2	90.6
Lead acid	15	18.5	163	7.72	90.4

The capacitor voltage V_C and inductor current I_L margins[2] (gain – GM and phase – PM) indicate the stability of the system. When both margins (gain and phase) are zero, the system is said to be neutrally stable. Positive margins indicate system stability; whereas, negative margins indicate system instability [9] – [10]. From the results in Table 5.2, for the lithiun NCM battery, both V_C and I_L have an infinite gain margin, and a large phase margin; thus indicating the stability of the system. On the other hand, for the lead acid battery, both V_C and I_L have a large gain margin and phase margin; thus indicating the stability of the system.

[2] In control systems, many gains, and phase margins occur over the system frequency ranges. However, in this study, we utilize the gain and phase margin definitions as in [9] – [10]. In this regard, gain margin is derived at phase $(-180°)$ and phase margin is derived at gain (0).

The time domain (step) response of the transfer functions of the capacitor voltage V_C and inductor current I_L for both batteries were determined from a 0.2 step in duty cycle. Fig 5.19 and Fig 5.20 shows the time domain response of G_{VC} and G_{IL} for the lithium NCM and lead acid batteries respectively. When observed closely, it is evident that the lead acid takes a slightly longer time to attain stability compared to the lithium NCM. This can be attributted to the differences in their electrochemical composition and internal stability.

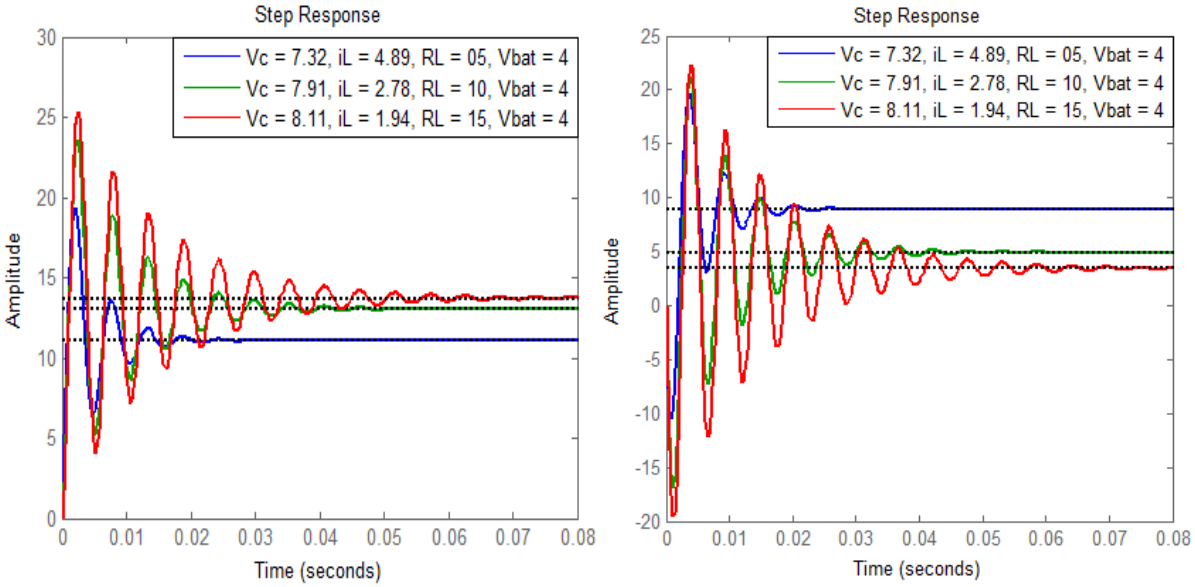

Fig 5.19 Time domain Step Response G_{VC} (a) and G_{IL} (b) for lithium NCM battery

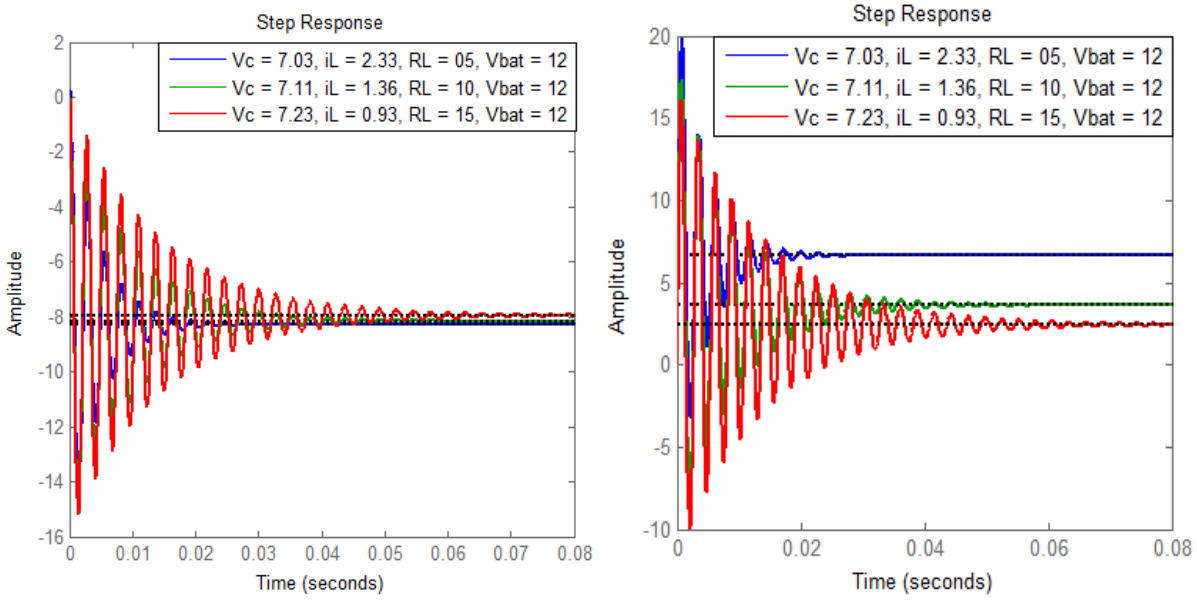

Fig 5.20 Time domain Step Response G_{VC} (a) and G_{IL} (b) for lead acid battery

(b) Controller Design

Open-loop control has no information on the system output and assumes that the output voltage remains constant. A robust closed-loop control is implemented for not only voltage

control but to ensure that the system has a high disturbance rejection (e.g. load change); because current injection (perturbation) for impedance spectroscopy measurement can only take place when the system is stable. In an online condition monitoring system, the output voltage must be constant regardless of variations in the input voltage. Since in batteries, the voltage varies as the battery gets discharged over time, the output voltage must thus be kept constant regardless of the applied load. To accomplish this, the power converter invariably requires a feedback mechanism. Hence, the converter control input – duty cycle must be continuously varied in a such a way that the output voltage is always equals a predetermined value [10]. Fig 5.21 describes the control algorithm applied for the proposed online condition monitoring system.

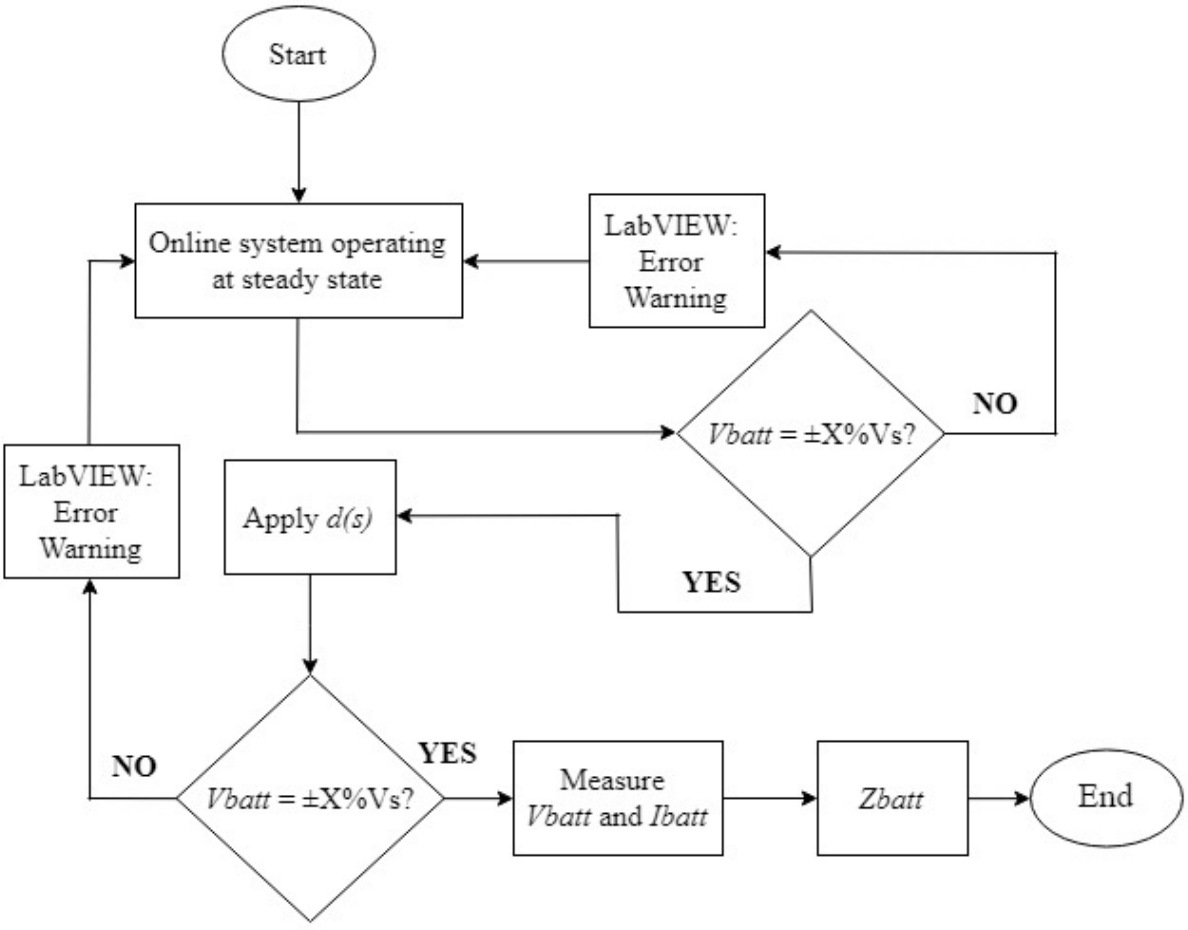

Fig 5.21 Flowchart of proposed online condition monitoring control algorithm.

Before EIS measurement is taken, the controller detects if the power converter is operating within the acceptable voltage set point region. If the converter is not operating within the acceptable voltage region (i.e. V_{batt} ≈ set point threshold), the system generates an "error warning," and waits for T seconds until the system attains steady state. If the converter is

operating within the acceptable voltage region, voltage control is suspended, and duty cycle sinusoidal excitation (AC current injection) is applied for impedance spectroscopy measurement. This duty cycle excitation results in generating a relatively small sinusoidal ripple superimposed over the battery DC voltage and DC current, as discussed in Chapter 5.4.2. Furthermore, during the period that EIS measurement is taken, the system ensures that the battery voltage remains within the set point region. If the battery voltage deviates outside this threshold, the system generates an "error warning," and the measurement is stopped until a stable condition is achieved by the controller (see Fig 5.21). The PID controller on the LabVIEW software is used to achieve this closed-loop control.

(c) Closed-loop control strategy

From the open-loop transfer function in (5 – 40) and (5 – 41), the relationship between the battery current/voltage and duty cycle was deduced. If the value of the DC source varies, which is typical of a battery due to change in load; then the controller will be unable to determine the duty cycle for a certain current or voltage. Therefore, a closed-loop control with a feedback as Fig 5.22 is implemented to eliminate these uncertainties. An optimal closed-loop control should be stable; have a good disturbance rejection; have a rapid set-point tracking; and should strike a balance between robustness and sensitivity [9] – [10]. It is thus the aim of this study, to incorporate these features into the closed-loop control of the online monitoring system.

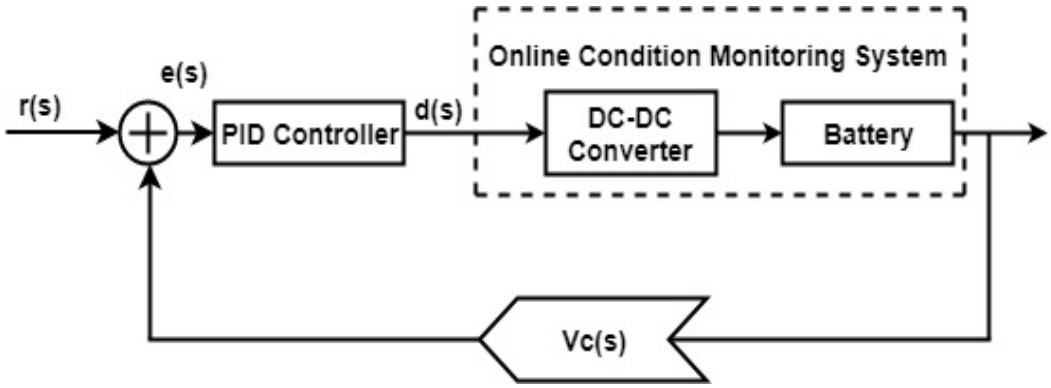

Fig 5.22 Schematic of closed loop control

From Fig 5.22, the system parameter to be controlled (process variable), serves as a feedback to the closed-loop control system. r(s) is the set-point value of the system parameter/process variable to be controlled. In this case, this is the DC bus voltage of the battery. e(s) is the error signal, which is the difference in the system parameter/process variable and the set-point value. Lastly, the actuator specifies the control algorithm that is applied to drive the system parameter to its set point value. In this study, a Proportional-Integral-

Derivative (PID) control in the LabVIEW software is utilized to continuously control the system parameters at a fixed loop rate. The system parameters are controlled by selecting an appropriate PID value to arrive at optimal gains for ideal system response.

The proportional component is dependent only on the difference between the system parameter/process variable and set point value. It also determines the ratio of the system parameter to the error signal. A proportional controller (K_p) is used to reduce the rise time and steady-state error. The integral component adds the error term over a set period. Thus, the integral component will start to increase over time once there is an error term. The steady-state error is termed as the final deviation of the system parameter from the set point. An integral controller (K_i) is used to eliminate steady state error, but adversely affects the transient response. The derivative component decreases the value of the output, if the system parameter is increasing quickly. The derivative response increases the overall speed of the control system and is termed as the rate of change of the process variable. The derivative control (K_d) is critical in increasing the system's stability, decreasing overshoot and improving the system's transient response [17]. The effect of each controller on the control system is presented in Table 5.3

Table 5.3 Effect of PID Controllers on online condition monitoring control system.

CL RESPONSE	RISE TIME	OVERSHOOT	SETTLING TIME	S-S ERROR
K_p	Decrease	Increase	Little change	Decrease
K_i	Decrease	Decrease	Increase	Eliminate
K_d	Little change	Decrease	Decrease	Little change

Once a control engineer understands the impact of each gain parameter as Table 5.2, the PID controller values can be obtained through trial and error method. Nonetheless, in this study, the PID controller parameters are firstly obtained through mathematical analysis as [21], before undergoing tuning. From Fig 5.21, (5 – 53) and (5 – 54) are obtained:

$$G_{PID} = K_p + \frac{1}{s}K_i + sK_d \qquad (5-53)$$

$$G_{PID} = \frac{K_p s + K_i + K_d s^2}{s} \qquad (5-54)$$

In (5 – 53) and (5 – 54), K_p, K_i *and* K_d are PID controller parameters for derivative, integral and proportional respectively. The closed loop transfer function *H* is expressed as:

$$H = \frac{G_{PID} \times G_{Vc}(s) - \boldsymbol{Zeros}}{1 + (G_{PID} \times G_{Vc}(s)) - \boldsymbol{Poles}} \qquad (5-55)$$

Replacing G_{Vc} from (5 – 40), we obtain (5 – 56) – (5 – 58):

$$H = \frac{\frac{K_p s+K_i+K_d s^2}{s} \times \frac{-\left[\frac{(V_{batt}-V_c)(1-D)}{LC}\right]+\frac{sI_L}{C}}{s^2+\frac{s}{R_{load}C}+\frac{(1-D)^2}{LC}}}{1+\left(\frac{K_p s+K_i+K_d s^2}{s} \times \frac{-\left[\frac{(V_{batt}-V_c)(1-D)}{LC}\right]+\frac{sI_L}{C}}{s^2+\frac{s}{R_{load}C}+\frac{(1-D)^2}{LC}}\right)} \quad (5-56)$$

$$H = \frac{\frac{(K_p s+K_i+K_d s^2)\left(-\left[\frac{(V_{batt}-V_c)(1-D)}{LC}\right]+\frac{sI_L}{C}\right)}{s^3+\frac{s^2}{R_{load}C}+\frac{s(1-D)^2}{LC}}}{\frac{s^3+\frac{s^2}{R_{load}C}+\frac{s(1-D)^2}{LC}+(K_p s+K_i+K_d s^2)\left(-\left[\frac{(V_{batt}-V_c)(1-D)}{LC}\right]+\frac{sI_L}{C}\right)}{s^3+\frac{s^2}{R_{load}C}+\frac{s(1-D)^2}{LC}}} \quad (5-57)$$

$$H = \frac{(K_p s+K_i+K_d s^2)\left(-\left[\frac{(V_{batt}-V_c)(1-D)}{LC}\right]+\frac{sI_L}{C}\right)}{s^3+\frac{s^2}{R_{load}C}+\frac{s(1-D)^2}{LC}+(K_p s+K_i+K_d s^2)\left(-\left[\frac{(V_{batt}-V_c)(1-D)}{LC}\right]+\frac{sI_L}{C}\right)} \quad (5-58)$$

To simplify (5 – 56) – (5 – 58), it is assumed that $-\frac{(V_{batt}-V_c)(1-D)}{LC} = X$ and $\frac{I_L}{C} = Y$.

$$H = \frac{(K_p sX+K_p s^2 Y+K_i X+K_i sY+K_d s^2 X+K_d s^3 Y)}{s^3(1+K_d Y)+s^2\left(\frac{1}{R_{load}C}+K_p Y+K_d X\right)+s\left[\frac{(1-D)^2}{LC}+(K_p X+K_i Y)\right]+K_i X} \quad (5-59)$$

From [9] – [10], a feedback control system is stable, if and only if, all the roots of the characteristic equation (poles) fall at the left of the complex plane's imaginary axis (negative half of the s-plane). Thus, to ensure that the poles are located at the negative half of the s-plane, the roots of the poles are taken as: (-1, -1 and -1). Since $(s+1)^3 = s^3 + 3s^2 + 3s + 1$, the coefficients are thus replaced to obtain $K_p, K_i \; and \; K_d$.

$$s^3(1+K_d Y) = 1$$

$$\left(\frac{1}{R_{load}C} + K_p Y + K_d X\right) = 3$$

$$\frac{(1-D)^2}{LC} + (K_p X + K_i Y) = 3$$

Hence, $K_p, K_i \; and \; K_d =$ 0.05, 1 and 0 respectively. Table 5.4 shows the gain margin, phase margin and bandwidth[3] at different loading points of both batteries; following the utilization of the calculated gains.

[3] The bandwidth of a control system indicates the frequency range in which set-point tracking occurs.

Table 5.4 Gain margin, phase margin and bandwidth values for closed-loop control

	Load	***GM***	***PM***	***BW (kHz)***
Lithium NCM	5	Inf	58.3	15.13
Lithium NCM	10	Inf	85.5	15.98
Lithium NCM	15	Inf	89.6	15.81
Lead acid	5	Inf	11.9	16.42
Lead acid	10	Inf	15.7	16.41
Lead acid	15	Inf	26.7	16.39

Although larger margins translate to a better closed loop control system, extreme margins can have a profound impact on the system. On one hand, large gain and phase margins corresponds to a slow closed-loop response, with a small overshoot; whereas, smaller values result in a faster/more oscillatory response, with a faster overshoot. More so, larger responses increase the robustness of the control system at the expense of control sensitivity [9] – [10]. Another important consideration is the fact that the bandwidth of the closed-loop control system is directly proportional to the speed of response and inversely proportional to the robustness of the system. This relationship is apparent in the results in Table 5.4. Care must thus be taken to ensure a compromise between the control system's robustness, sensitivity and bandwidth.

From Table 5.4, it can be observed that the lithiun NCM battery closed loop system has an infinite gain margin, and a large phase margin; thus indicating the stability of the system. More so, its bandwidth is sufficient for EIS characterizaton. On the other hand, the lead acid battery closed loop system has an infinite gain margin and a large phase margin. Its bandwidth is also sufficient for EIS characterizaition. Nonetheless, it is evident that, regardless of the robustness of the closed-loop control of both batteries, both control systems will suffer from insensitivity when exposed to external disturbances.

In general, a well-tuned controller should possess a gain margin between 1.7 – 6.0 and phase margin between 30 – 45% [9] – [10]. Consequently, the gain of our online condition monitoring system will be tuned to satisfy optimal control criterion. As Table 5.3, increasing the proportional gain results in an increasing overshoot and faster response (i.e. smaller gain and phase margin); while decreasing the integral gain does otherwise. Table 5.5 shows the gain-tuned results for gain margin, phase margin and bandwidth at different loading points of both batteries. For the lithium NCM battery the gains are tuned as: $K_p = 0.04423$ and $K_i =$

2.214. For the lead acid battery, the gains are tuned as: $K_p = 0.0312$ and $K_i = 1.765$. Fig 5.23 shows the closed loop control frequency response applied to the online condition monitoring system for the lithium NCM battery; while, Fig 5.24 shows the closed loop control frequency response applied to the online condition monitoring system for the lead acid battery.

Table 5.5 Gain margin, phase margin and bandwidth values for gain-tuned closed-loop control

	Load	***GM***	***PM***	***BW (kHz)***
Lithium NCM	5	2.33	36.41	11.85
Lithium NCM	10	2.47	40.65	10.92
Lithium NCM	15	2.98	41.12	10.22
Lead acid	5	3.49	32.33	12.91
Lead acid	10	3.77	34.71	12.87
Lead acid	15	3.84	35.40	12.82

It is evident from Table 5.5 that the closed-loop control results in a control bandwidth of approximately 11kHz for the lithium NCM battery. For the lead acid battery, the closed-loop control results in a control bandwidth of approximately 12kHz. The closed-loop control bandwidth is fast enough to capture the frequencies of interest of both batteries and thus adequately control the system over the period of EIS measurement. For both batteries, as the load increases, the bandwidth of the system decreases, albeit subtle for lead acid battery. Although the load values selected for both batteries can be controlled by the PI, care must be taken to ensure that the system does not supply a load that effectively takes it out of the controllable region of the PI – most especially in the case of the lithium NCM battery.

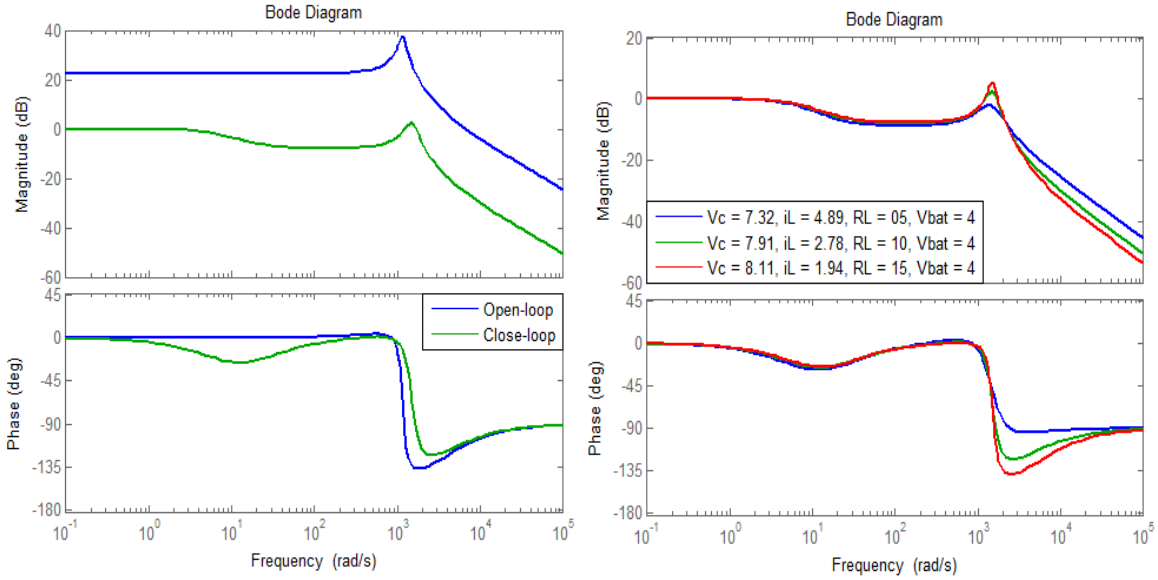

Fig 5.23 Frequency response of open loop and closed loop control for lithium NCM battery (a) and closed loop control at different operating conditions (b)

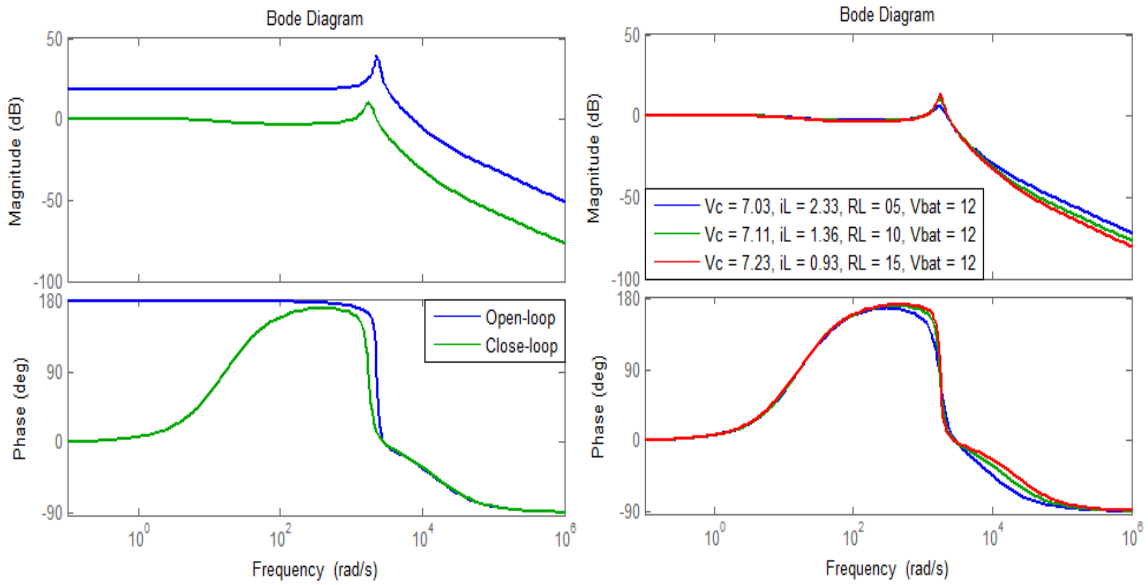

Fig 5.24 Frequency response of open loop and closed loop control for lead acid battery (a) and closed loop control at different operating conditions (b)

From Fig 5.25, it can be observed that regardless of the varying nature of the battery's DC bus voltage[4], the closed-loop control can maintain the DC bus voltage over the period required for EIS measurement on both batteries (i.e. 50 seconds for lithium NCM and 10 seconds for lead acid battery). This therefore depicts that the closed loop control system has a fast set-point tracking. Likewise, following a deviation in the applied resistive load (Constant Resistance – CR) for both the lithium NCM and lead acid batteries, it is evident that the batteries return to a stable region. This depicts that the closed loop control system has a good disturbance rejection.

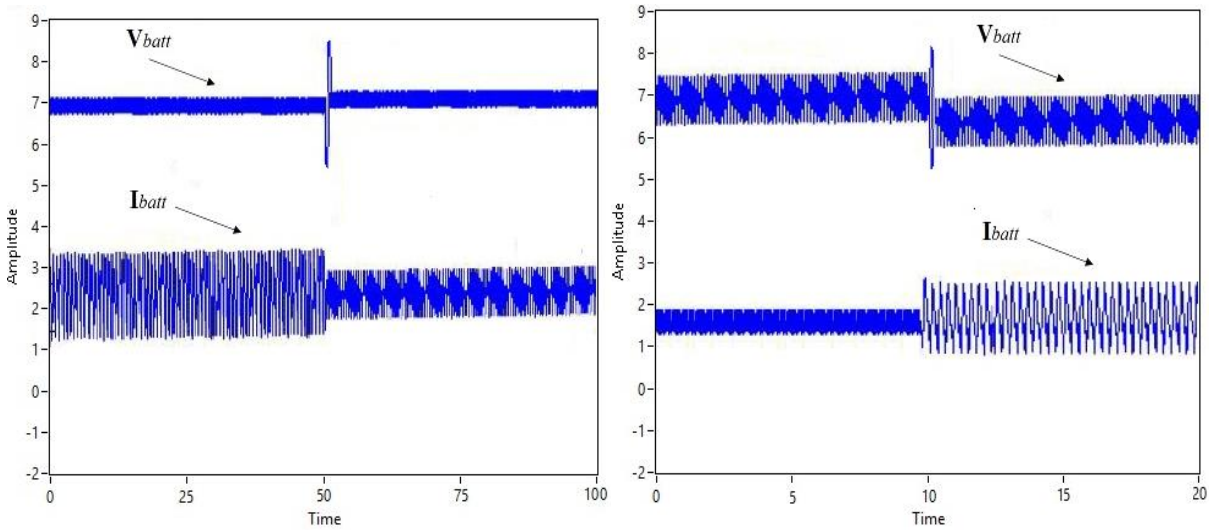

Fig 5.25 Validation of closed-loop control sensitivity to disturbances: lithium NCM battery (a) and lead acid battery (b).

[4] The voltage of a battery typically decreases when connected to a load.

It can hence be concluded that the control system embedded in the proposed online condition monitoring system fulfils the stability laws: stability, good disturbance rejection, rapid set-point tracking, robustness and sensitivity. The system is also sufficient to cover the key kinetic features required for characterizing both the lead acid and lithium NCM batteries.

(d) Current Perturbation for EIS

Kramers-Kronig relation requires EIS measurement to be carried out only during periods of stability. Stability condition requires that the output voltage is within the set-point range as designed by the control engineer. This definition was also applied in [6] as a ±10% threshold of the setpoint voltage. If the output voltage deviates outside the threshold value, the impedance spectroscopy measurement would stop until voltage control is reinstated. The output voltage range can be adjusted depending on the voltage requirements.

Based on the stability (chemical and control) investigation carried out on both batteries in earlier sections, the voltage requirements are thus selected to be stricter for the lead acid battery (±5%) compared to that of the lithium NCM battery (±10%). Since the design for the voltage control has been accomplished, now the impedance spectroscopy signal injection control through the power converter is explored. The current control design entails applying impedance spectroscopy signal to the converter after the suspension of voltage control. From (5 – 41), the small signal transfer function was derived for the inductor current I_L, which relates the current perturbation to the duty cycle. By replacing $S = 2\pi fi$, (5 – 60) is obtained:

$$\tilde{d}(f) = \tilde{\imath}_L(f)\frac{(2\pi fi)^2+(2\pi fi)\frac{1}{R_{load}C}+\frac{(1-D)^2}{LC}}{\frac{(2\pi fi)(V_{batt}-V_C)}{L}+\frac{(V_{batt}-V_C)}{R_{load}CL}+\frac{(1-D)I_L}{LC}} \qquad (5-60)$$

From (5 – 60), if $C = 470\mu F, L = 144\mu H,\ I_L = 2.78A, V_C = 7.91V, V_{batt} = 4V, R_{load} = 10\Omega, D = 0.7, \tilde{\imath}_L = 0.4A\ and\ f = 1Hz$; the AC duty cycle excitation that produces this current excitation at the associating frequency is: $\tilde{d}(f)$ = 0.006459.

5.8 SUMMARY

This Chapter discusses the variety of existing power converter topologies that have been utilized for online condition monitoring of electrochemical systems. The design of the components of the online condition monitoring in this study was also discussed. Most importantly, the design, operation and control of the selected power converter was discussed

in the context of EIS application. More so, the nuances that results from the control of both battery chemistries are highlighted and discussed.

5.9 REFERENCE

[1] W. Huang and J. A. A. Qahouq, "An Online Battery Impedance Measurement Method Using DC–DC Power Converter Control," IEEE TRANSACTIONS ON INDUSTRIAL ELECTRONICS, vol. 61, no. 11, pp. 5987-5995, 2014.

[2] R. Koch and A. Jossen, "Impedance Spectroscopy for Battery Monitoring with Switched Mode Amplifiers," in 16th International Power Electronics and Motion Control Conference and Exposition, Antalya, Turkey, 2014.

[3] D. Depernet, O. Ba and A. Berthon, "Online impedance spectroscopy of lead acid batteries for storage management of a standalone power plant," Journal of Power Sources, vol. 219, pp. 65-74, 2012.

[4] E. Din, C. Schaef, K. Moffat and J. T. Stauth, "A Scalable Active Battery Management System with Embedded Real-Time Electrochemical Impedance Spectroscopy," IEEE Transactions on Power Electronics, vol. 32, no. 7, pp. 5688-, 2017.

[5] J. A. A. Qahouq et al., "Single-Perturbation-Cycle Online Battery Impedance Spectrum Measurement Method with Closed-Loop Control of Power Converter," IEEE Transactions on Industrial Electronics, Vol. 64, No. 9, September 2017

[6] A. Debenjak, J. Petrovcic, P. Boskoski, B. Musizza and D. Juricic, "Fuel Cell Condition Monitoring System Based on Interconnected DC-DC Converter and Voltage Monitor," IEEE Transactions on Industrial Electronics, vol. 62, no. 8, pp. 5293-5305, 2015.

[7] P. Hong, J. Li, L. Xu, M. Ouyang and C. Fang, "Modeling and simulation of parallel DC/DC converters for online AC impedance estimation of PEM fuel cell stack," International Journal of Hydrogen Energy, vol. 41, no. 4, pp. 3004-3014, 2016.

[8] T.-T. Nguyen, V.-L. Tran and W. Choi, "Development of the Intelligent Charger with Battery State-Of-Health Estimation Using Online Impedance Spectroscopy," in Industrial Electronics (ISIE), Instanbul Turkey, 2014.

[9] Ned Mohan, Tore Undeland, and William Robbins, "Power Electronics - Converters, Applications and Design," Jon Wiley & Sons Inc., 2nd Ed., 1995.

[10] Robert W. Erickson, Dragan Maksimovic, "Fundamentals of Power Electronics," Kluwer Academic Publishers, 2nd Edition, 2004.

[11] Charles Alexander and Mathew N.O Sadiku, "Fundamentals of Electric Circuits,", Fourth edition, The McGraw-Hill Companies, 2009.

[12] D. Depernet, O. Ba and A. Berthon, "Online impedance spectroscopy of lead acid batteries for storage management of a standalone power plant," Journal of Power Sources, vol. 219, pp. 65-74, 2012.

[13] Marcel Allain et al., "The use of pseudo-random binary sequences to predict a DC-DC converter's control-to-output transfer function in continuous conduction mode," IEEE, CCECE/CCGEI, Saskatoon, May 2005

[14] Rodney H.G. Tan and Landon Y. H. Hoo, “DC-DC Converter Modelling and Simulation using State Space Approach,” IEEE Conference on Energy Conversion (CENCON), pp. 42-47, 2015.

[15] M. S. Hassan and A. A. Elbaset, “Small-Signal MATLAB/Simulink Model of DC-DC Buck Converter using State-Space Averaging Method,” in 17th International Middle-East Power System Conference (MEPCON'15), Mansoura, Egypt, 2015.

[16] J. Karki, “Active Low-Pass Filter Design,” Texas Instruments- AAP precision Anlag, Dallas, Texas, 2002.

[17] National Instrument, “PID Theory/Control Explained” – LabVIEW White Paper online software support.

[18] Sean Moore and Paul Barendse, “Online Condition Monitoring of Lithium-Ion Batteries Using Impedance Spectroscopy,” Energy Conversion Congress and Exposition (ECCE), 2017 IEEE, pp. 5617-5624.

[19] Current Transducer LA 55-P LEM Data Sheet – Available online: http://manuals.chudov.com/LEM-LA55-P-Current-Transducer.pdf

6. HARDWARE SET-UP

6.1 BATTERY CELLS

The cells utilized for this study was a pouch shaped EIG lithium Nickel-Cobalt-Manganese Oxide battery and a cuboid shaped Pulsar sealed lead acid battery (see Fig 6.1) [1] – [2]. During measurements, both batteries were contained within a thermally insulated container, to ensure that the ambient temperature did not interfere with the operating temperature.

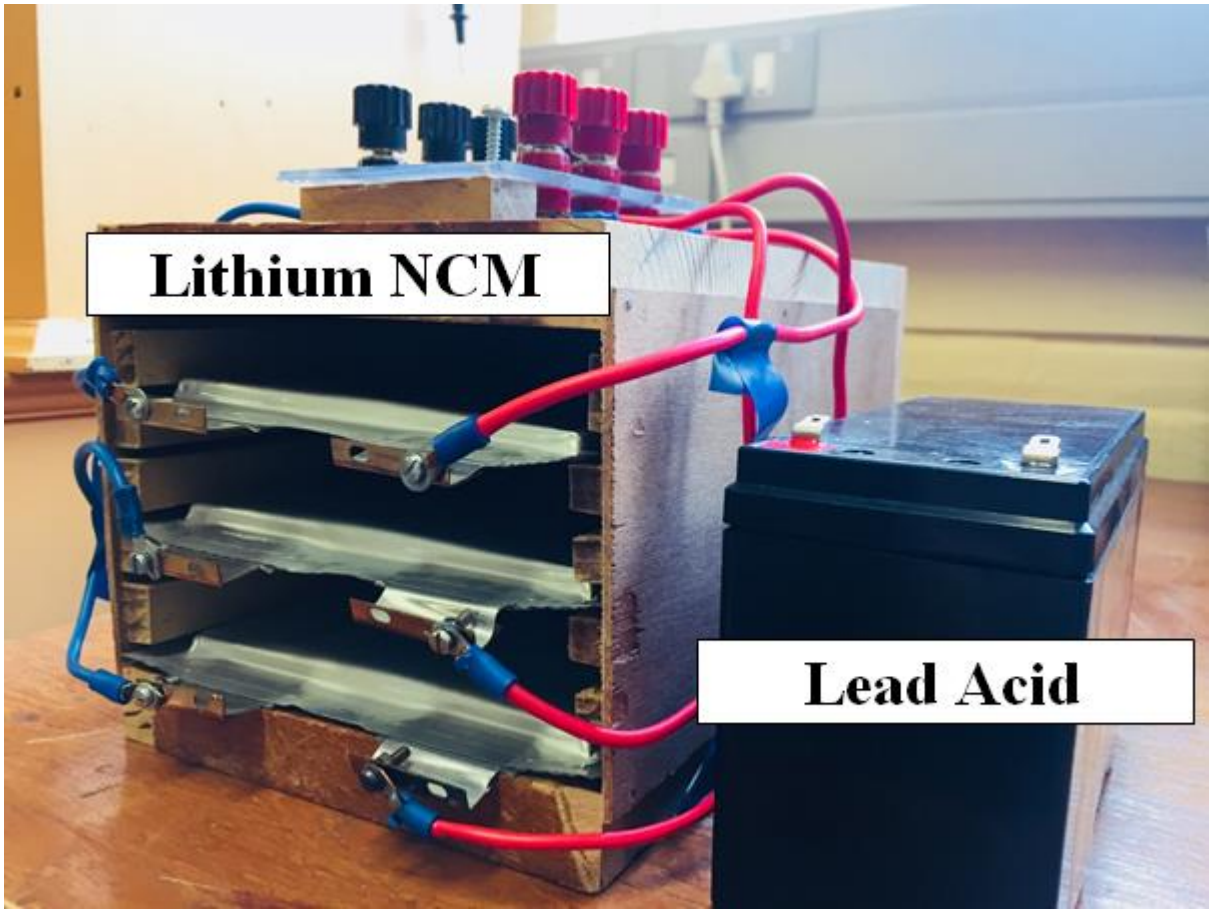

Fig 6.1 Lithium NCM Batteries (a) and lead acid battery (b)

(a) Electrical and mechanical characteristics

The lithium NCM cell has a nominal voltage of $3.65V$ and capacity of $20Ah$. The AC impedance at $1kHz$ is less than $3m\Omega$. It has a specific energy of $174Wh/Kg$ and an energy density of $370Wh/L$. In 10 seconds and at a depth of 50%, it has a specific power of $2300W/Kg$ and power density of $4600W/L$. The lithium NCM cell weighed approximately

$428g$ and measured $217 \times 130 \times 7\,mm$. On the other hand, the lead acid cell has a nominal voltage of $12V$ and capacity of $7Ah$ at 0.05C. It has an internal resistance of $25m\Omega$. Its specific energy and energy density is dependent on the discharge rate. The lead acid cell weighed $2.05kg$ and measured $151 \times 65 \times 100\,mm$.

(b) Operating conditions

i. Charge Conditions

For the lithium NCM battery, a $4.15V$ maximum charge voltage, $0.5C$ charge current and constant current – constant voltage (CC – CV) charge method is recommended by the manufacturer. For the lead acid battery, a $13V$ maximum charge voltage, $0.1C$ – $0.3C$ charge current and a constant voltage (CV) charge method is recommended by the manufacturer.

ii. Discharge Conditions

For the lithium NCM battery, the recommended cut-off voltage is 3.0V and the maximum allowable cut-off voltage is 2.5V. The maximum continuous discharge current is 5C and the maximum discharge current peak for less than 10 seconds is 10C. For the lead acid battery, the recommended cut-off voltage is 10.8V and the manufacturers maximum discharge current for 5 seconds is 105A.

iii. Operating Temperature

The lithium NCM cells are designed to be operated within the range of -30^oC to 55^oC. Its recommended charge temperature and storage temperature ranges are 0^oC to 40^oC and -30^oC to 55^oC respectively. Room temperature (approximately 25^oC) is the recommended operating temperature of the lead acid.

(c) Cell Performance

The rate capability of a battery is expressed as a graph of discharge voltage against time as in Fig 6.2. From Fig 6.2, the rate capability is estimated for both batteries at the manufacturers recommended temperature. From the results, it is apparent that as the discharge current increases, the less likely the battery can attain its rated capacity. It is also observed from the rate capability plot, that the higher the discharge current, the higher the internal resistance. This is indicated from the magnitude of the drop from open circuit voltage. The rate capability

effect is more significant in the lead acid battery, due to the Peukert's loss that occurs in a lead acid battery.

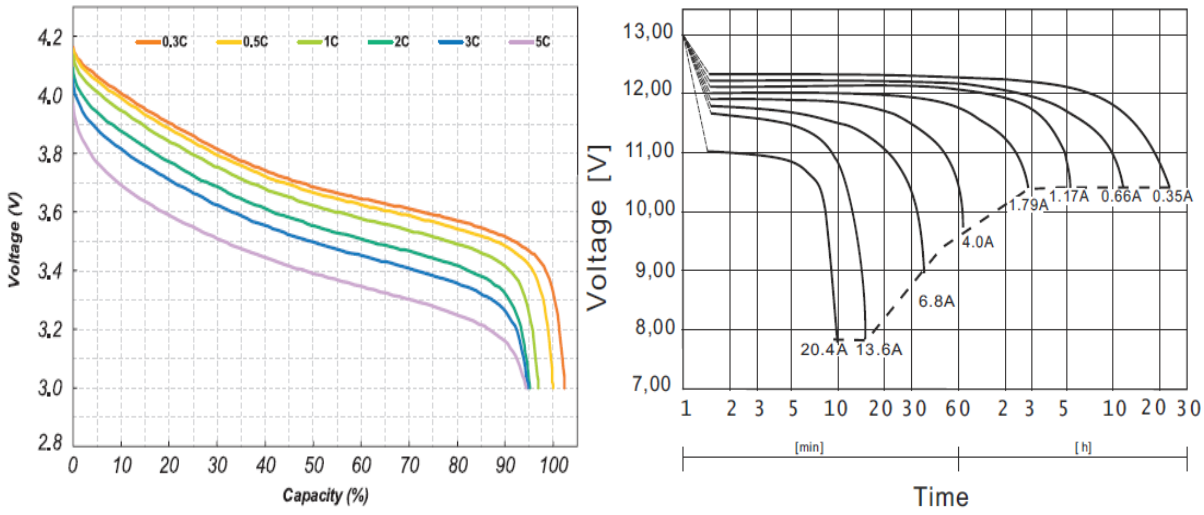

Fig 6.2 Discharge characteristics of a lithium-ion battery (a) and lead acid battery (b).

(d) Peukert's Analysis

Batteries are rated in amp-hour (Ah). This implies that the discharge time of a battery is dependent on the discharge rate. For instance, a battery with a 10Ah rating; if discharged with 2-amps current, will last for 5 hours. It is consequently expected that if the same battery is discharged with 10-amps current, it will last for 1 hour. This is usually not true as proposed by Josef Peukert for lead acid batteries in 1897 [3]. Peukert's equation, claimed that a battery's capacity is dependent on its discharge rate. Due to the simplicity of Peukert's equation, it has been largely applied to other battery chemistries as well as super capacitors [4]. For a 1A discharge rate (rated C):

$$C_{dis} = T_{dis} \times {I_{dis}}^{P} \qquad (6-1)$$

From (6 – 1), C_{dis} is the available discharge capacity, T_{dis} is the discharge time, I_{dis} is the discharge current and P is the Peukert's exponent. In general terms, the rate dependent discharge time for a battery is (6 – 2):

$$T = \frac{C\left(\frac{C}{R}\right)^{n-1}}{I^{n}} \qquad (6-2)$$

In (6 – 2), T is discharge time, C is battery specified capacity and R is battery hour rating. The Peukert's exponent P is unique to all batteries and is a parameter that is applied to account for the rate-dependent losses incurred due to discharging a battery at a higher discharge current.

P close to unity means an ideal operation (current-independent capacity) of the battery. More so, as P increases, the battery capacity's dependence on discharge current becomes more pronounced [5].

$$P = \frac{(log\ t_2 - log\ t_1)}{(log\ I_1 - log\ I_2)} \qquad (6-3)$$

In (6 – 3), t represents discharge time and I represents current of a battery. In this study, the Peukert's exponent for the lead acid battery was estimated at 1.3, whereas, that of the lithium NCM battery was estimated at 1.1. This implies that the discharge current of a lead acid battery has more effect on its capacity, compared to the lithium NCM battery. The high Peukert exponent of the lead acid battery is because of sulphation on the plate's surface which leads to clogging of the pores that limits: the time that acid must diffuse to complete the reaction and the polarization due to internal resistance [5].

6.2 COMMERCIAL EIS EQUIPMENT SET-UP

The commercial equipment used for EIS measurement of the batteries was the Autolab 302N Potentiostat/Galvanostat (PGSTAT302N) and Frequency Response Analyser (FRA) controlled via the NOVA software. The overall set-up is shown in Fig 6.3

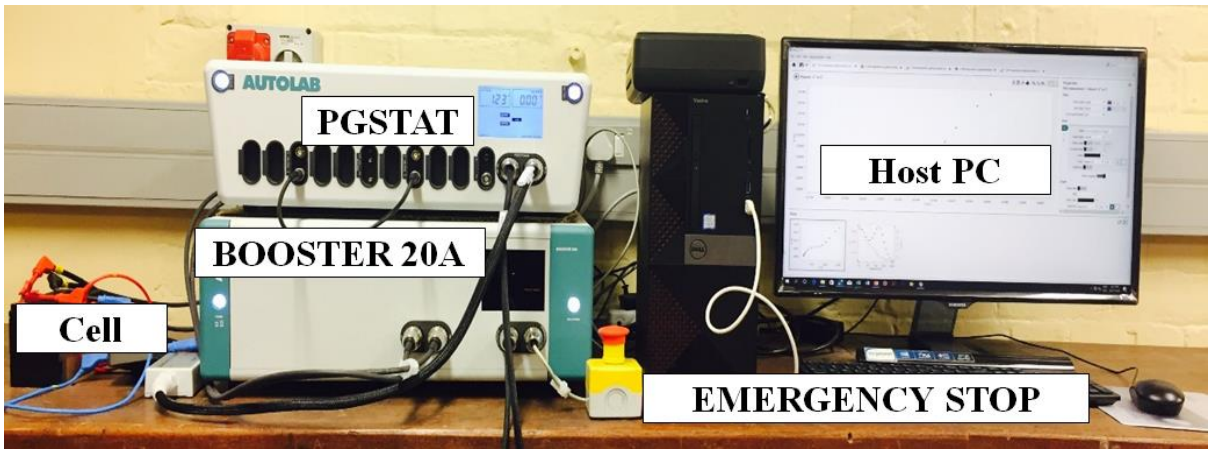

Fig 6.3 Experimental set-up of the Autolab Potentiostat/Galvanostat and 20A current booster.

i. Calibration

Before EIS measurements are carried out on the FRA – Autolab PGSTAT, C1 and C2 calibration factors must be determined. After purchase of the equipment, a predetermined C1 and C2 values are given. However, upon installation, C1 and C2 values must be experimentally determined within the FRA module. The NOVA software uses two procedures to determine the calibration factors: PGSTAT C1 calibration and PGSTAT C2 calibration. The

determination of C1 and C2 values required the utilization of the Autolab Dummy cell and Faraday cage. Both calibrations are presented as a Bode plot as in Fig 6.4. The value for C1 was 1.7E-11 F and that of C2 was 3.8 E-13. For more details on the procedure for calibrating C1 and C2, check page 1081 of the NOVA User Manual [6]

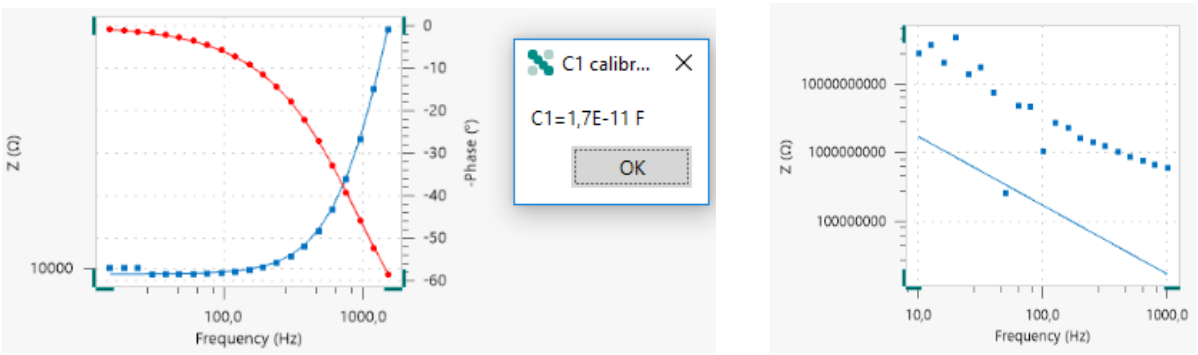

Fig 6.4 Calibration to obtain (a) C1 (b) C2

ii. Electrode Connections

Four (4) probes are available for the Metrohm Autolab PGSTAT and NI-DAQ connections. For the Autolab PGSTAT, two of the leads (working and counter) transmit current, while the other two (sense and reference) are sense leads and are used to quantify the potential (measure voltage). Unlike the Autolab PGSTAT, there are no dedicated electrodes in the NI-DAQ. Nevertheless, the NI-DAQ cables (electrodes) are connected in a similar fashion.

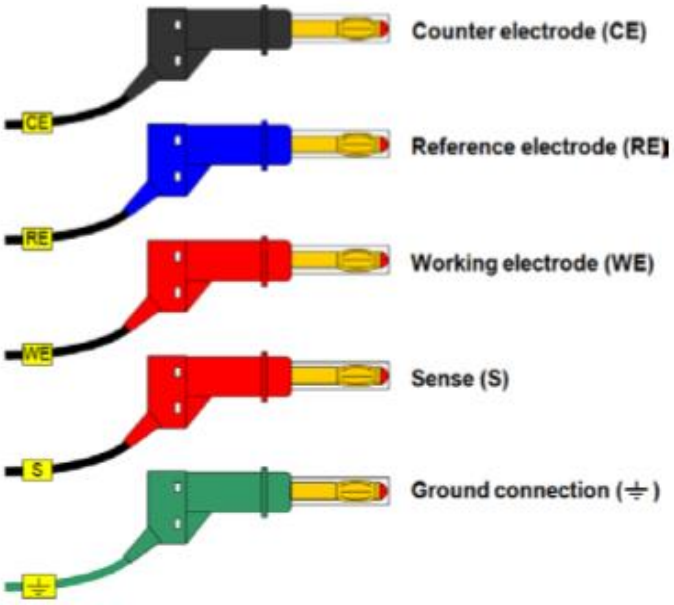

Fig 6.5 Autolab PGSTAT electrodes with their associating colour code

The four-probe instrument as shown in Fig 6.5, can be configured for EIS measurements on: two (2) electrodes, three (3) electrodes or four (4) electrodes. The common electrode designations are: working, reference and counter (or auxiliary). Working electrode is the electrode being studied in an electrochemical system. The counter electrode is used to complete the current path in the electrochemical cell but does not participate in the electrochemical reaction. The Reference electrodes serve as a reference point in the electrochemical cell under experimentation. They also serve as a reference for the potential (sense) measurements [7] – [9].

The two-electrode configuration as shown in Fig 6.6, is applied in this study, in order to understand the whole cell behaviour. The two-electrode configuration measures the whole cell using the sense leads, which measures the drop-in voltage across the whole electrochemical system. In this setup, the counter electrode and reference electrode are shorted at one end, while the working electrode and sense are shorted at the other end.

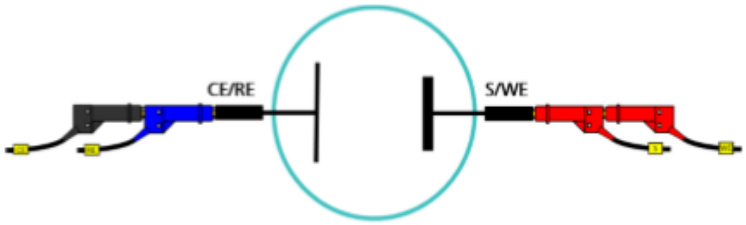

Fig 6.6 The two (2) electrode cell setup

6.2.1 Potentiostat/Galvanostat (PGSTAT)

The PGSTAT302N alongside the Frequency Response Analyser (FRA32M) module is used to carry out EIS measurements. The PGSTAT302N has a compliance voltage of $30V$, a potential range of $\pm 10V$ and a 1 MHz bandwidth. At a current range of $10nA$, the PGSTAT302N's current resolution is $30fA$. Likewise, it has a maximum current (AC and DC) of 2A. However, the Booster20A can be used to extend the range up to $20A$. The CA of the Autolab instrument, is designed with three different bandwidth settings, namely: high stability, high speed and ultra-high speed. The high stability mode is designed for low frequency electrochemical measurements (less than 10 kHz). The high-speed mode is for faster measurements, with a CA bandwidth up to 125 kHz. The ultra-high-speed mode is fastest with a CA bandwidth of 1.25 MHz [6] – [7]. Fig 6.7 shows the schematic of the PGSTAT.

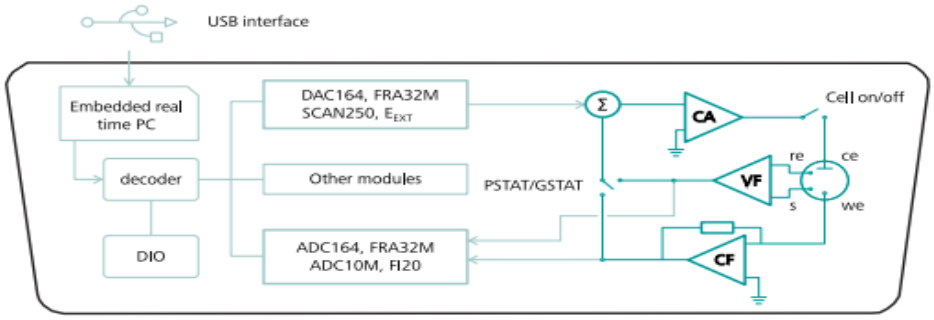

Fig 6.7 Schematic representation of the Autolab Potentiostat/Galvanostat.

In potentiostatic mode of EIS measurements, the PGSTAT will accurately control the counter electrode (CE) potential against that of the working electrode (WE). This is done to ensure that the potential difference (p.d) between the WE and reference electrode (RE) is properly defined and is in tandem with the user specified value. In the galvanostatic mode – used in this study, the flow of current between WE and CE is controlled. The p.d between RE and WE, and the current flow between CE and WE are monitored continuously. The PGSTAT ensures that the user specified value – current or potential is accurately and continuously controlled using a negative feedback technique.

6.2.2 Frequency Response Analyzer

EIS measurement in the potentiostatic or galvanostatic mode is performed with the FRA32M module. The FRA32M allows measurement over a wide range of frequencies (10 µHz to 32 MHz), but is limited to 1 MHz when connected to the Autolab PGSTAT. The FRA32M module is also embedded with a curve fitting tool for fitting EIS plots with an equivalent electric circuit. The signal types allowed in the FRA32M module are 1 sine, 5 sines and 15 sines. For further reading, the FRA measurement command properties and sampler configurations can be explored in the NOVA User Manual [6].

6.2.3 Current Booster

The Booster20A is used to extend the maximum current of the Autolab instrument from 2A to 20A. When the Booster20A is connected, all measurement commands in the NOVA software function as normal. The Booster20A can be utilized in either: bypass or operation mode. For the bypass mode, Booster20A is connected to the Autolab instrument but does not provide an extra current range. In this mode, the Booster20A is bypassed and only functions as a connection to the battery. In the operation mode, the Booster20A is connected to the Autolab instrument and provides the boosting capability. The specifications of the Booster20A are shown in Table 6.1

Table 6.1 Specifications of the Booster20A

Specification	***Value***
Maximum current	20 A
Compliance voltage	20 V
Maximum power	350 W
Current resolution	± 0.0003%
Current accuracy	± 0.02% of current range
PGSTAT bandwidth	18 kHz
GSTAT bandwidth	40 kHz

Lastly, given the high current output level that is associated with the Booster20A, an emergency stop button is attached to the front panel of the Booster for safety purpose. This button can be activated at any point in time to immediately disengage the operation of the Booster20A.

6.2.4 Voltage Multiplier

The maximum input voltage of the PGSTAT is $\pm 10V$. The lithium NCM battery is within this range, but the lead acid battery exceeds this. To measure voltage magnitudes greater than 10V, the voltage multiplier is utilized. The voltage multiplier increases the output voltage of the Autolab PGSTAT302N to its compliance voltage (± 30 V). In Fig 6.8, the voltage multiplier is connected to the battery via the S and RE terminals. The PGSTAT's S, RE and G leads are connected the voltage multiplier's PGSTAT port. The WE and CE leads are connected directly to the battery. The PGSTAT's potential measurements are divided by a factor of 10. This was automatically incremented by the Autolab NOVA software [10].

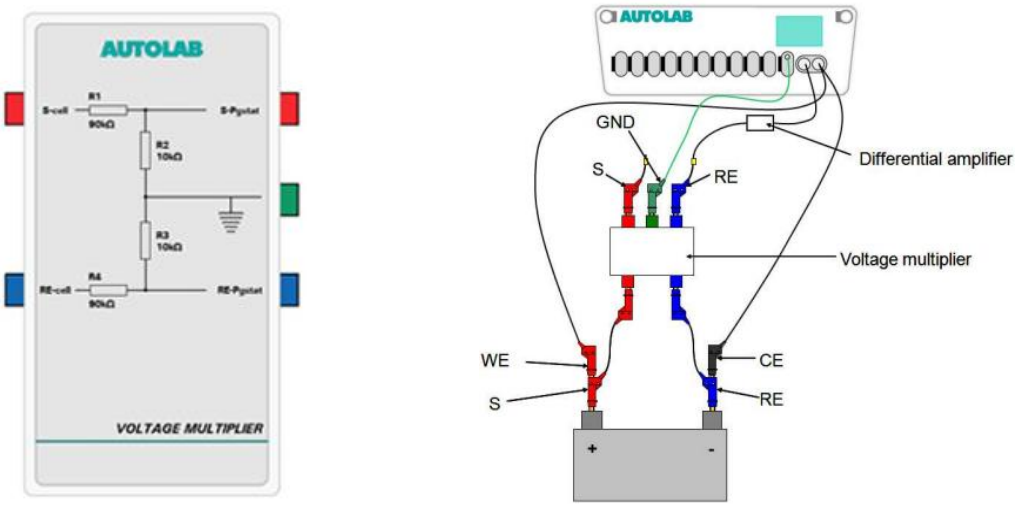

Fig 6.8 Schematic connection of the voltage multiplying feature of the Autolab PGSTAT

6.3 ONLINE CONDITION MONITORING SET-UP

The major components of the online condition monitoring set-up are the electronic load, digital acquisition and signal generation device and power electronics.

6.3.1 Electronic Load

The inexpensive TTI LD400 was selected as the laboratory-controlled DC electronic load. The TTI LD400 is capable of emulating real-life load like consumer electronics, off-grid systems and electric vehicle applications. The TTI LD400 has a current, voltage and power rating of 80A, 80V and 100W respectively. Most importantly, it is capable of operating at a frequency range of 0.1 Hz – 10 kHz – sufficient to cover the kinetic features of both batteries. The TTI LD400 has a current monitor output for waveform display and an analog remote control as shown in Fig 6.9. It can also attain up to a 600W power for up to a period of 1-minute [11].

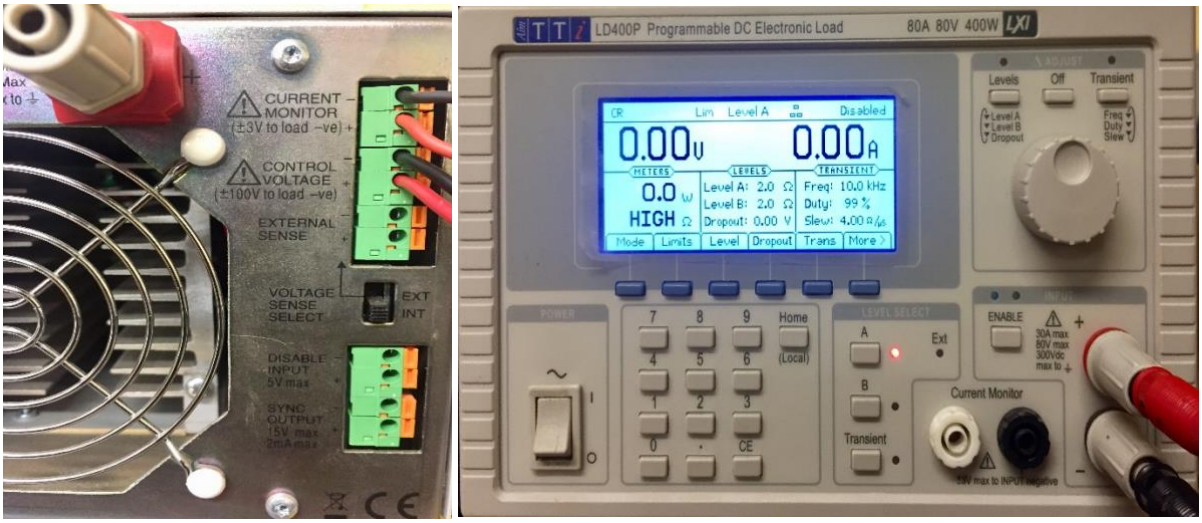

Fig 6.9 TTI LD400 current monitor and voltage control (a) and front view (b)

The TTI LD400 has four operating modes, namely: constant current (CC), constant resistance (CR), constant voltage (CV) and constant power (CP). The CC mode is utilized for constant discharge current of batteries. It also ensures rapid measurement of the V-I characteristics of the power source regulation. In EIS measurements, the CC mode was selected to emulate a load. The CR mode is used for emulating a controllable resistive load. The CR mode behaves like a resistive load by applying a current drain proportional to voltage. The CV mode is used for testing loads of constant current power supplies. Lastly, the CP mode is used to emulate a load whose consumptions of power is not dependent on the applied voltage.

Batteries get damaged when their output voltage frequently falls below their cut-off voltage. Besides, without a drop-out voltage protection, the battery voltage can drop completely to zero which can completely damage the battery. Fortunately, the TTI LD400 has an adjustable drop-out voltage that ensures that when the voltage of the lithium NCM or lead acid battery exceeds its cut-off voltage, the load current gradually drops to zero [11].

6.3.2 Data acquisition & Signal generation

The National Instrument (NI – USB) 6366 controlled by the LabVIEW software was used as the data acquisition device for the low-cost equipment setup. The NI-DAQ has eight analog input ($AI\ 0 - AI\ 7$) which is configured as either a floating source or grounded source combination. For the ground source (GS), the input is referenced to the ground, while for the floating source (FS), the input is in parallel with a $100G\Omega$ resistor and a 10pF capacitor. The NI USB 6366 has two analog output channels ($AO\ 0 - AO\ 1$), for generating different types of signal waveform. In this research, all the inputs were set to a ground source (GS). From the physical connection as shown in Fig 6.10, the BNC cables connected to $AI\ 0$ and $AI\ 1$ input channels are for measuring the current and voltage respectively. The BNC cable connected to the $AO\ 0$ output channel is for generating the EIS sine signal [12].

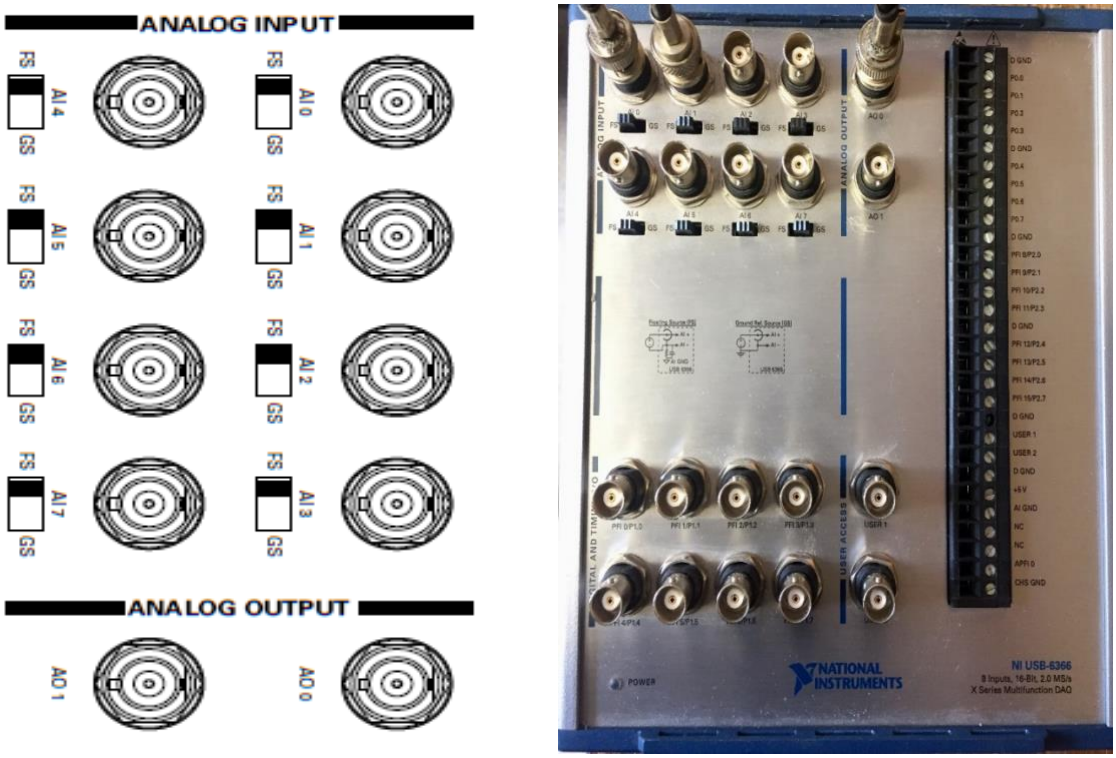

Fig 6.10 Schematic for the FS, GS (a) and physical connections of the BNC cable with the NI USB 6366 input and output channels (b)

The maximum sampling rate for the NI-DAQ is 2.00 MS/s – sufficient for ADC. The NI USB 6366 has a ±1V, ±2V, ±5V and ±10 V input range. Nonetheless, the maximum allowable voltage for all positive and negative inputs is ±11 V. The lithium NCM nominal voltage is within the ±5 V input range, but the lead acid battery has a nominal voltage of 12V, which exceeds the input range. A voltage divider circuit was therefore used to halve the lead acid battery voltage. For the current measurement, a multiplier of 20 was applied to the signal in LabVIEW to fall within the range required by the electronic load [12].

6.3.3 Power Electronics

The major power electronics component utilized in the online condition monitoring system are: analog comparator, low-pass analog filter and the DC-DC converter. Fig 6.11 shows the top view of the power electronics embedded within a protective container.

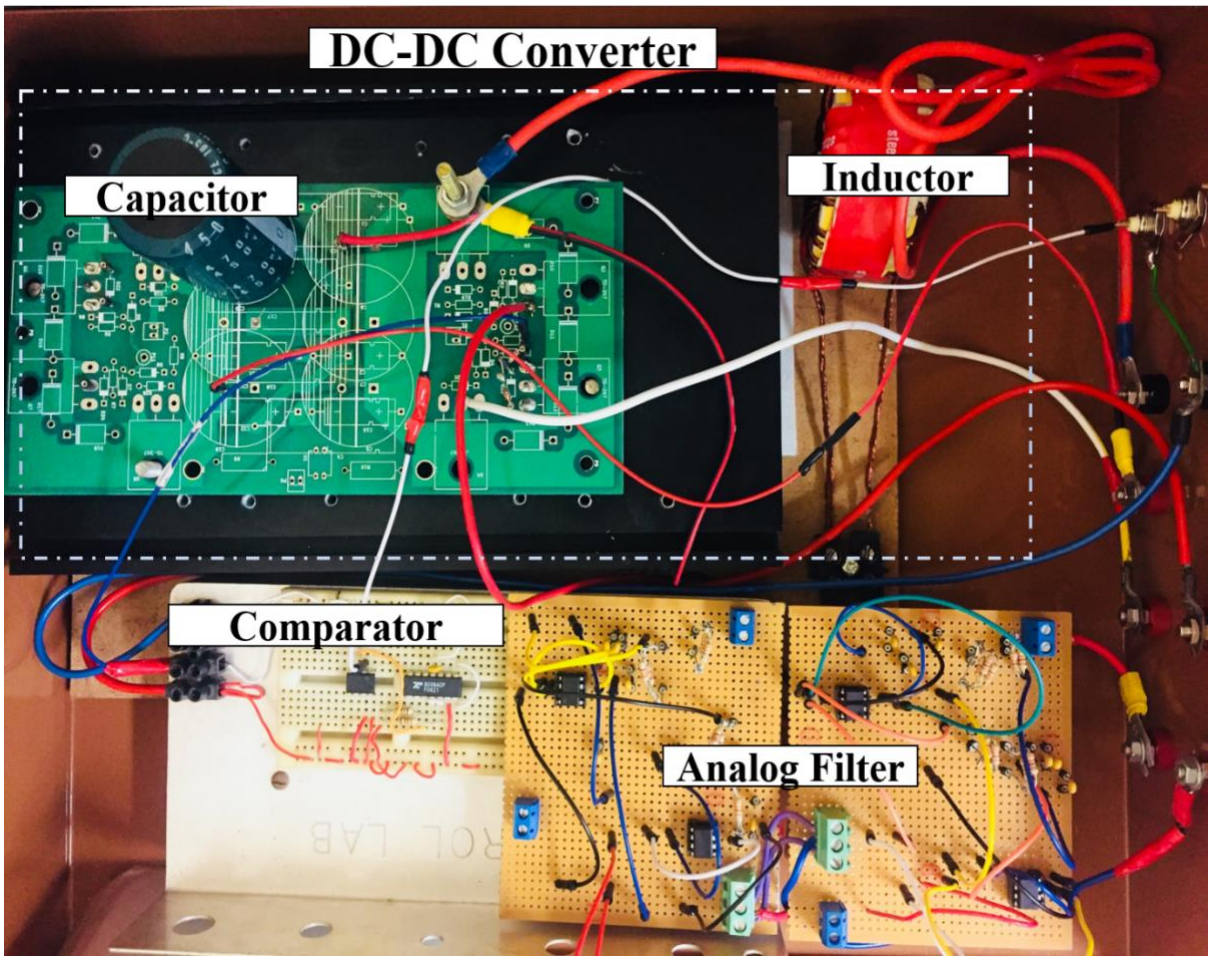

Fig 6.11 Power electronics set-up (Top View)

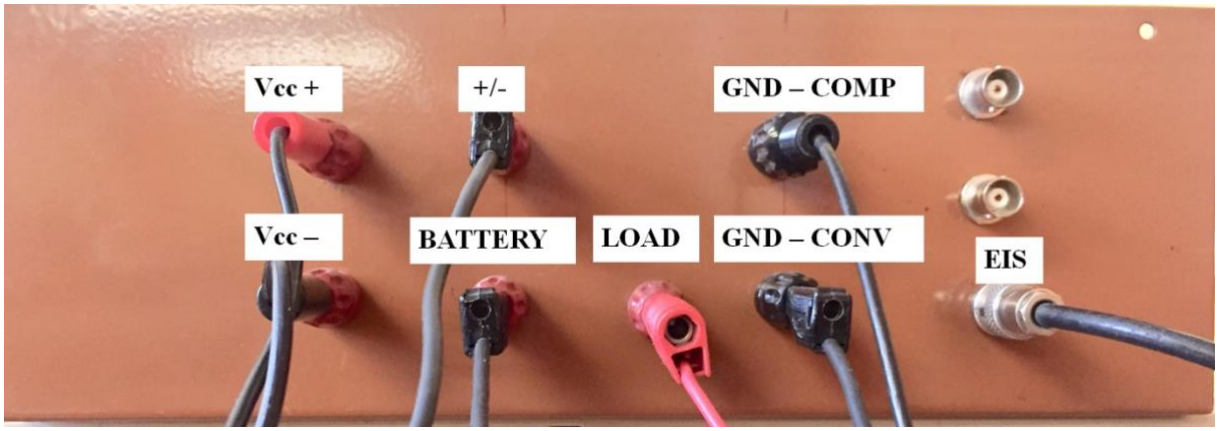

Fig 6.12 Front view of power electronics set-up showing input and output connections.

From the front view of the power electronics set-up in Fig 6.12, $V_{CC}{}^{+}$ and $V_{CC}{}^{-}$ are the DC supply voltage $(15V)$ to the 4th order low-pass Butterworth analog filter. BATTERY and GND – CONV is connected to the battery supply. LOAD and GND – CONV is connected to the electronic load. (+/-) – an $18V$ DC source and GND – COMP is connected to the comparator circuit to generate the saw-tooth waveform and is also the input of the analog comparator. The BNC (EIS) input port is connected to the function generator (NI-DAQ) that generates the sinusoidal impedance spectroscopy signal.

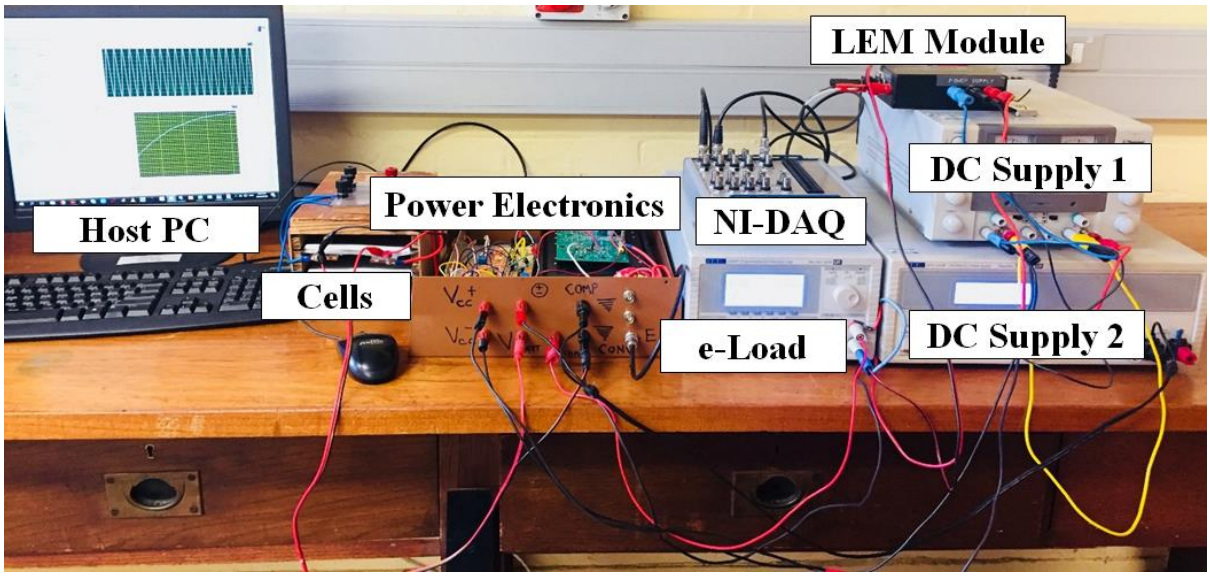

Fig 6.13 Overall set-up of online condition monitoring system

The overall set-up is shown in Fig 6.13. Starting from left to right, is the host PC that serves as the User Interface (UI) for the experimenter. This is followed by a stack of lithium NCM batteries, that is connected to the BATTERY port of the power electronics protective container. The first input BNC port of the NI-DAQ is connected to the battery for voltage

measurement, whereas, the second input BNC port is connected across the LEM current transducer output for current measurement. The electronic load is set in the Constant Resistance – CR mode. The output BNC port of the NI-DAQ is connected to the BNC (EIS) input port of the power electronics protective container. DC supply 1 generates the 15V DC for the filter circuit and DC supply 2 generates the 18V DC for the comparator circuit and analog filter.

6.4 SUMMARY

This Chapter presents the hardware and experimental setup utilized for condition monitoring of both the lead acid and lithium NCM batteries. In addition, it discusses in detail, the individual connections and the overall hardware set-up for both the commercial EIS equipment and online condition monitoring system.

6.5 REFERENCE

[1] G. EIG, "EIG-ePLB-C020 high energy product – Datasheet," Energy Innovation Group, 2012.

[2] FGB, “Sealed Lead Acid Maintenance Free Batteries – Datasheet,” The Puslar Company.

[3] Noshin Omar, Peter Van den Bossche, Thierry Coosemans & Joeri Van Mierlo, “Peukert Revisited—Critical Appraisal and Need for Modification for Lithium-Ion Batteries,” Energies 2013, 6, 5625-5641; doi: 10.3390/en6115625.

[4] Edmund Martin Mills and Sangtae Kim, “Determination of Peukert’s Constant Using Impedance Spectroscopy: Application to Supercapacitors,” The Journal of Physical Chemistry Letter 2016, 7, 5101−510.

[5] Mikäel Cugnet, Matthieu Dubarry, Bor Yann Liaw, “Peukert’s Law of a Lead-Acid Battery Simulated by a Mathematical Model,” ECS Transactions, 25 (35) 223-233 (2010).

[6] Metrohm Autolab “NOVA Autolab User Manual.”

[7] Autolab Application Note EC08, “Basic overview of the working principle of a potentiostat/galvanostat (PGSTAT)” – Electrochemical cell setup.

[8] Gamry Instruments, “Introduction - Two, Three and Four Electrode Experiments.”

[9] Autolab Application Note EIS02, “Electrochemical Impedance Spectroscopy (EIS) Part 2 – Experimental Setup, “Metrohm Autolab B.V

[10] Autolab Application Note BAT01, “High Voltage Measurements: Characterization of NiMH Batteries with Autolab PGSTAT302N in Combination with Voltage Multiplier,” Metrohm Autolab B.V

[11] TTI, " LD400 & LD400P Electronic DC loads | 80 amps, 80 volts and 400 watts – Datasheet," Thurlby Thandar Instruments Ltd.

[12] National Instruments, "NI 6366 X series data acquisition 2 MS/s/ch, 8 AI, 24 DIO, 2 AO," National Instruments.

7. RESULTS AND DISCUSSIONS

7.1 OPTIMUM PERTURBATION AMPLITUDE FOR EIS MEASUREMENTS

The perturbation amplitude is an important factor that relates to the linearity and accuracy of EIS measurements. A high perturbation amplitude maximizes signal to noise ratio (SNR) but results in a deviation of the linearity conditions of Kramers-Kronig [1]. Fig 7.1 shows the effect of the perturbation amplitude on the impedance spectrum accuracy. In Fig 7.1, the influence of variation in perturbation amplitude can be observed in the diffusion region of the impedance spectrum. This implies that if the optimal perturbation amplitude is unknown, the experimenter will be unable to determine the correct impedance plot. Due to the sensitivity of the condition monitoring system to the effect of nonlinearities, an investigation is therefore carried out to determine the optimum perturbation amplitude on both the lead acid and lithium NCM batteries.

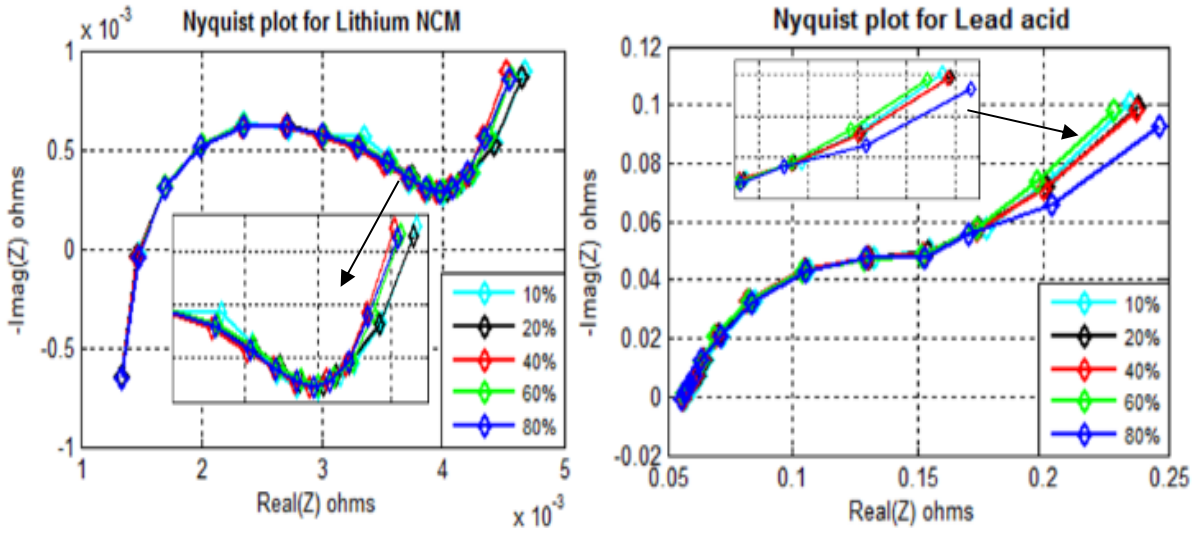

Fig 7.1 EIS plot for lithium NCM & lead acid battery at different perturbation amplitude (% of DC current)

As discussed in Chapter 3.1, analysis of the Total Harmonic Distortion (THD) of the frequency spectrum of the response signal will provide us with information on the optimal perturbation amplitude for EIS measurement. Hence, the THD of both batteries plotted against different perturbation amplitudes, as in Fig 7.2, depicts the perturbation amplitude with the lowest THD. It is observed that for the lithium NCM battery, the optimal perturbation amplitude lies at a low and high point, whereas, for the lead acid battery the optimal amplitude perturbation lies at a low point. In the lead acid battery, the THD value increases proportionally

with the perturbation amplitude. Although a high perturbation amplitude constituted a relatively low THD as the lithium NCM battery, this value should be refrained from. This is because a high perturbation amplitude will result in an evolution of the battery over the EIS measurement period. Therefore, for the lithium-ion NCM battery, 20% of the DC current is the optimal perturbation amplitude and for the lead acid battery, 15% of the DC current is the optimal amplitude perturbation. These values were consequently used for all the EIS tests in this study.

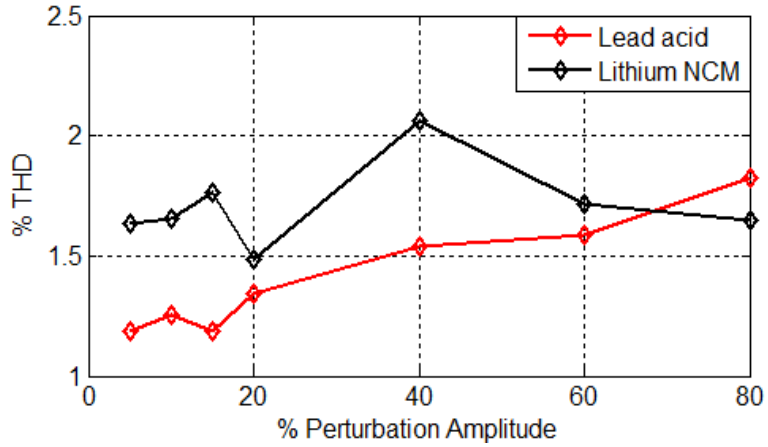

Fig 7.2 THD at different perturbation amplitude for lead acid and lithium NCM battery.

7.2 CHARACTERIZATION OF BATTERIES

State estimation information obtained from characterization of batteries is important for condition monitoring in a Battery Management System (BMS). Very little work has been done on the direct comparison of the impedance profile for the lithium NCM and lead acid battery using EIS. Moreover, it is important to compare these two battery technologies, to examine the complexities in identifying the trends associated with their impedance plots and subsequent determination of their equivalent circuit parameters for online condition monitoring purposes. This section therefore compares the impedance profile of both batteries from their EIS results, whereby variations in the results are linked back to the equivalent electrical circuit model.

7.2.1 EIS Results for Lithium NCM Battery

In [2], the lithium-ion battery's Nyquist plot is depicted as two time-constants or semi-circles (a small and large) representing the SEI/film formation at the electrode and charge transfer process respectively. However, the kinetic reaction for the SEI/film formation at the electrode and charge transfer process for the lithium-ion (NCM) utilized in this research overlapped each other resulting in an indistinguishable single time constant (semi-circle). Therefore, an equivalent circuit with a single time constant is considered in this work.

i. Effect of State of Charge

It can be observed from Fig 7.3 (a), that the value of the real impedance increases with SoC from (20 – 60) % and that the EIS plots are almost indistinguishable, especially for a high SoC. From Fig 7.3 (b), it can be observed that the ohmic resistance, charge transfer resistance, double layer capacitance and Warburg impedance are not totally a function of SoC from (20 – 100) % SoC. The charge transfer resistance that inhibits lithium-ion intercalation and de-intercalation process at the electrodes decrease with an increase in SoC from (20 – 80) %. This was also observed with other lithium-ion chemistries in [2], [3], [4]. Hence it can be concluded that although the Lithium NCM battery doesn't totally comply with Nernst and Butler-Volmer equations that predict SoC and reaction rate, EIS measurement is still capable of reasonably estimating its SoC.

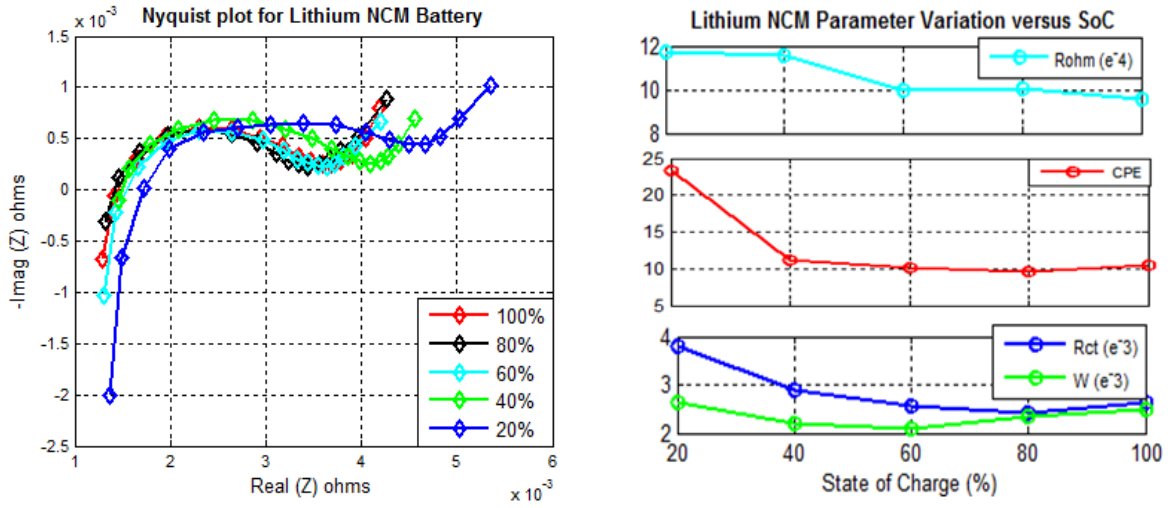

Fig 7.3 EIS plots for lithium NCM at varying state of charge (a) and parameter variation (b)

ii. Effect of Temperature

Fig 7.4 (a) shows the EIS plots for variations in temperature. In Fig 7.4 (b), as the temperature reduces, the semi-circle gets larger and the intersection with the real axis increases. This was also observed in [5]. From the extracted parameters in Fig 7.4 (b), as temperature increases, the ohmic resistance, charge transfer resistance and Warburg impedance decreases. The reduction in ohmic resistance with temperature increase is due to a decrease in internal resistance resulting from a decrease in voltage drop. The decrease in charge transfer resistance with an increase in temperature implies that the lithium-ion intercalation and de-intercalation process at the electrodes speeds up with an increase in temperature. Similar results were also found for a lithium-ion chemistry with two-time constants in [3]. In [2], a change in the shape of the impedance spectrum with varying

temperature was observed, but this was not the case for the lithium chemistry utilized in this research.

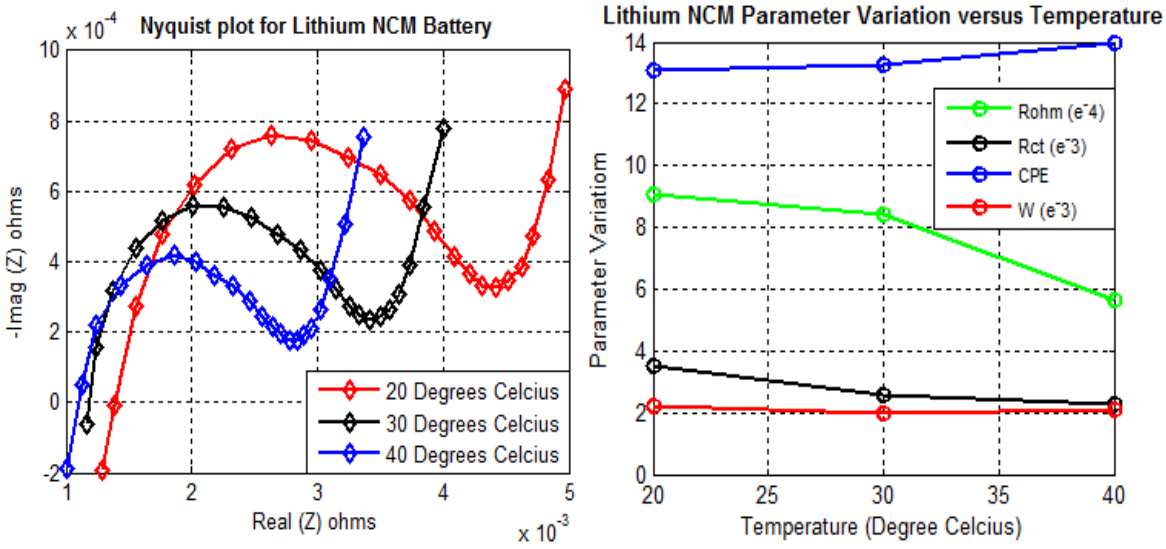

Fig 7.4 EIS plots for lithium NCM at varying temperature (a) and parameter variation (b)

iii. Effect of DC Current

In Fig 7.5 (a), the plots look identical. However, when the results are zoomed-in, shrinking of the semi-circle is observed as the DC current is increased. This is because an increase in DC current, ultimately results in a slight increase in temperature. In [6], the shrink was more distinct because the cell utilized for the test had a low amp-hour rating compared to the DC current that was applied. In addition, a general decrease of impedance parameters with increasing DC current was observed from the extracted parameters in Fig 7.5 (b).

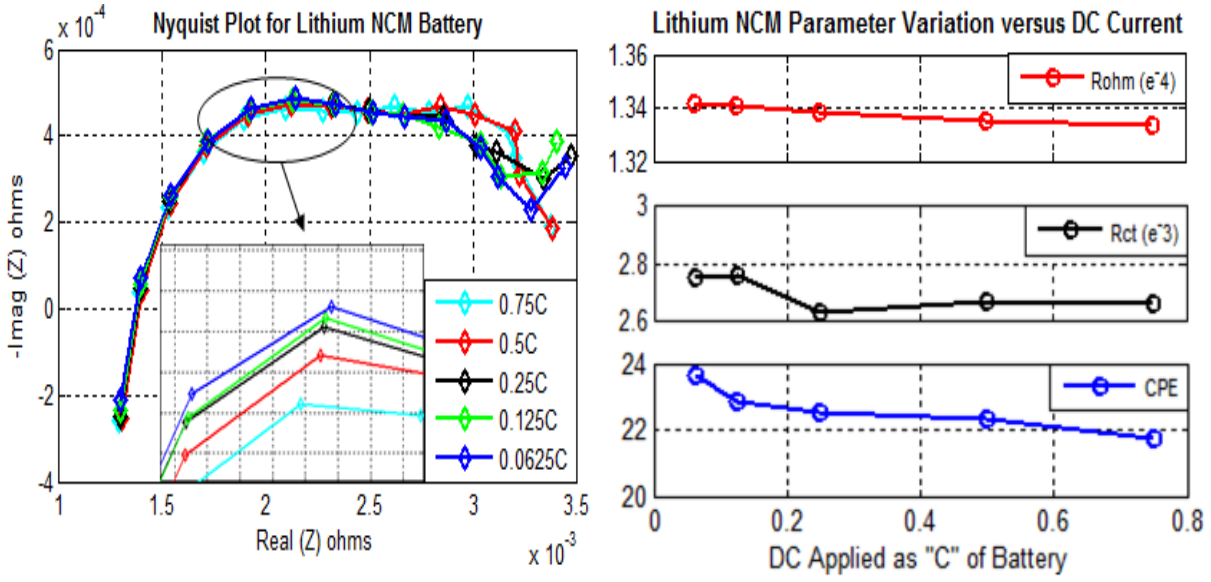

Fig 7.5 EIS plots for lithium NCM at varying DC current (a) and parameter variation (b)

7.2.2 EIS Results for Lead Acid Battery

i. Effect of State of Charge

Fig. 7.6 (a) shows the EIS plots for lead acid at varying SoC. It can be concluded from Fig 7.6 (a) that the intersection with the real axis of the plot (ohmic series resistance) of the lead acid battery moves rightwards as the battery is discharged. It can also be observed from the extracted parameters in Fig 7.6 (b), that the ohmic series resistance (internal resistance), is the only equivalent circuit parameter that varies linearly with SoC. This was also observed in [7] – [8], which is because the conducting ions in the electrolyte of a lead acid battery are the reactants that take part as an active specie in the electrode processes. Thus, a decrease in open-circuit voltage (OCV) during discharge results in an increase in ohmic resistance due to depletion of the concentration of the electrolyte. Nevertheless, relating OCV directly to SoC will be inaccurate because of acid stratification effects and diffusion time constants that also occur.

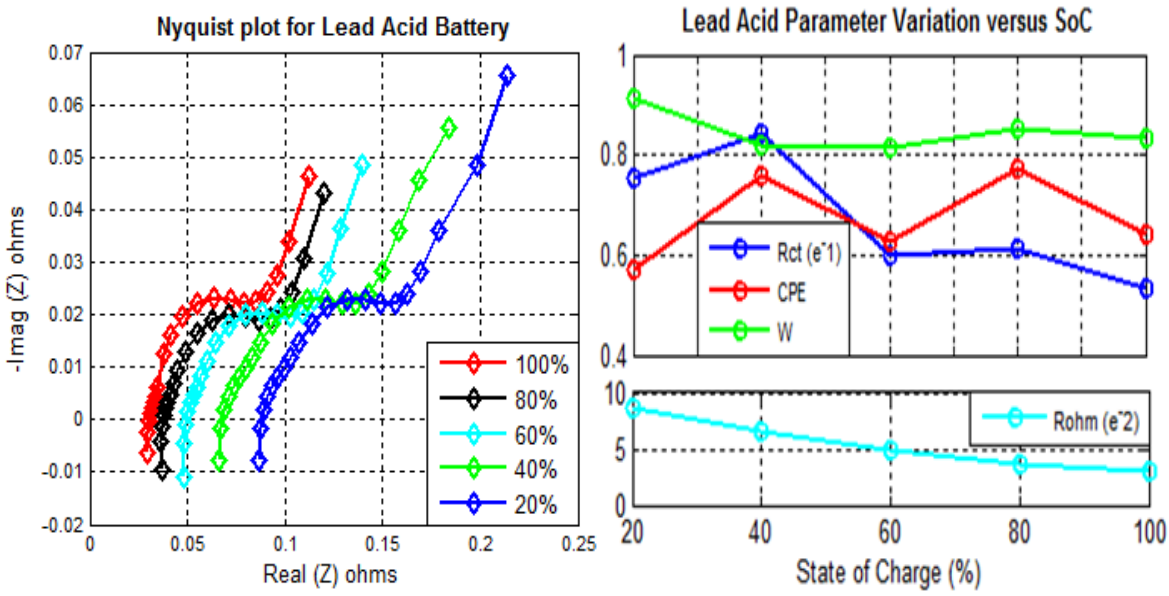

Fig 7.6 EIS plots for lead acid at varying state of charge (a) and parameter variation (b)

ii. Effect of Temperature

Fig 7.7 (a) shows the EIS plots for lead acid at varying temperature. In Fig 7.7 (a), the plots look similar, but for the semi-circle radius, which tends to increase for a reduction in temperature. It is also observed from the extracted parameters in Fig 7.7 (b), that a decrease in temperature results in an increase in the ohmic resistance, charge transfer resistance and double layer capacitance. This is supported by the Arrhenius and Butler-Volmer equation. This means that higher temperatures increase the rate of reaction and the active surface area of the PbO_2 layer.

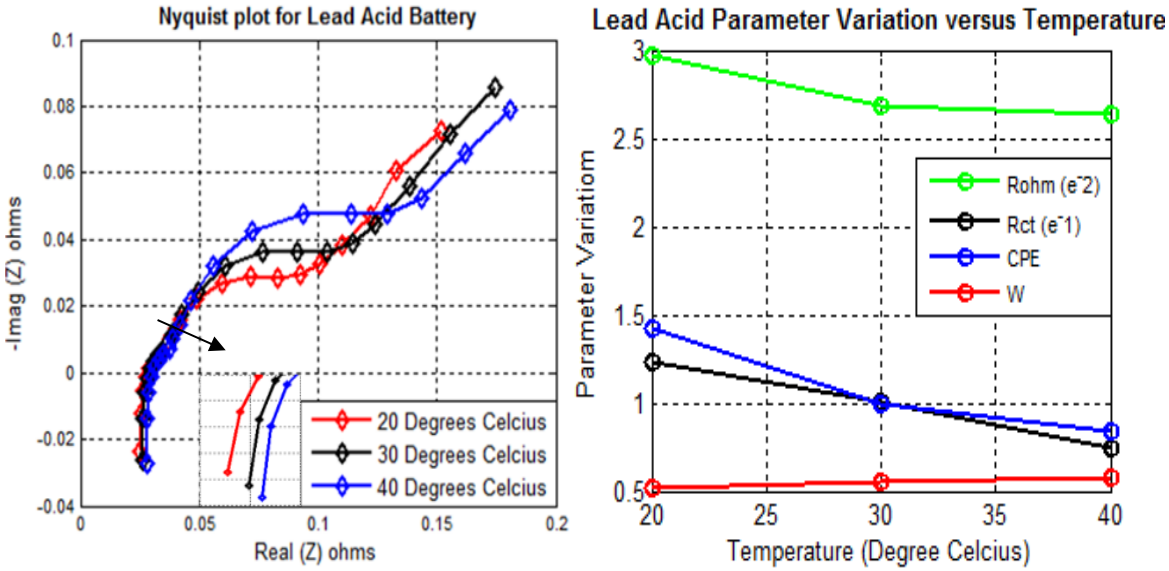

Fig 7.7 EIS plots for lead acid at varying temperature (a) and parameter variation (b)

iii. Effect of DC Current

Fig 7.8 (a) shows the EIS plots for lead acid at varying DC current. It is apparent that the pattern of the EIS plot varies with an increase in DC current. This trend was also observed for the same chemistry and operational condition in [5]. It is also observed from Fig 7.8 (b), that as the DC current increases, the real and imaginary impedance reduces. The shape of the plot also tends to depict an increase in diffusion along the axis of the pores. Lastly, from the extracted parameters in Fig 7.8 (b), an increase in DC current results in a decrease of all equivalent circuit parameters.

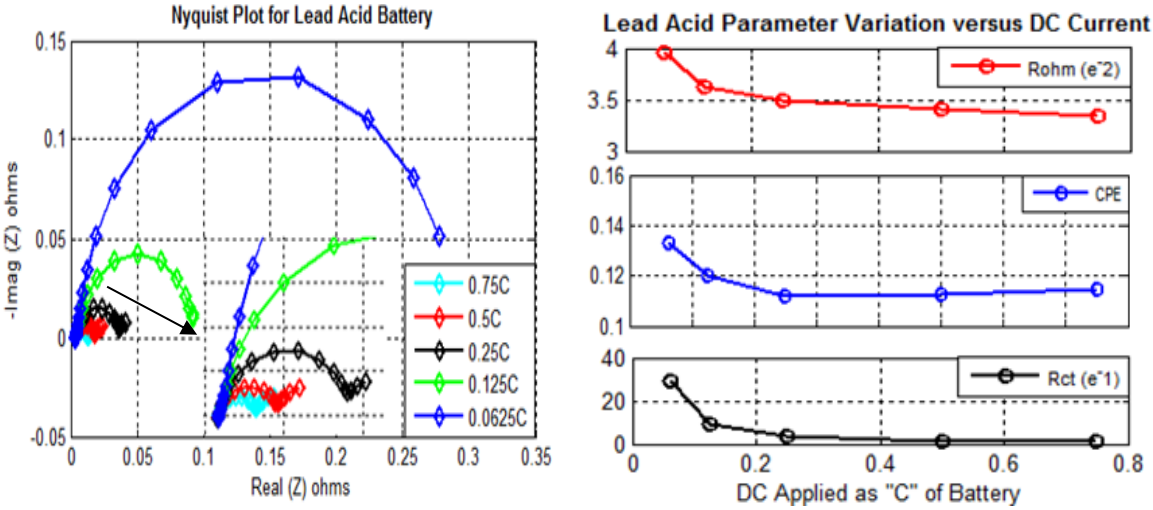

Fig 7.8 EIS plots for lead acid at varying DC current (a) and parameter variation (b)

7.2.3 Comparison between EIS Results of lithium NCM and lead acid

The results from the characterization of the lithium NCM and lead acid battery using EIS has revealed the typical impedance profiles for both batteries. It has also provided information on impedance parameter effect on certain operational conditions. Firstly, from the Nyquist plot of both batteries, it is apparent that the impedance magnitude of the lead acid battery is far greater than that of the lithium NCM. Also observed is the fact that the EIS technique is more sufficient for characterizing the lead acid batteries compared to lithium NCM batteries. This can be correlated to the higher impedance of the lead acid compared to the lithium.

From the EIS results of the Lithium NCM battery, it is concluded that EIS is unable to determine the SoC when the battery is almost fully charged. From 80% SoC to when the battery charge is low (20%), the radius of the semi-circle can be utilized for state estimation. For the temperature variation which also relates to the DC current, the ohmic resistance and charge transfer resistance relates to the temperature. Hence, the ohmic resistance in the high frequency region is sufficient to characterize the lithium NCM battery. However, given that the effect of a varying DC current is more apparent at the semi-circle, the varying DC current tests must be conducted up to the radius of the semi-circle.

For a lead acid battery, it was concluded that the ohmic resistance relates to the SoC due to its participation as a reactant in the electro-kinetic processes. This implies that the SoC can be deduced from the high frequency ohmic resistance. Unlike the Lithium NCM battery that has a unique ohmic resistance due to temperature variation, in the lead acid battery, the temperature will be accurately estimated from the charge transfer-double layer semi-circle. This same procedure can be followed for the estimation of the DC current variation.

7.3 ONLINE CONDITION MONITORING OF BATTERIES

In this section, the results for online and offline tests for both the lithium NCM and lead acid batteries are presented. As earlier discussed, an offline test implies that EIS tests are carried out without connection to a power converter; whereas, online test implies that EIS tests are carried out with a power converter used to interface the battery and the load.

7.3.1 Broadband IS (offline)

Fig 7.9 shows the offline broadband impedance spectroscopy results, benchmarked against the FRA for both the lithium NCM and lead acid battery. From the results, it can be concluded that rapid excitation signals: multisine, chirp and PRBS can reduce EIS measurement time.

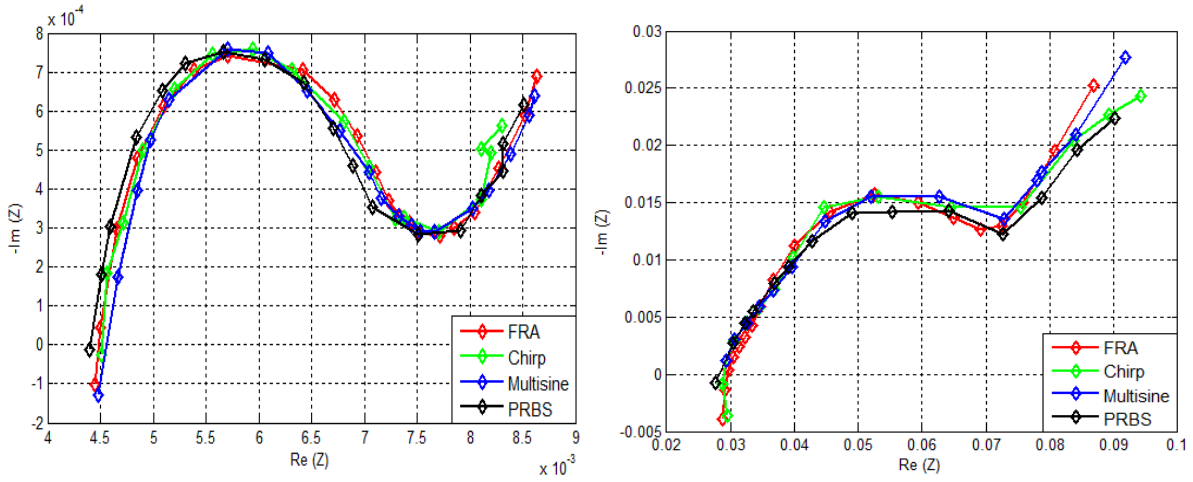

Fig 7.9 EIS plots for different broadband signals – offline (a) lithium NCM (b) lead acid

7.2.4 Broadband IS (online)

Fig 7.10 presents the online broadband impedance spectroscopy results, benchmarked against the FRA for both the lithium NCM and lead acid battery. From the results, it can be concluded that broadband impedance spectroscopy measurements can be carried out while the system is online.

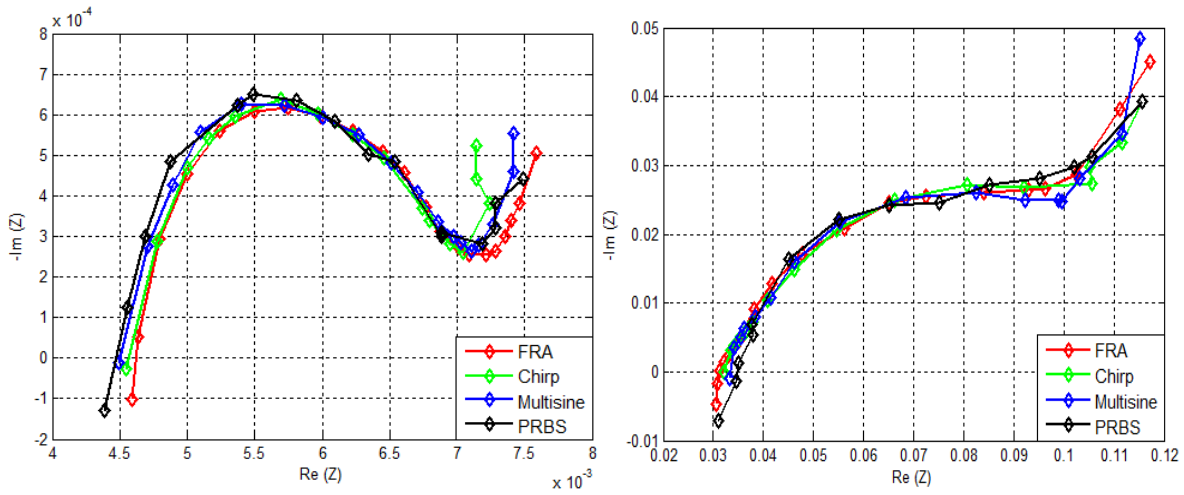

Fig 7.10 EIS plots for different broadband signals – online (a) lithium NCM (b) lead acid

7.2.5 Deductions from online and offline BIS

Because of the increase in the EIS measurement speed, the impedance spectrum accuracy of broadband signals appears to be slightly compromised. Thus, it is of utmost importance to study the time-frequency characteristics (already established in Chapter 4) of these signals, as well as their impedance spectrum accuracy to determine the most suitable for state estimation of both batteries while operating offline and online. The extracted parameters of FRA used to benchmark both online and offline tests are presented in Table 7.1

Table 7.1 Parameter extracted from FRA measurement for both offline and online investigation.

Lead acid (FRA)				
	R1	**R2**	**CPE**	**W**
Offline test	0.02945	0.0304	0.6404	0.8321
Online test	0.030167	0.0413	0.7742	0.8544
Lithium NCM (FRA)				
	R1	**R2**	**CPE**	**W**
Offline test	0.0044055	0.003005	13.08	0.00222
Online test	0.00465055	0.002812	13.28	0.002134

The deviation of all the broadband signals (offline and online) investigated in this study against the FRA extracted impedance parameters are presented in Table 7.2. For the lithium NCM (offline and online) extracted parameters, it can be observed that the chirp signals have the least deviation from the FRA at the ohmic resistance (R1), charge transfer resistance (R2) and double layer capacitance (CPE). However, at the diffusion region (W), the chirp signal performs poorly compared to the multisine signal. The broadband signal impedance spectrum accuracy results for the lead acid is like the lithium NCM, except that it has poorer accuracy. This can be attributed to the difference in electrochemistry of both batteries (already discussed in Chapter 4). In addition, from the extracted parameters in Table 7.2, it is observed that the quality of the offline impedance spectrum is higher than that of the online. Although a low-pass filter was used to minimize the effect of the buck-boost converter switching frequency, it was unable to keep the SNR as high as the offline system.

Table 7.2 EIS plots for varying DC current (a) and parameter variation (b)

Lead acid (Offline)				
	ΔR1	**ΔR2**	**ΔCPE**	**ΔW**
Chirp	0.0132	0.0157	0.113	0.0233
Multisine	0.0148	0.0189	0.119	0.00987
PRBS	0.0267	0.0201	0.203	0.0259
Lithium NCM (Offline)				
	ΔR1	**ΔR2**	**ΔCPE**	**ΔW**
Chirp	0.000081	0.0000771	0.23	0.000143
Multisine	0.0001221	0.0000971	0.44	0.000096
PRBS	0.0001319	0.0001431	0.93	0.000236
Lead acid (Online)				
	ΔR1	**ΔR2**	**ΔCPE**	**ΔW**
Chirp	0.0158	0.0163	0.125	0.0269
Multisine	0.0182	0.0195	0.137	0.00109

PRBS	0.0207	0.0214	0.225	0.0273
Lithium NCM (Online)				
	ΔR1	**ΔR2**	**ΔCPE**	**ΔW**
Chirp	0.000092	0.0000854	0.57	0.000154
Multisine	0.0001392	0.0001221	0.78	0.000113
PRBS	0.0001439	0.0001319	1.03	0.000348

Reduction of the CF ensures that the system is measured in a linear region, thus avoiding non-linear system behaviour. Amongst the three (3) broadband signals, the PRBS has the lowest CF – 1, followed by the chirp signal – 1.4 and optimized multisine – 2.8. In theory, a broadband signal's impedance spectrum accuracy is directly proportional to the CF and a unity CF will present the most accurate impedance spectrum. However, this is not always the case, because for instance, a PRBS signal only possess a unitary CF when the full-band signal spectrum is utilized. In this study, only a frequency band of interest was selected for the PRBS perturbation signal, and this resulted in an average CF value of 1.56 over the frequency bands (low and high) of both batteries. In all the tests, the PRBS performed the worst. Another reason for the poor performance of the PRBS was that the low frequency components, just like a square wave [9], generated odd harmonics (multiple of the low frequency) that summed up with higher frequencies impedance information. This resulted in a low SNR at high frequencies for the PRBS, thus reducing the accuracy of the impedance spectrum of the PRBS.

The multisine had the worst CF but has a more similar Nyquist plot shape as the FRA over the impedance spectrum. This is because the excitation energy for the multisine is distributed evenly across the user-defined set of frequencies. The chirp signal can be generated in an infinitesimal time – as low as, one-tenth the time of the multisine and PRBS. Nonetheless, the chirp signal duration must be long enough to maximize the signal energy and thus SNR. In this study, it took the FRA 3.4 minutes; multisine and PRBS 10 seconds; and chirp signal 5 seconds to complete EIS measurement for the lead acid battery. On the other hand, it took the FRA 6.8 minutes; multisine and PRBS 50 seconds; and chirp signal 25 seconds to complete EIS measurement for the lithium NCM battery. The chirp signal has a flat spectrum which results in a good SNR over the whole excited frequency range. However, most of its excitation energy is concentrated at the high frequency. This implies that the high frequency decade will benefit the most from the high SNR of the chirp signal. This was apparent from the results of both batteries, as the chirp signal performed best at the mid – high frequency region (i.e. R1, R2 and CPE). From investigations in Chapter 7.2, these parameters are sufficient for state estimation of both batteries.

7.4 SUMMARY

This section showed the results obtained from this research study. In this regard, the optimum perturbation amplitude for EIS measurement on both batteries were ascertained. Secondly, the key impedance parameters required for state estimation of both batteries were determined (see Table 7.3). Lastly, the EIS results from the different broadband signal techniques were compared against the commercial EIS measurement equipment – Frequency Response Analyzer (FRA). The findings are summarized in Table 7.4; where it was observed that the chirp signal performs as well as the Multisine, albeit taking a shorter time to complete EIS measurement.

Table 7.3 Key impedance parameters required for state estimation of the lithium NCM and lead acid batteries

State/Battery	Lithium NCM	Lead Acid
State of Charge	Charge transfer resistance - Double layer capacitance	Ohmic resistance
Temperature	Ohmic resistance	Charge transfer resistance
DC Current	Ohmic resistance and Charge transfer resistance	Charge transfer resistance

Table 7.4 Broadband signals compared against different measurement metrics for both the lithium NCM and lead acid batteries

Batteries	Metrics	FRA	Multisine	Chirp
Lithium NCM	*Measurement time*	Long	Short	Shorter
	EIS accuracy	Very accurate	Relatively accurate	Relatively accurate
	Online application	Impracticable	Yes	Yes
Lead Acid	*Measurement time*	Long	Short	Shorter
	EIS accuracy	Very accurate	Relatively accurate	Relatively accurate
	Online application	Impracticable	Yes	Yes

7.5 REFERENCES

[1] C. de Beer, P. S. Barendse and P. Pillay, "Fuel Cell Condition Monitoring Using Optimized Broadband Impedance Spectroscopy," IEEE Trans. Ind. Electron., vol. 62, pp. 5306-5316, 2015.

[2] D.I Stroe, et.al. "Diagnosis of Lithium-Ion Batteries State-of-Health based on Electrochemical Impedance Spectroscopy Technique," Energy Conversion Congress and Exposition (ECCE) pp. 4576-4582, 2014.

[3] Uwe Westerhoff, Kerstin Kurbach, Frank Lienesch and Michael Kurrat, “Analysis of Lithium-Ion Battery Models Based on Electrochemical Impedance Spectroscopy,” Energy Technol. vol. 4, pp. 1620 – 1630, 2016.
[4] Li Wang, et al. “Electrochemical Impedance Spectroscopy (EIS) Study of LiNi1/3Co1/3Mn1/3O2 for Li-ion Batteries,” Int. J. Electrochem. Sci., 7 (2012) 345 – 353
[5] L. W. Juang et al, "The impact of DC bias current on the modelling of lithium iron phosphate and lead-acid batteries observed using electrochemical impedance spectroscopy," in 2014 IEEE Energy Conversion Congress and Exposition (ECCE), 2014, pp. 2575-2581.
[6] D. Andre et al, "Characterization of high-power lithium-ion batteries by electrochemical impedance spectroscopy. II: Modelling," J. Power Sources, vol. 196, pp. 5349-5356, 2011.
[7] Li Wang, et al. “Electrochemical Impedance Spectroscopy (EIS) Study of LiNi1/3Co1/3Mn1/3O2 for Li-ion Batteries,” Int. J. Electrochem. Sci., 7 (2012) 345 – 353
[8] F. Huet, “A review of impedance measurements for determination of the state-of-charge or state-of-health of secondary batteries,” Journal of Power Sources 70 (1998).
[9] Ned Mohan et al.“Power Electronics – Converters, Applications and Design,” 2nd Ed. John Wiley & Sons, Inc. 1995.

8. CONCLUSION AND RECOMMENDATIONS

8.1 CONCLUSION

The major aim of this study was to explore the differences in the internal chemistries of the lithium-ion and lead acid batteries and to shorten the time associated with their condition monitoring. In this regard, the Electrochemical Impedance Spectroscopy (EIS) was utilized due to its robustness for electrochemical state estimation purposes. The limitations of the EIS is its sensitivity to the Kramers-Kronig relations; its uniqueness to different electrochemical systems; and its lengthy acquisition time, that makes it impracticable for online condition monitoring. In this research study, all these limitations are relatively eliminated.

To determine the appropriate methodology for EIS measurement, the optimum perturbation amplitude is investigated. From the investigations, it was observed that the optimum amplitude perturbation is the largest possible amplitude perturbation that can be applied to the battery for a high SNR without resulting in non-linearity of the system. More so, it was concluded that the widely used 10% perturbation amplitude is not the optimum perturbation amplitude for all battery chemistries; because this value varies from system to system. The investigations also revealed that the optimum perturbation amplitude for the lead acid and lithium NCM battery that was utilized in this test are 15% and 20% of the DC current respectively.

Secondly, the electrochemical processes in both the lead acid and lithium NCM battery using EIS measurements were critically analysed and from the results, the unique electrochemical dynamics and impedance characteristics was observed for both battery chemistries. It was also observed that the electrochemical/mathematical analysis of the battery can furnish us with information on how the impedance of the battery will vary at certain conditions. Most importantly, the result in the study provided useful information on the unique impedance profile of both batteries. It also showed to what extent certain operational conditions affect the impedance parameters of both batteries; which is important in shortening EIS measurement time. Another interesting deduction is the fact that the EIS technique was more sufficient for characterizing the lead acid batteries compared to lithium NCM batteries. This evidence can be correlated to the higher impedance margin of the lead acid battery in comparison with the lithium NCM battery.

Broadband excitation signals were applied to reduce EIS measurement time. More so, these broadband excitation signals were applied for state estimation, without disconnecting the battery from the system. It is however important to note that an increase in measurement speed results in a compromise of the impedance spectrum accuracy. Thus, before applying a broadband signal for online/offline test on an electrochemical system, it is pertinent to understand how the choice of the broadband signal can influence system instrumentation, to mitigate loss of impedance spectrum accuracy. It was observed that over the whole impedance spectrum, results from the multisine excitation share very close comparison to the FRA, compared to the results of the chirp signals. However, the chirp signal offers a shorter measurement duration – half the time required for multisine excitation. It is also important to note that the chirp signal, more accurately determines the most important impedance parameters sufficient for characterizing/state estimation of the battery.

Lastly, it is evident that, although EIS was more sufficient for impedance estimation of lead acid batteries compared to lithium-ion batteries; in the case of broadband signals, the lead acid battery performed worse. This deduction can be correlated to the fact that the lead acid battery is less chemically stable and is more sensitive to rapid pulses compared to the lithium NCM batteries. These instabilities posed by the lead acid battery was also substantiated in the controller design nuances of both batteries.

8.2 RECOMMENDATIONS

As an extension of the work covered in this study, future work could include a condition monitoring system capable of determining the breakdown stages of both batteries. This can be achieved with an accelerated ageing equipment. In addition, the viability of these broadband impedance techniques for state estimation could be implemented on emerging battery technologies like the redox flow and lithium-sulphur battery. Lastly, online condition monitoring of the batteries in a cascaded configuration – series-parallel combination as in electric vehicle applications could be explored.

9. APPENDIX

9.1 APPENDIX A – LABVIEW SIGNAL DESIGN

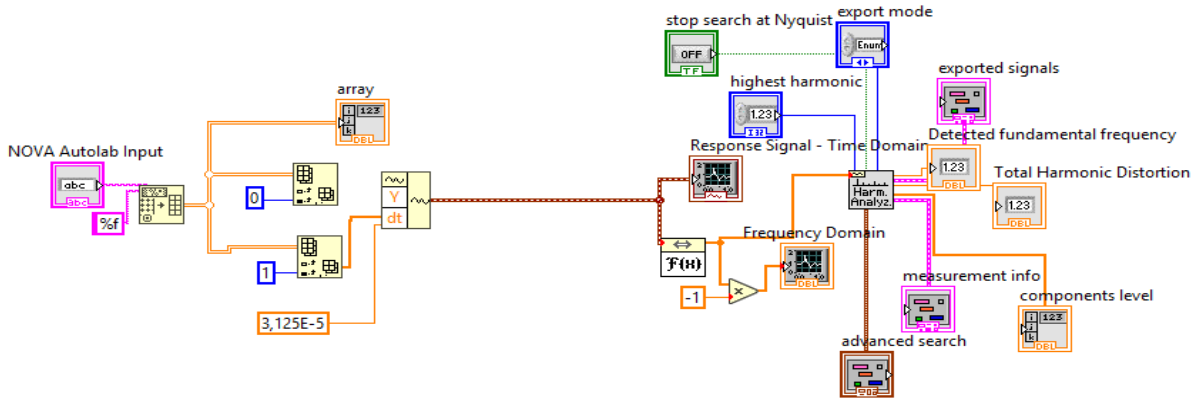

Fig 9.1 THD analysis LabVIEW code

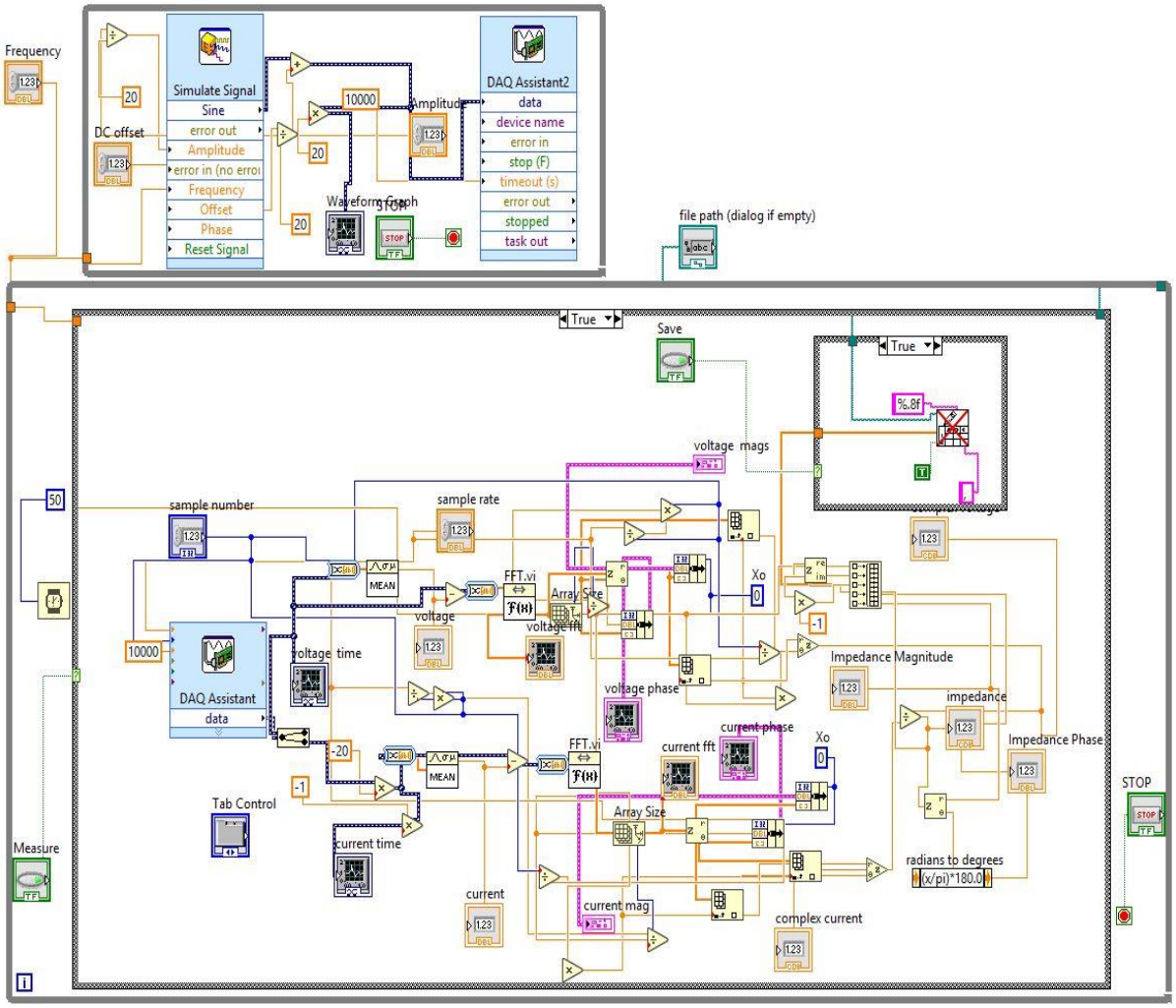

Fig 9.2 EIS signal generation and processing LabVIEW code

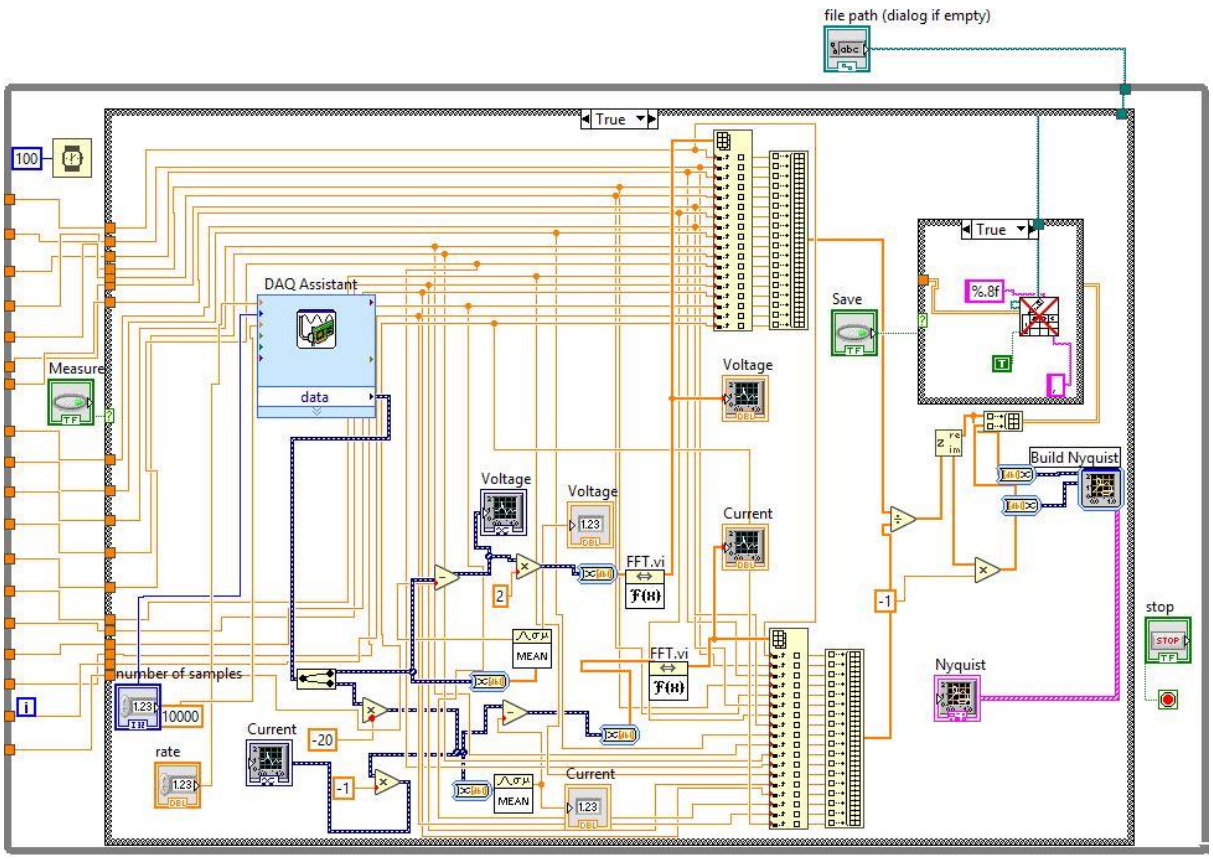

Fig 9.3 Broadband impedance spectroscopy processing LabVIEW code

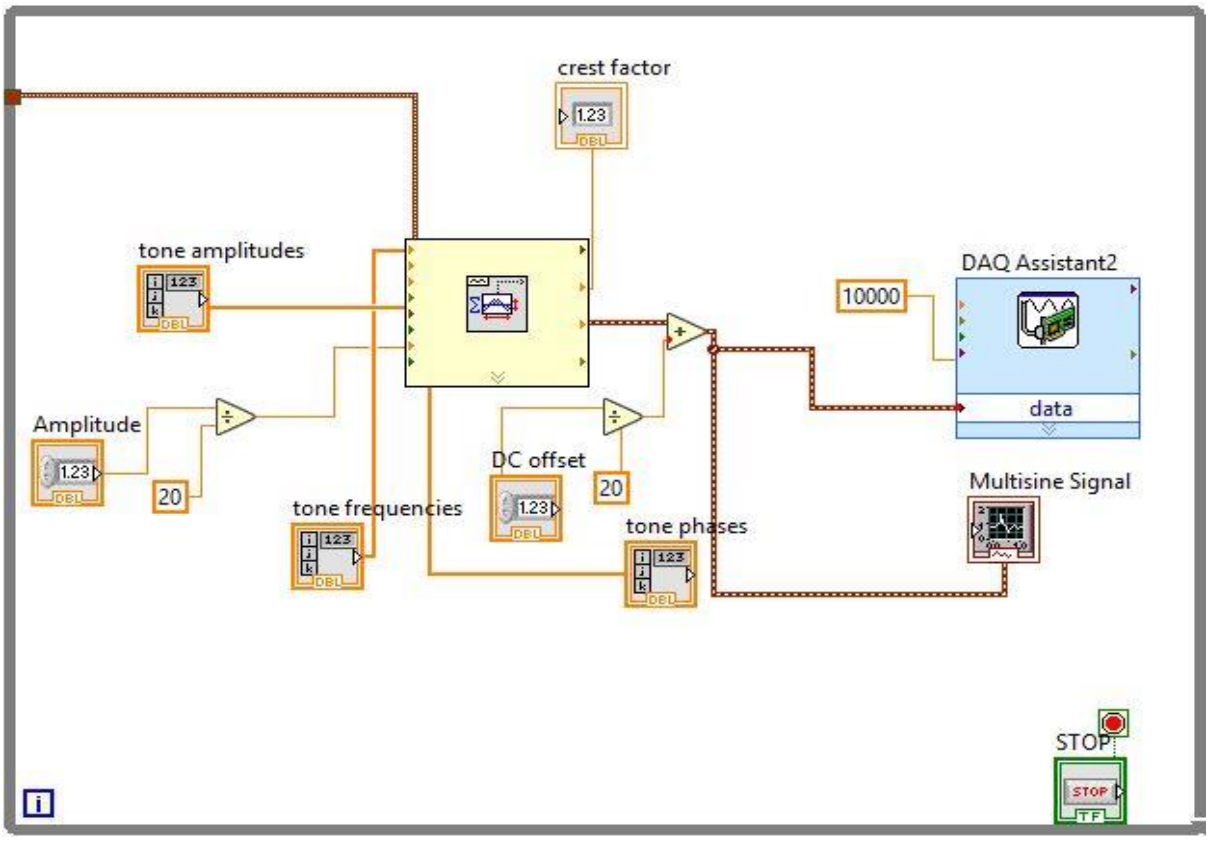

Fig 9.4 Multisine generation LabVIEW code

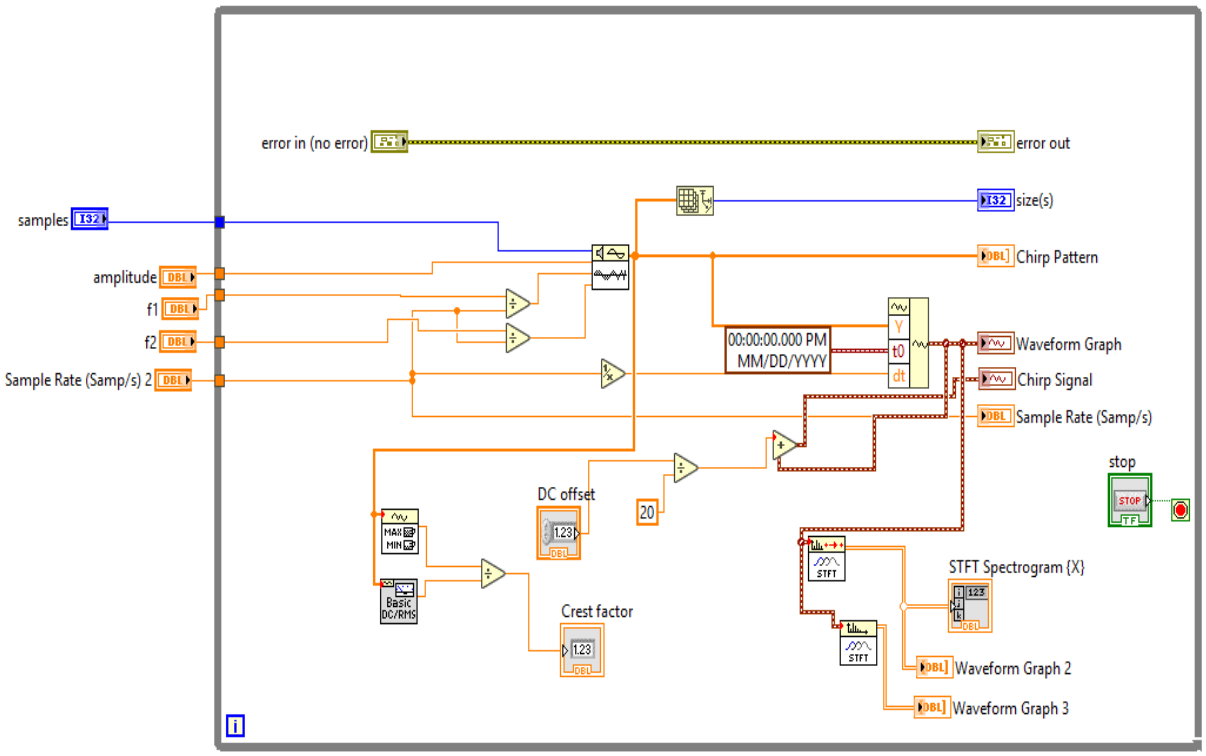

Fig 9.5 Chirp signal generation LabVIEW code

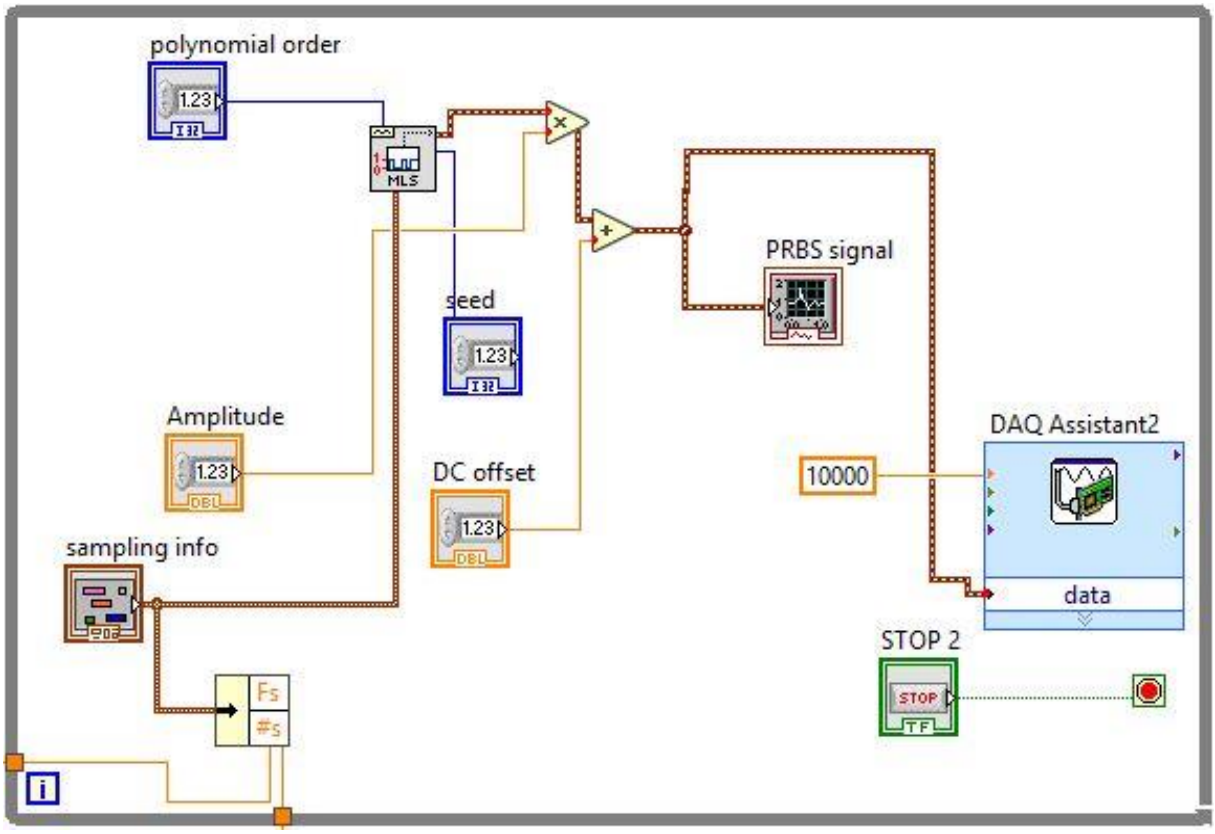

Fig 9.6 PRBS generation LabVIEW code

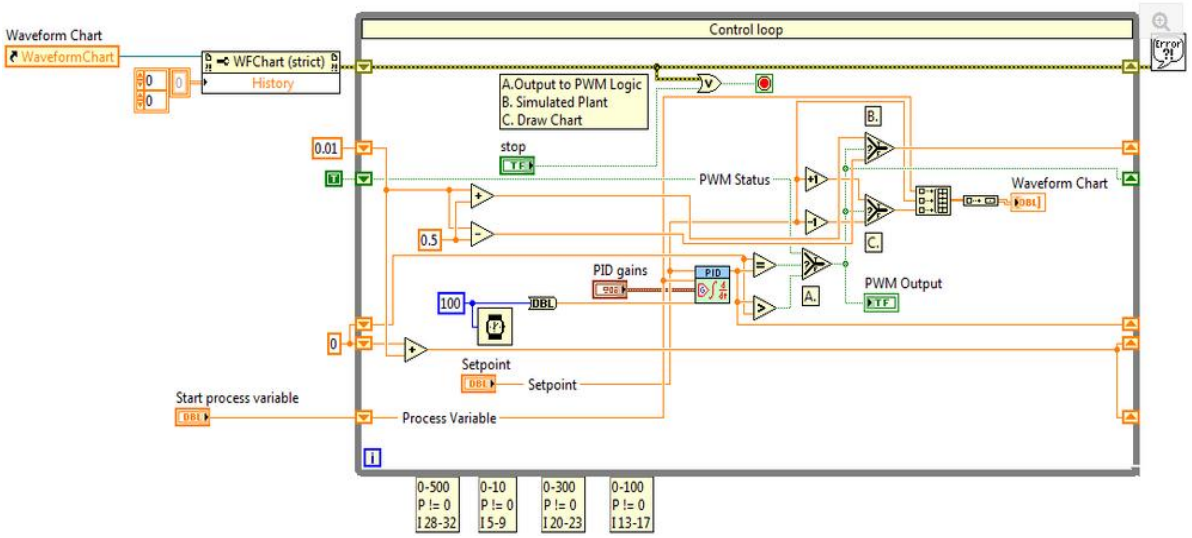

Fig 9.7 Closed-loop control of buck-boost converter on LabVIEW

9.2 APPENDIX B – MATLAB CODE AND SIMULATION

(a) Code for Nyquist plot curve-fitting to equivalent electric circuit

Adapted from MATLAB Zfit Function

```
% ZFIT is a function that FIT impedance data.
% Name: Olakunle Alao
% Student Number: ALXOLA001
% Class: Master's by Dissertation Candidate
% School: University of Cape Town
% MAIN function

function [pbest,zbest,fval,exitflag,output]=Zfit(varargin)
    switch nargin
        case 0 % not allowed
        error('PLEASE, supply at least a 3-columns wise data matrix:
[FREQ,RealZEXP,ImagZEXP]')
        % Zfit(data)
        case 1
        data=varargin{1};
        freq=data(:,1);
        plotz(freq,size(data)*nan,data,'z')
        return

        % Zfit(data,plotstring)
        case 2
        data=varargin{1};
        freq=data(:,1);
        plotstring=varargin{2};
        if
        plotz(freq,size(data)*nan,data,plotstring)
        return

        case 3 % not allowed
        error('PLEASE, if circuit simulation is wishing then supply at
least a parameter vector')
```

```
% [pbest,zbest]=Zfit(data,plotstring,circuitstring,circuitparameters)
        case 4
        data=varargin{1};
        freq=data(:,1);
        plotstring=varargin{2};
        circuitstring=varargin{3};
        pbest=varargin{4};

%
[pbest,zbest]=Zfit(data,plotstring,circuitstring,circuitparameters,indexes)
        case 5
        data=varargin{1};
        freq=data(:,1);
        plotstring=varargin{2};
        circuitstring=varargin{3};
        pbest=varargin{4};
        indexes=varargin{5};if
isempty(indexes),indexes=1:length(freq);end,freq=data(indexes,1);

% [pbest,zbest,fval,exitflag,output]=
% ... Zfit(data,plotstring,circuitstring,circuitparameters,indexes,'fitP'
or 'fitNP')
        case 6
        data=varargin{1};
        freq=data(:,1);
        plotstring=varargin{2};
        circuitstring=varargin{3};
        pbest=varargin{4};
        options=[];
        indexes=varargin{5};if
isempty(indexes),indexes=1:length(freq);end,freq=data(indexes,1);
        fitstring=varargin{6};
        LB=-inf*ones(length(pbest),1);UB=inf*ones(length(pbest),1);
        zrzi=[data(indexes,2),data(indexes,3)];

[pbest,fval,exitflag,output]=curfit(pbest,circuitstring,freq,zrzi,@computec
ircuit,LB,UB,fitstring,options);

% [pbest,zbest,fval,exitflag,output]=
% ... Zfit(data,plotstring,circuitstring,circuitparameters,indexes,'fitP'
or 'fitNP',LB)
        case 7
        data=varargin{1};
        freq=data(:,1);
        plotstring=varargin{2};
        circuitstring=varargin{3};
        pbest=varargin{4};
        options=[];
        indexes=varargin{5};if
isempty(indexes),indexes=1:length(freq);end,freq=data(indexes,1);
        fitstring=varargin{6};
        LB=varargin{7};
        UB=inf*ones(length(pbest),1);
        zrzi=[data(indexes,2),data(indexes,3)];

[pbest,fval,exitflag,output]=curfit(pbest,circuitstring,freq,zrzi,@computec
ircuit,LB,UB,fitstring,options);

% [pbest,zbest,fval,exitflag,output]=
```

```
% ... Zfit(data,plotstring,circuitstring,circuitparameters,indexes,'fitP'
or 'fitNP',LB,UB)
        case 8
        data=varargin{1};
        freq=data(:,1);
        plotstring=varargin{2};
        circuitstring=varargin{3};
        pbest=varargin{4};
        options=[];
        indexes=varargin{5};if
isempty(indexes),indexes=1:length(freq);end,freq=data(indexes,1);
        fitstring=varargin{6};
        LB=varargin{7};
        UB=varargin{8};
        zrzi=[data(indexes,2),data(indexes,3)];

[pbest,fval,exitflag,output]=curfit(pbest,circuitstring,freq,zrzi,@computec
ircuit,LB,UB,fitstring,options);

% [pbest,zbest,fval,exitflag,output]=
% ... Zfit(data,plotstring,circuitstring,circuitparameters,indexes,'fitP'
or 'fitNP',LB,UB,options)
        case 9
        data=varargin{1};
        freq=data(:,1);
        plotstring=varargin{2};
        circuitstring=varargin{3};
        pbest=varargin{4};
        indexes=varargin{5};if
isempty(indexes),indexes=1:length(freq);end,freq=data(indexes,1);
        fitstring=varargin{6};
        zrzi=[data(indexes,2),data(indexes,3)];
        LB=varargin{7};
        UB=varargin{8};
        options=varargin{9};

[pbest,fval,exitflag,output]=curfit(pbest,circuitstring,freq,zrzi,@computec
ircuit,LB,UB,fitstring,options);
        otherwise
        error('No more than 9 inputs in Zfit')
    end
zbest=computecircuit(pbest,circuitstring,freq);
if
~strcmp(plotstring,'z')&&~strcmp(plotstring,'y')&&~strcmp(plotstring,'c')&&
~strcmp(plotstring,'m')&&~isempty(plotstring)
    error('The second input has to be one of these strings: ''z'', ''y'',
''c'', ''m'' or left empty: ''''')
end
if ~isempty(plotstring)
plotz(freq,zbest,data,plotstring)
end
end                     % END of ZFIT
%%%%%%%%%%%%%%%%%%%%%%%%%%%%%%%%%%%%%%%%%%%%%%%%%%%%%%%%%%%%%%%%%%%%%%%%%%%%
%%%
function z=computecircuit(param,circuit,freq)
% Computes the complex impedance Z
% process CIRCUIT to get the elements and their numeral inside CIRCUIT
A=circuit~='p' & circuit~='s' & circuit~='(' & circuit~=')' & circuit~=',';
element=circuit(A);

k=0;
```

```
% for each element
for i=1:2:length(element-2)
    k=k+1;
    nlp=str2num(element(i+1));% idendify its numeral
    localparam=param(1:nlp);% get its parameter values
    param=param(nlp+1:end);% remove them from param
    func=[element(i),'([',num2str(localparam),']',',freq)'];% buit an
functionnal string
    z(:,k)=eval(func);% compute its impedance for all the frequencies
  circuit=regexprep(circuit,element(i:i+1),['z(:,',num2str(k),')'],'once');
end

z=eval(circuit);% compute the global impedance
z=[real(z),imag(z)];% real and imaginary parts are separated to be
processed

end             % END of COMPUTECIRCUIT
% sub functions for the pre-buit elements
function z=R(p,f)% resistor
z=p*ones(size(f));
end

function z=C(p,f)% capacitor
z=j*2*pi*f*p;
z=1./z;
end

function z=L(p,f)% inductor
z=j*2*pi*f*p;
end

function z=E(p,f)% CPE
z=1./(p(1)*(j*2*pi*f).^p(2));
end
% sub functions for the operators parallel and series
function z=s(z1,z2) % 2 zs in series
z=z1+z2;
end

function z=p(z1,z2) % 2 zs in parallel
z=1./(1./z1+1./z2);
end
end
%%%%%%%%%%%%%%%%%%%%%%%%%%%%%%%% END %%%%%%%%%%%%%%%%%%%%%%%%%%%%%%%%%%%%%%%
```

(b) Simulation of open-loop and closed-loop control system frequency response

```
% This program is used in simulating frequency responses of the open loop
and control loop system
% Name: Olakunle Alao
% Student Number: ALXOLA001
% Class: Master's by Dissertation Candidate
% School: University of Cape Town
% MAIN function

% Sub program for open-loop control system for capacitor voltage
cap_voltage = 10;
ind_current = 2;
```

```
duty = 0.5;
batt_vol = 4;
inductor = 0.000144;
capacitor = 0.000470;
load = 10;
A = (-(((batt_vol-cap_voltage)*(1-duty))/(inductor*capacitor)));
B = (ind_current/capacitor);
C = (1/(load*capacitor));
D = (((1-duty)*(1-duty))/(inductor*capacitor));
s = tf('s');
H = ((A+(B*s))/((s^2)+(C*s)+D));
bode(H);
set(findall(gcf,'type','line'),'linewidth',2)
set(gcf,'color','w');
grid on;
[Gm,Pm,Wgm,Wpm] = margin(H)
margin(H)
Gm_dB = 20*log10(Gm)
% Sub program for open-loop control system for inductor current
cap_voltage = 10;
ind_current = 2;
duty = 0.5;
batt_vol = 4;
inductor = 0.000144;
capacitor = 0.000470;
load = 10;
A = ((batt_vol-cap_voltage)/inductor);
B = ((batt_vol-cap_voltage)/(load*inductor*capacitor));
C = (((1-duty)*ind_current)/(inductor*capacitor));
D = (1/(load*capacitor));
E = (((1-duty)*(1-duty))/(inductor*capacitor));
s = tf('s');
H = ((A*s+B+C)/((s^2)+(D*s)+E));
bode(H);
set(findall(gcf,'type','line'),'linewidth',2)
set(gcf,'color','w');
grid on;
[Gm,Pm,Wgm,Wpm] = margin(H)
margin(H)
Gm_dB = 20*log10(Gm)
% Sub program for closed-loop control system
cap_voltage = 10;
ind_current = 2;
duty = 0.5;
batt_vol = 4;
inductor = 0.000144;
capacitor = 0.000470;
load = 10;
kp = 0.05;
ki = 1;
A = (kp*(ind_current/capacitor));
B = ((kp*(-(((batt_vol-cap_voltage)*(1-
duty))/(inductor*capacitor))))+(ki*(ind_current/capacitor)));
C = (ki*(-(((batt_vol-cap_voltage)*(1-duty))/(inductor*capacitor))));
D = 1;
E = ((1/(load*capacitor))+ (kp*(ind_current/capacitor)));
F = (((1-duty)*(1-duty)/(inductor*capacitor))+(kp*(-(((batt_vol-
cap_voltage)*(1-
duty))/(inductor*capacitor))))+(ki*(ind_current/capacitor)));
G = C;
s = tf('s');
```

```
H = (((A*(s^2))+((B*s)+C))/((D*(s^3))+(E*(s^2))+(F*s)+G));
bode(H);
set(findall(gcf,'type','line'),'linewidth',2)
set(gcf,'color','w');
grid on; [Gm,Pm,Wgm,Wpm] = margin(H)
margin(H)
Gm_dB = 20*log10(Gm)
%%%%%%%%%%%%%%%%%%%%%%%%%%%%%%%%%% END %%%%%%%%%%%%%%%%%%%%%%%%%%%%%%%%%%
```

(c) Simulation of buck-boost converter

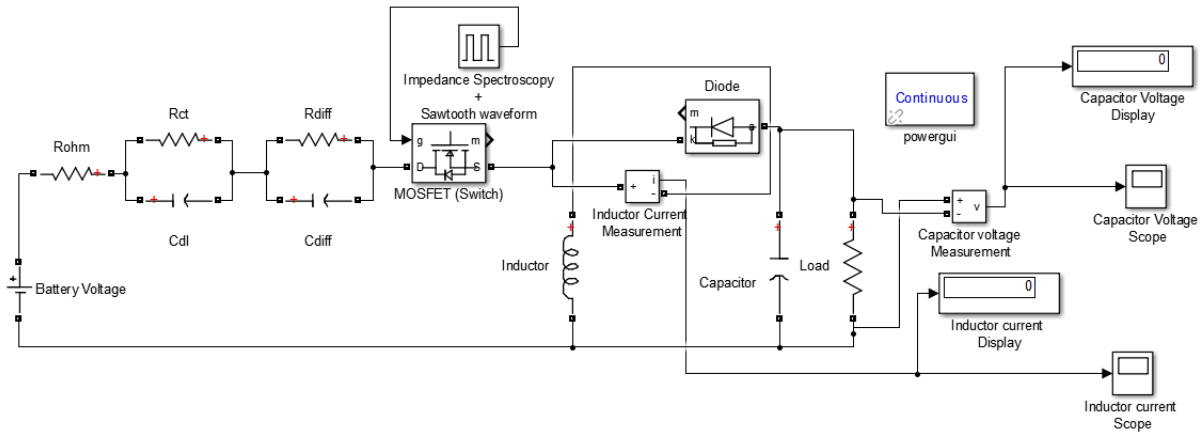

Fig 9.8 Buck-boost converter configuration on MATLAB simulink for lithium NCM battery

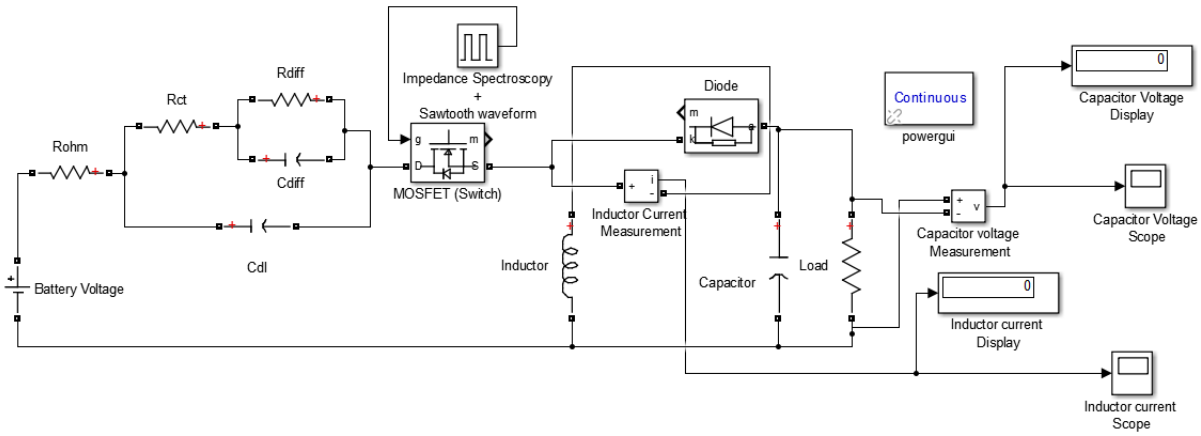

Fig 9.9 Buck-boost converter configuration on MATLAB simulink for lead acid battery

9.3 APPENDIX C – EIS SIGNAL DESIGN

Table 9.1 EIS signal design for lithium NCM battery

S/N	*Injected frequency (Hz)*	*Period (s)*	*Number of cycles*	*Recovery period (s)*	*Total Time Taken (s)*
1	0.02	50	3	12	162
2	0.04	25	3	12	87

3	0.08	12.5	3	12	49.5
4	0.16	7.25	3	6	27.75
5	0.32	3.125	3	6	15.37
6	0.64	1.5625	3	6	10.68
7	1.28	0.78125	10	3	10.81
8	2.56	0.390625	10	3	6.91
9	5.12	0.195313	10	3	4.95
10	10.24	0.097656	10	3	4
11	20.48	0.048828	20	3	4
12	40.96	0.024414	40	3	4
13	81.92	0.012207	81	3	4
14	163.84	0.006104	163	3	4
15	327.68	0.003052	327	3	4
16	655.36	0.001526	655	3	4
17	1310.72	0.000763	1310	3	4
18	2000	0.0005	2000	3	4
∑			**6.8 min**		

Table 9.2 EIS signal design for lead acid battery

S/N	***Injected frequency (Hz)***	***Period (s)***	***Number of cycles***	***Recovery period (s)***	***Total Time Taken (s)***
1	0.1	10	3	24	42
2	0.32	3.125	3	24	21.375
3	0.64	1.5625	3	24	16.6875
4	1.28	0.78125	10	6	13.8125
5	2.56	0.390625	10	6	9.90625
6	5.12	0.195313	10	6	7.953125
7	10.24	0.097656	10	6	7
8	20.48	0.048828	20	6	7
9	40.96	0.024414	40	6	7
10	81.92	0.012207	81	6	7
11	163.84	0.006104	163	6	7
12	327.68	0.003052	327	6	7
13	655.36	0.001526	655	6	7
14	1310.72	0.000763	1310	6	7
15	2621.44	0.000382	2621	6	7
16	4242.8	0.000091	5243	6	7
17	6000	0.000143	6000	6	7
∑			**3.4 min**		

9.4 APPENDIX D – BROADBAND SIGNAL DESIGN

Table 9.3 Multisine optimization for lithium NCM battery

Frequency	***Amplitude***	***Phase***
2000	2	0
1124.7	1.9221	10.58824
632.46	1.8693	42.35294
355.66	1.8313	95.29412
200	1.8055	169.4118
112.47	1.77135	264.7059
63.246	1.73295	381.1765
35.566	1.70255	518.8235
20	1.6639	677.6471
11.247	1.62135	857.6471
6.3246	1.5526	1058.824
3.5566	1.49805	1281.176
2	1.40955	1524.706
1.1247	1.3144	1789.412
0.63246	1.21675	2075.294
0.35566	1.1091	2382.353
0.2	0.9911	2710.588
0.11247	0.8816	3060
0.063246	0.79855	3409.412
0.035566	0.70855	3758.824
0.02	0.60855	4108.235

Table 9.4 Multisine optimization for lead acid battery

Frequency	***Amplitude***	***Phase***
6000	1	0
5242.1	0.9999429	10.58824
2621.44	0.999866	42.35294
1310.72	0.9997827	95.29412
655.36	0.999686	169.4118
327.68	0.9995728	264.7059
163.84	0.9994248	381.1765
81.92	0.9992106	518.8235
40.96	0.9988366	677.6471
20.48	0.9981406	857.6471
10.24	0.9969381	1058.824
5.12	0.9951239	1281.176
2.56	0.9929194	1524.706
1.28	0.9906596	1789.412
0.64	0.9884773	2075.294

0.32	0.9864153	2382.353
0.1	0.9837197	2710.588

Table 9.5 PRBS design for lithium NCM battery

Number of bits	***Sample number***	***Sampling frequency***	***User Frequency***
9	511	10.2	0.02
9	511	10.2	0.04
9	511	10.2	0.08
9	511	10.2	0.16
9	511	10.2	0.32
9	511	10.2	0.64
9	511	10.2	1.28
9	511	10.2	2.56
9	511	10.2	3.4
10	1023	6000	5.865
10	1023	6000	11.73
10	1023	6000	23.46
10	1023	6000	46.92
10	1023	6000	93.84
10	1023	6000	187.68
10	1023	6000	375.36
10	1023	6000	750.72
10	1023	6000	1501.44
10	1023	6000	2000

Table 9.6 PRBS design for lead acid battery

Number of bits	***Sample number***	***Sampling frequency***	***Frequency***
8	255	25.5	0.1
8	255	25.5	0.2
8	255	25.5	0.4
8	255	25.5	0.8
8	255	25.5	1.6
8	255	25.5	3.2
8	255	25.5	6.4
8	255	25.5	8.5
10	1023	18000	17.6
10	1023	18000	35.2
10	1023	18000	70.4
10	1023	18000	140.8
10	1023	18000	281.6
10	1023	18000	563.2

10	1023	18000	1126.4
10	1023	18000	2252.8
10	1023	18000	4505.6
10	1023	18000	6000

Table 9.7 Polynomial Order for PRBS signal design

Bits (n)	***Feedback Polynomial***	***Period ($2^n - 1$)***
2	x^2+x+1	3
4	$x^3+ x^2+1$	15
5	$x^4+ x^3+1$	31
6	$x^5+ x^3+1$	63
8	$x^8+ x^6+x^5+ x^4+1$	255
9	$x^9+ x^5+1$	511
10	$x^{10}+ x^7+1$	1,023
12	$x^{12}+ x^{11}+x^{10}+ x^4+1$	4,095
14	$x^{13}+ x^{12}+x^{11}+ x^8+1$	16,383

9.5 APPENDIX E – REAL-TIME IMPEDANCE SPECTROSCOPY

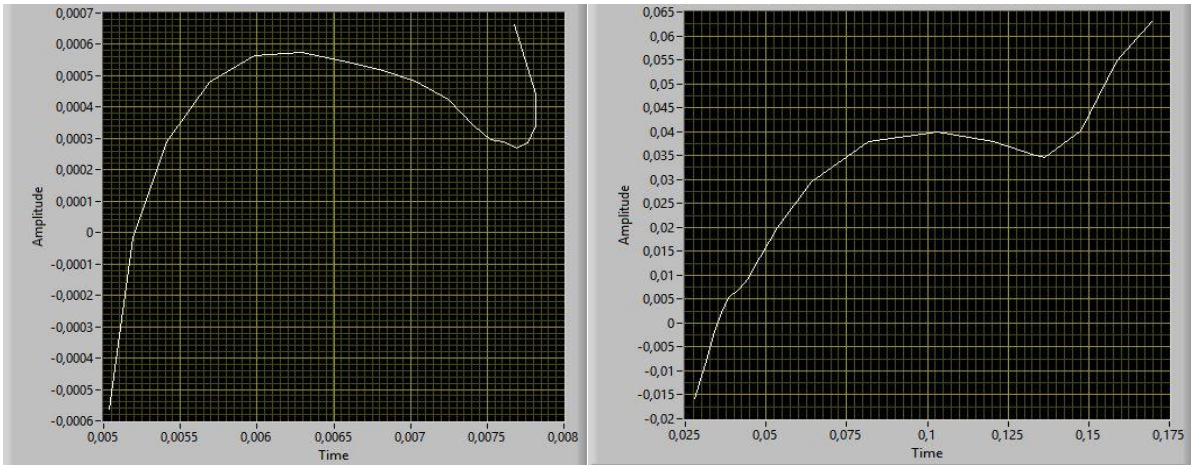

Fig 9.10 Real-time EIS plot for optimized multisine signal lithium NCM (a) and lead acid (b)

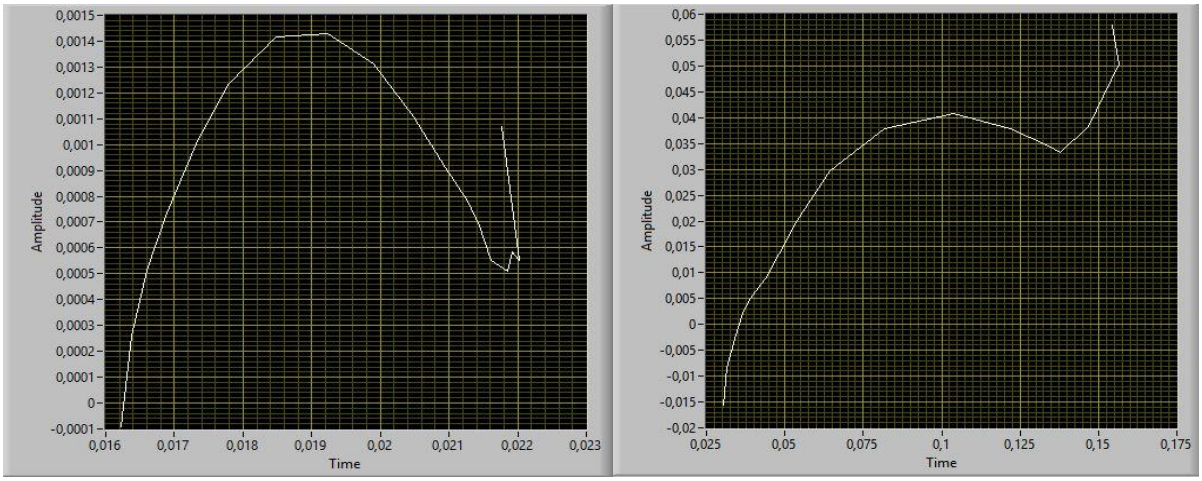

Fig 9.11 EIS plot from optimized chirp signal for lithium NCM (a) and lead acid (b)

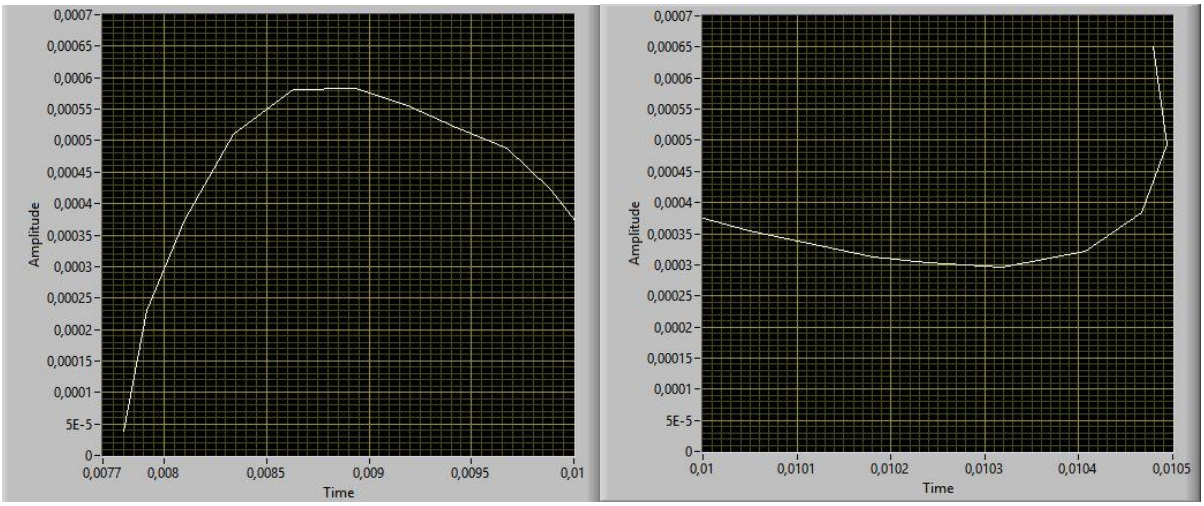

Fig 9.12 Real-time Lithium NCM EIS plot from optimized PRBS signal at frequency bands – 0.02:0.02:3.4 and 5.865:5.865:2000

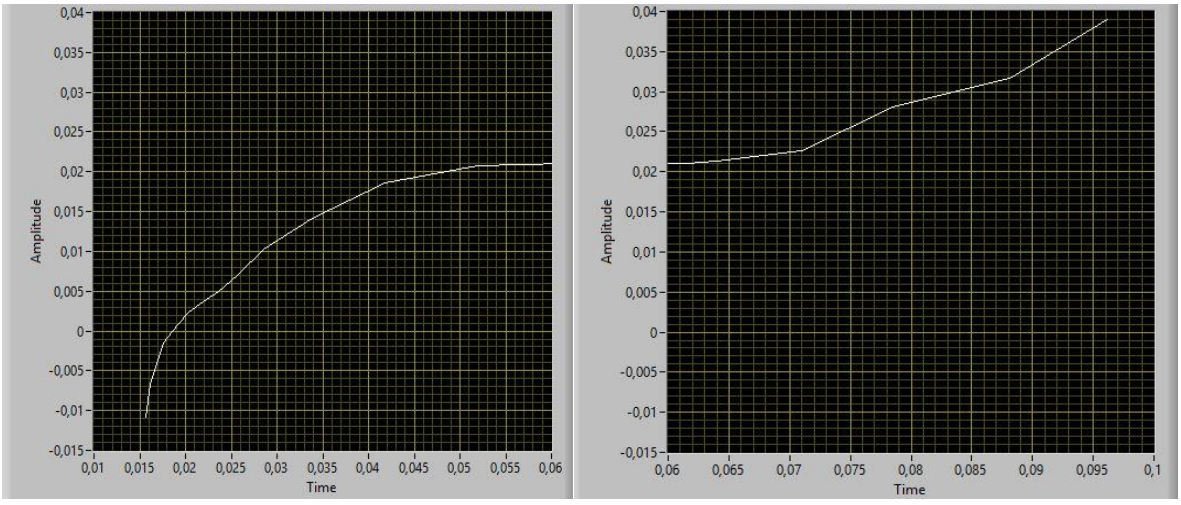

Fig 9.13 Real-time lead acid EIS plot from optimized PRBS signal at frequency bands – 0.1:0.1:8.5, 17.6:17.6:6000